

AD-A061 335

GENERAL DYNAMICS SAN DIEGO CA CONVAIR DIV
THE AERODYNAMIC AND THERMODYNAMIC CHARACTERISTICS OF FOUNTAINS --ETC(U)
AUG 78 A KAREMAA, C W SMITH, H A WEBER
CASD-NSC-78-001

N00014-76-C-0698

F/G 1/3

ONR-CR212-237-1F

NL

UNCLASSIFIED

1 OF 3
AD
A061335



AD A061335

DDC FILE COPY

LEVEL 1

REPORT ONR-CR212-237-1F

12



**THE AERODYNAMIC AND THERMODYNAMIC
CHARACTERISTICS OF FOUNTAINS AND
SOME FAR-FIELD TEMPERATURE DISTRIBUTIONS**

A. KAREMAA H. A. WEBER
C. W. SMITH J. E. GARNER

GENERAL DYNAMICS
Comair Division
Fort Worth Division

CONTRACT NO. N00014-76-C-0908
ONR TASK NR212-237

JULY 1978

FINAL REPORT

DDC
NOV 17 1978
RECEIVED
FULTON

Approved for public release; distribution unlimited.



PREPARED FOR THE

OFFICE OF NAVAL RESEARCH • 800 N. QUINCY ST. • ARLINGTON • VA • 22217

78 11 13 112

Unclassified

SECURITY CLASSIFICATION OF THIS PAGE (When Data Entered)

REPORT DOCUMENTATION PAGE		READ INSTRUCTIONS BEFORE COMPLETING FORM
1. REPORT NUMBER ONR-CR212-237-1F	2. GOVT ACCESSION NO.	3. RECIPIENT'S CATALOG NUMBER
4. TITLE (and Subtitle) The Aerodynamic and Thermodynamic Characteristics of Fountains and Some Far Field Temperature Distributions		5. TYPE OF REPORT & PERIOD COVERED TECHNICAL REPORT 1 MAY 1976 - 30 JUNE 1978
7. AUTHOR(s) Karemaa, Aadu Smith, Charles W.		6. PERFORMING ORG. REPORT NUMBER CASD-NSC-78-001
Weber, Hank A. Garner, Jack E.		8. CONTRACT OR GRANT NUMBER(s) N00014-76-C-0698
9. PERFORMING ORGANIZATION NAME AND ADDRESS General Dynamics Convair Division P.O. Box 80847 San Diego, California 92138		10. PROGRAM ELEMENT, PROJECT, TASK AREA & WORK UNIT NUMBERS 62241N RF41-411-801 NR212-237
11. CONTROLLING OFFICE NAME AND ADDRESS Office of Naval Research (Code 211) 800 N. Quincy Street Arlington, Va. 22217		12. REPORT DATE August 1978
14. MONITORING AGENCY NAME & ADDRESS (if different from Controlling Office) Aadu /Karemaa, Charles W. /Smith Hank A. /Weber Jack E. /Garner		13. NUMBER OF PAGES 103p
15. SECURITY CLASS. (of this report) Unclassified		15a. DECLASSIFICATION/DOWNGRADING SCHEDULE
16. DISTRIBUTION STATEMENT (of this Report) Approved for public release; distribution unlimited		
17. DISTRIBUTION STATEMENT (of the abstract entered in Block 20, if different from Report)		
18. SUPPLEMENTARY NOTES		
19. KEY WORDS (Continue on reverse side if necessary and identify by block number) VTOL Fountains Induced Effects Hover in Ground Effect Near Field Reingestion Far Field Reingestion		
20. ABSTRACT (Continue on reverse side if necessary and identify by block number) This document addresses the flow fields about and below a multi-nozzle VTOL vehicle hovering in the presence of ground. Three specific topics are covered: far field temperature distributions, and the thermodynamic and aerodynamic characteristics of the fountain segment of the near field. An extensive amount of test data was obtained in all three areas, and analyzed in order to model the key aspects of this flow field, and to		

DD FORM 1 JAN 73 1473

EDITION OF 1 NOV 65 IS OBSOLETE

Unclassified

SECURITY CLASSIFICATION OF THIS PAGE (When Data Entered)

147 650

permit the development of methodology for the prediction of fountain induced forces and flow field temperature distributions.

It was determined that the fountains between multiple jets entrain significantly less of the surrounding and/or ambient air than do comparable radial ground jets. Fountains between two nozzles exhibited negative entrainment characteristics in all cases tested. This loss of mass is directly attributed to the entrainment action of the powerful ground jet. The test data indicated that a zero mass flow situation is realized in most cases before the fountains can reach the blocking surface.

Other significant conclusions include observation that the average temperature in the fountain will be significantly higher than at a comparable location in a ground jet. This is attributed to the fact that the ground jet upstream of the fountain entrains the high temperature air from the fountain as well as the cooler ambient air.

APC 100
Title _____
Section _____
Date _____
Page _____

DISTRICT TOWNSHIP / JAMES MARRIOTT TRUSTS
BY _____ SEAL

A

SUMMARY

This document addresses the flow fields about and below a multi-nozzle VTOL vehicle hovering in the presence of ground. Three specific topics are covered: far-field temperature distributions, and both the thermodynamic and aerodynamic characteristics of the fountain segment of the near field. The last two are closely related and subject to the major portion of this report.

An extensive amount of test data was obtained in all three areas, and are presented in Reference 1¹. The analysis of this data was accomplished for the purpose of understanding the complex flow phenomenon associated with hovering VTOL vehicles, the prediction of certain effects, such as fountain induced forces and flow field temperature distributions. Certain key conclusions drawn from this analysis are listed below.

In the area of fountain induced effects, it was determined that the lift contribution of the fountain core is of a second order importance in most cases of interest (for 2, 3, and 4 nozzle arrangements). By far the most powerful effects are the so-called fountain interference effects (see Section 3.6). Analytical and experimental efforts that consider only the fountain core will overlook a major fraction of the fountain contribution.

The second phenomenon that needs attention is that the fountains between multiple jets entrain significantly less of the surrounding and/or ambient air than do comparable radial ground jets. Fountains between two nozzles exhibited negative entrainment characteristics in all cases tested. This means that they experience a net loss of mass as a function of fountain height. This loss of mass is directly attributed to the entrainment action of the powerful ground jet. In other words, the fountain is entrained by the upstream ground jet (between the fountain and the nozzle). For the fountains between two nozzles, the test data indicate that a zero vertical mass flow situation is realized before the fountains can reach the blocking surface. The only exception to this rule occurred when the nozzles were spaced 3.32 diameters from the fountain and the blocking surface was located 2.5 diameters from the ground.

The third principle states that the fountain itself acts as a blocking surface and reduces the entrainment rate of the ground jet located below the blocking surface and between the nozzle and the fountain. Another way to state this is to say that the ground

¹ Eilert, et al, Report GD LST 711 and 712, Low Speed Wind Tunnel Tests to Evaluate the Aerodynamic and Thermodynamic Characteristics of VSTOL Fountains and Inlet Reingestion, 29 August 1977.

jet will entrain less because of the presence of the fountain. What it does entrain, comes from the fountain as well as from the surrounding ambient air supply.

It is recognized that in addition to the fountain, the model or the blocking surface has the most profound effect on the quantity of air available for ground and primary jet entrainment. In this test, only one aspect ratio or plate size was used with each nozzle configuration and spacing. Wider or narrower blocking surfaces would not only influence the entrainment action of the ground and free jets, but are also expected to have a quantitative effect on the blocking effectiveness of the fountain.

These three principles lead to other significant conclusions. For example the average temperature in the fountain will be shown to be significantly higher than at a comparable location in a ground jet. This is attributed to the fact that the ground jet upstream of the fountain entrains the high temperature air from the fountain as well as the cooler ambient air.

These three principles are also the basis for predicting the forces produced by fountains. Specifically the relatively large net losses produced by fountains between two jets (at most h/D 's) are shown to be related to the fact that the fountains usually dissipate prior to reaching the blocking surface and consequently contribute little if any positive lift to the hovering system. At the other end of the spectrum we find that the positive ground effect experienced by a multiple nozzle arrangement, such as the four nozzle case, derives as much or more of its lift from the interference effects as from the core of the fountain. This is in contradiction to the popular conception that attributes all or most of the lift gains to the fountain core.

The examination of the thermodynamic test data from numerous fountains reveals that the combined free jet and ground jet entrain more air from the fountain than from surrounding or ambient atmosphere. The entrainment rates from the ambient regions increase with model height while the air entrained from the fountain diminishes with increased fountain height. As the fountain rises from the ground plane, the two-nozzle fountains lose large amounts of mass and entrain some ambient air for a net loss in mass. The three nozzle fountain also loses mass while the four-nozzle fountain gains mass isothermally.

TABLE OF CONTENTS

<u>Section</u>	<u>Page</u>
1 INTRODUCTION	1
2 TEST AND MODEL DESCRIPTION	2
2.1 MODEL DESCRIPTION	4
2.2 TEST PROCEDURES	8
2.3 INSTRUMENTATION	14
3 FOUNTAIN AERODYNAMIC CHARACTERISTICS	17
3.1 NET FOUNTAIN FORCES	18
3.1.1 Nozzle Number and Spacing Effects	18
3.1.2 Temperature Effects	18
3.1.3 Wind and Pitch Effects	22
3.2 VELOCITY	22
3.3 VERTICAL COMPONENT OF MOMENTUM	40
3.3.1 Integration Scheme	42
3.3.2 Fountain Core Force	42
3.4 FOUNTAIN ENTRAINMENT CHARACTERISTICS	51
3.4.1 Mass Flow Integration	51
3.4.2 Fountain Entrainment Results	54
3.5 THE EFFECT OF THE FOUNTAIN ON THE GROUND JET	58
3.6 FOUNTAIN INTERFERENCE EFFECTS	64
3.7 SUGGESTED METHODOLOGY FOR PREDICTING FOUNTAIN EFFECTS	71
3.8 RECOMMENDATIONS FOR ADDITIONAL RESEARCH	74
4 THERMODYNAMIC CHARACTERISTICS OF FOUNTAINS	77
4.1 FOUNTAIN TEMPERATURE DISTRIBUTION	77
4.2 FOUNTAIN ENTRAINMENT CHARACTERISTICS	91
4.3 METHOD FOR ESTIMATING FOUNTAIN TEMPERATURES	102
4.4 RECOMMENDATIONS FOR ADDITIONAL RESEARCH	104
5 FAR-FIELD TEMPERATURE DISTRIBUTIONS	106
5.1 FAR-FIELD TEMPERATURE DISTRIBUTION AND EFFECT ON INLET TEMPERATURE	109
5.2 FAR-FIELD VELOCITY DISTRIBUTION	115
5.3 CONCLUSIONS AND RECOMMENDATIONS FOR ADDI- TIONAL RESEARCH	115

TABLE OF CONTENTS (Cont.)

<u>Section</u>	<u>Page</u>
REFERENCES	118
APPENDIX A — FOUNTAIN INDUCED FORCES	119
APPENDIX B — FOUNTAIN VELOCITY AND MASS FLOW CHARACTERISTICS	133

LIST OF FIGURES

<u>Figure</u>		<u>Page</u>
1	The Large Section of the General Dynamics Low-Speed Wind Tunnel Was Used	2
2	The Rake Was Positioned Over the Fountain	3
3	The Model was Sting Mounted and Supplied with Heated, High-Pressure Air	4
4	A Pressure and Temperature Rake Was Used to Survey the Flow	5
5	A Multi-purpose Ground Effects Model Was Used	6
6	Selected Plenum Outlets Were Used to Provide Desired Nozzle Spacings	7
7	Rectangular Plates Formed Blocking Surfaces for the Two and Four Nozzle Configurations	9
8	Circular and Triangular Plates Formed Blocking Surfaces for the Single and Three Nozzle Configurations	10
9	Typical Installation of Rectangular Plate (P_{11}) with Two Nozzles	11
10	Typical Installation With Three Nozzles	12
11	Typical Installation With Four Nozzles	13
12	Instrumentation was Provided to Obtain Inlet Temperatures	16
13	The Fountain Effects Were Isolated by Mounting Different Sections of the Plates on the Balance	19
14	Data Were Obtained in Order to Isolate the Total Incremental Fountain Effect	20
15	The Incremental Fountain Lift is Highest With Four Nozzles	21
16	The Temperature Effect Appears to Decrease with Increasing Temperature	21
17	The Total Effect of the Wind Was to Produce Higher Lift Losses	23
18	Wind Increases the Fountain Lift Increment	24

LIST OF FIGURES (Cont.)

<u>Figure</u>		<u>Page</u>
19	Additional Data Were Required to Isolate the Fountain Effect in the Presence of a Wind	25
20	Model Pitch Attitude Has an Irregular Effect on Induced Forces	26
21	Fountain Flow Directions Between Two Nozzles are Orderly	27
22	Fountain Model for Two Nozzles	29
23	Fountain Flow Angles Between Two Nozzles Can Be Estimated By an Extension and Rotation of the Ground Jet	30
24	Fountain Dynamic Pressure Contours Between Two Nozzles	31
25	The Fountain Between Three Unequally Spaced Nozzles is Inclined	32
26	Estimate of Fountain Inclination for Three Unequally-spaced Nozzles	33
27	A Central Core Fountain is Formed Between Three Nozzles	35
28	Four Nozzle Fountain Flows Coalesce Towards the Center of the Fountain	36
29	A Central Core Fountain is Formed Between Four Nozzles	37
30	Dynamic Pressure Decay Characteristics are Dependent on the Number of Nozzles	37
31	In Some Cases the Low Position of the Blocking Surface Reduces the Dynamic Pressure in the Fountain (Two Nozzles)	38
32	Three-nozzle Fountain Decay Characteristics Depend on Nozzle Spacing and Blocking Surface Position (h/D)	39
33	Blocking Surface Height Has a Strong Effect on Four-nozzle Fountain Decay Characteristics	40
34	Fountain Strength Increases with Number of Nozzles	41
35	The Fountain Core Force with Two Widely-spaced Nozzles	43
36	The Fountain Core Force with Two Medium-spaced Nozzles	45

LIST OF FIGURES (Cont.)

<u>Figure</u>		<u>Page</u>
37	Temperature, Wind and Pitch Effect the Fountain Core Lift	46
38	Pitch and Wind Decrease the Fountain Core Lift	47
39	Four-nozzle Fountain Lift is Concentrated Near the Fountain Center	48
40	A Partial Fountain Core Force with Three Nozzles	49
41	Four Nozzle Fountains Exert a Positive Force on the Blocking Surface	50
42	Blocking Surface Height Has a Significant Effect on the Fountain Lift	52
43	The Fountains Between Three Nozzles become Stronger When the Blocking Surface is Raised Up (h/D Increased)	53
44	Mass Flows are Determined by Integrating Fountain Flow Characteristics	54
45	Fountains Between Two Nozzles Lose Mass as a Function of Height	56
46	The Fountain Blocks the Flow of Gas to the Ground Jet	57
47	The Fountain Reaches Zero Mass Flow Prior to Contacting the Blocking Surface Except for Closely-spaced Nozzles (Two Nozzles)	58
48	At Higher Locations of the Blocking Surface More of the Entrained Air Can Be Obtained Through the Sides (Cross-Hatched Areas)	59
49	Maximum Fountain Height is a Function of Nozzle Spacing (Two Nozzles)	60
50	Fountains Between Four Nozzles Gain Mass as a Function of Height	61
51	Ground Jet Entrainment is greatly Reduced by the Presence of a Fountain (Two Nozzles)	62
52	Ground Jet Entrainment is Greatly Reduced by the Presence of a Fountain Between Three and Four Nozzles	63

LIST OF FIGURES (Cont.)

<u>Figure</u>		<u>Page</u>
53	At Certain Blocking Surface Height (h/D) the Fountain Has Little Or No Effect On the Ground Jet Entrainment Characteristics	63
54	Fountains Between Two Nozzles Generate Mostly Negative Interference Effects	65
55	Fountain Between Four Nozzles Produce Positive Interference Effects	66
56	The Fountain Produced Interference Effects are Referenced to the Area S_f Between the Nozzle and the Fountain Theoretical Centerline	67
57	Positive Interference Effects Exist Only for Widely Spaced Nozzles at Close Proximity to the Ground (Two Nozzles)	68
58	Positive Interference Effects of the Fountain Increase With Decrease in Ω	69
59	The Interference Effects for Fountains Between Four Nozzles are Significantly More Positive than for Comparably Spaced Two Nozzles	70
60	The Arrangement of a Large Number of Nozzles in a Circular or Elliptical Pattern Will Produce Positive Pressure Fields	70
61	After the Planform is Divided into Segments Along Fountain Centerlines, each Segment is treated as a Separate Problem and the Lift Losses from Ground Jet and Fountain Effects are Estimated	71
62	Proposed Sequence for Calculating Induced Effects	72
63	Even for Configurations Involving Powerful Fountains, The Induced Effects are Equal to or More Significant than the Fountain Core Contributions	74
64	Flow Field Temperatures Were Surveyed for the Two Nozzle Configuration ($d_f/D = 6.38$)	78
65	Flow Field Temperature Profiles for the Two Nozzles Configuration ($d_f/D = 6.38$) at $h/D = 5.0$	79

LIST OF FIGURES (Cont.)

<u>Figure</u>		<u>Page</u>
66	Flow Field Temperature Profiles for the Two Nozzles Configuration ($d_f/D = 6.38$) at $Z/D = 1.5$	80
67	Flow Field Temperatures Were Surveyed for the Three Nozzle Configuration ($D = 1.61$)	82
68	Flow Field Temperature Profiles for the Three Nozzle Configuration ($D = 1.61$) at $h/D = 5.0$	83
69	Flow Field Temperatures Were Surveyed for the Three Nozzle Configuration ($D = 1.32$)	84
70	Flow Field Temperature Profiles for the Three Nozzle Configuration ($D = 1.32$) at $h/D = 5.0$	85
71	Flow Field Temperatures Were Surveyed for the Four Nozzle Configuration	86
72	Flow Field Temperature Profiles for the Four Nozzle Configuration at $h/D = 5.0$	87
73	Flow Field Temperatures Were Surveyed for the Two Nozzle Configuration ($d_f/D = 3.32$)	88
74	Flow Field Temperature Profiles for the Two Nozzle Configuration ($d_f/D = 3.32$) at $h/D = 5.0$	89
75	Model Pitch Shifts the Fountain Core Forward	90
76	Wind Reduces Fountain Temperatures, Two Nozzles	92
77	Flow Field Temperatures Decay Rapidly Near the Edge of the Blocking Surface	93
78	Nondimensionalized Fountain Temperatures Increase as Nozzle Jet Temperature is Reduced, Two Nozzles	94
79	Fountain Temperatures Decay with Height, Two Nozzles	95
80	Fountain Temperatures Do Not Decay with Height, Three and Four Nozzles	96
81	An Adiabatic Control Volume Defines Flow Field Thermal Balance	96

LIST OF FIGURES (Cont.)

<u>Figure</u>		<u>Page</u>
82	Free Plus Ground Jet Entraines Ambient Air and Fountain Mass	99
83	Fountain Flow Entrained by the Ground Jet Diminishes with Fountain Height	100
84	The Fountain Loses Mass and Entraines Ambient Air, Two Nozzle Configurations	101
85	The Three Nozzle Fountain Loses Mass, The Four Nozzle Fountain Gains Mass	102
86	Fountain Entrainment and Mass Loss is Influenced by Local Dynamic Pressure and Fountain/Model Height Ratio	103
87	Fountain Temperatures are Considerably Higher than Comparable Temperatures in Radial Ground Jet	105
88	The Hot-gas Recirculation-cloud Geometry Had Been Appraised	107
89	The Flow Field Was Surveyed at Various Locations in Front of the Model	108
90	The Reingestion Test Utilized 3 Model Configurations and Various Model and Rake Positions	109
91	The Temperature Profiles in Front of the Model Were Typically Independent of Tranverse Location	110
92	The Flow-field Temperature Profiles in Front of the 2-jet Configuration are influenced by Wind Velocity	111
93	The Inlet Temperatures of the 2-jet Configuration are Influenced by Velocity	112
94	The Flow-field Temperature Profiles in Front of the 3-jet Configuration are Influenced by Wind Velocity	113
95	The Inlet Temperatures of the 3-jet Configuration are Influenced by Wind Velocity	114
96	The Inlet Temperatures of the 3-jet Configuration Were Not Influenced by the Scab-on Plate	115

LIST OF FIGURES (Cont.)

<u>Figure</u>		<u>Page</u>
97	The Flow-field Temperature Profiles are Cooler at 67° Sideslip Than at 0° Sideslip for the 3-jet Configuration	116
98	The Inlet Temperatures of the 3-jet Model are Influenced by Sideslip	117
A-1	Fountain Effect on Lift with Two Closely-Spaced Nozzles	120
A-2	Fountain Effect on Lift with Two Medium-Spaced Nozzles at 400°F	121
A-3	Fountain Effect on Lift with Two Medium-Spaced Nozzles at 200°F	122
A-4	Fountain Effect on Lift with Two Medium-Spaced Nozzles at 70°F	123
A-5	Fountain Effect on Lift with Three Small Nozzles	124
A-6	Fountain Effect on Lift with Three Large Nozzles	125
A-7	Fountain Effect on Lift with Four Small Nozzles	126
A-8	Temperature Effect on Lift with a Single Nozzle and a Rectangular Plate	127
A-9	Temperature Effect on Lift with Two Nozzles and a Rectangular Plate	128
A-10	Temperature Effect on Lift with a Single Nozzle and a Triangular Plate	129
A-11	Temperature Effect on Lift with a Single Nozzle and a Rectangular Plate	130
A-12	Temperature Effect on Lift with a Single Nozzle and a Small Circular Plate	131
A-13	Temperature Effect on Lift with a Single Nozzle and a Large Circular Plate	132
B-1	Mass Flow and Dynamic Pressure Profiles with Two Nozzles; $d_f/D = 6.38$, $h/D = 2.52$, $Z/D = 1.36$	134

LIST OF FIGURES (Cont.)

<u>Figure</u>		<u>Page</u>
B-2	Mass Flow and Dynamic Pressure Profiles with Two Nozzles; $d_f/D = 6.38$, $h/D = 3.53$, $Z/D = 1.55$	135
B-3	Mass Flow and Dynamic Pressure Profiles with Two Nozzles; $d_f/D = 6.38$, $h/D = 3.53$, $Z/D = 2.35$	136
B-4	Mass Flow and Dynamic Pressure Profiles with Two Nozzles; $d_f/D = 6.38$, $h/D = 5.03$, $Z/D = 1.48$	137
B-5	Mass Flow and Dynamic Pressure Profiles with Two Nozzles; $d_f/D = 6.38$, $h/D = 5.04$, $Z/D = 2.48$	138
B-6	Mass Flow and Dynamic Pressure Profiles with Two Nozzles; $d_f/D = 6.38$, $h/D = 5.04$, $Z/D = 3.80$	139
B-7	Mass Flow and Dynamic Pressure Profiles with Two Nozzles; $d_f/D = 6.38$, $h/D = 8.03$, $Z/D = 1.55$	140
B-8	Mass Flow and Dynamic Pressure Profiles with Two Nozzles; $d_f/D = 6.38$, $h/D = 8.03$, $Z/D = 3.52$	141
B-9	Mass Flow and Dynamic Pressure Profiles with Two Nozzles; $d_f/D = 6.38$, $h/D = 8.03$, $Z/D = 5.55$	142
B-10	Mass Flow and Dynamic Pressure Profiles with Two Nozzles; $d_f/D = 3.32$, $h/D = 2.52$, $Z/D = 0.79$	143
B-11	Mass Flow and Dynamic Pressure Profiles with Two Nozzles; $d_f/D = 3.32$, $h/D = 2.52$, $Z/D = 1.35$	144
B-12	Mass Flow and Dynamic Pressure Profiles with Two Nozzles; $d_f/D = 3.32$, $h/D = 3.56$, $Z/D = 0.77$	145
B-13	Mass Flow and Dynamic Pressure Profiles with Two Nozzles; $d_f/D = 3.32$, $h/D = 3.56$, $Z/D = 1.50$	146
B-14	Mass Flow and Dynamic Pressure Profiles with Two Nozzles; $d_f/D = 3.32$, $h/D = 3.55$, $Z/D = 2.29$	147
B-15	Mass Flow and Dynamic Pressure Profiles with Two Nozzles; $d_f/D = 3.32$, $h/D = 5.05$, $Z/D = 1.51$	148
B-16	Mass Flow and Dynamic Pressure Profiles with Two Nozzles; $d_f/D = 3.32$, $h/D = 5.05$, $Z/D = 2.48$	149

LIST OF FIGURES (Cont.)

<u>Figure</u>		<u>Page</u>
B-17	Mass Flow and Dynamic Pressure Profiles with Two Nozzles; $d_f/D = 3.32$, $h/D = 3.32$, $h/D = 5.05$, $Z/D = 3.75$	150
B-18	Mass Flow and Dynamic Pressure Profiles with Two Nozzles; $d_f/D = 3.32$, $h/D = 8.04$, $Z/D = 1.55$	151
B-19	Mass Flow and Dynamic Pressure Profiles with Two Nozzles; $d_f/D = 3.32$, $h/D = 8.05$, $Z/D = 3.47$	152
B-20	Mass Flow and Dynamic Pressure Profiles with Three Nozzles; $D = 1.32$, $h/D = 2.58$, $Z/D = 0.83$	153
B-21	Mass Flow and Dynamic Pressure Profiles with Three Nozzles; $D = 1.32$, $h/D = 2.58$, $Z/D = 0.90$	154
B-22	Mass Flow and Dynamic Pressure Profiles with Three Nozzles; $D = 1.32$, $h/D = 2.58$, $Z/D = 1.22$	155
B-23	Mass Flow and Dynamic Pressure Profiles with Three Nozzles; $D = 1.32$, $h/D = 3.56$, $Z/D = 0.72$	156
B-24	Mass Flow and Dynamic Pressure Profiles with Three Nozzles; $D = 1.32$, $h/D = 3.56$, $Z/D = 1.52$	157
B-25	Mass Flow and Dynamic Pressure Profiles with Three Nozzles; $D = 1.32$, $h/D = 3.56$, $Z/D = 2.24$	158
B-26	Mass Flow and Dynamic Pressure Profiles with Three Nozzles; $D = 1.32$, $h/D = 5.05$, $Z/D = 1.57$	159
B-27	Mass Flow and Dynamic Pressure Profiles with Three Nozzles; $D = 1.32$, $h/D = 5.05$, $Z/D = 2.56$	160
B-28	Mass Flow and Dynamic Pressure Profiles with Three Nozzles; $D = 1.32$, $h/D = 5.05$, $Z/D = 3.74$	161
B-29	Mass Flow and Dynamic Pressure Profiles with Three Nozzles; $D = 1.32$, $h/D = 8.07$, $Z/D = 1.57$	162
B-30	Mass Flow and Dynamic Pressure Profiles with Three Nozzles; $D = 1.61$, $h/D = 3.58$, $Z/D = 1.52$	163
B-31	Mass Flow and Dynamic Pressure Profiles with Three Nozzles; $D = 1.61$, $h/D = 3.58$, $Z/D = 2.44$	164
B-32	Mass Flow and Dynamic Pressure Profiles with Three Nozzles; $D = 1.61$, $h/D = 5.07$, $Z/D = 1.63$	165

LIST OF FIGURES (Cont.)

<u>Figure</u>		<u>Page</u>
B-33	Mass Flow and Dynamic Pressure Profiles with Three Nozzles; $D = 1.61$, $h/D = 5.08$, $Z/D = 2.56$	166
B-34	Mass Flow and Dynamic Pressure Profiles with Four Nozzles; $D = 1.32$, $h/D = 3.60$, $Z/D = 1.56$	167
B-35	Mass Flow and Dynamic Pressure Profiles with Four Nozzles; $D = 1.32$, $h/D = 3.62$, $Z/D = 2.20$	168
B-36	Mass Flow and Dynamic Pressure Profiles with Four Nozzles; $D = 1.32$, $h/D = 5.15$, $Z/D = 1.55$	169
B-37	Mass Flow and Dynamic Pressure Profiles with Four Nozzles; $D = 1.32$, $h/D = 5.11$, $Z/D = 2.55$	170
B-38	Mass Flow and Dynamic Pressure Profiles with Four Nozzles; $D = 1.32$, $h/D = 5.11$, $Z/D = 3.75$	171
B-39	Mass Flow and Dynamic Pressure Profiles with Four Nozzles; $D = 1.32$, $h/D = 8.11$, $Z/D = 3.56$	172
B-40	Mass Flow and Dynamic Pressure Profiles with Four Nozzles; $D = 1.32$, $h/D = 8.10$, $Z/D = 6.70$	173
B-41	Mass Flow and Dynamic Pressure Profiles with Two Nozzles at 200°F; $d_f/D = 3.32$, $h/D = 5.05$, $Z/D = 1.52$	174
B-42	Mass Flow and Dynamic Pressure Profiles with Two Nozzles at 200°F, $d_f/D = 3.32$, $h/D = 5.05$, $Z/D = 2.52$	175
B-43	Mass Flow and Dynamic Pressure Profiles with Two Nozzles at 200°F, $d_f/D = 3.32$, $h/D = 5.05$, $Z/D = 3.82$	176
B-44	Mass Flow and Dynamic Pressure Profiles with Two Nozzles Pitched 10°; $d_f/D = 3.32$, $h/D = 5.04$, $Z/D = 1.50$	177
B-45	Mass Flow and Dynamic Pressure Profiles with Two Nozzles in a 30 Knot Wind; $d_f/D = 3.32$, $h/D = 5.03$, $Z/D = 1.50$	178
B-46	Mass Flow and Dynamic Pressure Profiles with Two Nozzles in a 30 Knot Wind; $d_f/D = 3.32$, $h/D = 5.03$, $Z/D = 2.48$	179
B-47	Mass Flow and Dynamic Pressure Profiles with Two Nozzles in a 30 Knot Wind; $d_f/D = 3.32$, $h/D = 5.03$, $Z/D = 3.77$	180

NOMENCLATURE

A	Nozzle Spacing Dimension	in.
A	Area Used in Fountain Integration	in. ²
B	Nozzle Spacing Dimension	in.
b	Reference Span for Rolling Moment Coefficients	in.
c_p	Constant Pressure-Specific Heat	Btu/lb _m /°F
c	Reference Chord for Pitching Moment Coefficients	in.
D	Nozzle Exit Diameter	in.
D _p	Diameter of Circular Plate	in.
d _f	Distance From One of Two Jets to the Fountain on a Line Perpendicular to the Fountain	in.
F	Force Vector used in Fountain Integration	lb _f
F _j	Total Isolated Thrust of all Jet Nozzles for Single or Multiple-jet Configurations	lb _f
H, h	Height of the Blocking Surface Above the Ground Surface	in.
h _f	Maximum Height of Fountain	in.
H _c	Height of the Reingestion Cloud Above the Ground Surface	in.
K _{fi}	Incremental Lift due to Fountain Interference Normalized by Area S _F	—
ΔL	Total Induced Lift on the Blocking Surfaces	lb _f
ΔL _F	Total Incremental Effect of the Fountain on the Induced Lift	lb _f
L _{FC}	Lift of the Fountain Core Obtained from Integrations	lb _f
ΔL _{fi}	Incremental Lift due to Fountain Interference	lb _f
t _f	Length of the Fountain Measured from a Line Perpendicular to the Line Between Two Jets	in.

NOMENCLATURE (Cont.)

ΔM	Total Induced Pitching Moment on the Blocking Surface about the Centroid of the Nozzle Configuration	in. -lb _f
\dot{m}	Mass Flow per Unit Area Obtained from the Rake Measurements	lb _m /in. ² sec
\dot{m}_{af}	Fountain Mass Flow Entrained by Ground Jet	lb _m /sec
\dot{m}_e	Total Mass Flow Entrainment	lb _m /sec
\dot{m}_{ef}	Mass Flow Lost by Vertical Core of Fountain Between Two Designated X-Y Planes	lb _m /sec
\dot{m}_{ea}	Mass Flow Entrained Between any Two Specified Points in the Flow Field with Assumed Temperature Equal to Ambient Temperature	lb _m /sec
\dot{m}_F	Total Mass Flow Through an X-Y Plane Cut Through the Fountain	lb _m /sec
\dot{m}_j	Nozzle Exit Mass Flow or Subtended Portion of Total Flow	lb _m /sec
\dot{m}_T	Total Mass Flow at a Given Point in the Flow Field	lb _m /sec
N_j^i	Nozzle Designation where j = Location on the Plenum (See Figure 6) i = 1, Nozzle Diameter = 1.32 in. i = 2, Nozzle Diameter = 1.41 in. i = 3, Nozzle Diameter = 1.61 in.	—
NPR	Nozzle Pressure Ratio	—
P_k	Blocking Surface Designation Where k Indicates Plate Used (see Figures 7 and 9)	—
P_5	Total Pressure Tap on the Rake Cone Probe	psi
Q_F	Dynamic Pressure in the Fountain	psi
Q_{FV}	Vertical Component of the Fountain Dynamic Pressure	psi
Q_n	Nozzle Dynamic Pressure	psi

NOMENCLATURE (Cont.)

Q_w	Dynamic Pressure of the Free Stream Wind	psi
R	Longitudinal Distance from the Nozzle (in the reingestion cloud)	in.
ΔR	Total Induced Rolling Moment on the Blocking Surface about the Model Plane of Symmetry	in. -lb
R_S	Longitudinal Distance from the Nozzle to the Point at Which the Reingestion Cloud Separates from the Ground	in.
S_F	Area Between Nozzle and Fountain that Represents the Region over Which the Fountain and Induced Effects will be Concentrated (see Figure 56)	in. ²
T	Temperature	°F
T_A, T_∞	Ambient Air Temperature	°F
T_f	Temperature of Gas in Fountain	°F
\bar{T}_f	Average Fountain Gas Temperature	°F
T_N	Nozzle Plenum Gas Temperature	°F
ΔT_R	Flow Field Temperature Ratio, $(T - T_\infty)/(T_N - T_\infty)$	—
V	Velocity in the Fountain	fps
V_J	Nozzle Exhaust Velocity	kts
V_w	Velocity of the Ambient Wind	kts
X	Distance from the Centroid of the Nozzle Configuration Perpendicular to the Rake Path—Used in the Fountain Surveys	in.
X_R	Distance Along Model Centerline From the Nose of the Model Used in the Far-Field Reingestion Surveys	in.
Y	Distance from the Centroid of the Nozzle Configuration Along the Rake Path Used in the Fountain Surveys	in.
Y_R	Distance from the Plane of Symmetry Perpendicular to the Model Centerline Used in the Far-Field Reingestion Surveys	in.

NOMENCLATURE (Cont.)

Z	Distance Above Ground Plane Used in the Fountain Surveys	in.
Z_R	Distance of the Rake Center Above the Ground Plane Used in the Far Field Reingestion Surveys	in.
α	Angle-of-Attack of the Blocking Surface	deg
γ_F	Fountain Flow Angularity from Vertical in the XZ Plane, Positive to the Rear of the Model	deg
δ	True Flow Angularity From Vertical	deg
θ_F	Fountain Flow Angularity from Vertical in the YZ Plane, Positive to the Right (as viewed from the pilot's position)	deg
ρ	Density	slugs/ft ³
Ω	Angle Formed by Fountain Stagnation Line at Ground (Figure 58)	deg

SECTION 1

INTRODUCTION

The research activity outlined in this report was sponsored by the Office of Naval Research under Contract No. N00014-76-C-0698 and executed by General Dynamics Corporation. Both the Convair and Fort Worth Divisions participated in this research program. The contracted activity spans the period from 1 May 1976 through 30 June 1978. Tests were conducted in May of 1977 at the Convair low speed test facility. A major portion of the test data analysis was accomplished at the Fort Worth Division.

This research activity was monitored and guided by Dr. Robert E. Whitehead of ONR. The program was managed by Aadu Karemaa of Convair. He was also Lead Research Engineer for the fountain induced aerodynamic effects. Mr. C.W. Smith of Fort Worth Division accomplished most of the force data reduction and analysis and is a major contributor to this final report.

Mr. H.A. Weber of Convair was the Lead Research Engineer in the area of thermodynamic characteristics of the near and far fields. He directed all testing and the data analysis related to the fountain thermodynamics. He was assisted in his efforts by Dr. J.E. Garner of the Fort Worth Division. Dr. Garner also accomplished all far field analytical activities and contributed the section addressing that specific area.

The tests were conducted by Mr. M.W. Eilert.

SECTION 2

TEST AND MODEL DESCRIPTION

Testing was conducted in the large downstream section, 16 by 20 feet, of the General Dynamics Low-Speed Wind Tunnel, Figures 1 and 2, at San Diego, California. Heated high-pressure air was supplied to the model as shown in the installation diagram of Figure 3. Model-induced forces and moments, exclusive of the nozzle thrust, were measured by a six-component internal strain gage balance system. Fountain and reingestion flow-field characteristics were measured by means of a transversing cone-probe pressure and temperature rake, Figure 4, which allowed the determination of the flow angularity. Additionally, inlet flow temperatures were recorded at all test conditions.

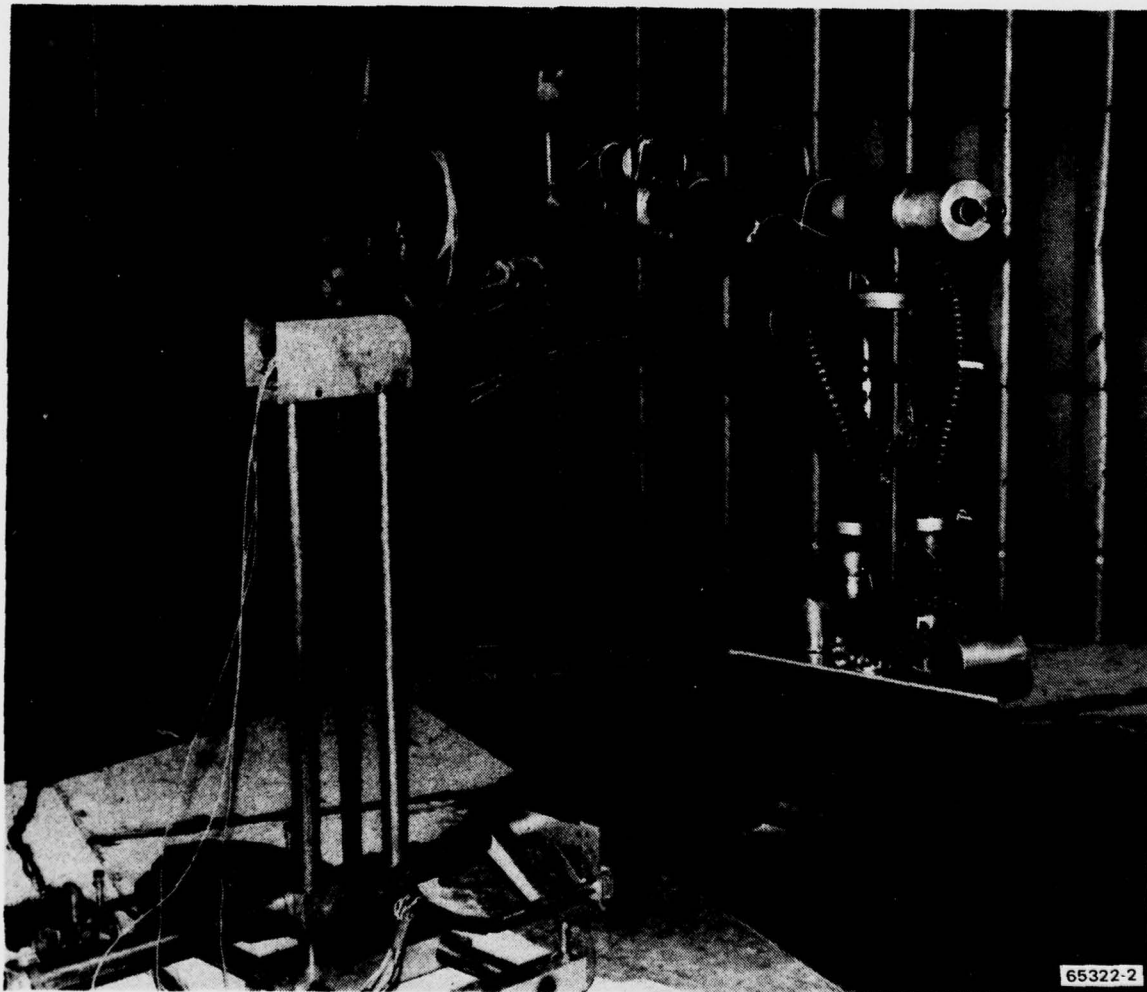
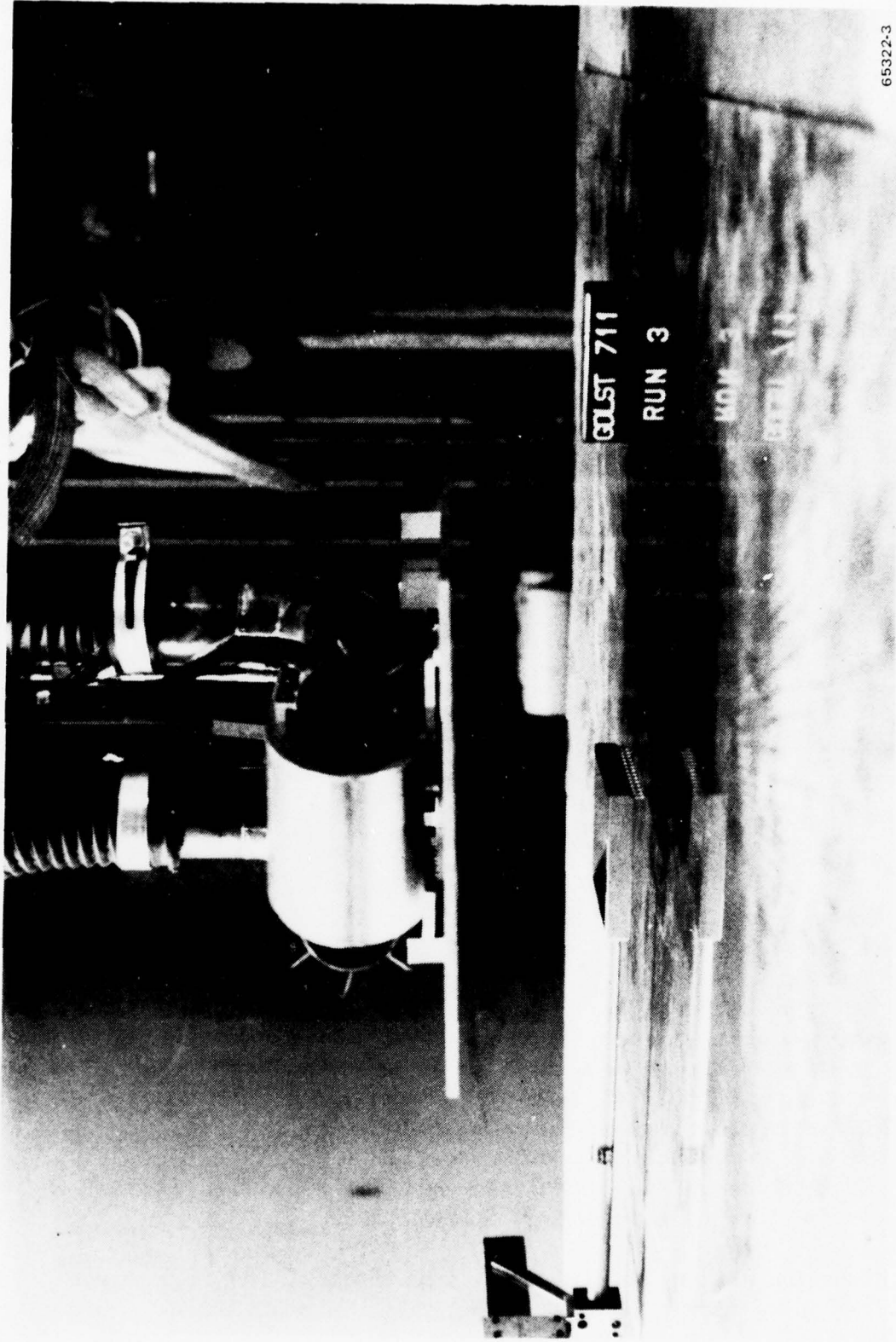


Figure 1. The Large Section of the General Dynamics Low-Speed Wind Tunnel Was Used



65322-3

Figure 2. The Rake Was Positioned Over the Fountain

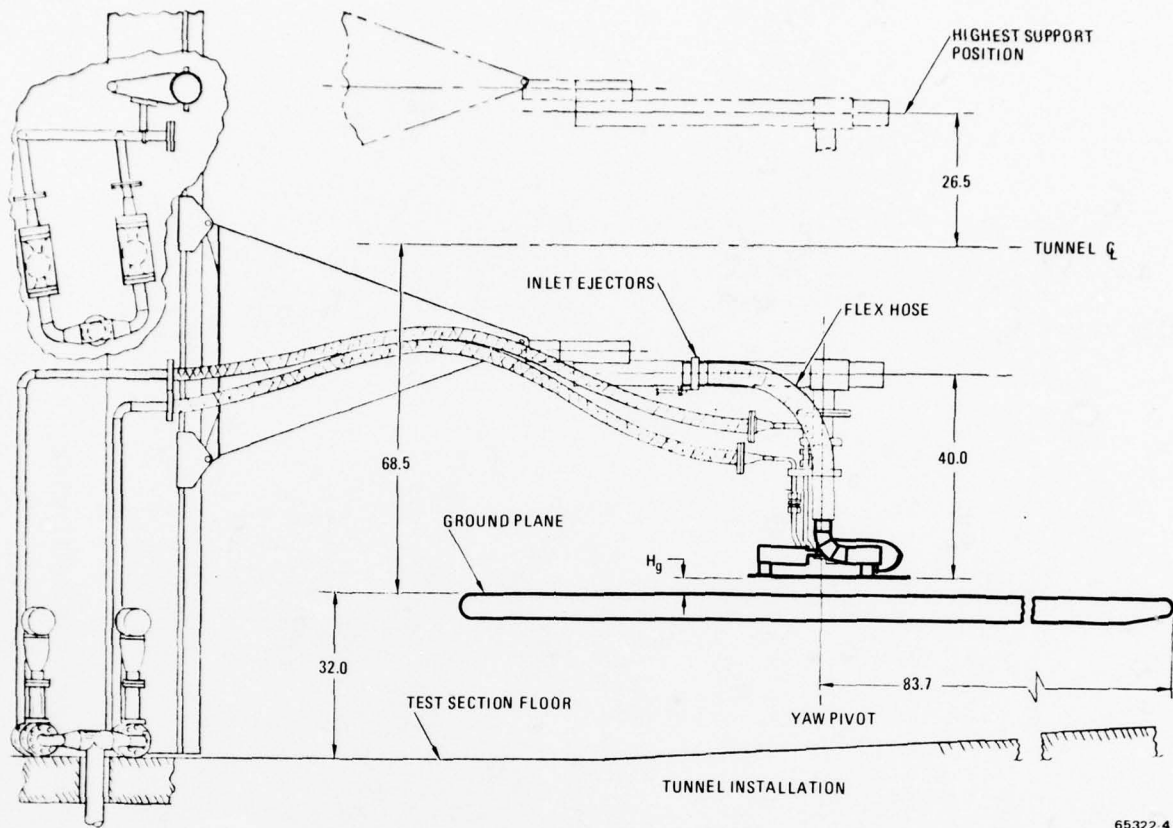


Figure 3. The Model was Sting Mounted and Supplied with Heated, High-Pressure Air

2.1 MODEL DESCRIPTION

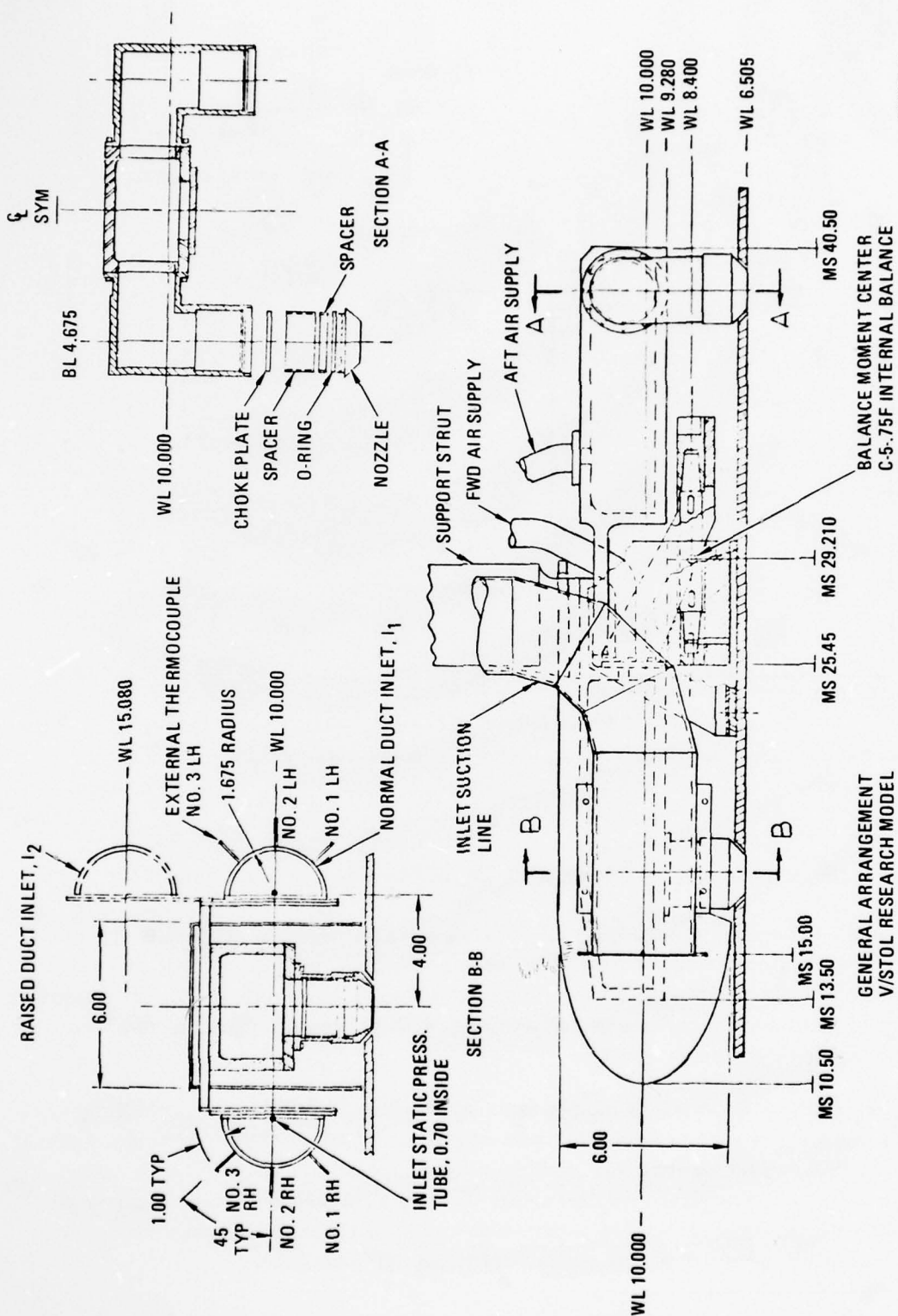
The basic, modular-type model utilized is nominally a 1/15-scale model representation of a multitude of fighter-type VTOL aircraft. Composed of two general aerodynamic configurations, the model can simulate several propulsion arrangements with a fuselage, delta wing and canard configuration. For the purposes of this test, the fuselage and wings were removed from the model substructure and various flat plates installed. A family of circular, rectangular and triangular plates was employed for the purpose of conducting this basic research. These plates can be mounted on a balance, and the propulsion system or nozzle-induced forces read directly. It is also possible to remove sections of these plates or to mount sections of these plates off balance. All flat plates are made of aluminum and have sharp 90-degree edges. A general arrangement of the model is provided in Figure 5.

The model substructure is constructed of steel and consists of two high-pressure plenums, an internal balance, a balance cooling jacket, and a fuselage or flat plate



support bracket. The plenums are machined from a single piece of steel with the bottom surface welded into place. Three sides of each plenum include several two-inch diameter holes to allow for installation of various nozzles. The nozzle locations used for the multi-nozzle configurations tested are shown in Figure 6. Cover plates are provided for the non-blowing positions.

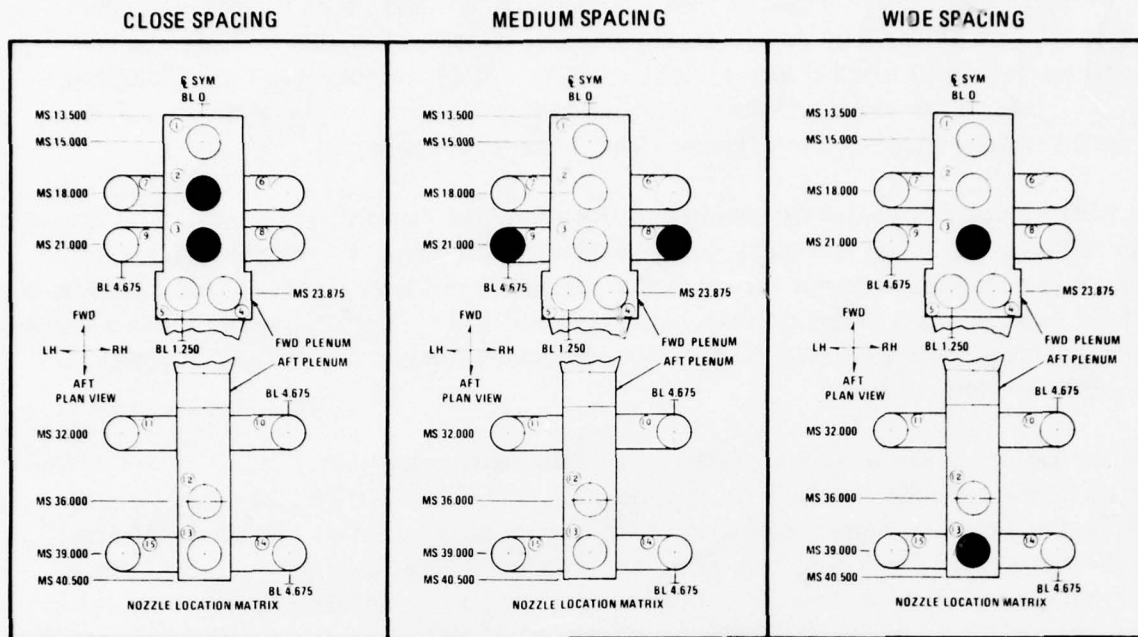
²Tyler, S. P. Calibration of the VSTOL Propulsion Induced Interference Research Model Jet Nozzles, Convair Report TM-73-VSTOL-02, 1973.



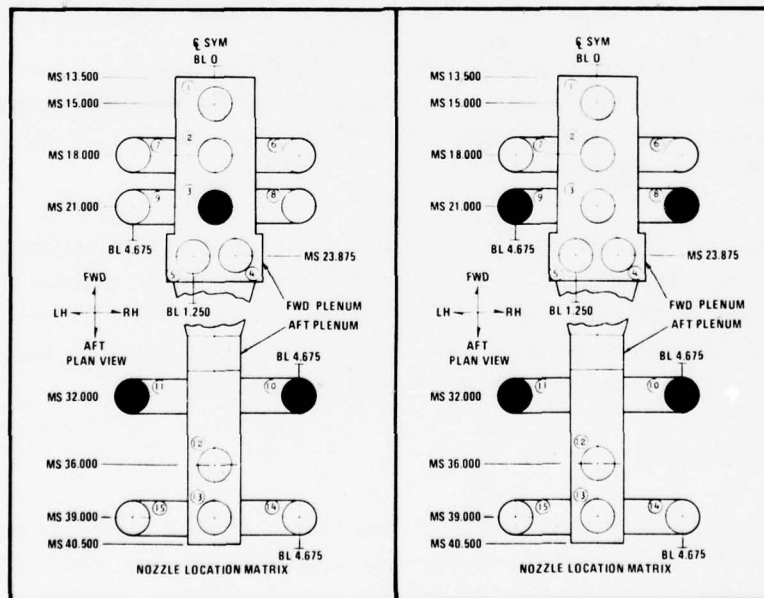
65322 6

Figure 5. A Multi-purpose Ground Effects Model Was Used

TWO NOZZLE CONFIGURATIONS



THREE NOZZLE CONFIGURATIONS FOUR NOZZLE CONFIGURATIONS



65322-7

Figure 6. Selected Plenum Outlets Were Used to Provide Desired Nozzle Spacings

The following rationale was used to designate blocking surfaces or plates (P). Subscripts 1 through 9 are reserved for circular plates with a single nozzle. Subscripts 11 through 19 are used for plates with two nozzles, 31 through 39 for three nozzles, and 41 through 49 for four nozzle arrangements. A portion of the plate that can be separately attached to a balance is designated by a dash number one (-1). Example is P_{41-1} . This is the corner of the rectangular plate P_{41} that can be isolated and attached to the balance. See Figures 7 and 8 for test specimens.

All nozzles are designated by subscripts (location) and superscript (size). The location subscript is keyed to Figure 6 and designates the nozzle location on the plenum chambers. The superscript refers to the nozzle diameter (1 = 1.32 in., 2 = 1.41 in., and 3 = 1.61 in.). A complete test configuration $N_3^3 N_{10}^3 N_{11}^3 P_{31}$ would mean a three nozzle arrangement with 1.62 inch diameter nozzles located at points 3, 10, and 11. The plate number is 31.

Three basic flat-plate configurations were used during this test. The first set of flat plates is designed for testing with two nozzles (Figures 7 and 9). The three plates are configured to be tested with a nozzle diameter of 1.41 inches and three different nozzle spacings. The respective plate areas are 396.5 in.², 515 in.², and 674 in.². Limited data were also obtained with two circular, single-nozzle plates. These plates had areas of 77.8 in.² and 265.3 in.² and are shown in Figure 8. In both cases a 1.41 inch diameter nozzle was used.

The second type of plate is designed for three nozzles (Figures 8 and 10). Again, a section of the plate can be removed to permit testing with one nozzle only. The total plate area is 278 in.². Both 1.32 inch and 1.61 inch diameter nozzles were used.

The third plate is rectangular in shape, Figures 7 and 11, 345 in.² in area and designed to accommodate four nozzles. A corner of the plate can be removed or mounted separately on a six-component balance. Only the smaller nozzles of 1.32 inches in diameter were used with this configuration.

A forebody fairing and simulated inlets were added to the model substructure to allow the acquisition of reingestion data. The inlets are semicircular, with a radius of 1.67 in., and attached to the sides of the fuselage forebody, see Figure 5. Each inlet was connected to an ejector drive system. Note that all blocking surfaces heights (h) are nondimensionalized in respect to a single nozzle diameter (D).

2.2 TEST PROCEDURES

Since this test was to be accomplished in a wind tunnel (closed system), particular efforts were made to ensure that there were no wall effects or ambient air heating problems that would adversely affect the quality of the results. A tufted pole was used to visually survey the flow field for a typical configuration to assure that there was no recirculation of the ground jet flow up the tunnel walls and back to the model.

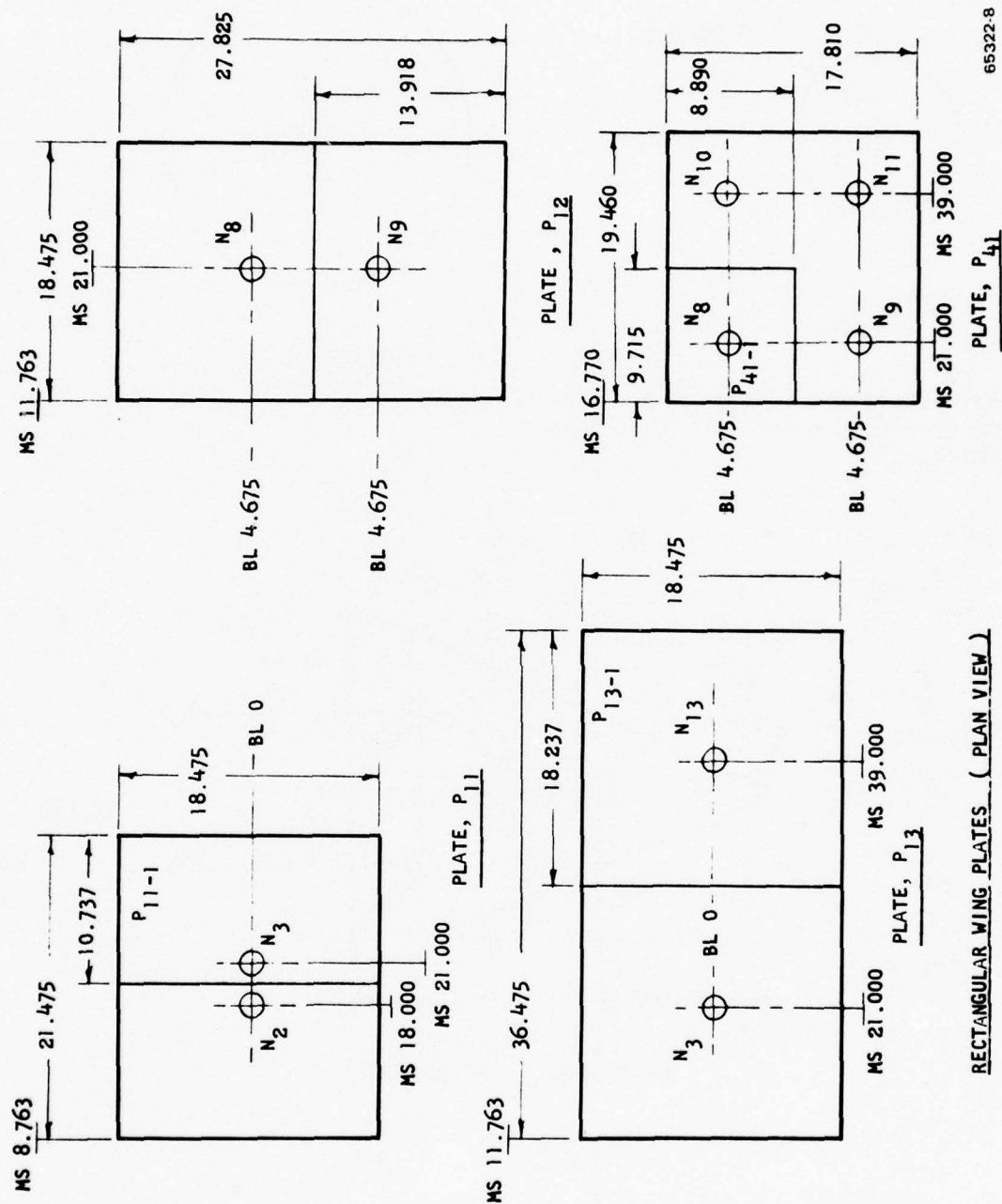


Figure 7. Rectangular Plates Formed Blocking Surfaces for the Two and Four Nozzle Configurations

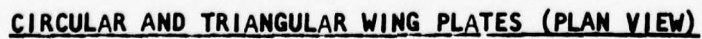
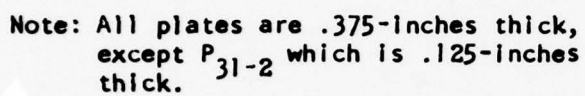


Figure 8. Circular and Triangular Plates Formed Blocking Surfaces for the Single and Three Nozzle Configurations

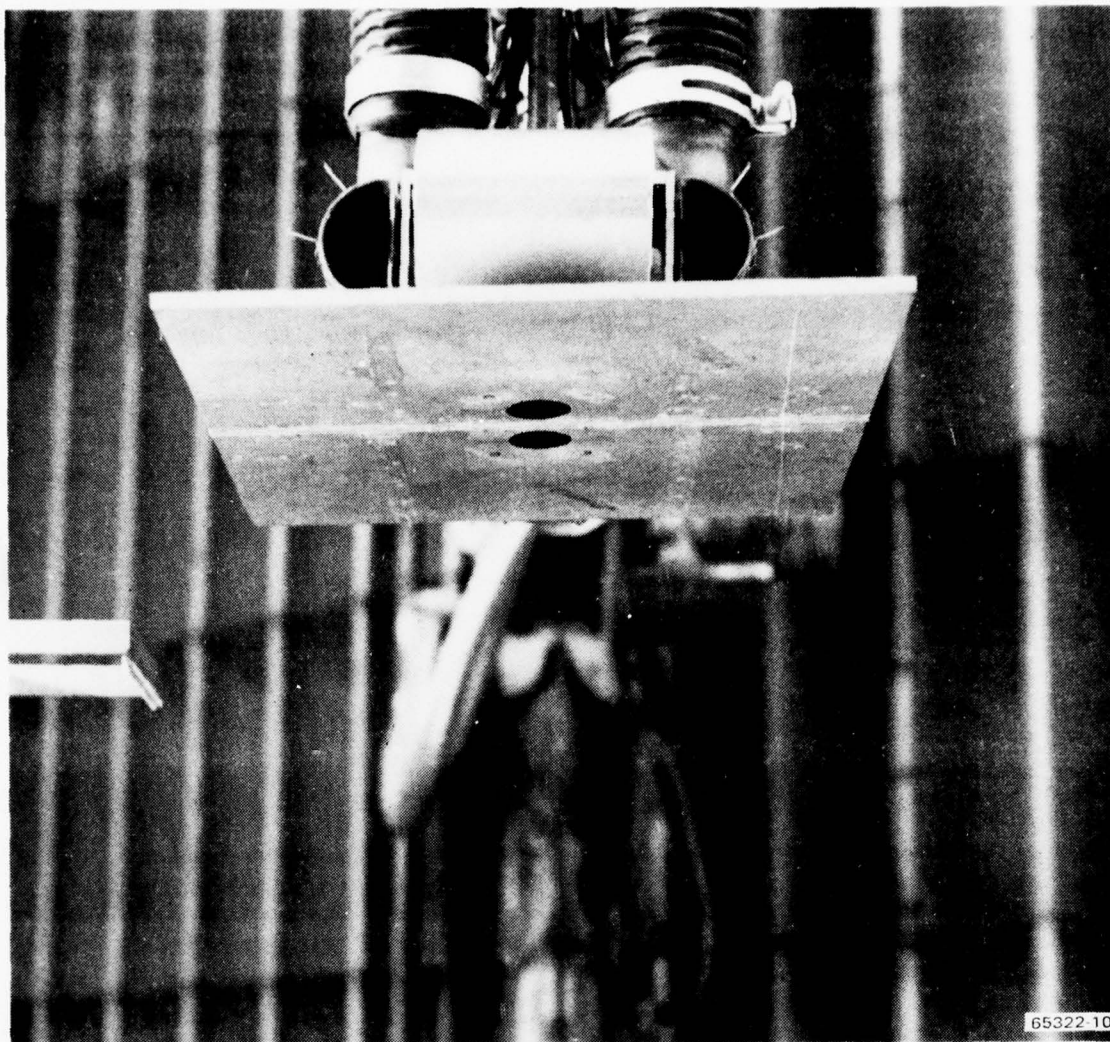


Figure 9. Typical Installation of Rectangular Plate (P_{11}) with Two Nozzles

Additionally, the tunnel was vented to eliminate the possibility of tunnel heating during a run. For the "zero" velocity case, the tunnel was completely vented (blocked) and a very low airflow (3 mph) maintained to purge the test section. When significant forward velocities (20 knots) were required for testing, the tunnel venting was reduced consistent with the forward-velocity requirement. The ambient temperature in the test section was continually recorded and monitored to verify that no significant temperature rise occurred.

All tests were conducted at nozzle pressure ratio (NPR) of about 2.0, with corresponding $Q_n = 10.8$ psi.



Figure 10. Typical Installation With Three Nozzles

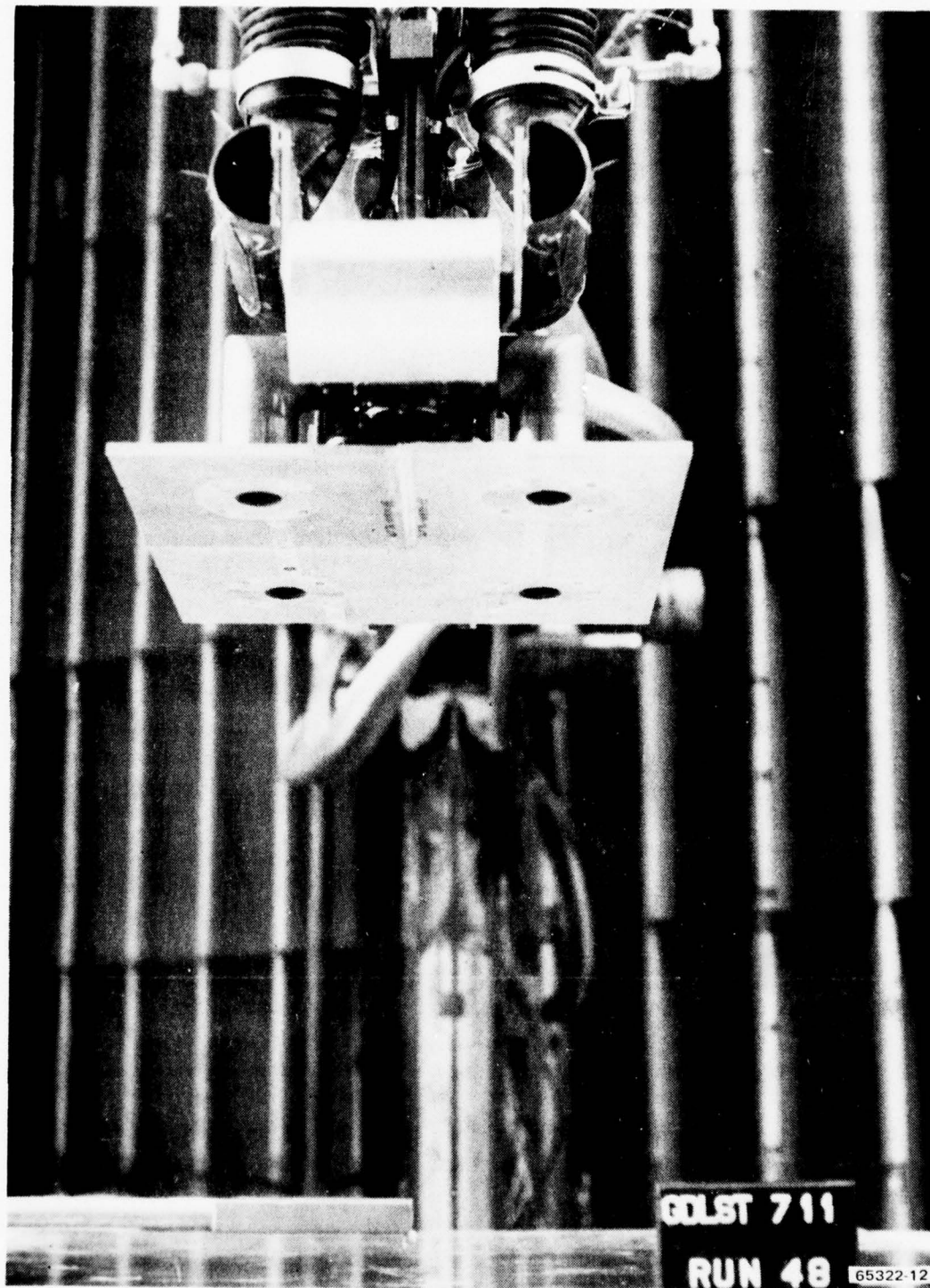


Figure 11. Typical Installation With Four Nozzles

2.3 INSTRUMENTATION

The flow-field survey rake, Figure 4, was the primary data acquisition tool for both the fountain test and the reingestion test. The rake was equipped with 13 chromel/alumel thermocouples and 14 cone probes. Each of the cone probes had four orifices on the conical surface and one total-pressure port in the nose. Data obtained with the cone probes were used to determine local total pressure and local flow direction. The thermocouples also measured the local temperatures. Although the cone-probe pressures were sampled with Scanivalves, the pressure at each port on a given probe was sampled simultaneously by the following technique. Five Scanivalves were employed; the number one orifice (see Figure 4) on each probe was connected to one Scanivalve, all the number two orifices were connected to another Scanivalve, and so forth. Thus by reading all five Scanivalves at the same time, the five pressures on any given cone probe were sampled simultaneously. However, it is obvious that each of the 14 cone probes was sampled at a different time. The interval between probe readings was approximately 3.5 sec; thus about 50 sec was required to take data from all the rake's probes.

Each of the Scanivalves discussed above contained a single transducer which was hand picked for accuracy from a group which were calibrated in the wind tunnel prior to the tests. The accuracy criterion was the best straight line curve fit through the calibration points. The calibrations were performed with a tertiary standard commonly used at the Convair Low-Speed Tunnel.

Typically cone probes are not very accurate for determining flow direction when the flow angles exceed about 40 degrees. Therefore, based on an evaluation of the calibration data, certain constraints were placed in the test data reduction procedure to suppress data output when the indicated flow angles or the total pressure exceeded certain limits.

Thus,

- 1) if either θ_F or γ_F was greater than 42 degrees,
- 2) if P_5 was less than tunnel freestream static pressure, or
- 3) if the total pressure correction factor was less than -0.9,

then the cone probe data was considered invalid and no attempt was made to calculate local flow direction or local dynamic pressure.

The Scanivalves which sampled the cone-probe data were equipped with a Statham differential pressure transducer, Model PM 131TC. For the fountain test, transducers with a range of ± 10 psia were used and the tunnel's data system was set up for ± 8 psi equal to ± 8000 counts. For the reingestion test transducers with a range of ± 2.5 psia

were used and the tunnel's data system was set up for ± 0.2 psi equal to ± 2000 counts. For each test P_5 was constrained to the positive side of this range. For both tests the combined error for the transducer and the tunnel's data system was no more than ± 6 counts. This error translates to ± 0.006 psi (dynamic pressure) at zero flow angularity, which corresponds to an error in velocity calculation of ± 27 fps for the fountain test. The velocities measured in the fountain test ranged from 0 to about 400 fps. For the reingestion test, the ± 6 count error translates to ± 0.0006 psi at zero flow angularity, which corresponds to an error in velocity calculation of ± 8.5 fps. The velocities measured in the reingestion test ranged from 0 to 34 fps. These errors would be slightly larger at nonzero flow angularities. For example, at a flow angularity of $\theta_F = \gamma_F = 20$ degrees, the additional velocity error would be 3 fps or less.

The flow-field survey rake was designed for measuring the temperature, local total-pressure and local flow direction of the hot fountain gases. Although the applicable ranges of the thermocouples and transducers were not in good agreement with the values to be measured in the reingestion flow field, it was decided to use the existing rake because (1) the lead time and costs related to new transducers and thermocouples was inconsistent with the program schedules and financial constraints, and (2) there were no available alternatives that offered a more acceptable method of traversing the flow field or more accurate data acquisition.

As stated earlier, the flow-field survey rake was equipped with chromel/alumel thermocouples. The error limits for a chromel/alumel thermocouple are $\pm 4^\circ\text{F}$ in the range of 32 to 530°F . This range covered both the fountain and the reingestion test.

The inlets were instrumented, as shown in Figure 12, with copper/constantan thermocouples that have error limits of $\pm 1.5^\circ\text{F}$ in the range of -75 to 200°F ; these were well suited for the temperature range to be measured.

The induced forces and moments on the blocking surfaces (flat plates) were obtained with the C-5 -0.75F six-component internal strain gage balance. The normal force output is accurate to within ± 0.28 pounds. In terms of the nondimensionalized induced force, $\Delta L/F_j$, this error corresponds to ± 0.0043 for the two nozzle configurations and ± 0.0024 for the four nozzle configuration.

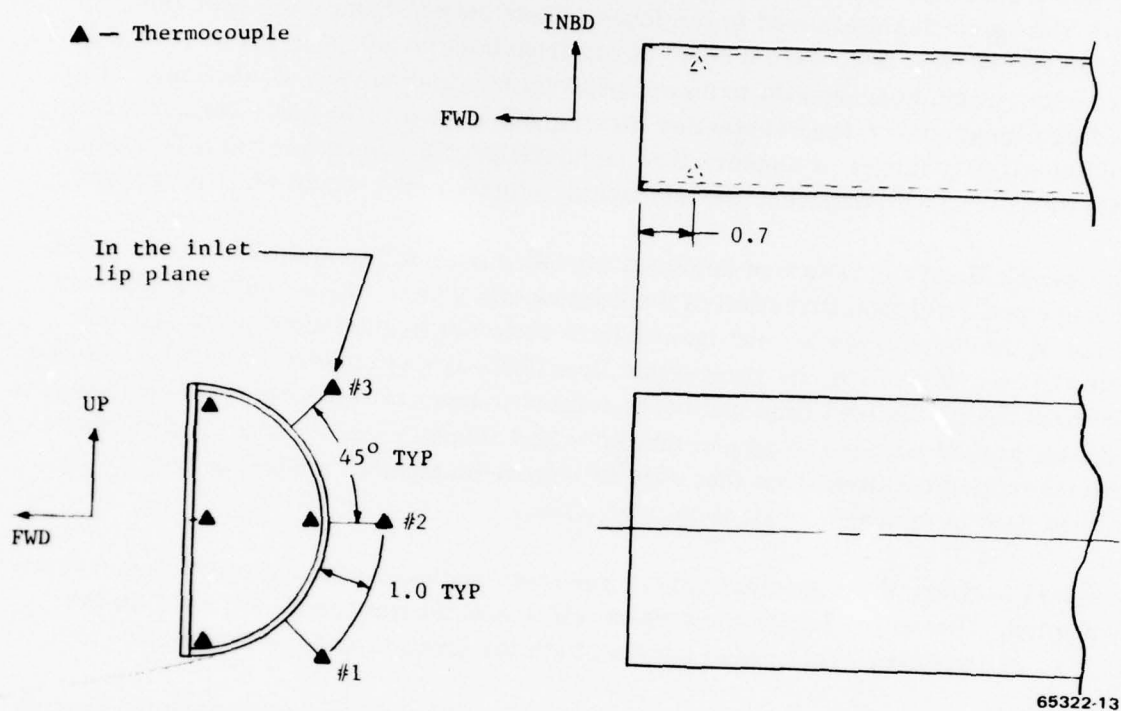


Figure 12. Instrumentation was Provided to Obtain Inlet Temperatures

SECTION 3

FOUNTAIN AERODYNAMIC CHARACTERISTICS

When two or more jets impinge normally on a plane surface, the resulting flow-field exhibits radially expanding ground jets along the ground. In addition, the ground jets from the different sources meet to form a vertical upflow region or fountain. This fountain phenomenon accompanies hovering multiple-jet VSTOL direct lift and/or vectored thrust configurations. Under certain conditions the fountain core impacts the fuselage or the blocking surface, produces lift, and counteracts the induced lift losses caused by the entrainment action of the radial ground jet. In addition, pressure fields are often produced as a result of fountain-blocking surface interference. This leads to additional lift losses or gains. Consequently, the fountain phenomenon is treated as two separate but additive effects: fountain associated lift gains, and interference effects. The core of the fountain is characterized by an up-flow region that is very sensitive not only to small imbalances between the two jets but also to changes in their relative angles of inclination. It also appears to be highly turbulent under all conditions. Since the fountain phenomenon is a three-dimensional, turbulent flow, it has received little theoretical analysis.

Since there is no analytical methodology currently available to predict the fountain phenomenon or the related interference effects, an attempt has been made to develop empirical methodology using test data on the multiple-jet configurations developed in the course of Convair research programs (References 3 and 4)^{3,4} and supplemented by tests conducted under this contract. Specifically, these contracted activities were directed at the nature of the fountain core, its momentum characteristics, the related flow angularities and entrainment characteristics. In addition, the fountain related interference effects were to be defined. This has been accomplished.

The net effect of the fountain was determined from balance measurements utilizing the model test setup discussed in Section 2. This effect is comprised of two parts: the force due to the fountain core itself, and the effect of the fountain core on the surrounding flow patterns (interference effects). The force due to the fountain core is determined from integration of the dynamic pressure determined from pressure rake

³ Karemaa, A. and Ramsey, J. C., Aerodynamic Methodology for the Prediction of Jet-Induced Lift in Hover, General Dynamics Convair Aerospace Division Report CASD-ERR-73-012, December 1973.

⁴ Karemaa, A., Abbreviated Methodology for the Prediction of Jet-Induced Lift in Hover, General Dynamics Convair Aerospace Division Report CASD-ERR-74-024, December 1974.

surveys through the fountain. The difference between the fountain core force and the total fountain increment determined from the balance or force measurements constitutes the interference effects. Details of this approach and the results are discussed in this section along with the fountain flow characteristics (velocity, direction and entrainment) determined from the rake surveys.

3.1 NET FOUNTAIN FORCES

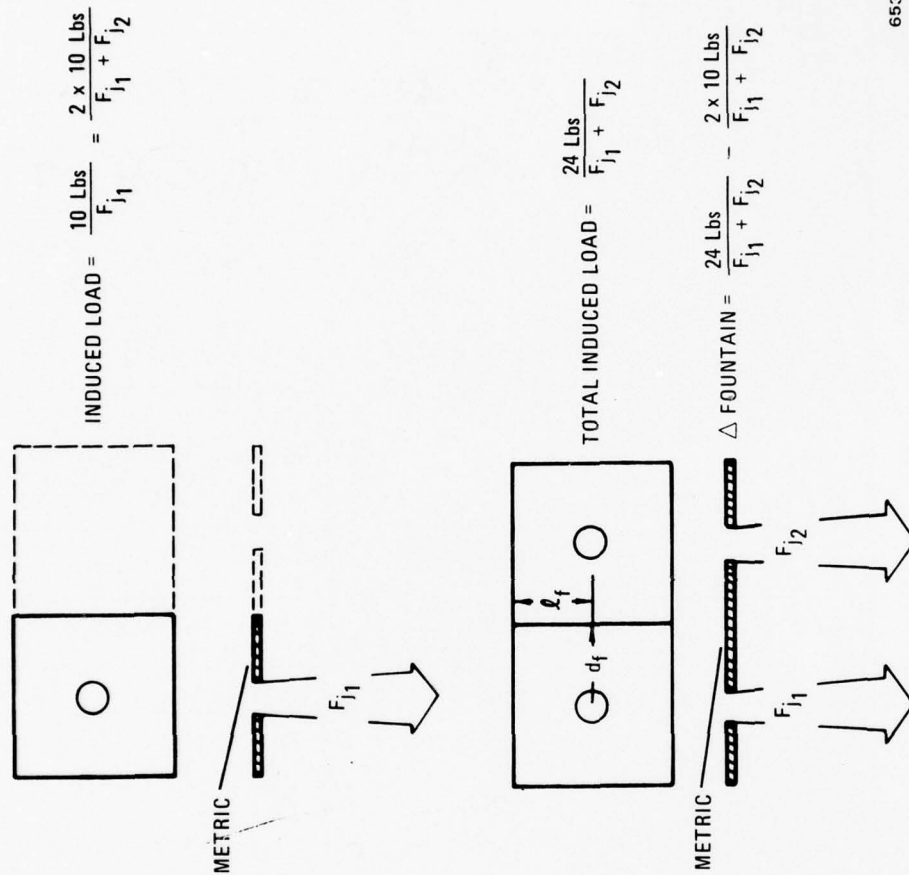
The fountain-produced forces were measured by utilizing the capability of the model to attach various portions of the blocking surfaces to the balance. An example of the approach is shown in Figure 13. First, a rectangular flat plate equal to one-half of the total plate area was placed on the balance and tested at various ground heights in the presence of its mirror image. Only the nozzle located on the metric side of the plate was operative. The resulting induced force was then nondimensionalized with the thrust from the single nozzle. This nondimensional force is applicable to either half of the plate with one nozzle or all of the plate with two nozzles and no fountain between the nozzles. The next step was to test with the complete plate on the balance and both nozzles operating. This determined the total induced force including the fountain effects. The difference between these runs was equal to the net fountain effect. A similar approach was used for each nozzle/plate combination.

3.1.1 NOZZLE NUMBER AND SPACING EFFECTS. Suckdown or induced force data (balance data) for two medium-spaced nozzles are presented in Figure 14. The difference between the two curves is equal to the net fountain effect as discussed above. The fountain produces a net positive effect only at the low model heights. Induced force data for each configuration tested are presented in this form in Appendix A. A complete set force and moment data is available in Reference 1. A summary of the net fountain effects for two, three, and four nozzles at various spacings is shown in Figure 15. With two nozzles, a large effect of nozzle spacing is apparent at the lower model heights. The close spacing ($d_f/D = 1.06$) shows a large lift loss indicating that the free jets have probably merged before striking the ground, thus eliminating the fountain. Both the medium and large spacings show the positive net effect of the fountain at low heights.

The effect of nozzle spacing with three nozzles was simulated by testing two nozzle diameters with the same flat plate. A stronger fountain effect than experienced with two nozzles is present at moderate model heights, Figure 15. The different spacings result in similar curves with the closer spacing (large nozzles) generally having a stronger fountain effect.

A very strong fountain effect was obtained with the four nozzle configuration, as shown in Figure 15. Positive net fountain forces were present at all model height tested.

3.1.2 TEMPERATURE EFFECTS. The effect of nozzle exit temperature on the net fountain force is significant. Figure 16 shows the effect of a temperature range from



65322-14

Figure 13. The Fountain Effects Were Isolated by Mounting Different Sections of the Plates on the Balance

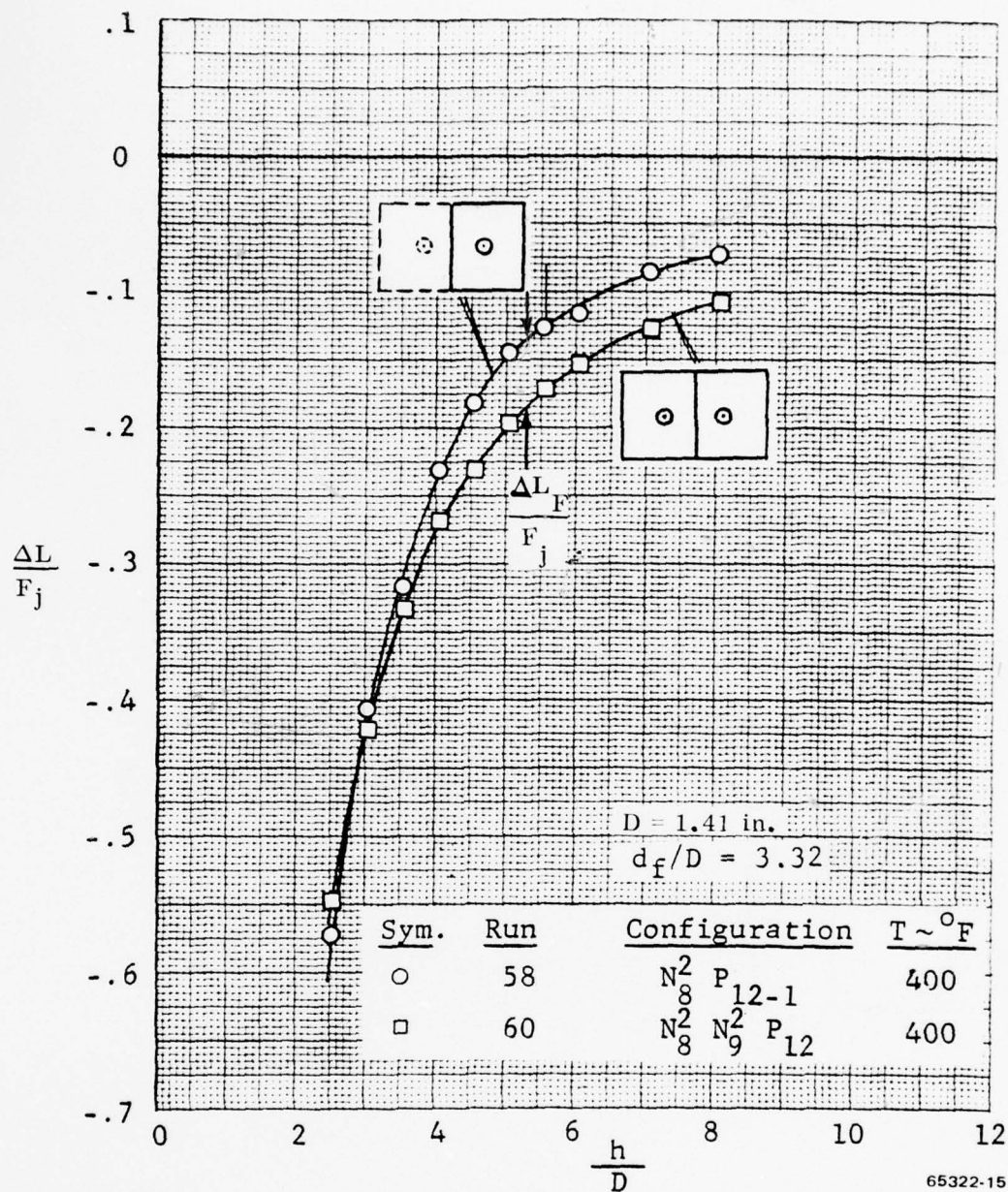


Figure 14. Data Were Obtained in Order to Isolate the Total Incremental Fountain Effect

70 to 400°F. A large increase in the net fountain force is noted when the temperature is increased from 70 to 200°F, but essentially the same level is obtained for 200 and 400°F. This is a very significant result in that if the fountain effects do flatten out with increasing temperature so that a relatively low temperature (200°F) can be used to simulate hot engine exhaust, ground effects testing in general would become much

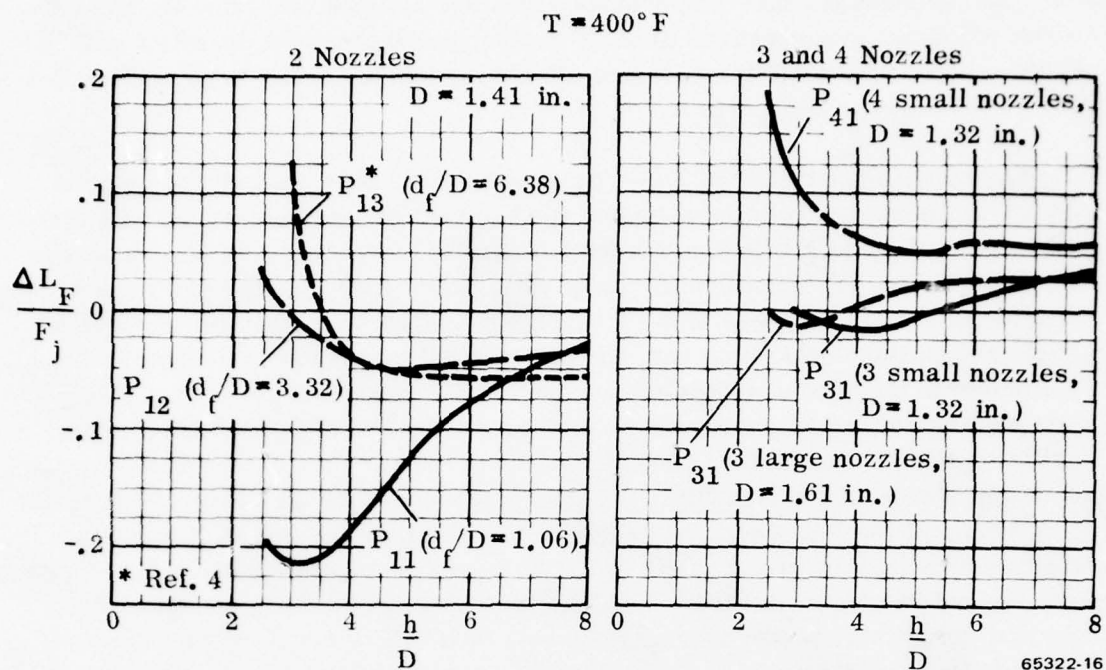


Figure 15. The Incremental Fountain Lift is Highest With Four Nozzles

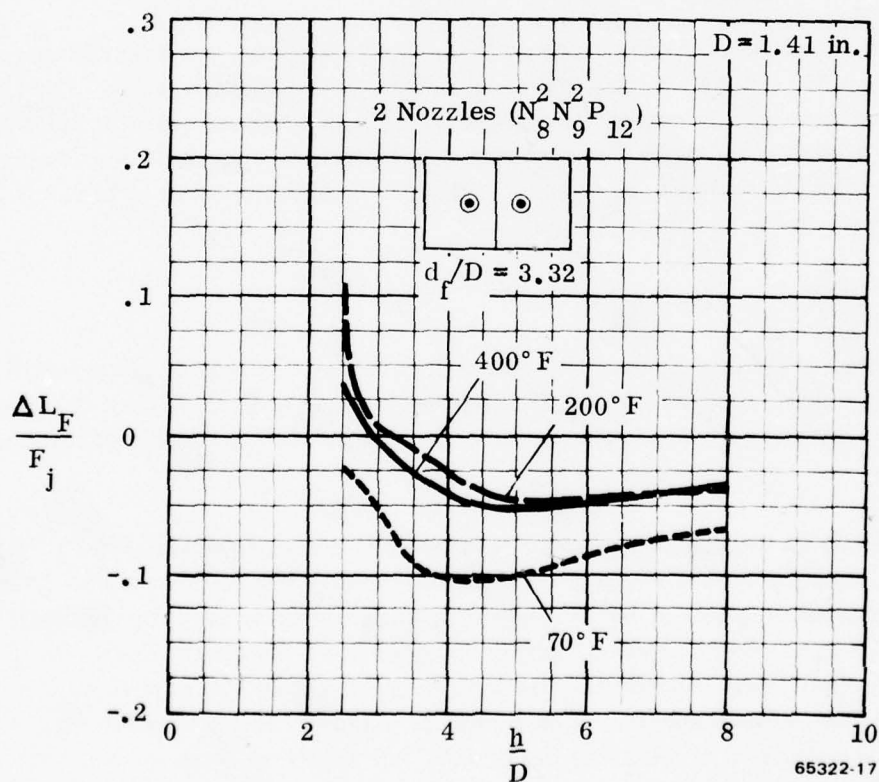


Figure 16. The Temperature Effect Appears to Decrease with Increasing Temperature

easier. The reasons for this temperature effect are not apparent from the present tests and additional investigations must be accomplished to verify the effect and discover its cause. Additional temperature effects for single nozzles with various flat plates are presented in Appendix A.

3.1.3 WIND AND PITCH EFFECTS. The effect of wind over deck on the induced forces and moments has been investigated for two medium spaced nozzles with a rectangular plate. The wind effect on the total forces and moments with two nozzles is presented in Figure 17. Significantly large total induced lift losses and a nose-up pitching moment are shown due to the 30 knot wind. Note that this data includes the effect of wind on the plate. However, the incremental or net fountain effect is actually more positive in the presence of the 30 knot wind, as shown in Figure 18. This positive increase is not due to a stronger fountain core (Section 3.3), but is due to a change in the flow pattern below the blocking surface that leads to a decrease in the negative interference effects of the fountain. The interference effects are discussed in further detail in Section 3.6. It is noted that a slightly different testing technique was required to determine the incremental fountain effect in the presence of a crosswind. Since the nozzles are not located in the center of the plates, which results in nonsymmetric effects in a crosswind, it was necessary to test each half of the plate with its nozzle operative in the presence of its mirror image. The sum of the individual plate loads was then compared with the total load with both nozzles, as shown in Figure 19 to determine the incremental net fountain effect.

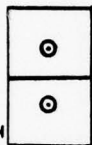
Pitch effects were briefly addressed with the two moderately spaced nozzles. The effect on the total induced forces and moments is shown in Figure 20. The irregular nature of the data as a function of model height for 10 degrees pitch is indicative of the complicated recirculation flow pattern. Integrations of the limited fountain core data, Figure 38 in Section 3.3.2, show a slightly weaker fountain at $h/D = 5$, which is consistent with the force data of Figure 20.

3.2 VELOCITY

Flow velocities and directions in the fountain core have been determined with the pressure rake described in Section 2. Representative plots that illustrate the basic fountain flow characteristics for two, three, and four nozzles are presented in this section.

Flow directions in the fountain formed between two nozzles, which are 12.76 nozzle diameters apart ($d_f/D = 6.38$), are shown in Figure 21 for several model heights. Measurements were made at three heights in the fountain except for the lowest model height, $h/D = 2.5$, where physical restrictions of the rake size reduced the sweeps to two. The dashed lines indicate the fountain flow directions derived from the measured values. The two nozzle configuration forms a fountain "sheet." A similar flow system could be developed by rotating the ground jets emitting from each nozzle upward at a line along their intersection, as illustrated in Figure 22 and compared to right

$$d_F/D = 3.32$$



$D = 1.41 \text{ in.}$

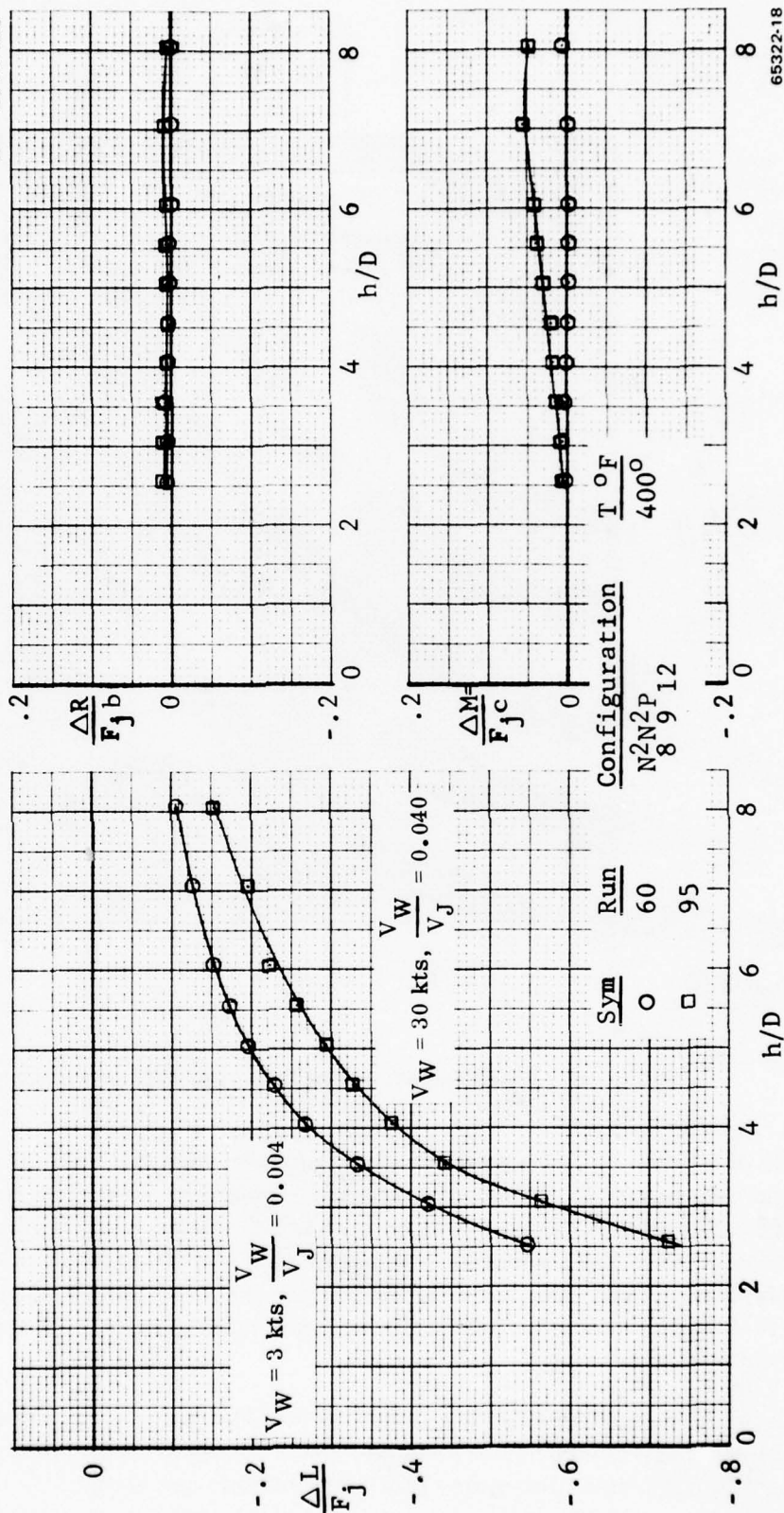


Figure 17. The Total Effect of the Wind Was to Produce Higher Lift Losses

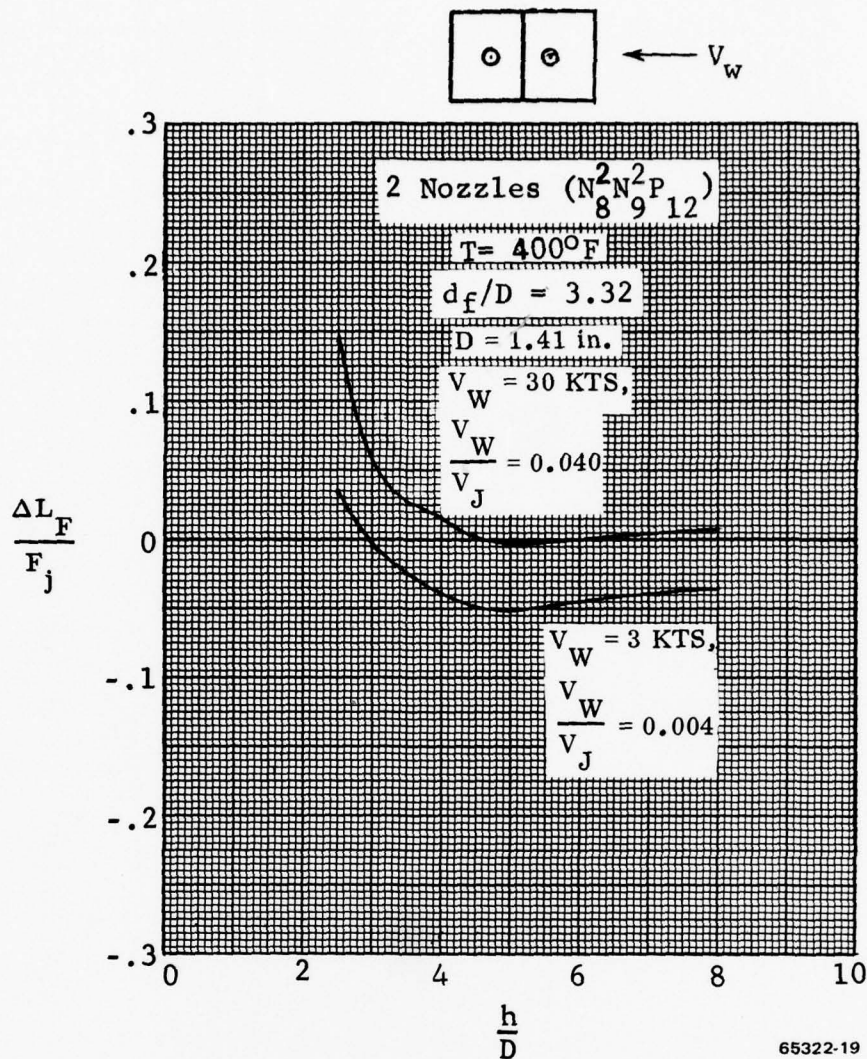


Figure 18. Wind Increases the Fountain Lift Increment

hand side of Figure 21. The streamlines in the intersection (Y-Z) plane are generally linear and well behaved. The fountains have a non-linear pattern in the X-Z plane indicative of the effects of mass entrainment and the decay of the fountain strength. A comparison between the measured flow angles (θ_F) of Figure 21 at $h/D = 5.0$ and angles obtained by extending and rotating the ground jet is presented in Figure 23. Good agreement is obtained, thus verifying the rotated ground jet analogy for this two nozzle configuration.

Dynamic pressure contours for the same two nozzle configuration are presented in Figure 24 at an h/D of 5.0. The fountain "sheet" is apparent at the lower rake heights. At a height of 3.8 nozzle diameters (Z/D) the fountain has decayed to low values of dynamic pressure and the contours have become irregular in shape.

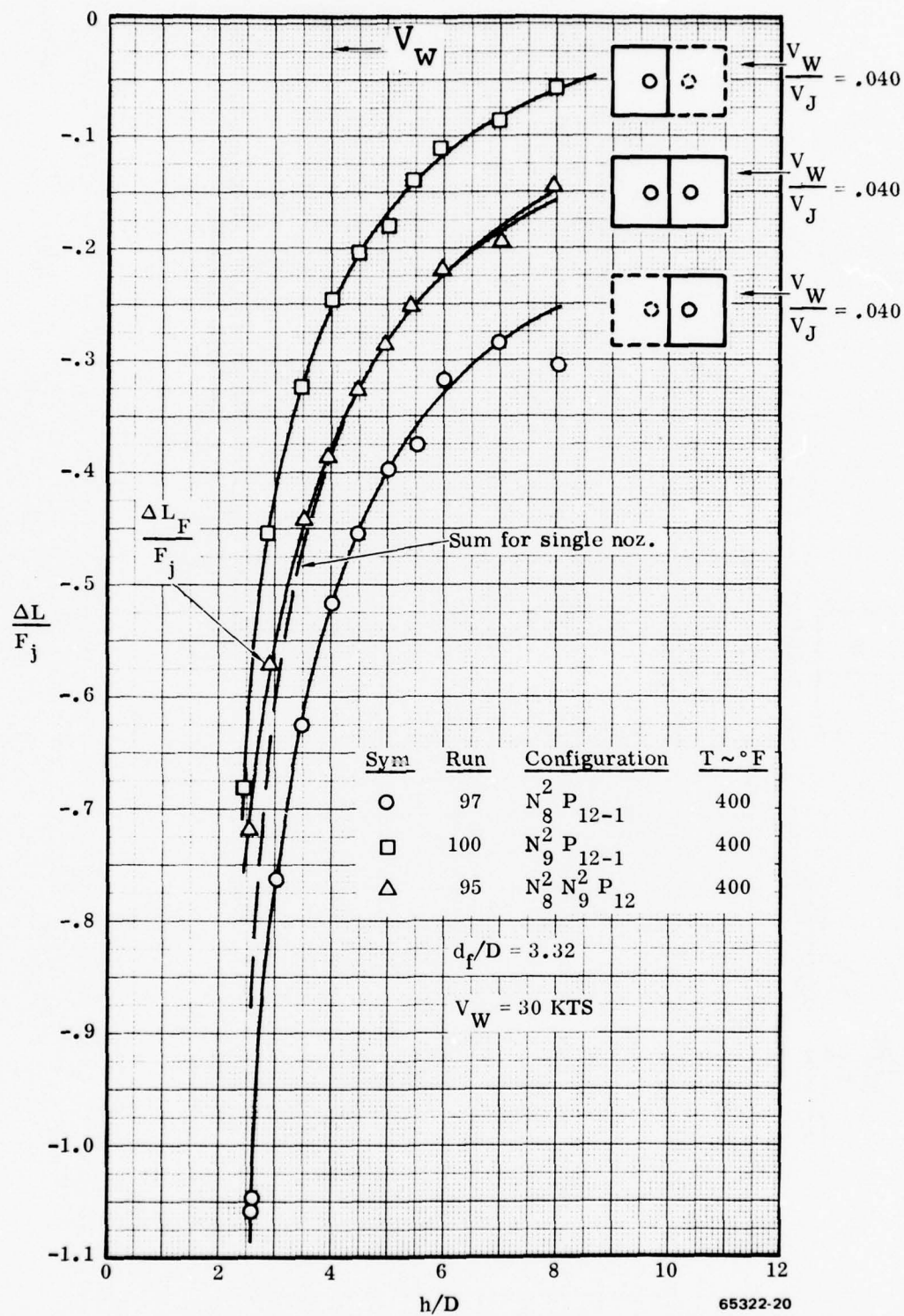


Figure 19. Additional Data Were Required to Isolate the Fountain Effect in the Presence of a Wind

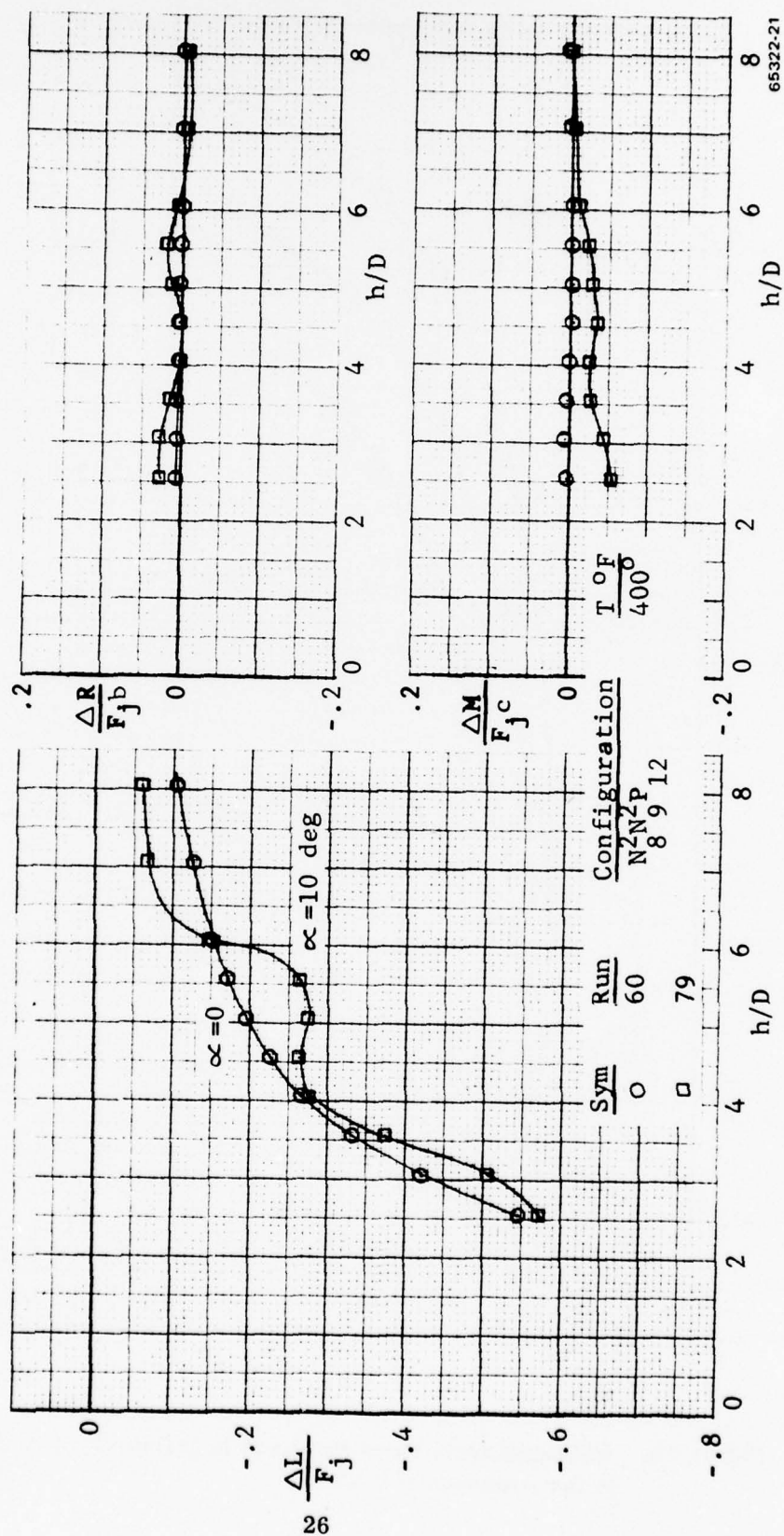
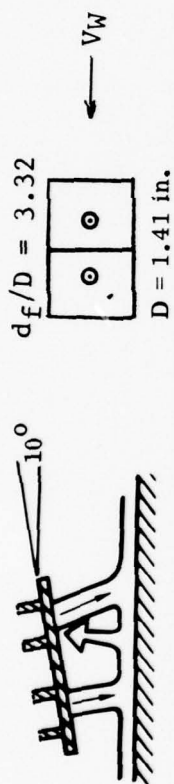


Figure 20. Model Pitch Attitude Has an Irregular Effect on Induced Forces

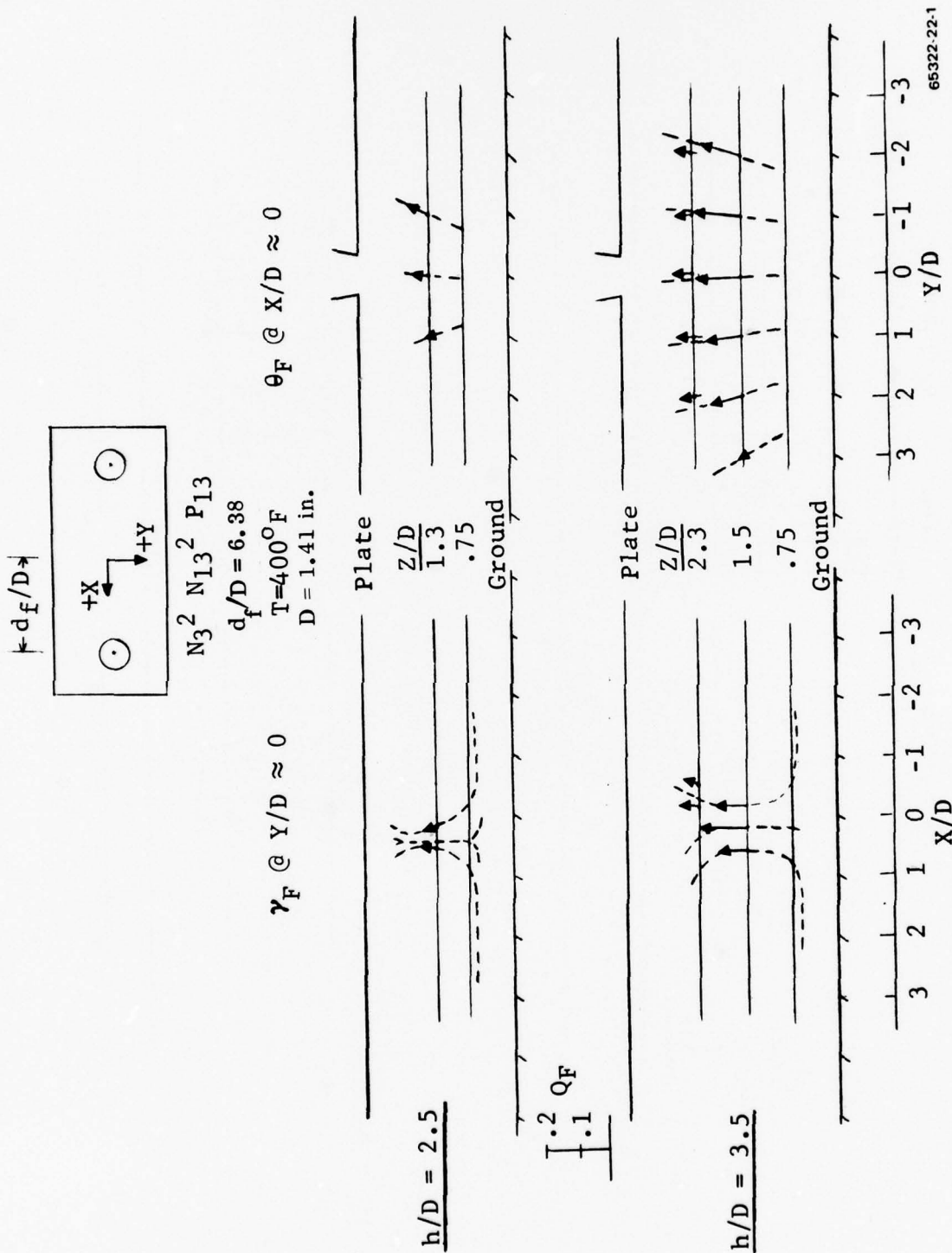
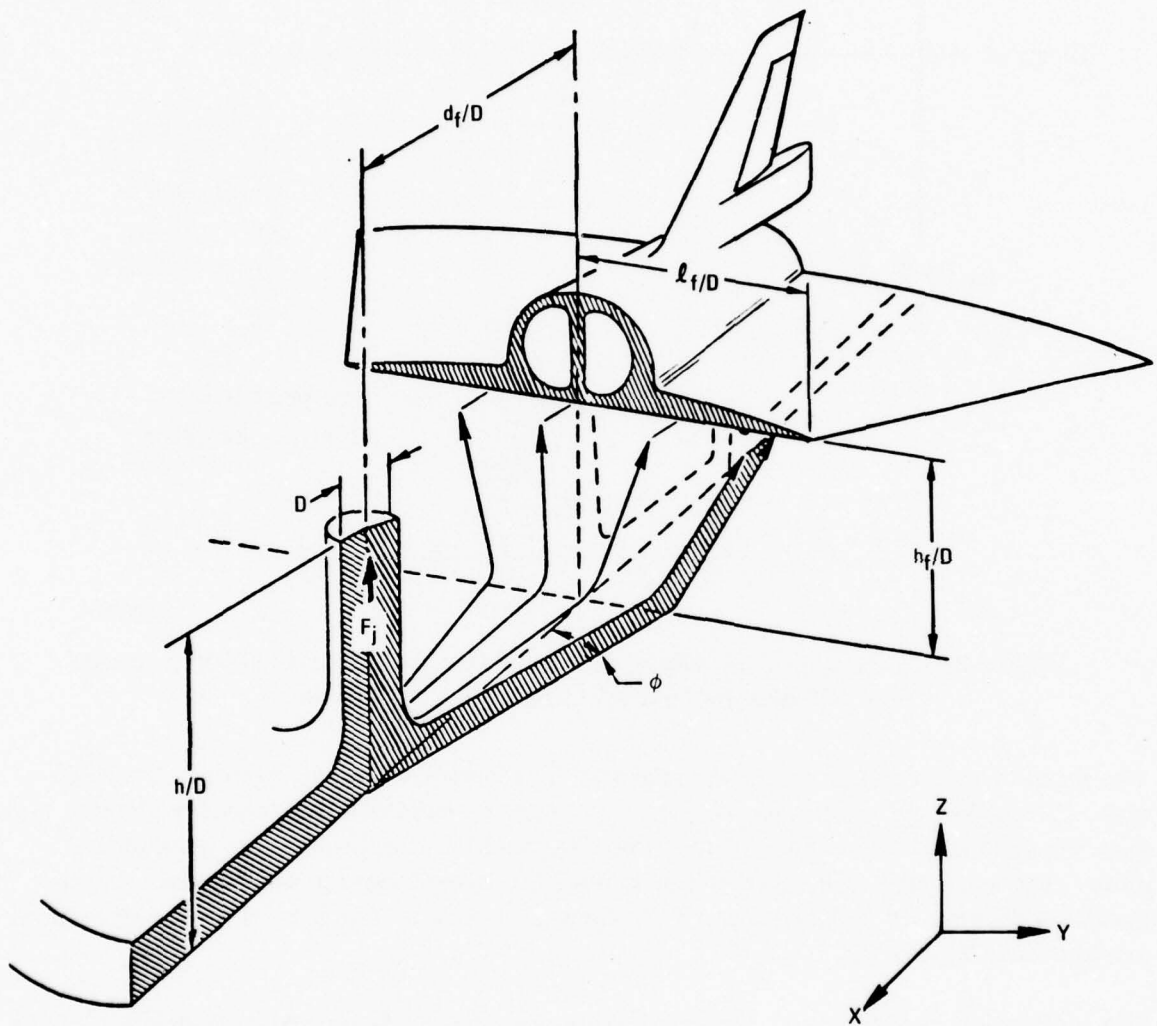


Figure 21. Fountain Flow Directions Between Two Nozzles are Orderly (Sheet 1 of 2)

65322-22-1



65322-23

Figure 22. Fountain Model for Two Nozzles

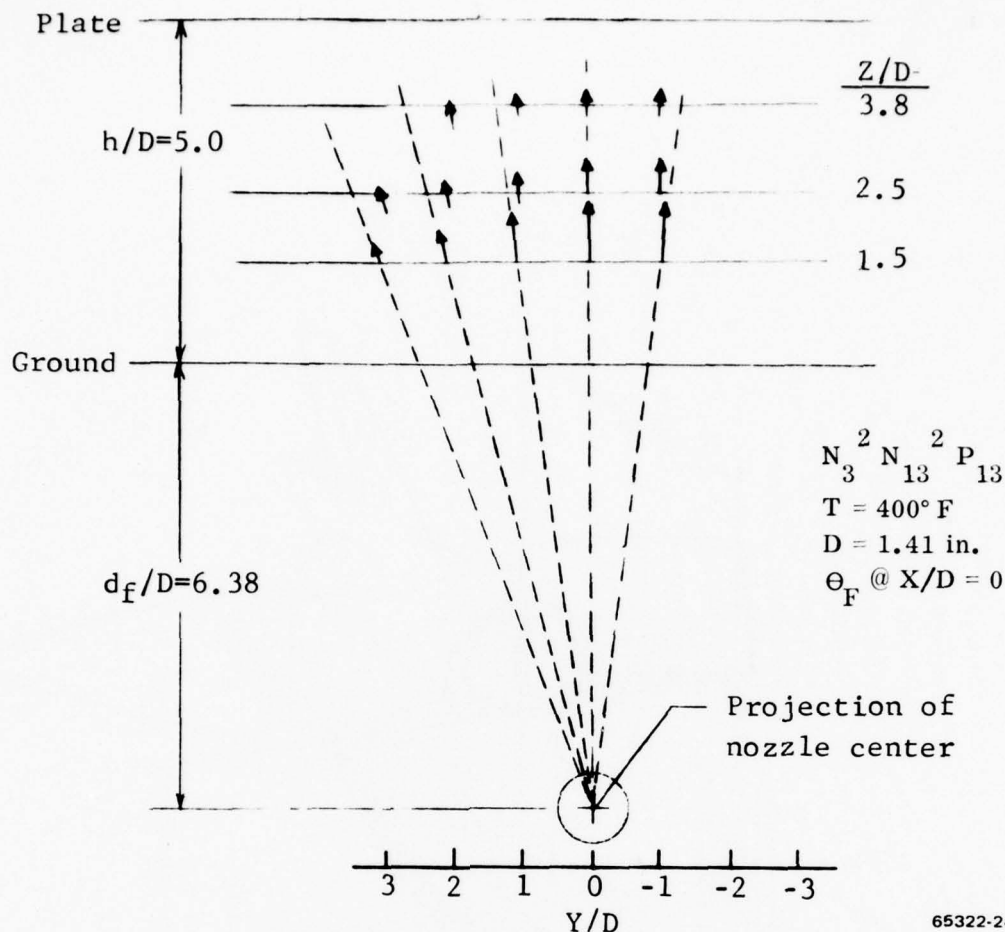


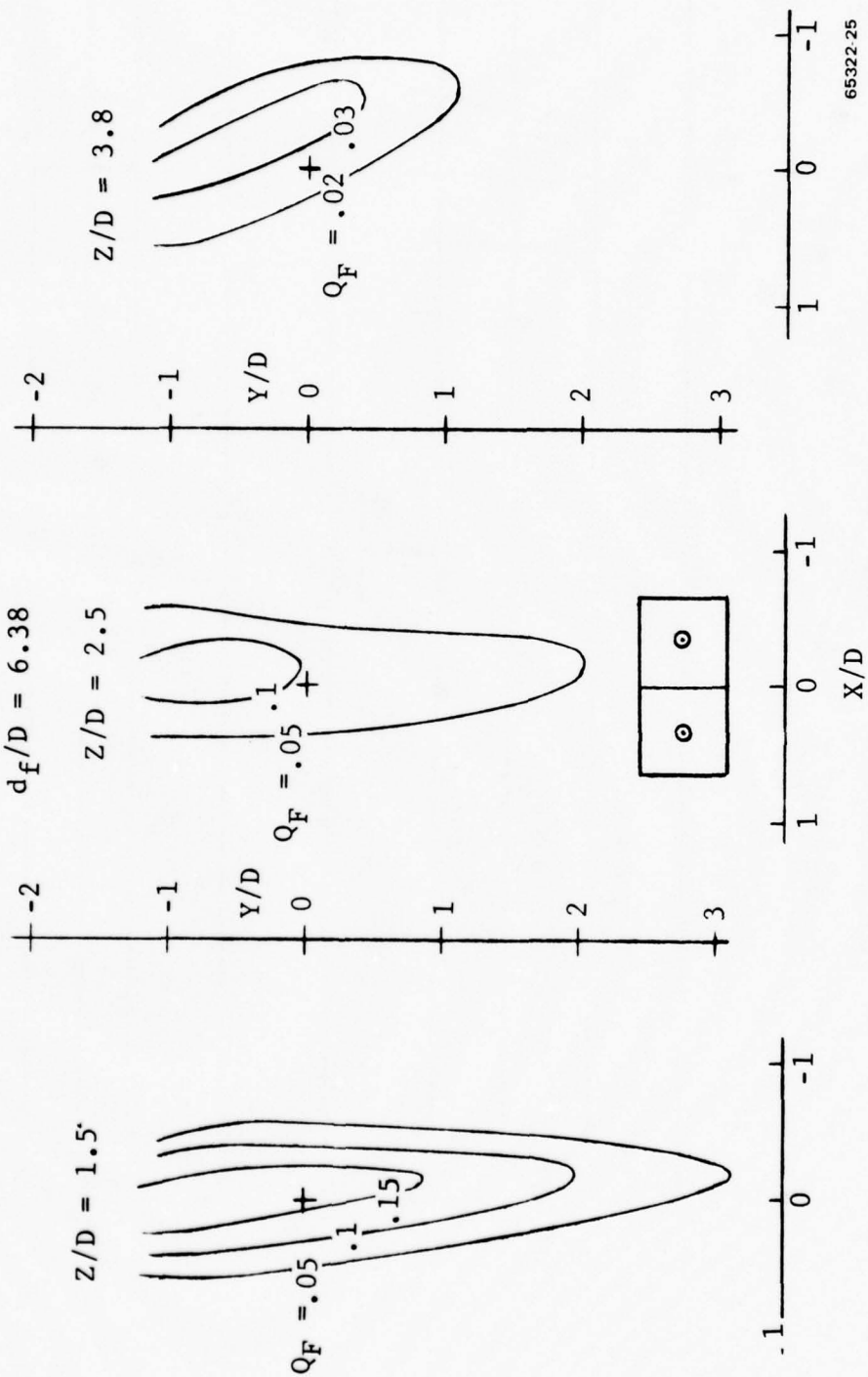
Figure 23. Fountain Flow Angles Between Two Nozzles Can Be Estimated By an Extension and Rotation of the Ground Jet

The three nozzle configuration is dominated by the geometric asymmetry of the nozzles. The spacing between the two nozzles near the base of the triangular plate is less than the spacing between each of these nozzles and the nozzle near the apex of the plate. Consequently, the two nozzles at the base overpower the third nozzle and the resulting fountain is inclined toward the forward nozzle. The resulting flow directions are shown in Figure 25.

The inclination of the central core flow from vertical, δ , is plotted as a function of the ratio of the relative nozzle spacings, B/A , in Figure 26. For equally spaced nozzles, $B/A = 1.0$, there would be no inclination of the flow. At zero B/A , the inclination should be the same as for a two jet configuration with the aft jet having twice the thrust as the forward jet. This data is available from Reference 5⁵. The data for the three

⁵ Kotansky, D.R. et al, Multijet Induced Forces and Moments on VTOL Aircraft Hovering In and Out of Ground Effect, Naval Air Development Center Report Number NADC-77-229-30, June 1977.

$D = 1.41 \text{ in.}$
 $T = 400^\circ \text{F}$
 $N_3^2 \text{ N}_{13}^2 \text{ P}_{13}$
 $h/D = 5.0$
 $d_f/D = 6.38$



65322-25

Figure 24. Fountain Dynamic Pressure Contours Between Two Nozzles

$T = 400^\circ \text{F}$

$D = 1.32 \text{ IN.}$

$N_3^1 N_{10}^1 N_{11}^1 P_{31}^1$

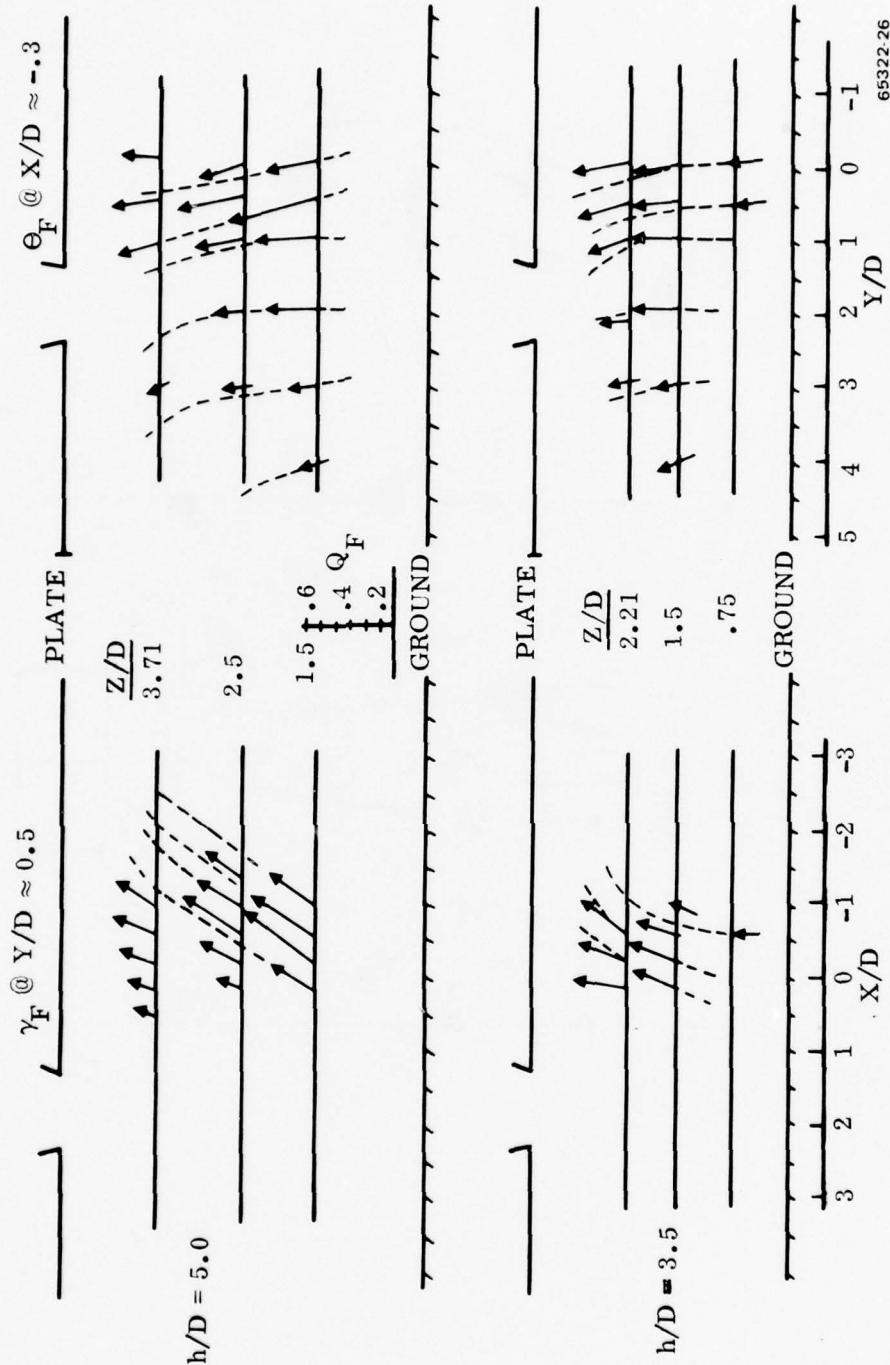


Figure 25. The Fountain Between Three Unequally Spaced Nozzles is Inclined

65322-26

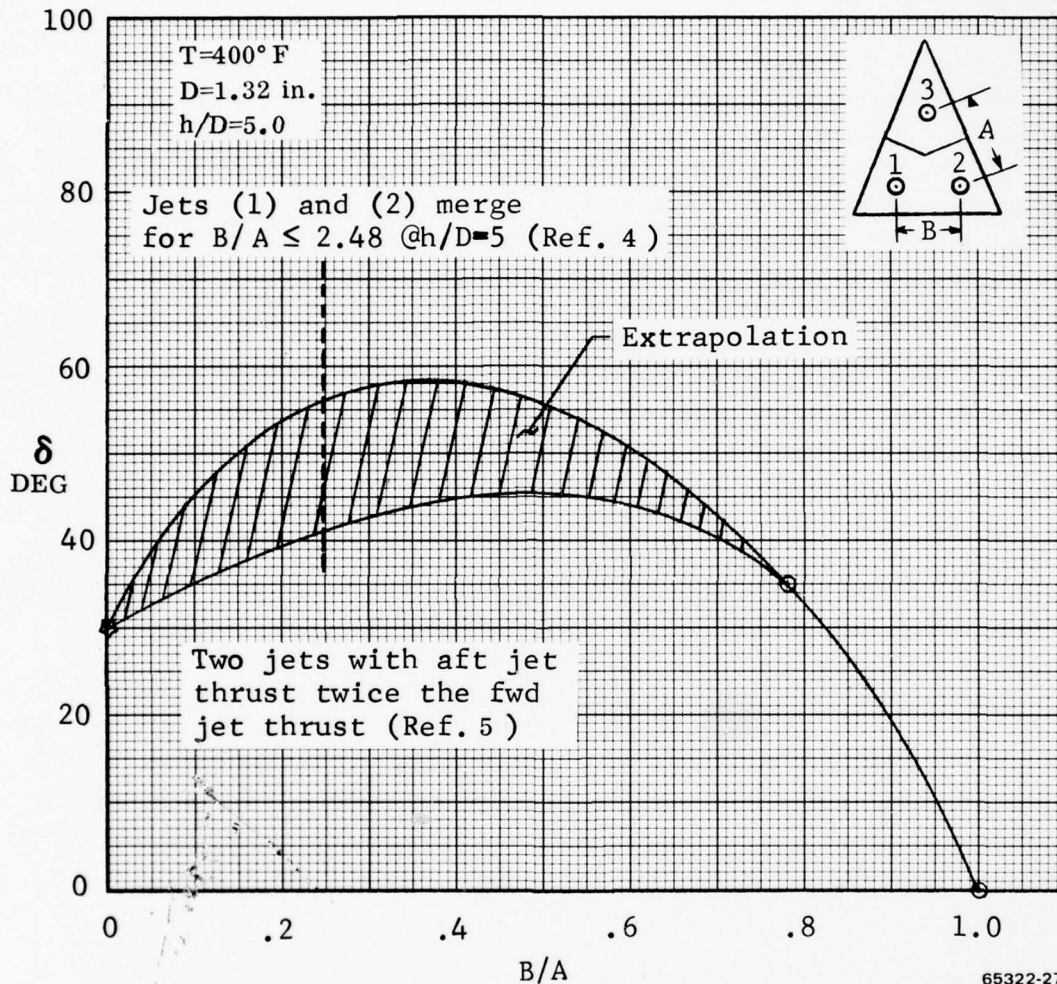
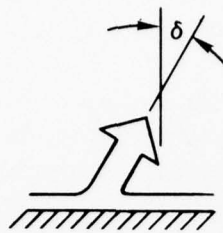


Figure 26. Estimate of Fountain Inclination for Three Unequally-spaced Nozzles

nozzle configuration, $B/A = 0.78$, indicate a significantly higher inclination than would be expected with two nozzles of unequal thrust (one nozzle twice the size of second nozzle). This may well be the result of a reinforced ground jet between the aft nozzles (at low Z/D) overpowering the ground jet from the forward nozzle. (A limited amount of ground jet data were obtained during these tests with the rake for a two nozzle configuration. These data showed that the reinforced ground jets between the

nozzles exhibit dynamic pressures which are an order of magnitude higher than the corresponding dynamic pressures in the radial ground jet.)

Typical dynamic pressure contours with three nozzles, Figure 27, show three fountain legs at low height in the fountain. However, as the flow rises in the fountain, a strong central core is formed and the legs no longer are present.

Flow directions and contours, Figures 28 and 29, for the four nozzle configuration also illustrate the formation of a strong central fountain core at moderate heights above the ground. At low height in the fountain, $Z/D = 1.5$, distinct fountain legs exist between the wider spaced pair of nozzles but are not apparent between the closer spaced nozzles. The rake was not swept between the closely spaced nozzles, but did cover the region from $2.46 X/D$ to $-2.46 X/D$ during the sweep between the widely spaced nozzles. There was no indication of a fountain in the outer regions of the surveyed area, but the current evidence is insufficient to exclude the existence of a weak fountain leg outside the rake range (between the closer spaced nozzles or to the left of $X/D = 2.5$ and to the right of $X/D = -2.5$).

The variation in the maximum vertical component of the dynamic pressure in fountains between two, three and four nozzles at $h/D = 5.0$ is shown in Figure 30. A rapid decay with height in fountain strength is noted for the two and three nozzle fountains. The fountain for the closer spaced two nozzle configuration, $d_f/D = 3.32$, has a higher initial strength than that for the corresponding wider spaced nozzles, $d_f/D = 6.38$, but decays faster to about the same level at increased heights (Z/D). With three nozzles, the closer nondimensionalized spacing (simulated by a larger nozzle diameter with the same physical spacing) has a higher strength at all heights.

The fountains formed by four nozzles are distinctive in that the dynamic pressure increases with height in the fountain (Figure 30). This is similar to the flow conditions in a venturi, a converging area which is accompanied by an increase in velocity. As discussed previously, the fountain legs formed by four nozzles at low Z/D coalesce into a strong central core at moderate heights above the ground, as shown by pressure contours of Figure 29. The curvature of the resulting streamline, Figure 28, are indicative of the "venturi" type flow, and show the increasing velocity.

One of the surprising effects from this study is that the blocking surface height, h/D , has a strong influence on the maximum dynamic pressure, as illustrated in Figures 31, 32, and 33 for two, three, and four nozzles, respectively. The effects of the blocking surface height (h/D) are a function of both the number of nozzles and the nozzle spacing. For the widely spaced two nozzle (weak fountain, $d_f/D = 6.38$) case, the maximum dynamic pressure increases with increasing blocking surface heights, as shown in Figure 31. This is also true for the medium spaced nozzles (stronger fountain) at the higher Z/D , but there is a crossover at the low Z/D values.

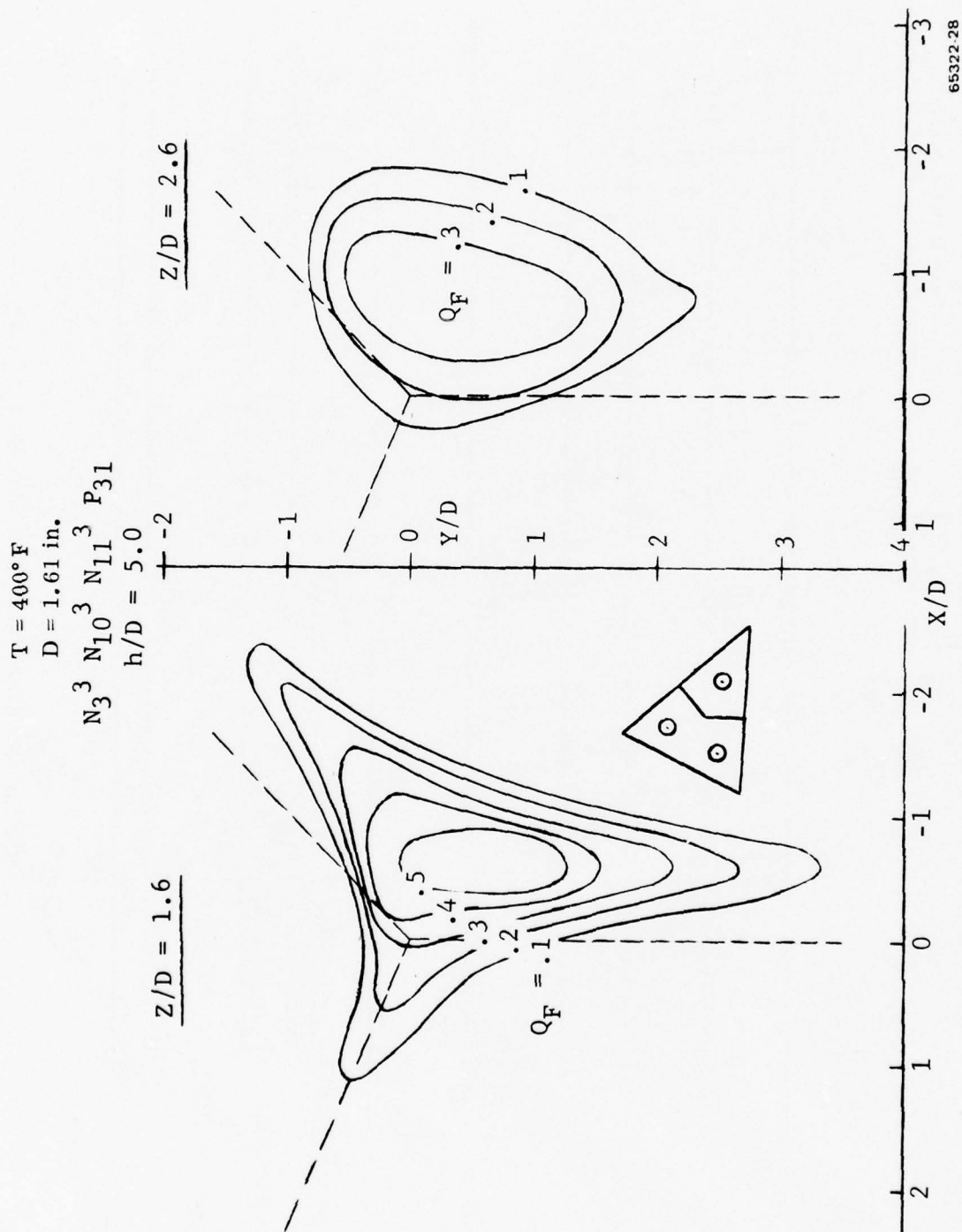
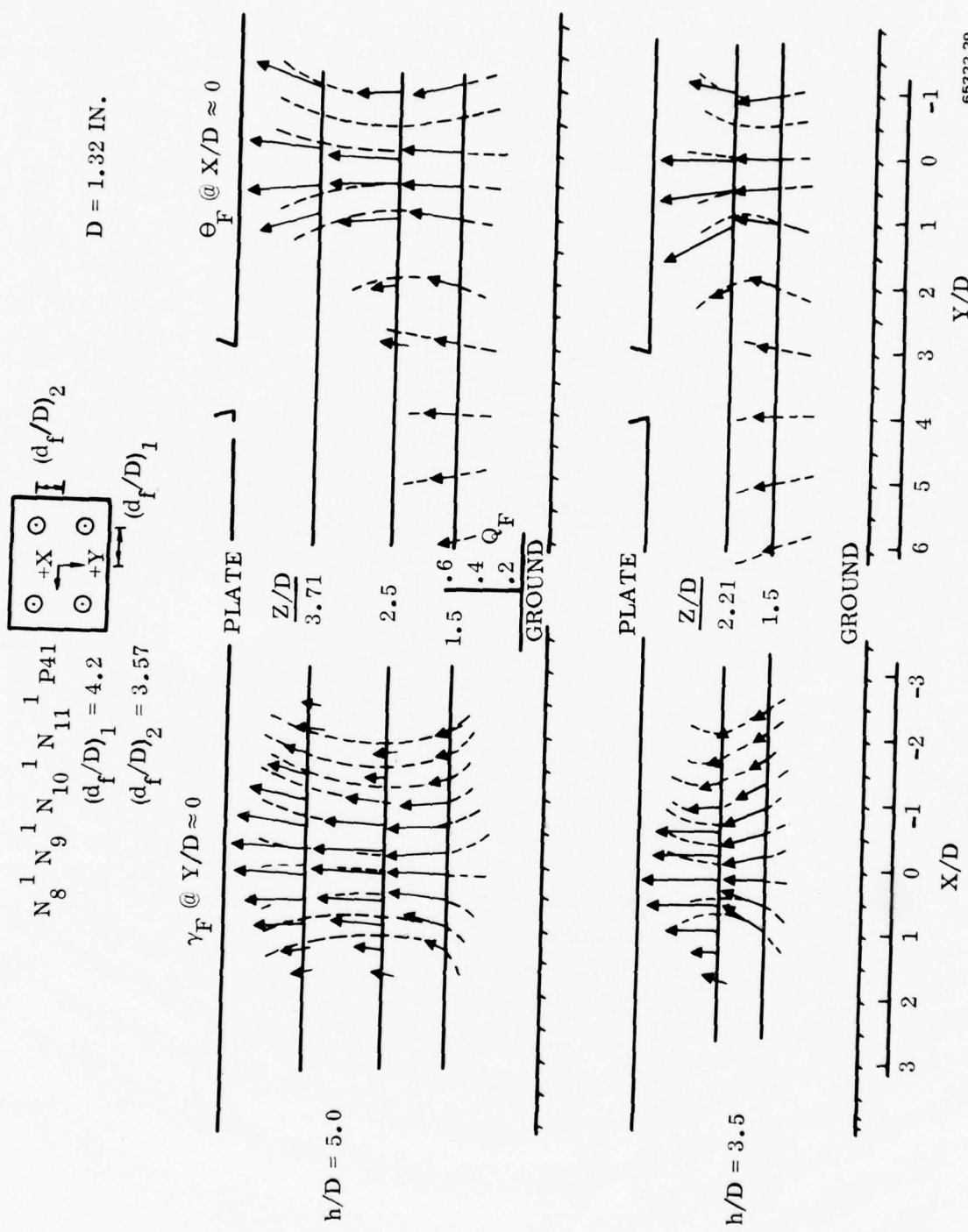


Figure 27. A Central Core Fountain is Formed Between Three Nozzles



65322-29

Figure 28. Four Nozzle Fountain Flows Coalesce Towards the Center of the Fountain

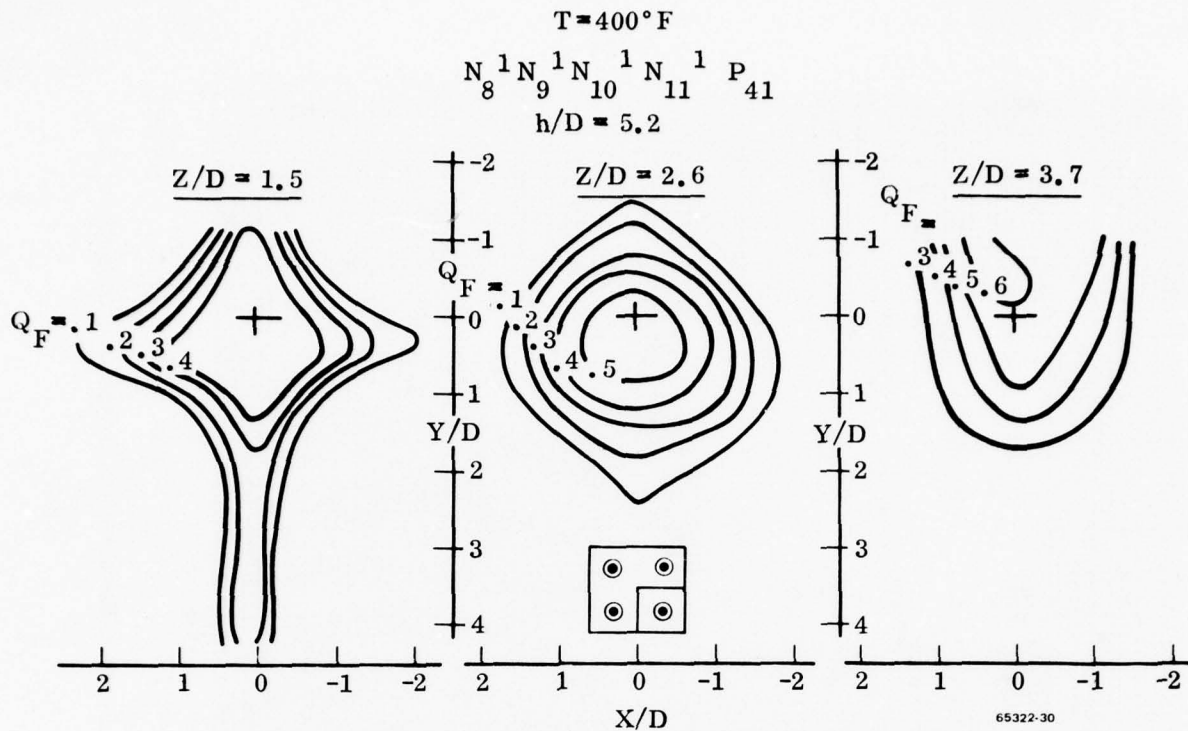


Figure 29. A Central Core Fountain is Formed Between Four Nozzles

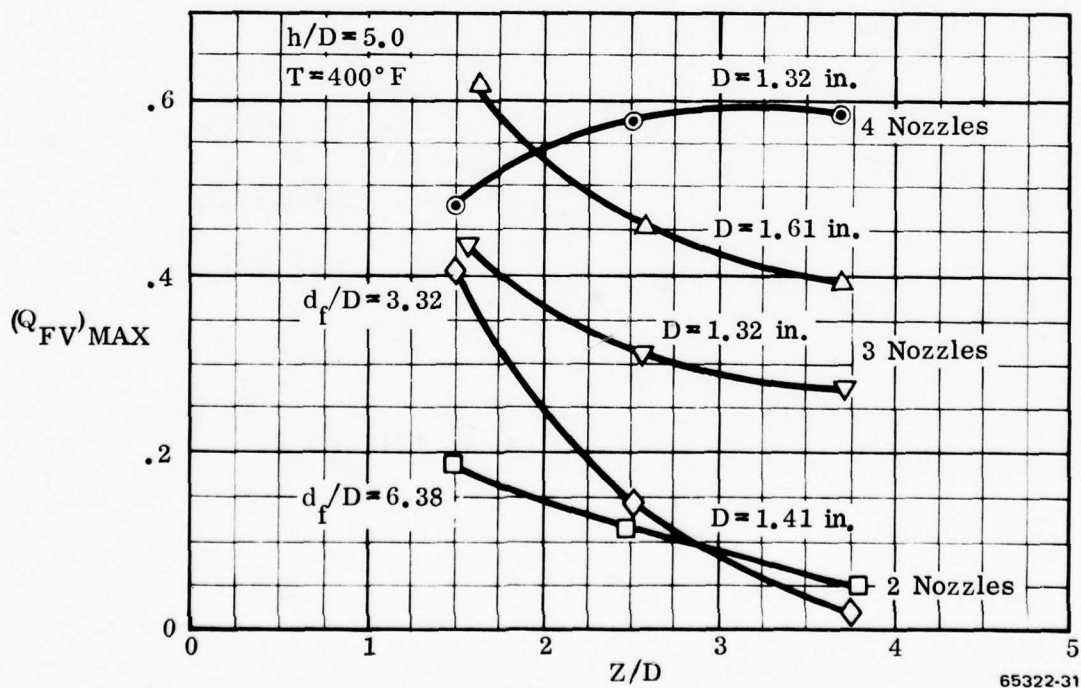
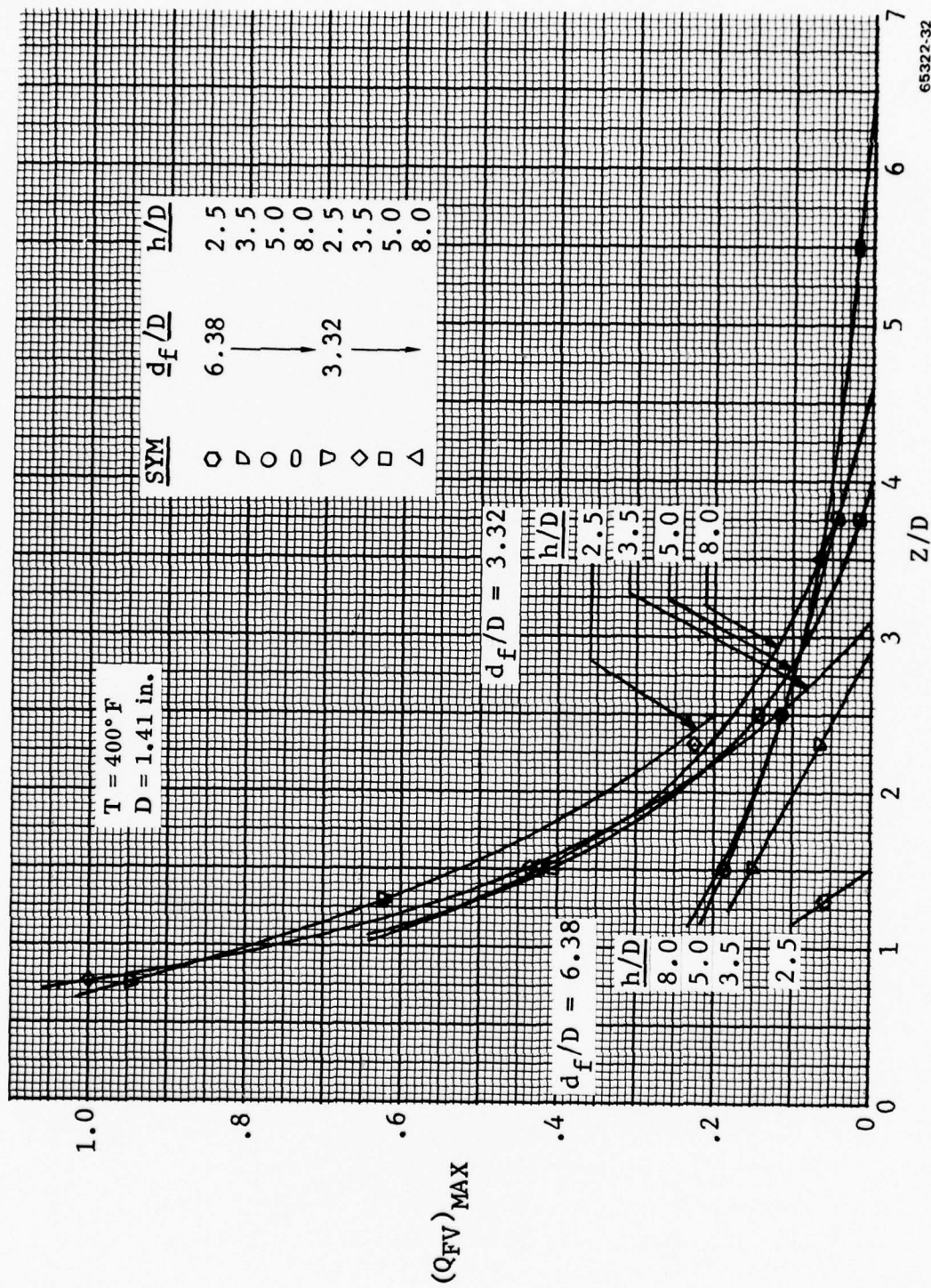


Figure 30. Dynamic Pressure Decay Characteristics are Dependent on the Number of Nozzles



65322-32

Figure 31. In Some Cases the Low Position of the Blocking Surface Reduces the Dynamic Pressure in the Fountain (Two Nozzles)

$$T=400^{\circ}\text{F}$$


The three nozzle configuration data, Figure 32, include points at low Z/D where the ground jets are just combining into the fountain, and thus have low vertical velocity components. There is a rapid increase in the vertical velocity up to Z/D values of about 1.4, then the values decrease. The larger diameter three nozzle configuration (closer spacing) forms a stronger fountain than the small diameter nozzles. There is also a crossover in the variation of the maximum dynamic pressure with blocking surface height (Figure 32), a characteristic of the strong fountain formed by the four nozzle configuration, Figure 33.

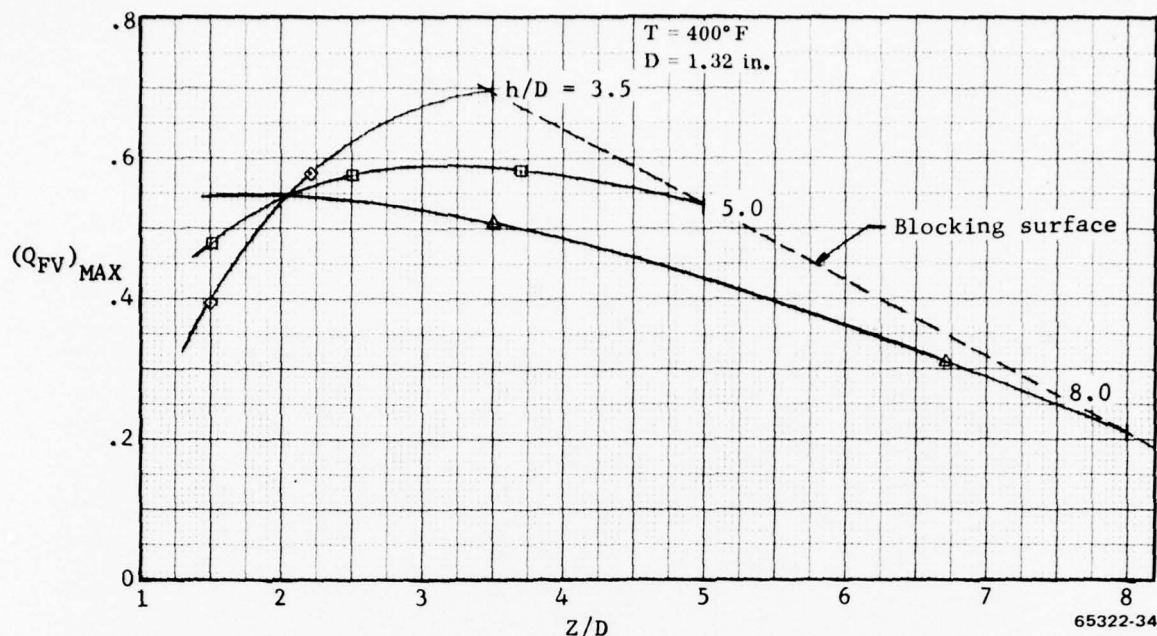


Figure 33. Blocking Surface Height Has a Strong Effect on Four-nozzle Fountain Decay Characteristics

The effect of h/D on the four nozzle configuration dynamic pressure is shown in Figure 33. The rate of increase of dynamic pressure with height in the fountain decreases with increasing blocking surface height for these fountains with strong central cores. Another way to state this is to say that the blocking surface, or especially a low position of the blocking surface, plays a prominent role in the structuring of the fountain in the "venturi" configuration. Note that this effect is more pronounced at low h/D where the fountain region is the most confined between the blocking surface and the ground board.

The pronounced effect of the number of nozzles on the strength of the resulting fountain is highlighted in Figure 34. The maximum dynamic pressure is several times higher with four nozzles than with two nozzles at moderate heights in the fountain ($Z/D = 2.0$) increasing to an order of magnitude higher at $Z/D = 4.0$.

3.3 VERTICAL COMPONENT OF MOMENTUM

As discussed at the beginning of this section, the net fountain effect on the induced forces is comprised of two parts: the force due to the fountain core itself, and the interference effects of the fountain on the surrounding flow. An estimate of the fountain core force is determined by integrating the vertical component of the fountain

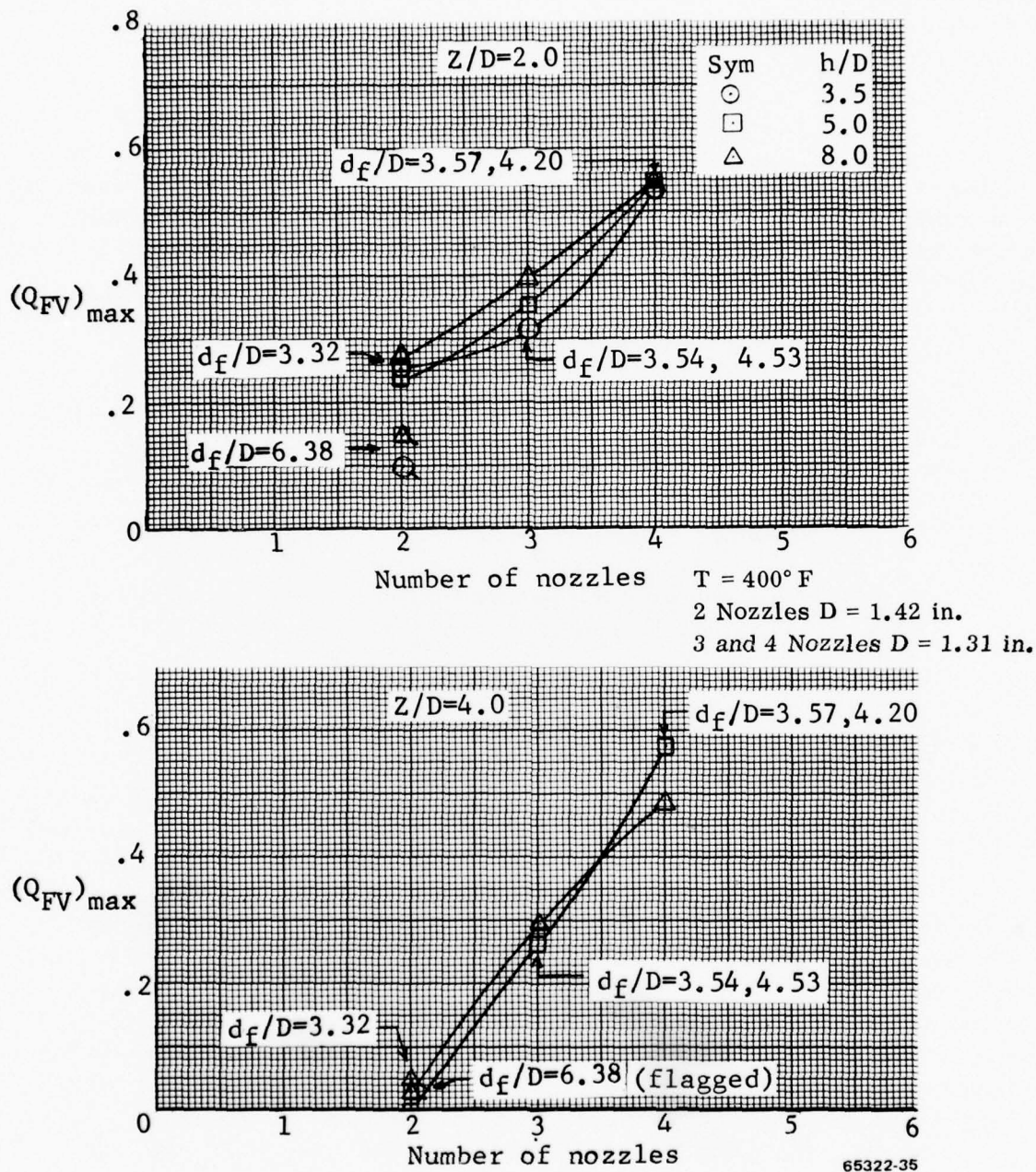


Figure 34. Fountain Strength Increases with Number of Nozzles

dynamic pressures. A discussion of the integration process and the resulting fountain core force characteristics follows.

3.3.1 INTEGRATION SCHEME. The fountain momentum flux passing through a plane parallel to the ground at any height can be determined from the rake pressure data. For steady flow and negligible body forces, the momentum flux equation can be expressed as

$$\vec{F} = \iint \vec{V} (\rho \vec{V} \cdot d\vec{A}).$$

An estimate of the effective fountain core force at any height can be found by assuming that, if a solid surface were placed in the flow at that height, all of the momentum would be converted to a force on the plate with no losses. Integrating in the X-Y plane for the vertical component of this force, this equation becomes

$$L_{FC} = \frac{1}{144} \iint \rho V^2 \cos^2 \theta_F \cos^2 \gamma_F dx dy$$

where L_{FC} = vertical component of the fountain core force - lb_f

ρ = density - slugs/ft³

θ_F, γ_F = Euler angles of the flow inclination from vertical - deg

V = Velocity, fps

In terms of dynamic pressure in the fountain, Q_F , psi:

$$L_{FC} = \iint 2 Q_F \cos^2 \theta_F \cos^2 \gamma_F dx dy$$

In dealing with large amounts of pressure data that require mechanized integration it is necessary to review the data to eliminate the few erroneous data points that are inevitably present. To this end, an interactive computer procedure was developed that plotted the rake dynamic pressures and allowed the data to be edited. It then faired the edited data with an interactive capability for the user to smooth the fairing, and integrated the results. Edited and faired data for all of the fountain rake surveys are presented in Appendix B in the form of profiles of the vertical component of the dynamic pressure at the tested locations along the fountain. The "raw" rake data from the test are presented in Reference 1.

3.3.2 FOUNTAIN CORE FORCE. The results of such an integration involving two widely spaced, $d_f/D = 6.38$, nozzles are shown in Figure 35. Rake sweeps were

$T = 400^\circ \text{F}$
 $N_2^2 N_{13}^2 P_{13}$
 $d_f/D = 6.38$
 $d = D = 1.41 \text{ in.}$

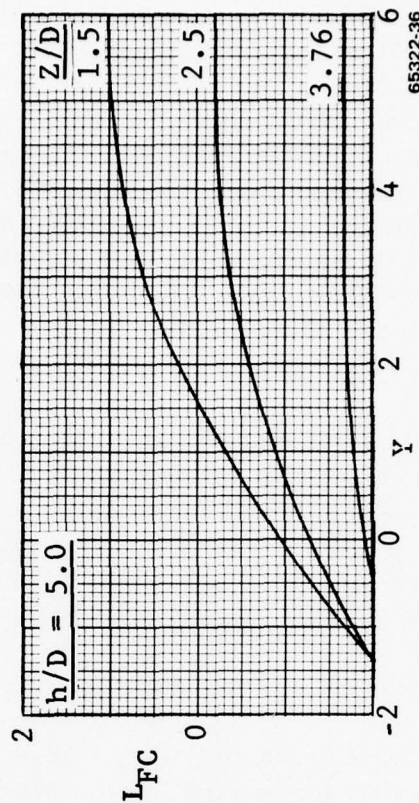
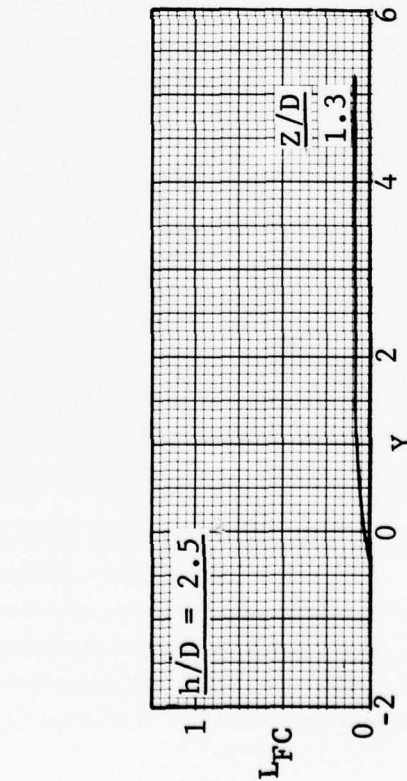
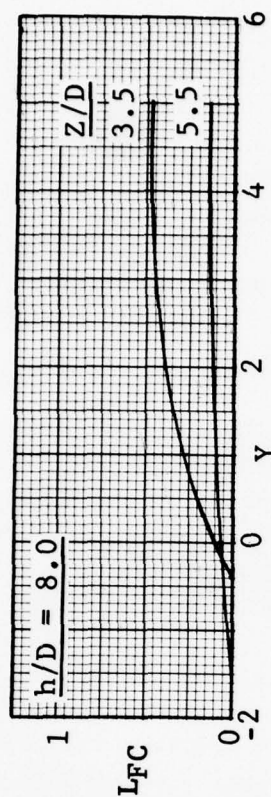
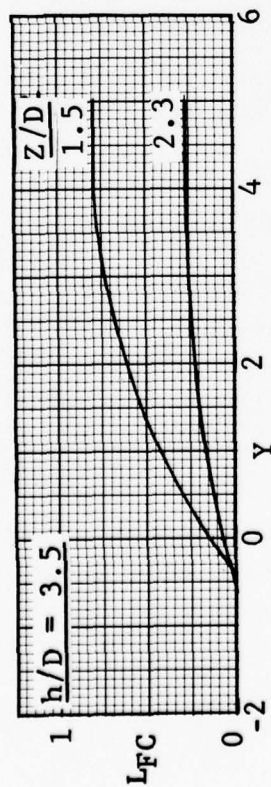
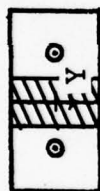


Figure 35. The Fountain Core Force with Two Widely-spaced Nozzles

conducted over slightly more than one-half of the fountain length. The fountain forces shown in Figure 35 were obtained by doubling the integration from the point of symmetry, outboard. The net force is shown as a function of the length (Y-direction) of the fountain from the point of symmetry. Thus, the maximum force at each height in the fountain is the total core force for that configuration. A strong decay in force with height is evident and, as expected, the lifting force increases less rapidly with distance along the fountain centerline. Similar trends are apparent for the medium spaced, $d_f/D = 3.32$, nozzles although the fountain strength is significantly larger at the lower model heights, Figure 36. Rake surveys were also conducted for two closely spaced, $d_f/D = 1.06$, nozzles, but a fountain was not detected. Apparently, the nozzle flows merged before striking the ground.

The effects of jet temperature, model pitch angle, and a 30 knot wind on the fountain force for the medium spaced nozzles are shown in Figure 37. At h/D of 5.0 very little effect of a 200 degree temperature change from 200°F to 400°F is noted, which is consistent with the force data results, Figure 16. However, the force data (Figure 16) also indicate that a significant change would be expected for temperature change from 70°F to 200°F. Unfortunately, rake data were not obtained at this condition.

The 30 knot wind has no significant effect on the fountain core force at the base of the fountain, $Z/D = 1.5$, but the force appears to decay more rapidly with height in the fountain. The fountain core vertical force is reduced when the model is pitched 10 degrees due to the resulting inclination of the fountain. There is also evidence of a reduced positive net effect of the fountain due to pitch in the force data at an h/D of 5.0, see Figure 20. The loss in fountain core lift due to angle-of-attack and wind, nondimensionalized by the zero pitch, zero wind baseline is shown in Figure 38. These curves can be used to estimate the approximate effects of the pitch angles and wind velocities not tested.

The fountain force resulting from the four nozzle configuration, Figure 39, shows the presence of the strong central core at the higher values of Z/D . Most of the force is experienced within two nozzle diameters from the centroid of the four nozzles. As in the two nozzle case, the total force was obtained by doubling the integrated value from the point of symmetry to the side of the plate in the Y-direction. As discussed in Section 3.2, it is possible that there is a weak fountain leg at the low heights in the fountain between the closer spaced nozzles, which has not been included in this integration. However, the effects are believed small and would only exist close to the ground.

One leg of the fountain formed by the three nozzle configuration was also surveyed with the rake. Due to the unsymmetry of the configuration, and the associated inclination of the fountain, the actual total core force could not be determined by integration. However, useful trends are observed from the segment which was surveyed (shown by the crosshatched region in the sketch of Figure 40). The resulting fountain lifting forces for two size nozzles at the same physical spacing, thus representing two values

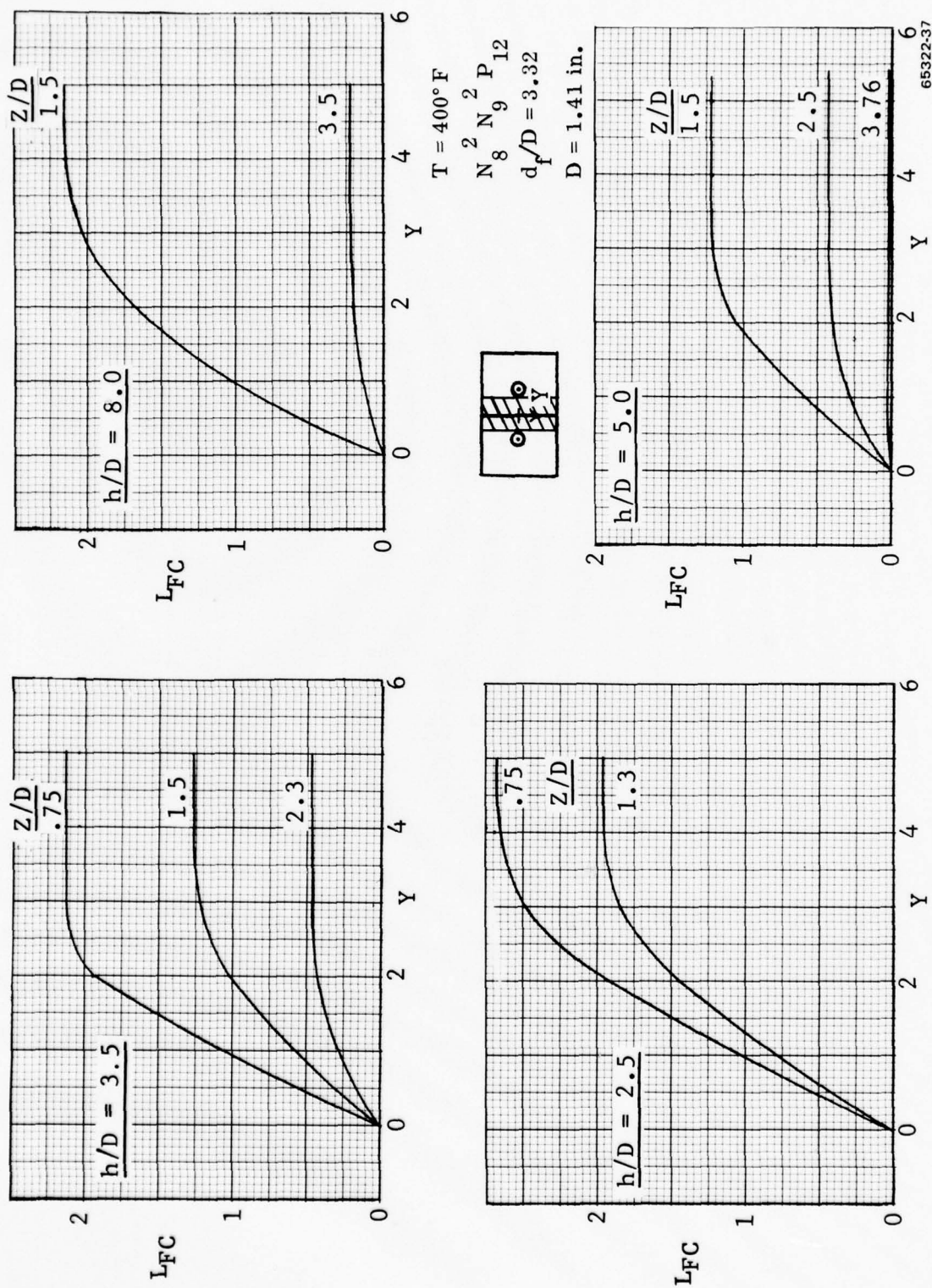
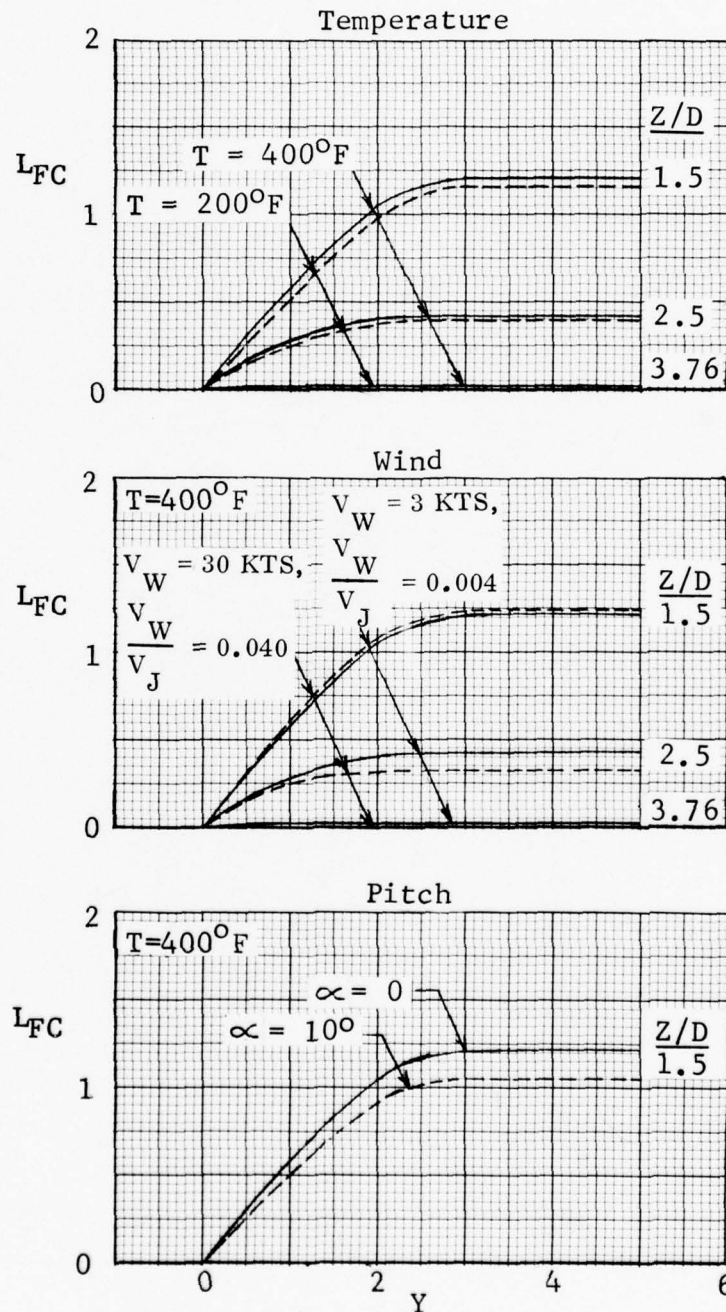
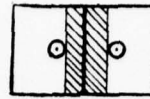


Figure 36. The Fountain Core Force with Two Medium-spaced Nozzles

$h/D = 5.0$
 $N_8^2 \quad N_9^2 \quad P_{12}$
 $d_f/D = 3.32$
 $D = 1.41 \text{ IN.}$



65322-38

Figure 37. Temperature, Wind and Pitch Effect the Fountain Core Lift

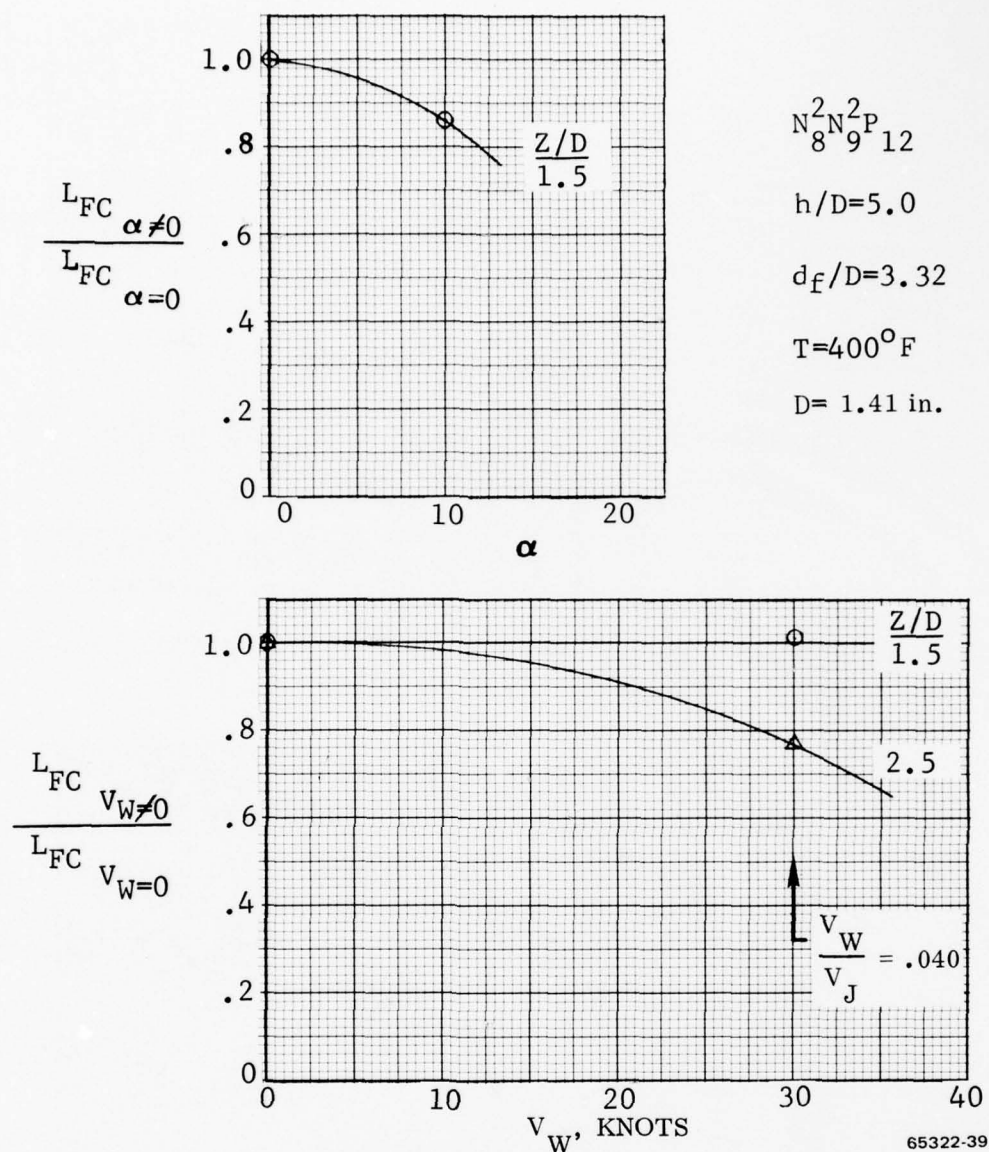
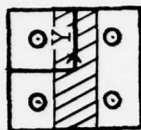
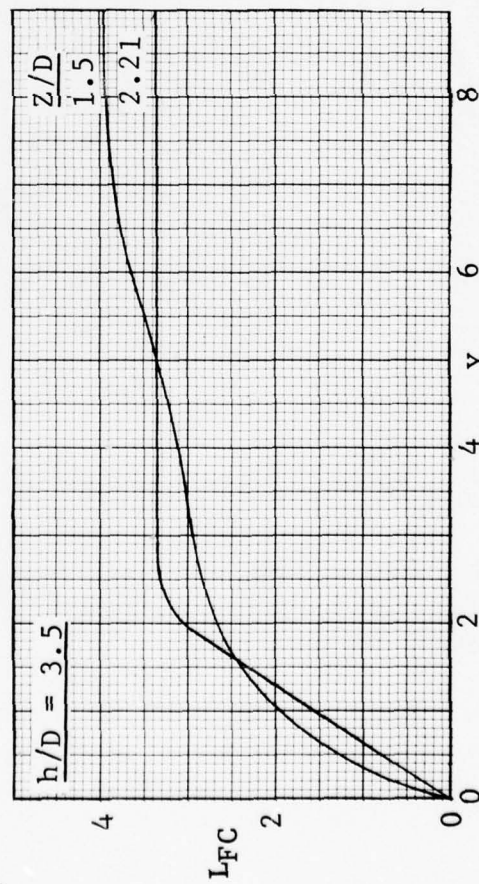
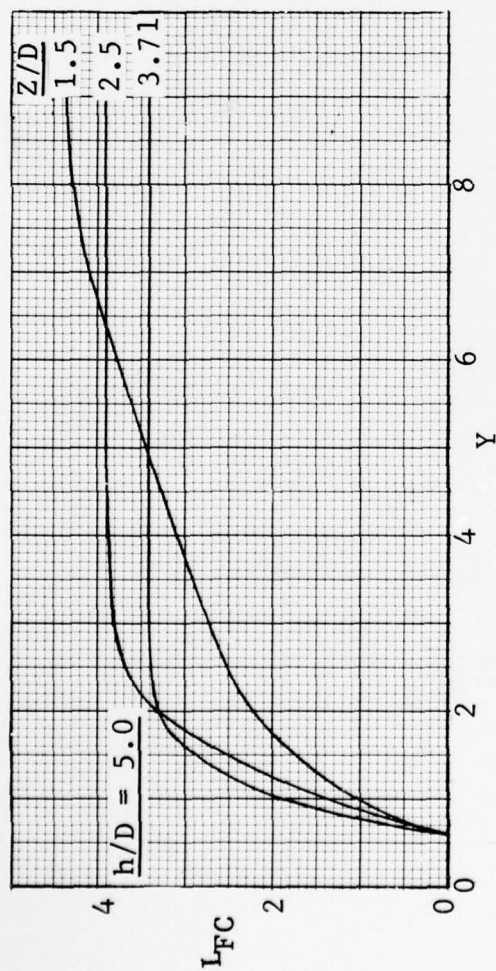


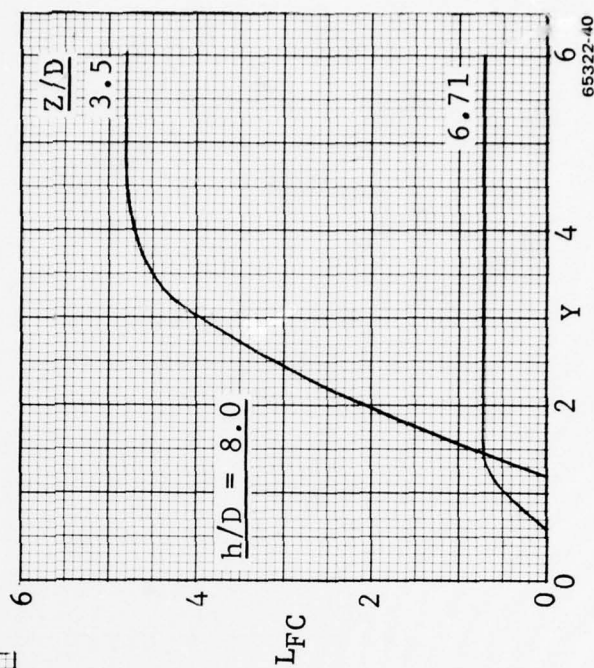
Figure 38. Pitch and Wind Decrease the Fountain Core Lift

of d_f/D , are shown in Figure 40. The larger nozzles result in the formation of a stronger fountain due to the increased thrust (mass flow), but both fountains decay at approximately the same rate.

The total fountain core lift (maximum value of L_{FC} , which occurs at Y values nominally from 3 to 8) for the two and four nozzle configurations at each height in the fountain (from Figures 35, 36, and 39) is shown in Figure 41. The forces have been nondimensionalized by the total thrust for each configuration. Extrapolation of the

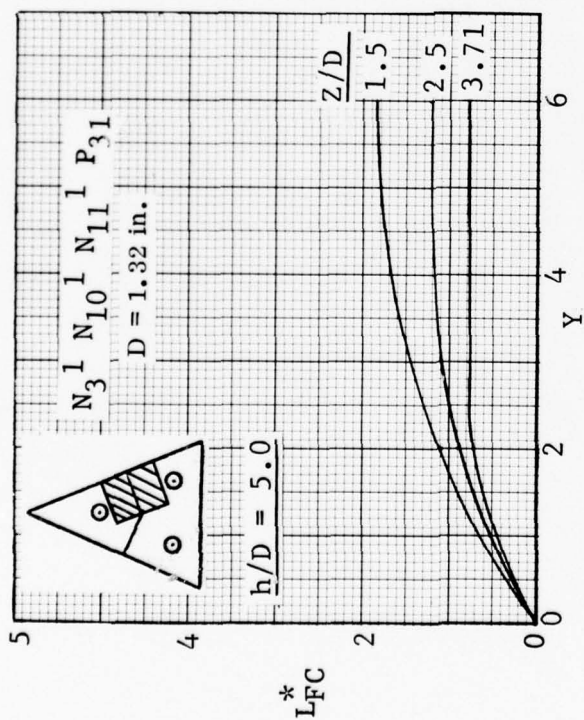
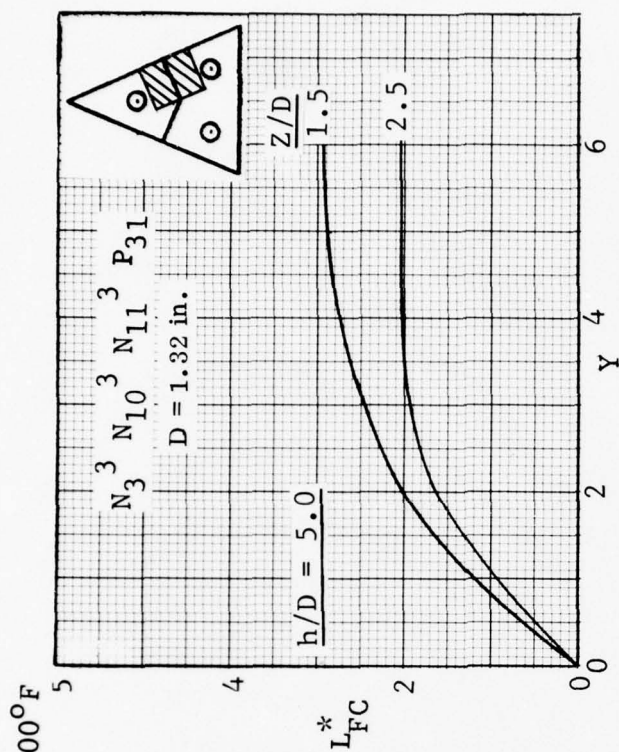


$N_8^1 N_9^1 N_{10}^1 N_{11}^1 P_{41}$
 $D = 1.32 \text{ in.}$
 $T = 400^\circ \text{F}$



65322-40

Figure 39. Four-nozzle Fountain Lift is Concentrated Near the Fountain Center



*Not total force

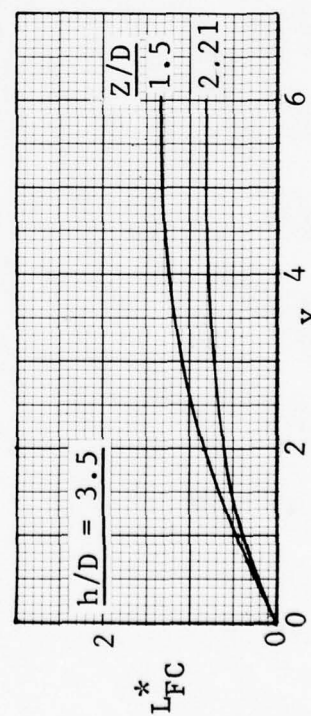
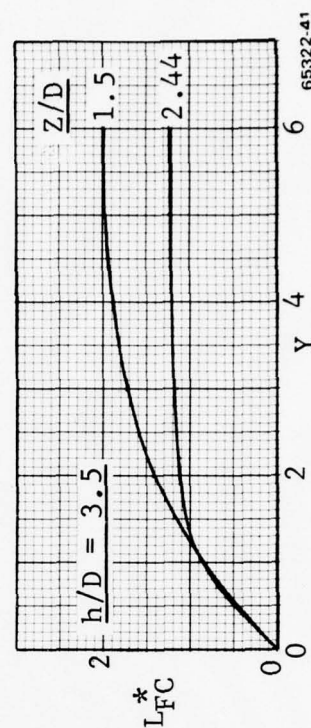


Figure 40. A Partial Fountain Core Force with Three Nozzles

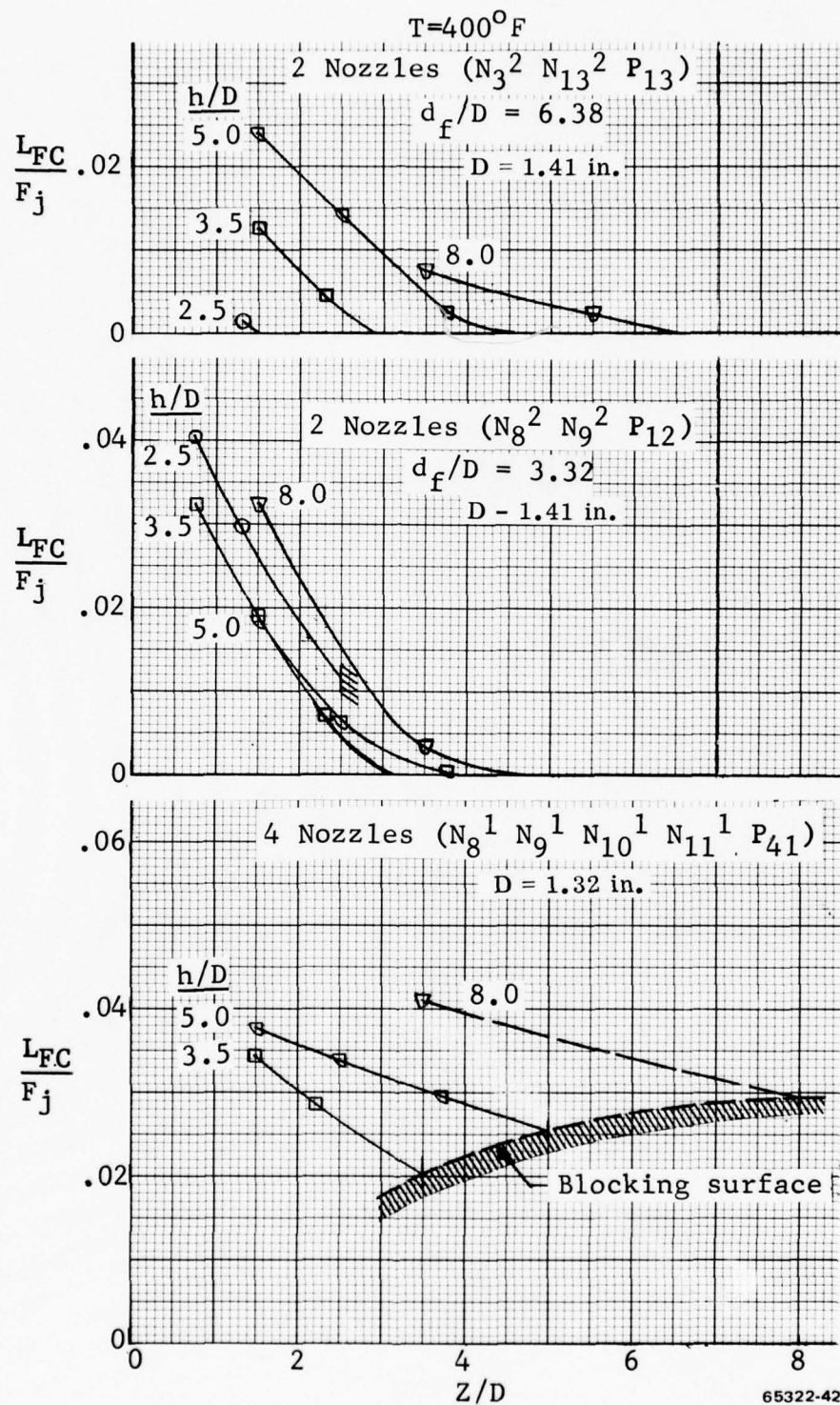


Figure 41. Four Nozzle Fountains Exert a Positive Force on the Blocking Surface

data to the height of the blocking surface yields an estimation of the fountain core force that acts on the plates. There is no positive force on the plates for most of the two nozzle configurations tested. In other words, the vertical components of momentum become zero before the fountain reaches the blocking surface. An exception is the medium spaced nozzle case at low heights, h/D of 2.5, where a lift force approximately equal to 1% of the nozzle thrust is experienced. As a contrast, the strong fountain produced by the four nozzle arrangement results in a positive force of 2 to 3% thrust at all model heights tested.

The effect of blocking surface height on the fountain core lift is highlighted in Figure 42. Generally, increased blocking surface height yields a stronger fountain (see discussion in Section 3.4 with the lone exception being intermediate nozzle spacings ($d_x/D = 3.32$) at low h/D). This effect is not completely understood at the present time.

The three nozzle configuration also produces positive fountain core forces on the blocking surface, Figure 43. However, as discussed previously, these are not total forces since only one portion of the fountain was considered. The data for the two different nozzle sizes tested tend to collapse when nondimensionalized by the thrust, but the configuration with lower equivalent spacing ($D = 1.61$) produces somewhat higher forces.

3.4 FOUNTAIN ENTRAINMENT CHARACTERISTICS

The fundamental flow mechanism responsible for the forces experienced by blocking surfaces or the lower surfaces of the hovering jet powered VTOL airplaces are the entrainment of the ambient gas by the free jets emitting from the nozzles, the radial ground jets, and the fountains. Extensive previous work with the free jet and the ground jet, References 3 and 2, has determined their entrainment characteristics. One of the principal goals of this specific investigation was to determine the missing link in the entrainment picture, that is, the fountain entrainment characteristics. Definition of the fountain entrainment rates, or their distributed sink strengths, is of primary importance in the modeling of the flow fields surrounding VTOL vehicles that are hovering near ground.

3.4.1 MASS FLOW INTEGRATION. The fountain mass flow characteristics were determined from the experimental data by means of integrating the velocity information obtained from the fountain rake. The mass flow per unit area is derived directly from the continuity equation:

$$\dot{m}_T = \iint (\rho \vec{V} \cdot d\vec{A})$$

To determine the mass flow through an X-Y plane parallel to the ground, the equation becomes

$$\dot{m}_F = \frac{32.2}{144} \iint \rho V \cos \theta_F \cos \gamma_F dx dy$$

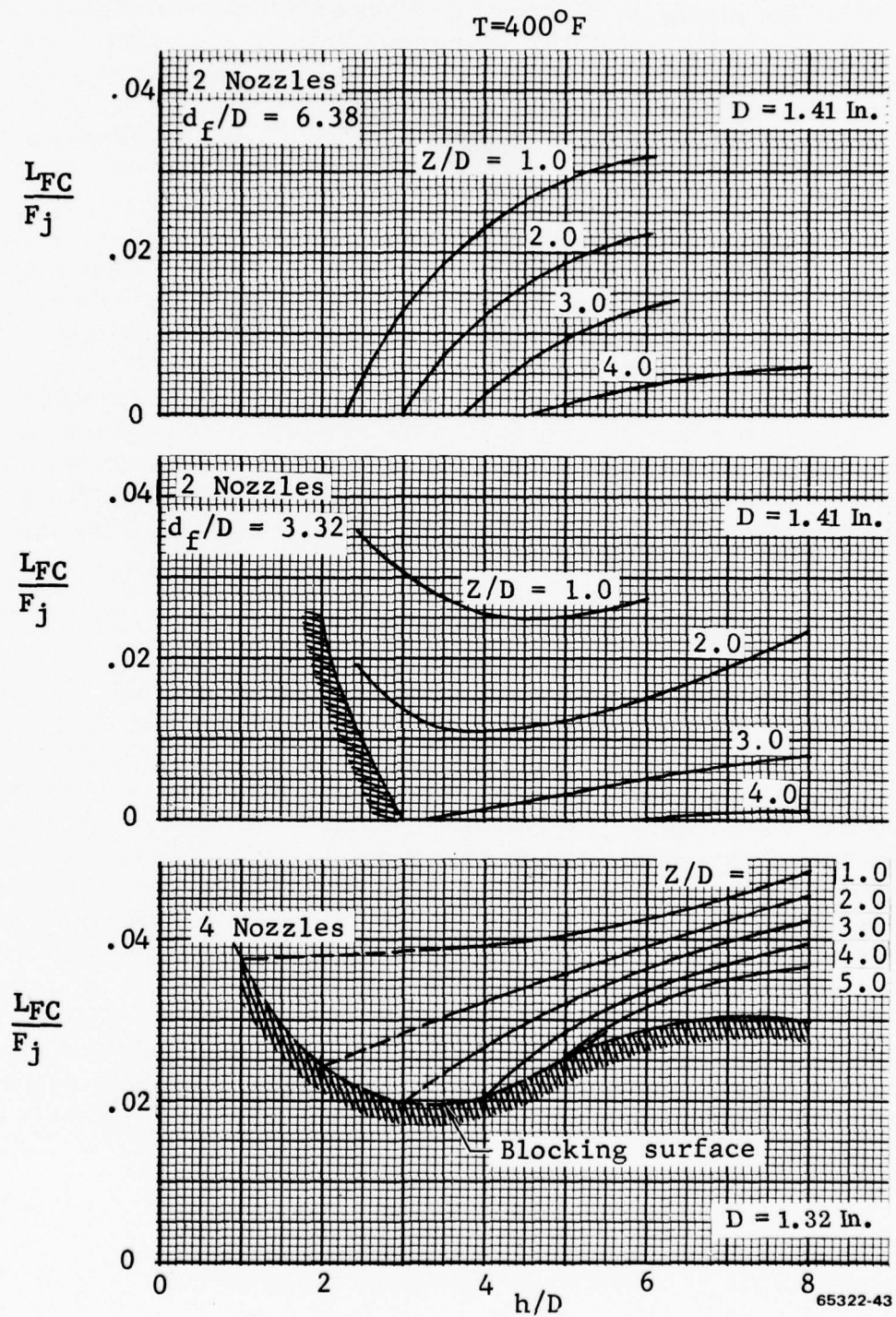


Figure 42. Blocking Surface Height Has a Significant Effect on the Fountain Lift

T=400°F

*Not total force - fountain
raked in one direction only

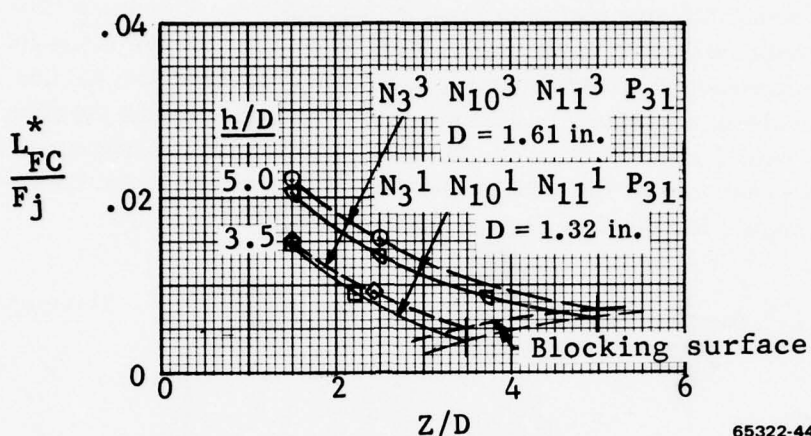


Figure 43. The Fountains Between Three Nozzles become Stronger When the Blocking Surface is Raised (h/D Increased)

where

\dot{m}_F = Total fountain mass flow through an X-Y plane,
lb_m/sec

ρ = density, slug/ft³

V = velocity, fps

θ_F, γ_F = Euler angles of the flow direction from vertical, deg

Since

$$\dot{m} = 2(32.2) Q_F/V = \frac{32.2}{144} \rho V$$

the expression becomes

$$\dot{m}_F = \iint \dot{m} \cos \theta_F \cos \gamma_F \, dx dy$$

where

\dot{m} = mass flow per unit area in the fountain,
lb_m/in²/sec

The interactive graphics procedure discussed in the previous section was also applied to the mass flow data so that they could be edited and faired. For convenience the term $(\dot{m} \cos \theta_F \cos \gamma_F)$ was used. The resulting faired values of this term are presented in Appendix B for each of the conditions tested.

To determine the mass entrainment in the fountain, it is necessary to develop flow streamlines so that a specific segment of the flow, within the rake survey boundaries, can be studied. A schematic of the procedure used is presented in Figure 44. The streamlines developed from the rake surveys are extended to the ground plane and a representative segment chosen, C-A, and D-B in Figure 44. The portion of nozzle mass flow entering this segment is defined by the angle ϕ . The mass flow through the X-Y plane at each value of Z is then calculated by integrating the mass flow per unit area in the X-direction and between the Y locations defined by the AC and BD streamlines. The resulting mass flow is then nondimensionalized by the fraction of the nozzle mass flow entering the segment ϕ , to obtain a total mass entrainment ratio, \dot{m}_F/\dot{m}_j . This ratio defines the sum of the mass entrainment in the free jet, the wall jet, and the fountain for the flow segment of interest.

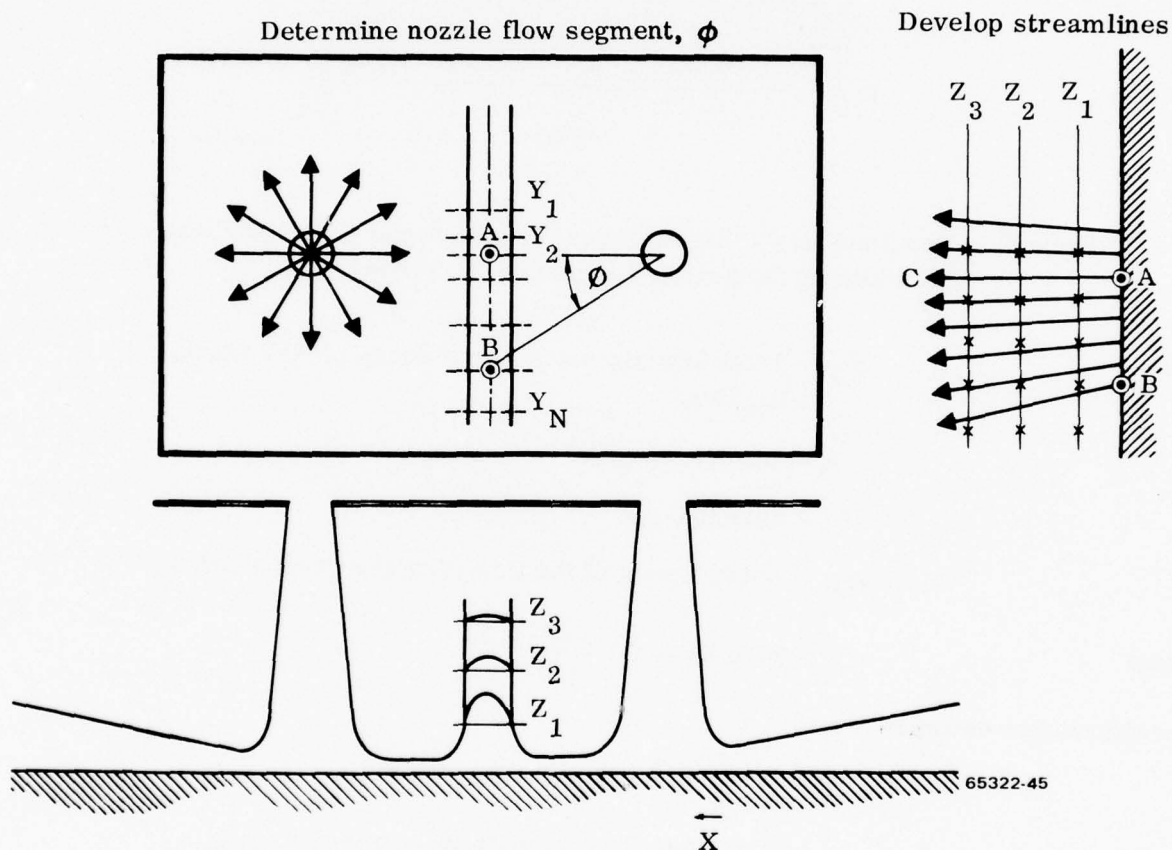


Figure 44. Mass Flows are Determined by Integrating Fountain Flow Characteristics

3.4.2 FOUNTAIN ENTRAINMENT RESULTS. The fountain is a physical extension of the ground jet and in this respect it is expected to retain certain ground jet characteristics. This is especially true for the fountains between two nozzles. Here we would

expect to find the usual lateral divergence of flow and entrainment of surrounding medium. The examination of the fountain test data, however, shows some surprising characteristics. The first striking result is that a fountain between two nozzles, unlike the ground jet, does not gain mass but loses mass (Figure 45). In other words the fountain is not entraining but is being entrained by a stronger source (Figure 46). This strong sink with an appetite for the fountain turns out to be the ground jet (see Sections 3.5 and 4). We can say the fountain is blocking off one avenue through which the ground jet is normally supplied with gasses for entrainment (Figure 46, Item B). As a consequence of this blockage and the resulting gas supply deficiency, the ground jet will entrain the relatively low energy gases in the fountain (Item C).

It is important to remember that in the context of this report the fountain is considered to be the definable vertical or near vertical column or sheet of flow raising from the ground. Flows of comparable velocities are present in the recirculation flow pattern in other directions, e.g., horizontal or down, but these are not considered to be part of the fountain for this analysis.

One most interesting point is that the mass flow in the fountain between two nozzles becomes zero in most cases before it can reach the blocking surface (Figure 45). In terms of a hovering airplane, this means that the fountain is unlikely to reach the underside of the airplane (blocking surface). It is entrained before it gets there. The exceptions to this rule are cases where the blocking surface is close to the ground $h/D = 3.0$ and the nozzles are relatively closely spaced (distance to fountain about four nozzle diameters $d_f/D = 4$). The locations where fountain mass flow \dot{m}_F/\dot{m}_j becomes zero are shown in Figure 47. Note that the data are applicable to two nozzles, rectangular plates, and exhaust temperatures of 400°F .

It is apparent from Figure 47 that the dissipation of the fountain is directly related to the height of the blocking surface. With a higher blocking surface location, more of the entrained gas can be supplied through the opening around the edges (cross-hatched area of Figure 48) and the fountain will survive for a longer distance.

The maximum fountain height data is plotted in Figure 49 and is based on the extrapolations of the information in Figure 47. The data are applicable to conditions where the blocking surface is sufficiently removed to have any effect on the fountain ($h/D = 10$) and is an indication of the maximum heights the fountain is expected to reach in the presence of "normal" ground jet entrainment action.

The fountain between three nozzles loses mass at a significantly reduced rate (Figure 50). Note that the fountain survives sufficiently long enough to reach the underside of the blocking surface. Consequently, we would expect to see a positive lift contribution here from the fountain core. This is in general agreement with the force data of Section 3.1.

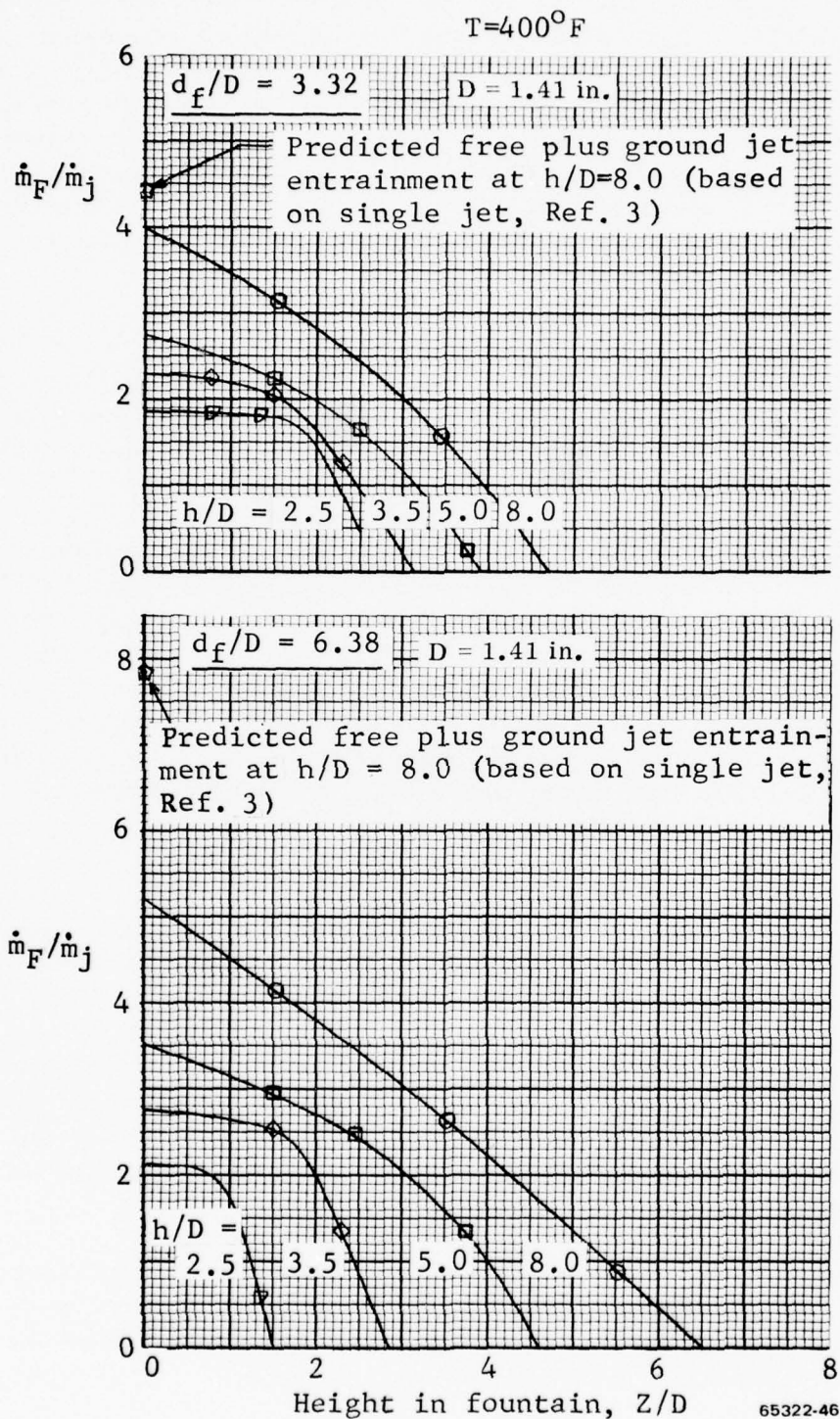
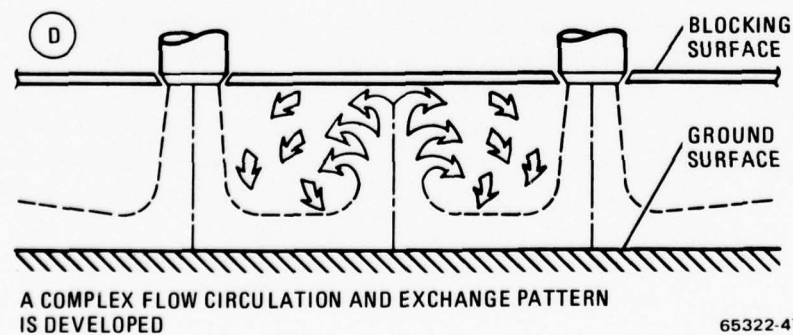
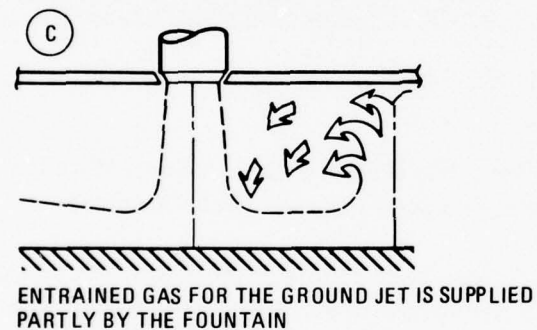
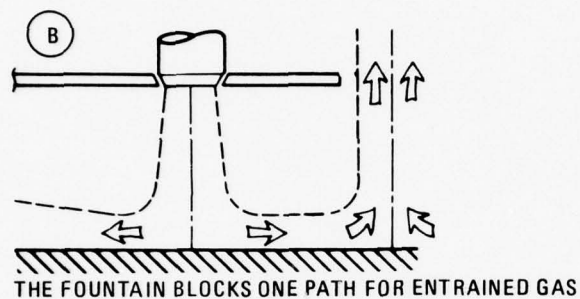
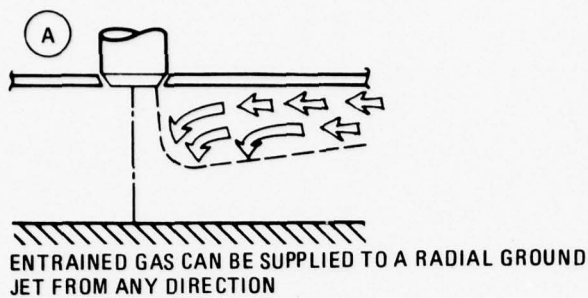


Figure 45. Fountains Between Two Nozzles Lose Mass as a Function of Height



65322-47

Figure 46. The Fountain Blocks the Flow of Gas to the Ground Jet

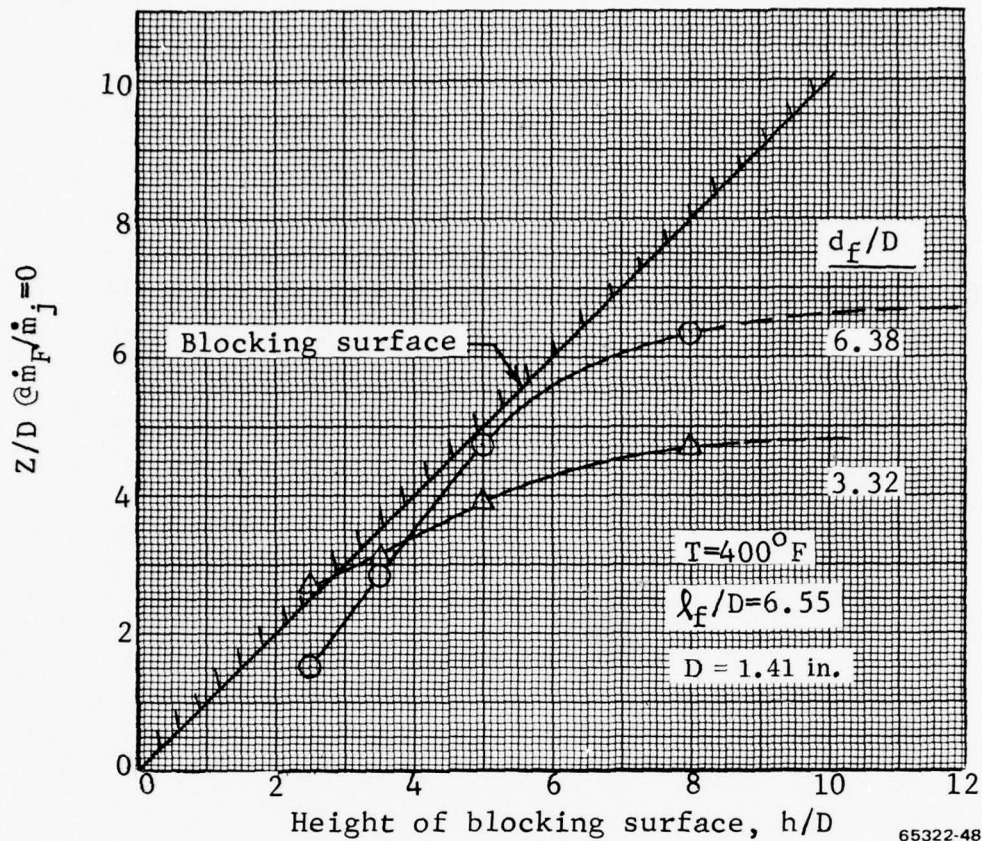
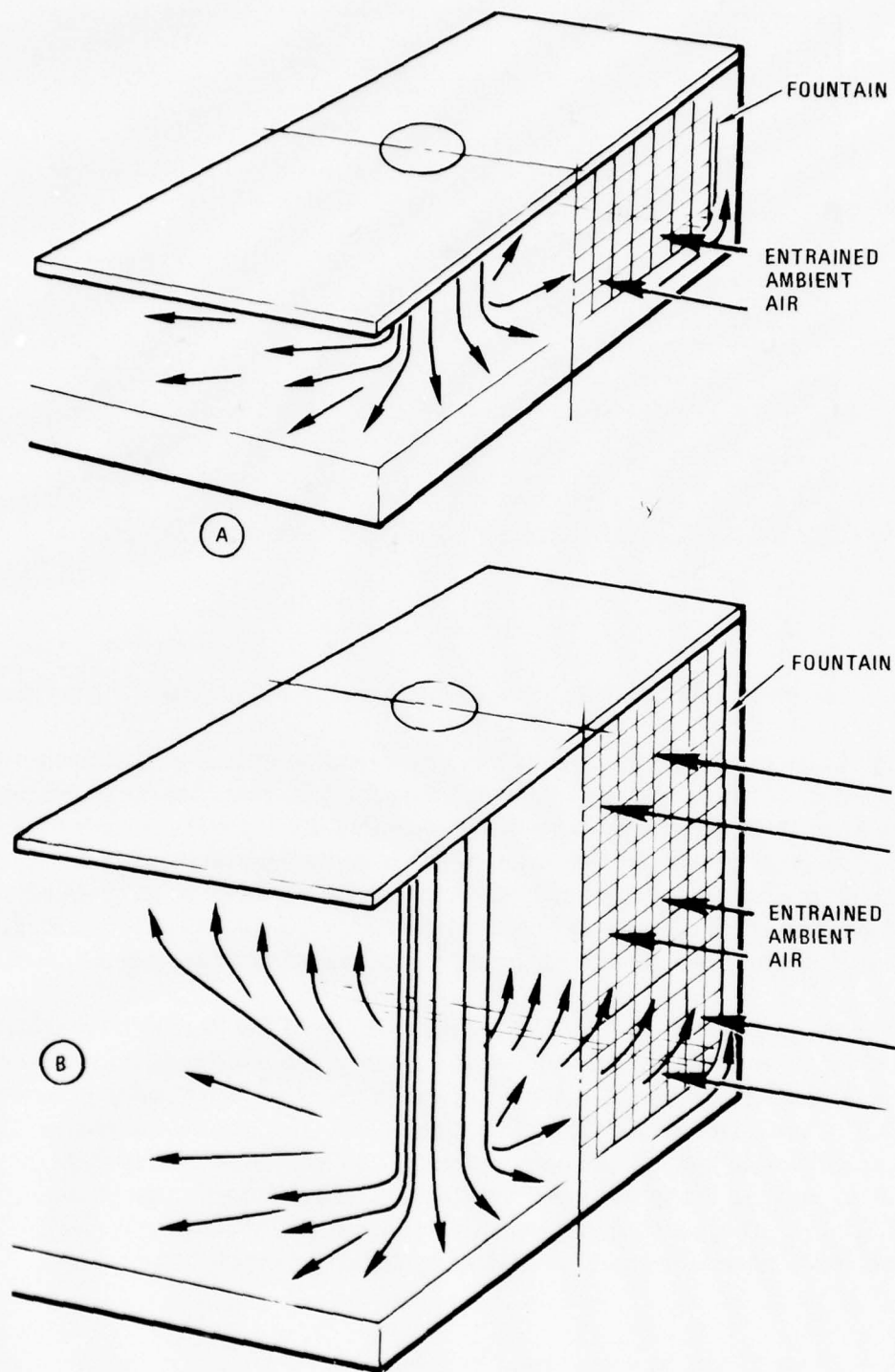


Figure 47. The Fountain Reaches Zero Mass Flow Prior to Contacting the Blocking Surface Except for Closely-spaced Nozzles (Two Nozzles)

The loss of mass phenomenon does not apply to fountains between four nozzles. Here we are dealing with a higher energy (Q) system that is less susceptible to the entrainment action of the ground jet. This can be seen from the lower plot of Figure 50. The fountains gain mass, that is, entrain surrounding air. The source of this air was not ascertained during the tests. However, the fountain temperatures (Section 4.0) seem to indicate that a significant percentage of the fountain gas is recirculated and reentrained subsequent to impacting with the blocking surface. The rapid disappearances of the legs of the Y and the X (Figures 27 and 29) also seem to indicate that these components of the fountain with relatively low Q s are entrained early. Also note that the fountain entrainment rate (slope of \dot{m}_F/\dot{m}_j with Z/D) becomes zero prior to impacting with the blocking surface for the models tested.

3.5 THE EFFECT OF THE FOUNTAIN ON THE GROUND JET

Of particular interest in Figure 45 are the intersections of the curves with the ordinate \dot{m}_F/\dot{m}_j . Since these extrapolations correspond to Z/D values of zero, they represent the entrainment in the free jet and ground jet up to the base of the fountain.



65322-49

Figure 48. At Higher Locations of the Blocking Surface More of the Entrained Air Can Be Obtained Through the Sides (Cross-Hatched Areas)

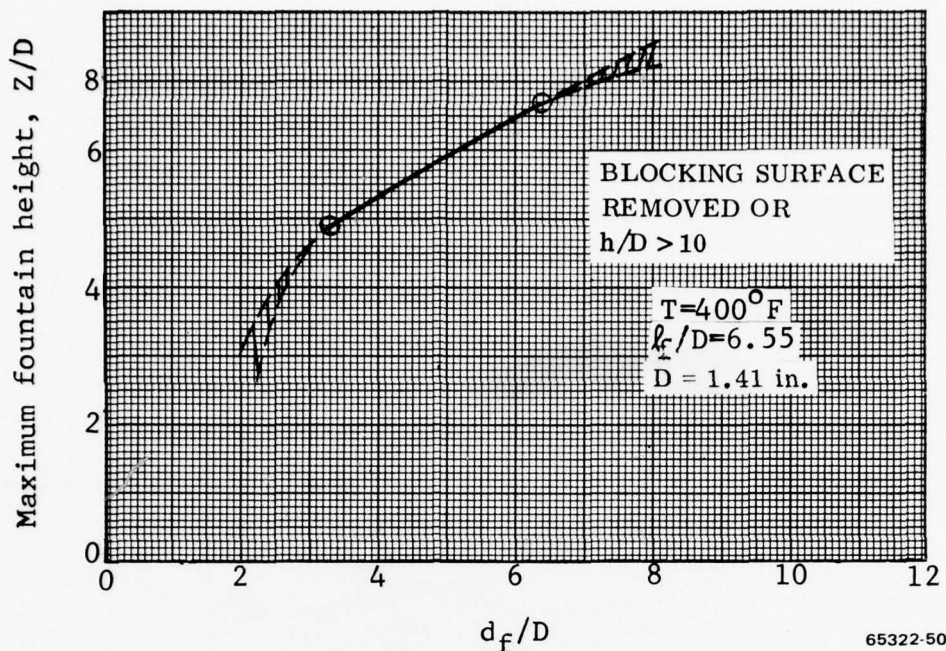


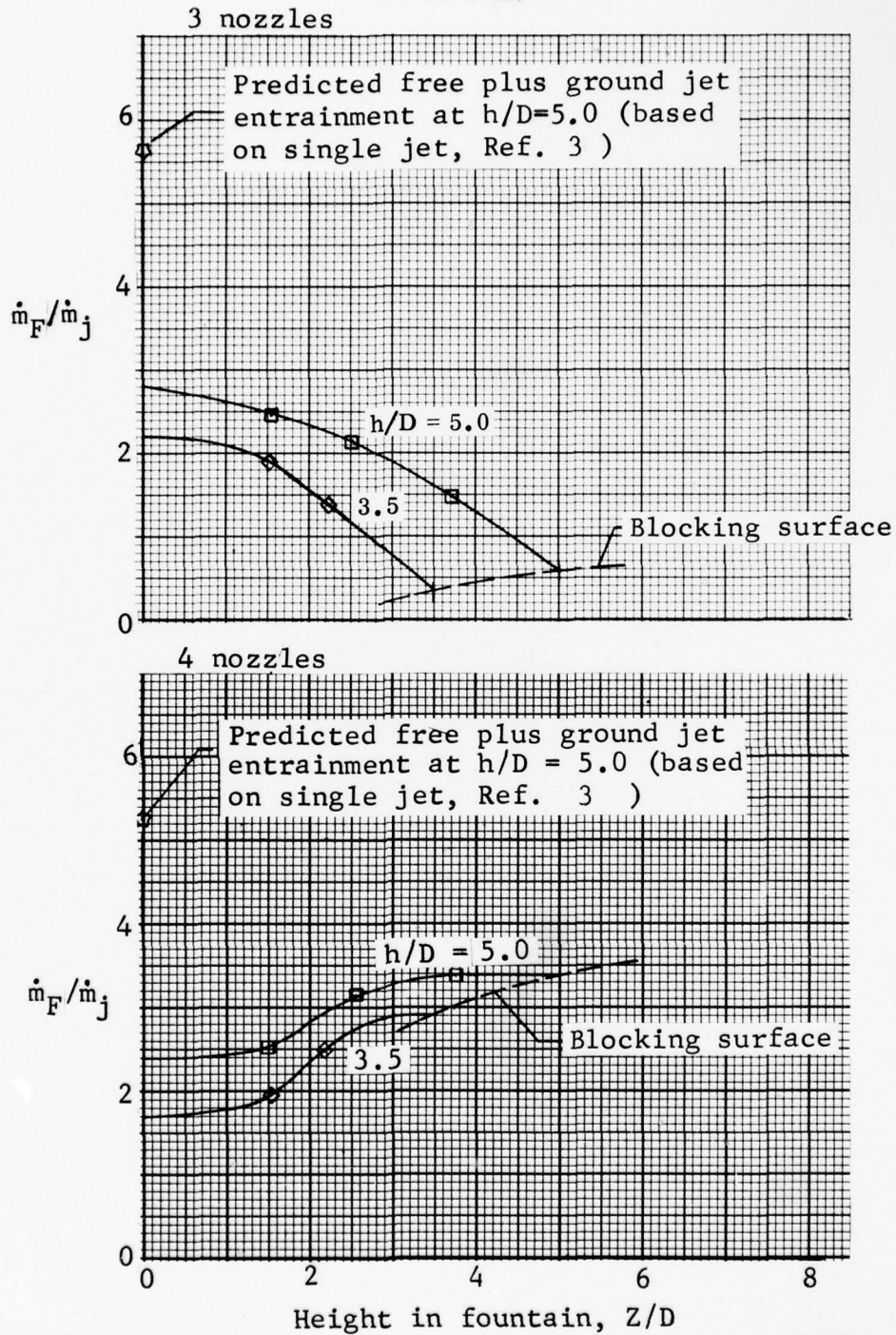
Figure 49. Maximum Fountain Height is a Function of Nozzle Spacing (Two Nozzles)

Comparison of these points with the predicted free jet plus ground jet entrainment with no fountain present, from Reference 3, shows that the free plus ground jet entrainment has been considerably reduced by the presence of the fountain, Figure 51. This reduction in free plus ground jet entrainment becomes less pronounced as the model or blocking surface height is increased and at values of h/D of 10 to 15, depending on nozzle spacing, the normal levels of free plus ground jet entrainment is reached. Similar information is presented in Figure 52 for the three and four nozzle cases.

This phenomenon, described as the significant reduction of the ground jet entrainment rates caused by the fountain, is considered to be one of the most significant discoveries during this research program. At the present time, Figure 48 and the description in Section 3.4.2 are advanced as the explanation of the phenomenon. It also demonstrates that all fountain and entrainment analytical models that do not include "second order" effects, such as the influence of the fountain on ground jet entrainment, are of little value, if any. It appears these so-called "second order" effects largely dominate the flow fields associated with multi-nozzle VTOL concepts. They can not be ignored.

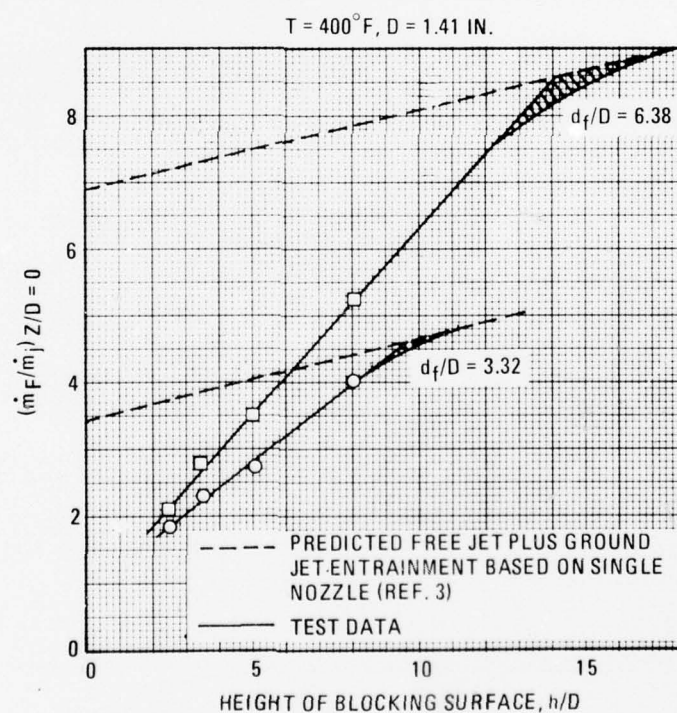
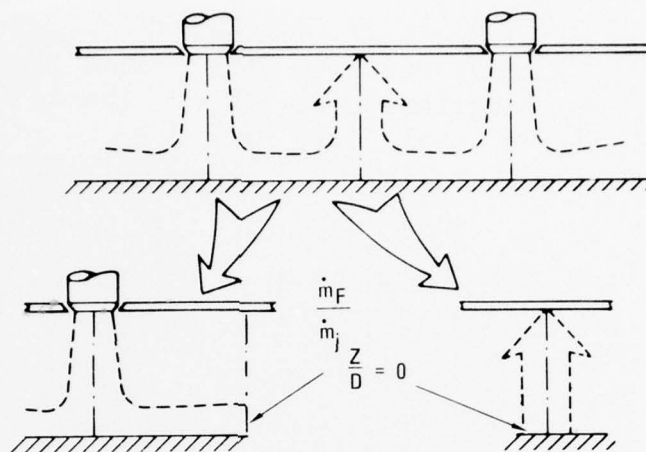
The data of Figures 51 and 52 can be used to determine the approximate limits where the fountain influence on ground jet entrainment disappears. This corresponds to the location (h/D) where normal ground jet entrainment rates are reached at the fountain intersection with the ground jet ($Z/D = 0$). This information is plotted in Figure 53. Needless to say, the data are based on extrapolations and should be considered to be

T = 400° F
D = 1.32 in.



65322-51

Figure 50. Fountains Between Four Nozzles Gain Mass as a Function of Height



65322-52

Figure 51. Ground Jet Entrainment is greatly Reduced by the Presence of a Fountain (Two Nozzles)

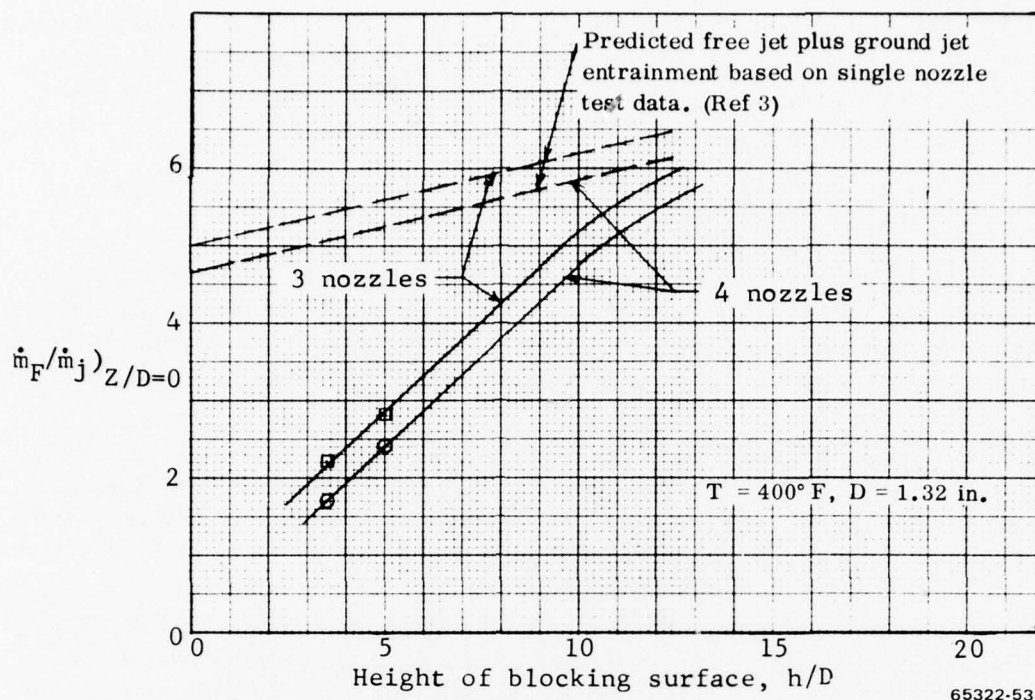


Figure 52. Ground Jet Entrainment is Greatly Reduced by the Presence of a Fountain Between Three and Four Nozzles

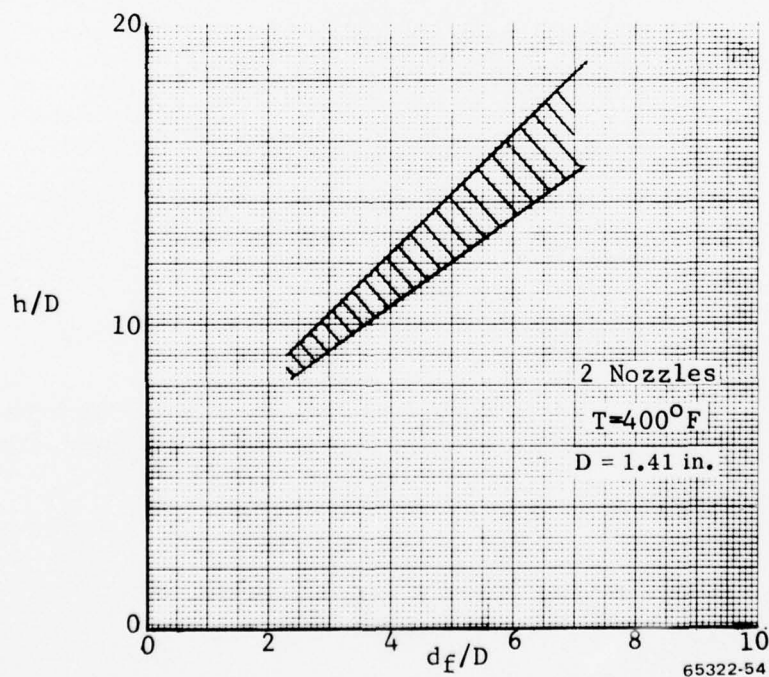


Figure 53. At Certain Blocking Surface Height (h/D) the Fountain Has Little Or No Effect On the Ground Jet Entrainment Characteristics

approximate. The data do indicate that for widely spaced nozzles ($d_f/D = 6$) the fountain has no influence on ground jet entrainment for blocking surface heights equal to more than 13.5 to 16 nozzle diameters. For closer nozzle spacing, $d_f/D = 3$, this fountain effect disappears at lower heights (about h/D of 9 to 10).

3.6 FOUNTAIN INTERFERENCE EFFECTS

It was pointed out in Section 3.0 that the fountain produced forces are categorized as lift generated by the fountain core, and interference effects. In the past, these interference effects were thought to be largely negative for the case of two nozzles (Reference 4). Data for three or four nozzles were not available at that time.

The accurate definition of fountain core generated forces (Section 3.3) has made it possible to reevaluate these interference effects, including Figure 4-6 of Reference 4. The new data for the two and four nozzle configurations is presented in Figures 54 and 55. These data were developed in the following manner.

The net effect of the fountain was derived as shown in Section 3.1 (Figure 15). The next question to be addressed was how much of these forces could be attributed to the interference effects. To answer this question, the lift due to the fountain core (Figure 41) was subtracted from the net fountain effect (Figure 15). The residue constituted the interference effect.

$$\frac{\Delta L_{fi}}{F_j} = \frac{\Delta L_f}{F_j} - \frac{L_{FC}}{F_j}$$

where ΔL_{fi} = Lift due to fountain interference

ΔL_f = Net effect of fountain (see Figure 15)

L_{FC} = Lift gain due to fountain core (see Figure 41)

These results were referenced to the area between the nozzle and the fountain, which represents the region over which the fountain and the induced effects will be concentrated as shown in Figure 56.

$$K_{fi} = \frac{\Delta L_{fi}}{F_j} / (S_f/D^2)$$

The term K_{fi} , estimated by the above equation, is presented in plotted form in Figures 54 and 55.

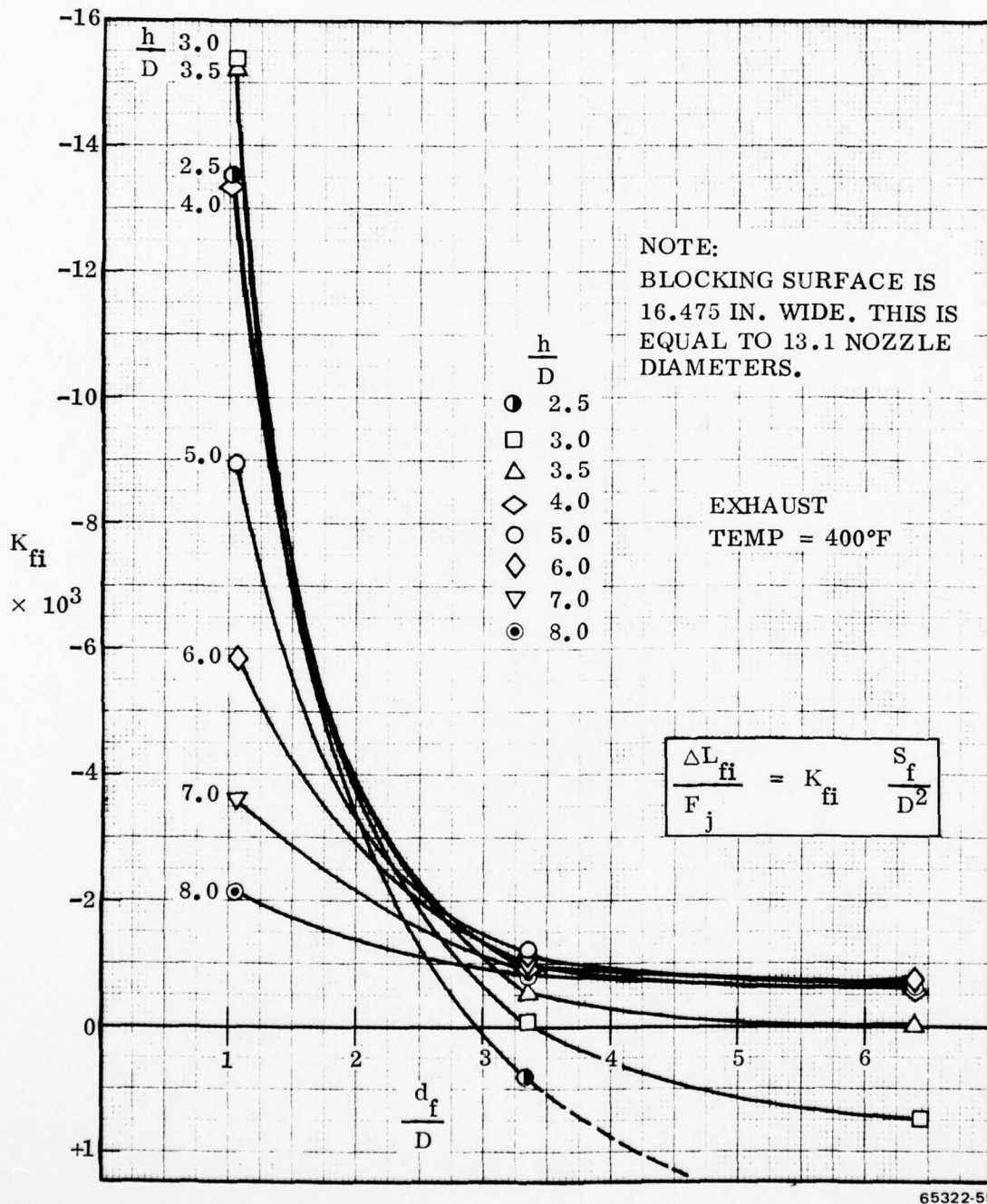
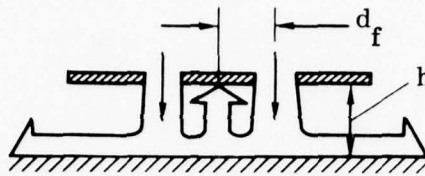
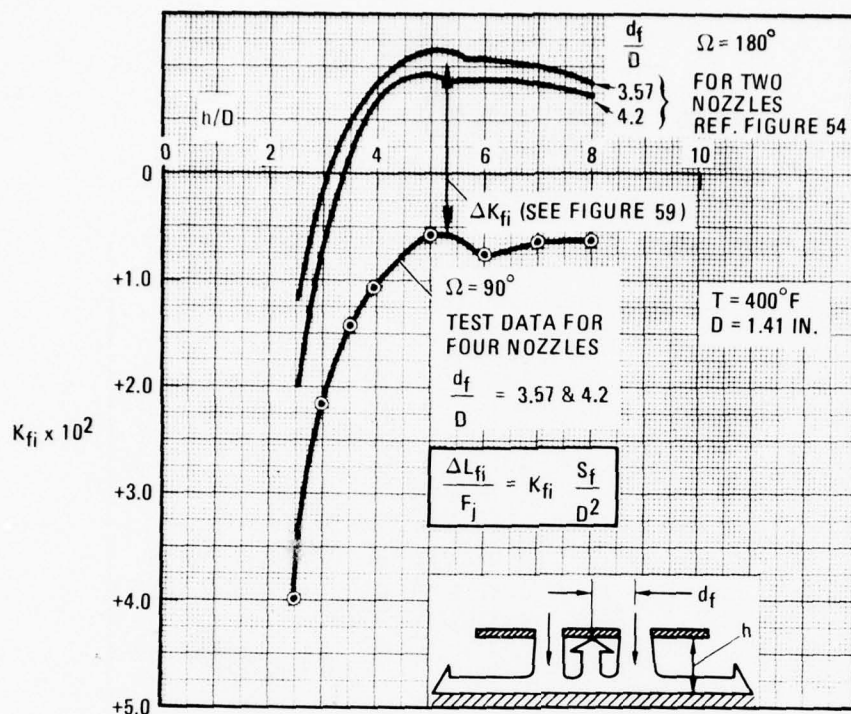


Figure 54. Fountains Between Two Nozzles Generate Mostly Negative Interference Effects



65322-56

Figure 55. Fountain Between Four Nozzles Produce Positive Interference Effects

Since the test data were inadequate to define the vertical component of momentum (ΔL_f) for the fountain between three nozzles, the interference effects could not be determined for this geometric arrangement.

The interference data presented in Figure 54 have one prominent feature: under certain conditions the interference effect is positive. The region where this was found to be true is shown in Figure 57. Note that the data apply to two nozzles only. As can be seen, this positive effect is only present at blocking surface positions close to the ground (for $h/D \leq 3.6$) and is most prominent for widely spaced jets. For jet nozzles only 5 diameters apart ($d_f/D = 2.5$), this positive effect disappears already at $h/D = 2.5$.

The exact nature of the flow field that produces this positive effect is unknown at the present time. Let us only point out that when two nozzles are widely spaced and the blocking surface is close to the ground, the total system assumes some of the characteristics of a ground effect vehicle or a flat bottom plate with a peripheral narrow slot jet.

The interference effects for the four nozzles are indicated in Figure 55, and are positive for all conditions. In other words, the positive lift experienced by the blocking surface is more than can be attributed to the fountain core. Evidently a more positive or less negative pressure field exists below the blocking surface.

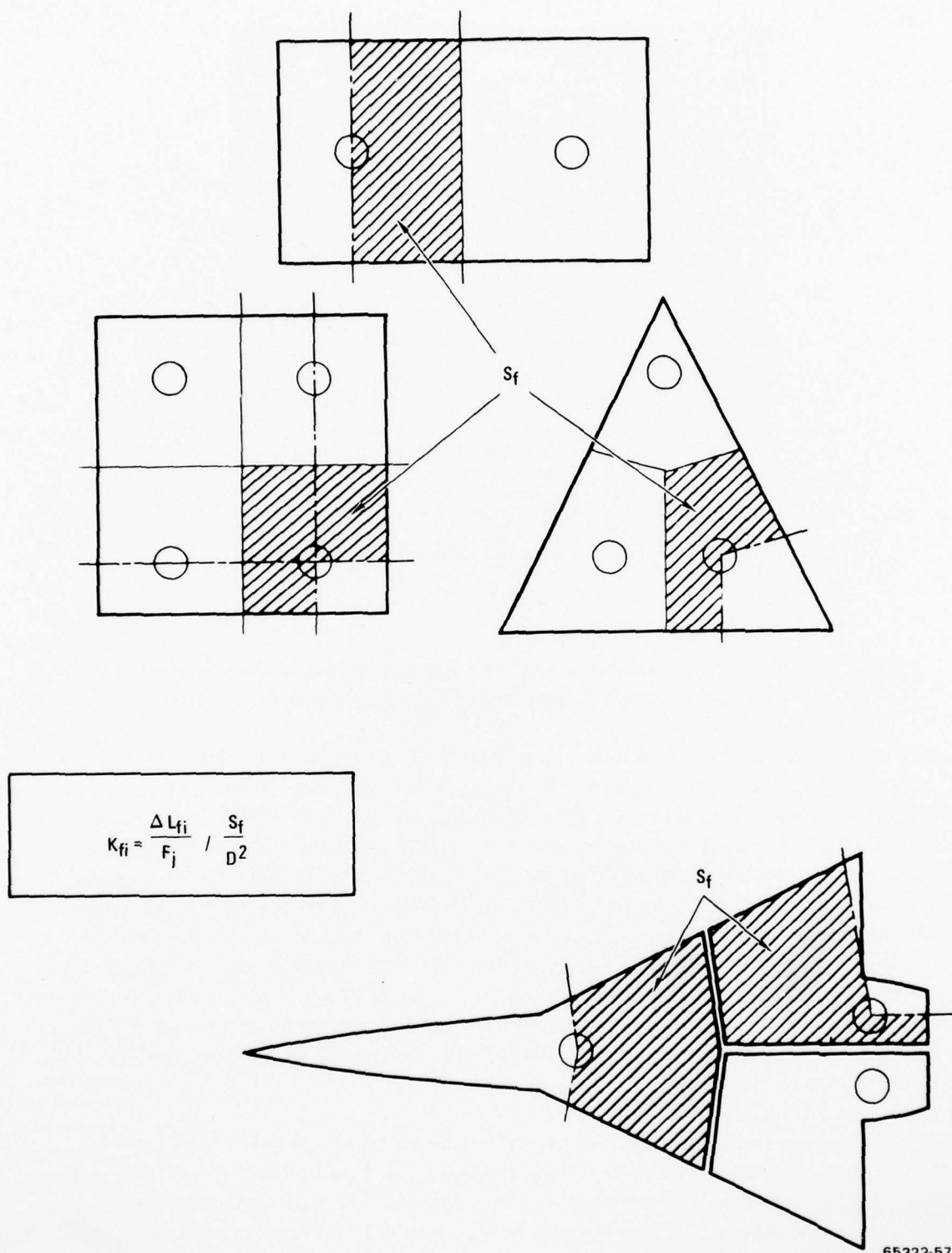


Figure 56. The Fountain Produced Interference Effects are Referenced to the Area S_f Between the Nozzle and the Fountain Theoretical Centerline

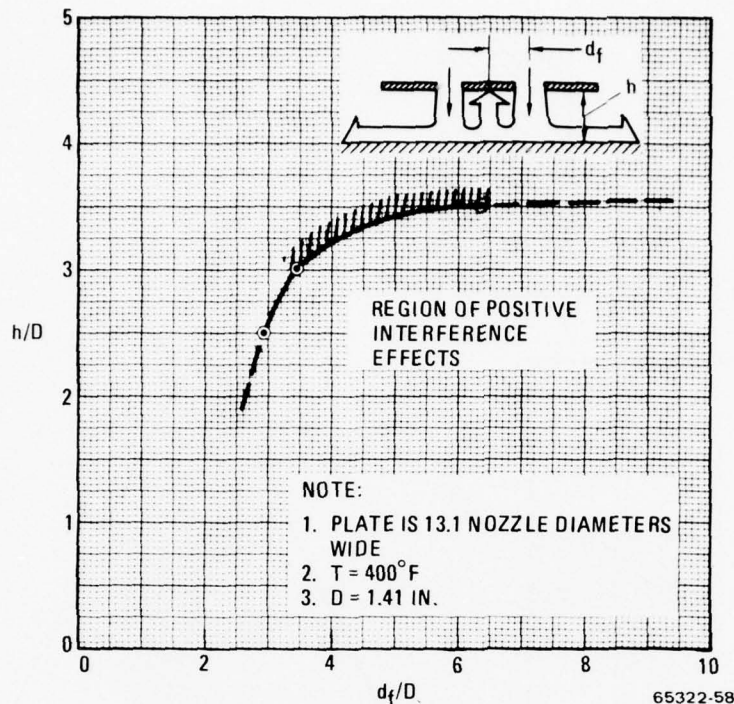
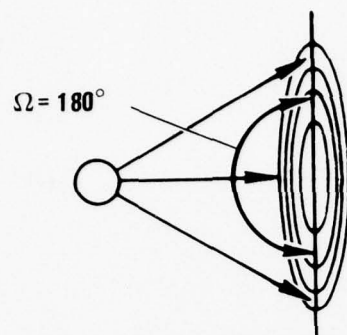


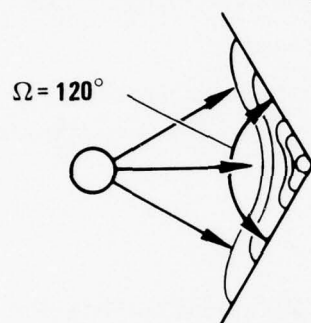
Figure 57. Positive Interference Effects Exist Only for Widely Spaced Nozzles at Close Proximity to the Ground (Two Nozzles)

One way to look at the flow field below a multi-nozzle concept is as shown in Figure 58. The diagrams depict conceptually the fountain close to the ground and do not represent any test data. For all cases the distance to the fountain (d_f/D) is the same. The fountains will produce increasingly more positive interference effects, as the angle Ω is decreased from 180 to 60 degrees. This effect is shown also on Figure 55 where interference effects for a straight fountain ($\Omega = 180$ deg) for identical nozzles to fountain spacing are presented (d_f/D). Note that the characteristics of the data are the same. However, the data for the fountain with a 90-deg bend is displaced significantly in the positive direction. This displacement, or ΔK_{fi} is presented in Figure 59. It is regrettable that the test data was insufficient to produce a similar curve for the three nozzle case. Should it be tested again, the data are expected to be about one-half of the values shown in Figure 59.

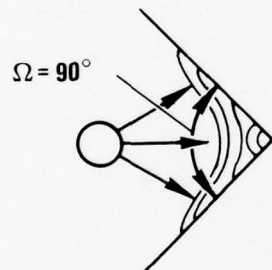
Again, we are faced with the question regarding these highly positive interference effects. These questions will remain unanswered until the complete flow fields surrounding the fountains are documented and understood. We will only point out again, that the larger the number of nozzles that are arranged in a circular pattern (Figure 60) the more we approach the flow field of a hovering ground effect vehicle. The test results with the four nozzles substantiate this trend.



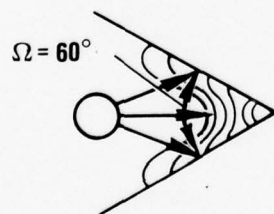
**STRAIGHT FOUNTAIN
BETWEEN 2 NOZZLES**



**CURVED FOUNTAIN
BETWEEN 3 NOZZLES**



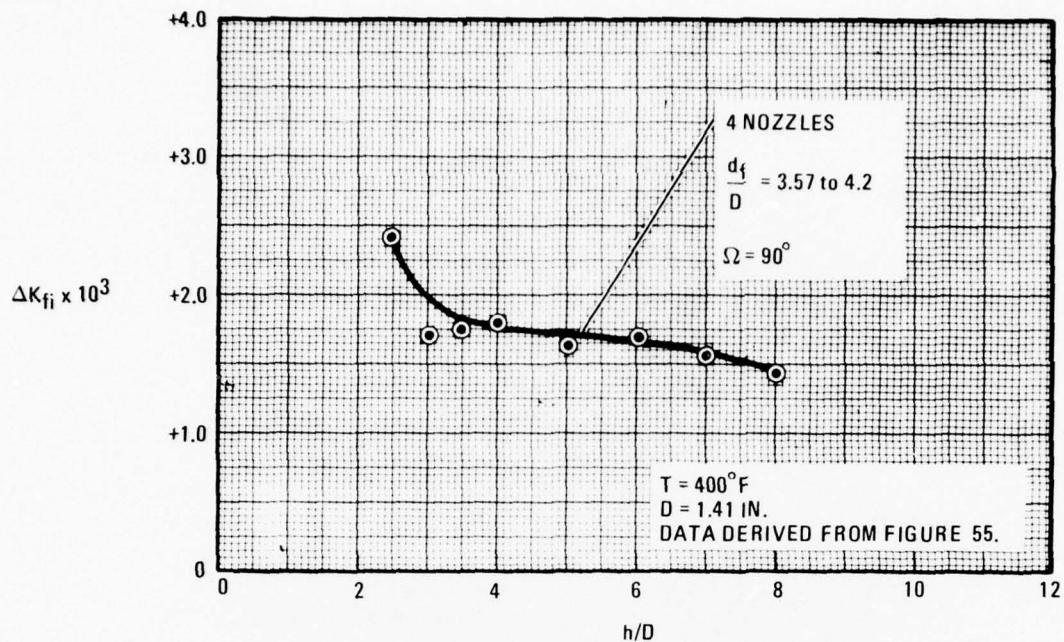
**CURVED FOUNTAIN
BETWEEN 4 NOZZLES**



**CURVED FOUNTAIN
BETWEEN 6 NOZZLES**

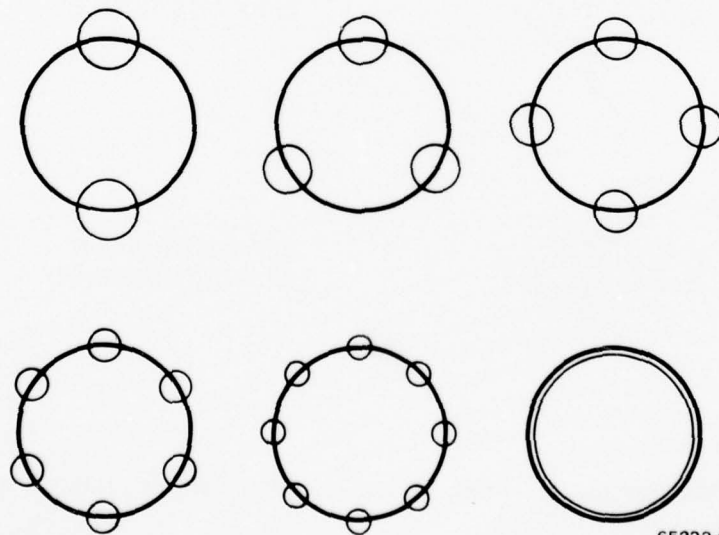
65322-59

Figure 58. Positive Interference Effects of the Fountain Increase With Decrease in Ω



65322-60

Figure 59. The Interference Effects for Fountains Between Four Nozzles are Significantly More Positive than for Comparably Spaced Two Nozzles



65322-61

Figure 60. The Arrangement of a Large Number of Nozzles in a Circular or Elliptical Pattern will Produce Positive Pressure Fields

3.7 SUGGESTED METHODOLOGY FOR PREDICTING FOUNTAIN EFFECTS

This document follows the basic approach outlined in Reference 4. First, the object of analysis (airplane) is divided into segments as shown in Figure 61. Note that each "cut" is made along the estimated fountain centerline. When the nozzles are of equal diameter and operate under identical pressure ratio and temperature conditions, then the divisions are made along lines equidistant from the nozzles (Step 1, Figure 62). Next, the induced effect of each radial ground jet on the corresponding segment is estimated (Step 2, Figure 62). This estimate assumes that no fountains exist, and can be made according to the number of empirical and analytical procedures currently available. The accomplishment of this calculation is not the subject of this document and consequently is not treated further. Next the output of Step 2 is corrected for fountain effects.

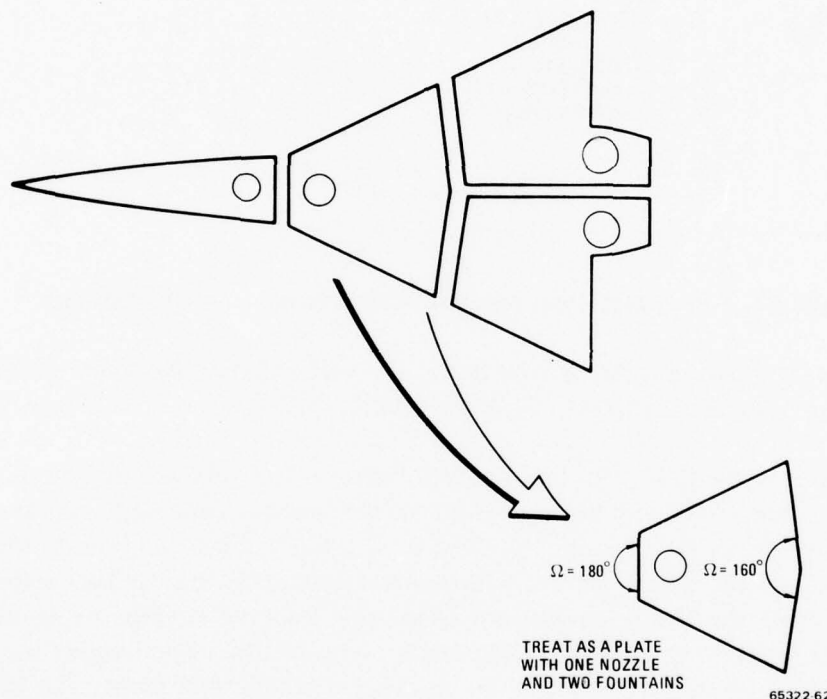
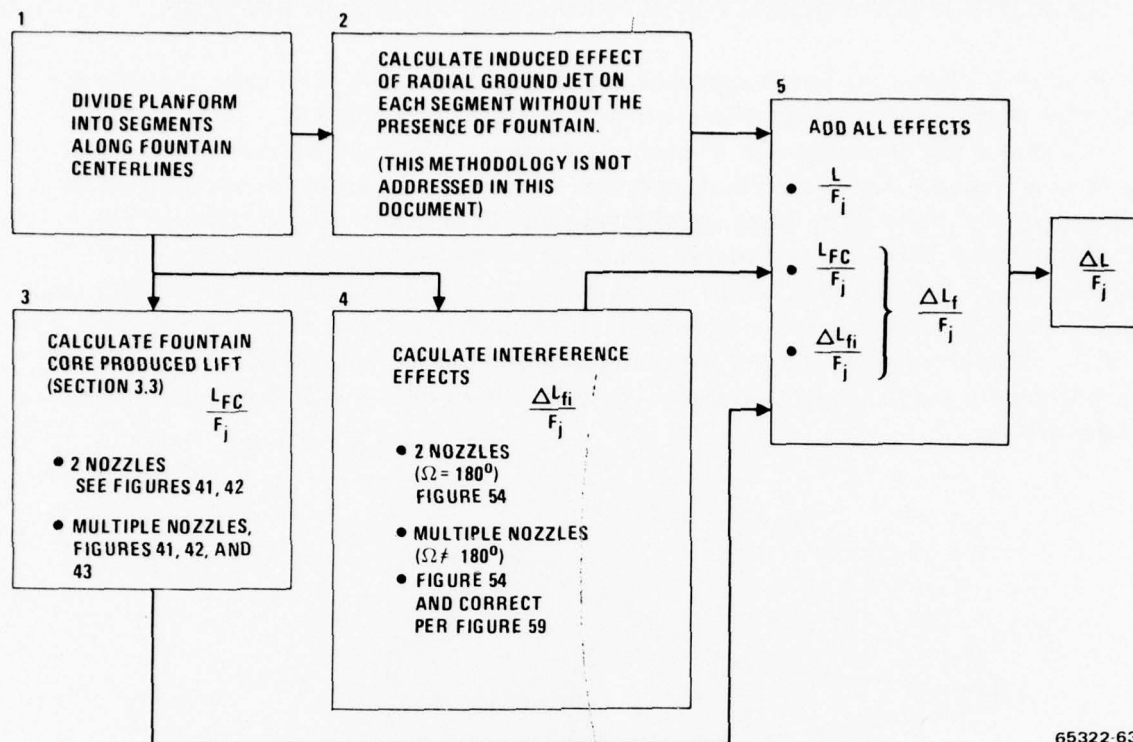


Figure 61. After the Planform is Divided into Segments Along Fountain Centerlines, each Segment is treated as a Separate Problem and the Lift Losses from Ground Jet and Fountain Effects are Estimated

The empirical approach for estimating these fountain effects, outlined in Reference 4, proposes that these effects consist of two principal components: the lift gains attributed to the raising column of gas, also referred to as the fountain core, and the interference effects generated by its subsequent interaction and response to the radial



65322-63

Figure 62. Proposed Sequence for Calculating Induced Effects

ground jet and its related entrainment action. We will address first the estimation of the fountain core generated lift (Step 3, Figure 62).

As was pointed out in Section 3.3, the fountain between two jets is very weak, dissipates early and seldom reaches the underside of the blocking surface. Unless the nozzles have an intermediate spacing ($d_f/D = 3.32$), the vehicle is close to the ground ($h/D \leq 2.5$ or 3), or the bottom of the fuselage extends significantly below the exit plane of the nozzles, the fountains will not reach the blocking surface or fuselage. In other words, the fountain core will not generate positive lift. Even under the most favorable conditions when the fountain does reach the blocking surface, the lift contribution will equal 1% of the engine thrust or a fraction thereof (see Figure 41).

The opposite is true for propulsion system arrangements incorporating three or more nozzles in a nonlinear arrangement (triangle, rectangle, pentagon, octagon, etc.). In all these cases, the fountain core is expected to reach the blocking surface and contribute to the lift at hover, as indicated on bottom of Figures 41, 42, and in Figure 43.

The data presented for four nozzles in Figure 41 are only applicable to a nozzle to fountain spacing (d_f/D) equal to 3.57 and 4.2 nozzle diameters. Should the spacing be different, then the data should be corrected. Figure 43 gives a clue to the magnitude

and direction of this correction, although the data is applicable to a three nozzle arrangement. Note that for the wider spacing ($D = 1.32$ versus $D = 1.61$) the fountain core lift decreases from 0.5% to 0.4% at h/D of 3.5, and from 0.7% to 0.6% at h/D of 5.0. (Increase in nozzle spacing is $1.61/1.32$ or 22%.)

Although the four nozzle arrangement produces a powerful fountain core relative to the two nozzle configuration, it should be noted that the lift gains recorded during the test ranged from 2% of engine thrust at h/D of 3.5, to 2.9% of engine thrust at h/D of 8.0. Both numbers are small when compared to the large lift losses produced by the ground jets (often exceeding 10 or 20% of engine thrust at low heights).

For cases involving fountains that impact extremely narrow fuselages or blocking surfaces, corrections can be derived from Figures 35, 36, and 37 for two nozzles, from Figure 40 for configurations involving three nozzles, and from Figure 39 for vehicles with four nozzles. In addition, indications for corrections for wind and ground plane inclination can be derived from Figure 38. Note that these specific data are applicable to two nozzle configurations only.

The last item to be derived is the interference effect (Item 4, Figure 62). Before this can be accomplished, the reference area for these interference effects must be calculated (see Figure 56). The interference coefficient (K_{fi}) for two nozzle configurations or for straight fountains ($\Omega = 180$ deg, see Figure 58) can be derived directly from Figure 54. Note that for most cases, the interference effect is negative. The lift loss is the product of K_{fi} and the nondimensionalized fountain reference area (S_f/D^2).

A similar procedure exists for a four nozzle case. For the nozzle to fountain spacings of 3.57 and 4.2 nozzle diameters, data from Figure 55 can be used directly. For other nozzle spacings, it is recommended that data from Figure 54 be used and corrected by the addition of the correction term (ΔK_{fi}) from Figure 59. Needless to say, this procedure becomes rapidly inaccurate when nozzle to fountain spacings differ significantly from 3.5 to 4.2 diameters.

A procedure is not presented for a three nozzle case. However, unless other data is available, the method described above can be used to calculate approximate interference lift gains. When using Figure 59, approximately one-half or less of the value should be used.

Anyone proceeding with the calculations suggested in the preceding paragraphs will undoubtedly be impressed with the relatively large magnitude of the fountain interference effects and the small contribution of the fountain core. For the two nozzle case ($\Omega = 180$ deg) the interference effects constitute all or a major share of the fountain contribution. Even in the case of a four nozzle arrangement, where a strong fountain core exists, the interference effects equal or exceed the core contribution. For the

case tested, these two effects are shown in Figure 63. Note that at h/D of 8.0, the core produced lift equals the interference effect (both are positive). For a h/D of 4.0, the core produces lift equal to 2% of thrust, while interference effects contribute 4.4%. At h/D of 2.5, the numbers are 2.15% and 15.85% respectively. We will conclude with the observation, that when it comes to fountain generated lift, it is not necessarily the fountain that matters, but the formerly called "second order" or interference effects.

3.8 RECOMMENDATIONS FOR ADDITIONAL RESEARCH

This program represents a major milestone in the research into the understanding of the basic nature of fountains and their role and contributions to the induced effects of a hovering jet powered VTOL vehicle. Like any proper research program, it suggests additional areas for investigation and exploration. A number of these areas are listed below.

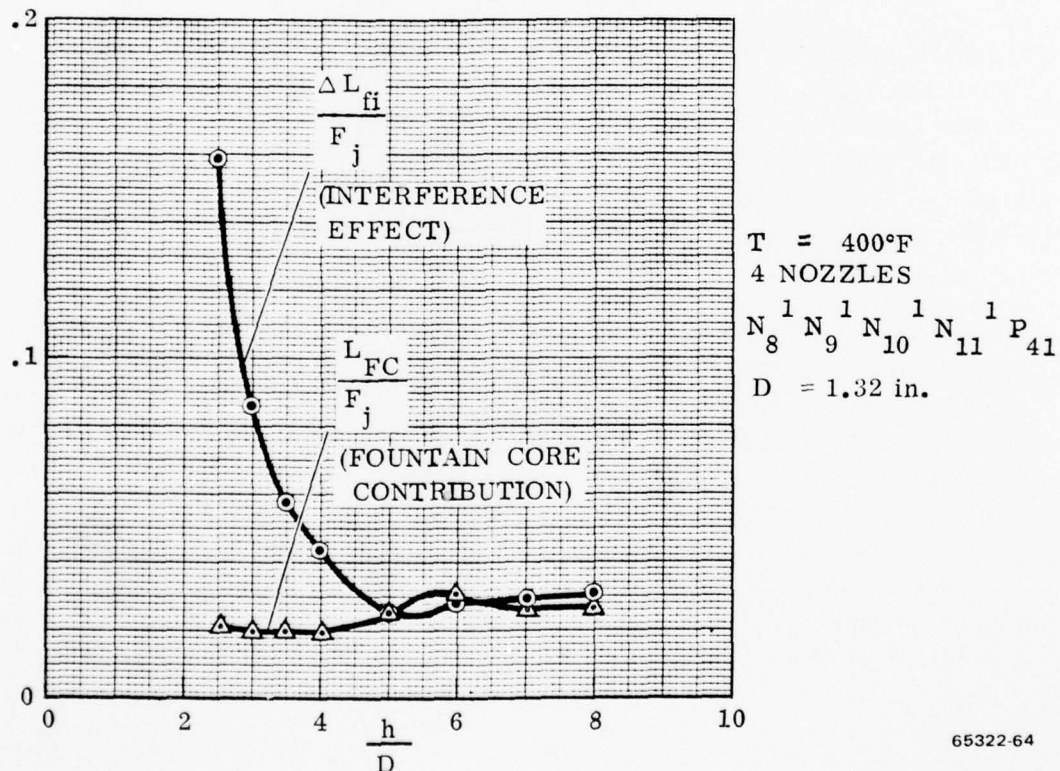


Figure 63. Even for Configurations Involving Powerful Fountains, The Induced Effects are Equal to or More Significant than the Fountain Core Contributions

1. Two fountain concept.

The exact combinations of nozzle spacings and heights (h/D) where the fountain does impact the blocking surface need to be defined. Currently we know that at the approximate nozzle spacing of 3.2 or less and at h/D of 2.5 or less, the fountain does reach the blocking surface. However, the nozzle spacings tested $d_f/D = 1.06, 3.32, 6.38$ were too far removed to permit pinpointing this critical region. It is suggested that the tests be repeated with nozzle to fountain spacings of 2, 2.5, 3.0 and 4.0 nozzle diameters and at $h/D = 2.0$ to 4.0 to define this area.

2. Three nozzles.

The interference effects for the three nozzle case could not be estimated because the fountain core was inadequately defined during the tests. To overcome this problem, the test equipment (rake) should be modified and tests repeated. The data should be obtained with at least two nozzle diameters. Additional tests should be accomplished with other unsymmetric nozzle spacings in order to determine this geometric effect on fountain core inclination (Figure 26).

3. Four nozzles.

The major deficiency is the fact that only one configuration was tested. That represented a rectangular and not a square nozzle arrangement with nozzle to fountain distances equal to 3.57 and 4.2 nozzle diameters (Figure 7). The dependence of the interference effects on this spacing parameter were consequently not determined (Figures 55 and 59). Tests should be repeated as a minimum with a square nozzle arrangement and with at least two nozzle sizes (or d_f/D ratios).

4. Temperature effects.

Tests have indicated repeatedly that a higher temperature fountain produces a more positive fountain effect (Figure 16 and Reference 4). The source of this effect needs to be determined. Specifically, it is due to a more powerful fountain core or reduced interference effects? At the present the latter seems to be the case, but this needs to be substantiated by a detailed examination of the fountain core. The temperature effects on fountains between three and four nozzles also need to be documented. Specifically, we need to address the large temperature effects between 70°F and 200°F, and the apparent small changes in fountain contributions when the exhaust temperature is raised from 200°F to 400°F.

5. The effect of wind and deck inclination was only touched upon during these investigations. It was found that wind produces a more positive net fountain effect when applied to two nozzles. It appears to reduce the losses

AD-A061 335

GENERAL DYNAMICS SAN DIEGO CA CONVAIR DIV
THE AERODYNAMIC AND THERMODYNAMIC CHARACTERISTICS OF FOUNTAINS --ETC(U)
AUG 78 A KAREMAA, C W SMITH, H A WEBER
CASD-NSC-78-001

N00014-76-C-0698

F/G 1/3

ONR-CR212-237-1F

NL

UNCLASSIFIED

2 OF 3
AD
A061335



attributed to fountain induced effects (Figure 18). The deck inclination produced highly irregular effects (Figure 20). Both subjects merit separate research programs in order to understand, model and to develop prediction methodology for these key effects. Either are of paramount importance to designers faced with developing VTOL airplanes that operate from pitching, rolling and wind swept decks.

SECTION 4

THERMODYNAMIC CHARACTERISTICS OF FOUNTAINS

This section is concerned with the near or fountain related flow fields that impinge on the lower surfaces of the aircraft and that can be entrained directly into the engine inlets. The velocity and direction of the fountain gasses were assessed in Section 3, based on total and static pressure readings from a rake traversed through the fountain for various nozzle/blocking surface configurations. The rake also included chromel-alumel bare wire thermocouples that recorded temperature distributions in the flow field between the ground plane and blocking plate (see Section 2). Temperature data and plots of temperature versus rake height and position in the horizontal plane are presented in Reference 1.

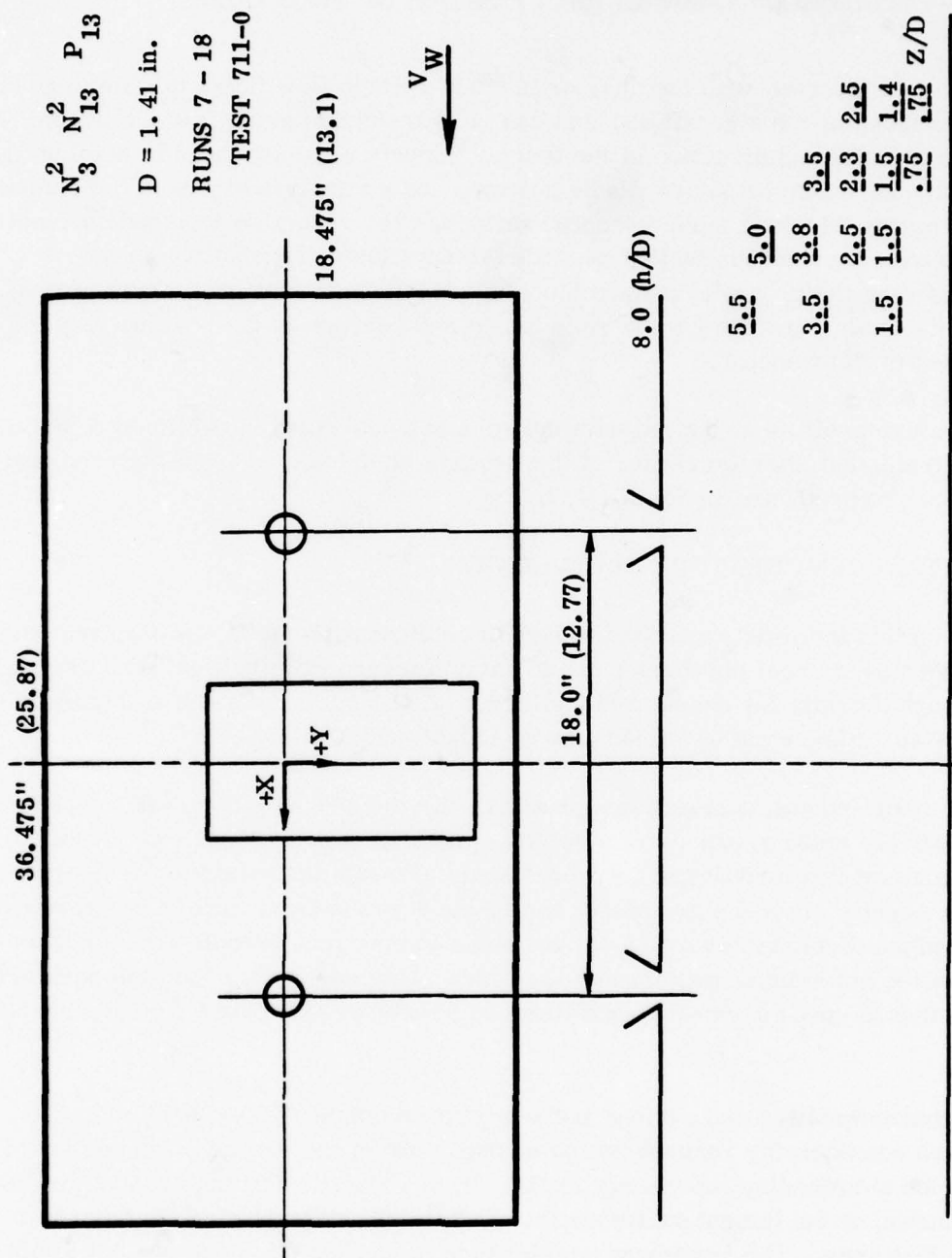
The temperature profiles measured with the rake are described in Section 4.1 and the apparent entrainment characteristics of the fountain as calculated from the recorded temperatures are presented in Section 4.2.

4.1 FOUNTAIN TEMPERATURE DISTRIBUTION

Test variables for the widely spaced two nozzle configuration ($d_f/D = 6.38$), are outlined in Figure 64. From the thermocouple data, temperature profiles were drawn, fairing through the data for constant model height at various rake heights (Figure 65), and for constant rake height at various model heights (Figure 66).

At constant model height, temperature profiles near the ground plane ($Z/D = 1.5$) develop relatively steep gradients in a vertical plane through the nozzles. In this plane, the temperature profiles are symmetrical, although the maximum temperature recorded is slightly aft of the geometric center between nozzles. There is a forward shift in the plane of symmetry at lateral positions (increasing Y) indicating a net forward flow of the hot fountain gasses into the wind. This skewness of the temperature is probably due to small geometric variations in nozzle/ground plane/blocking surface angularity.

The same characteristics are evident at the next rake height ($Z/D = 2.45$) although gradients are considerably reduced as the central core of the fountain diffuses and mixes with the surrounding low energy areas. This reduction in temperature gradient is not as marked at the lateral extremes (e.g., $Y/D > 4$) reflecting a lower fountain strength in that area. The maximum temperature in the fountain core has not diminished with fountain height (between $Z/D = 1.5$ and 2.45) but is reduced by continuing mixing at $Z/D = 3.8$. At this latter rake height that is 75% of model height, the longitudinal temperature gradients have disappeared — indicating complete mixing and diffusion of the fountain gasses. The remaining lateral temperature gradients are



65322-65

Figure 64. Flow Field Temperatures Were Surveyed for the Two Nozzle Configuration ($d_f/D = 6.38$)

ΔT_R TEMPERATURE PROFILES

$N_3^2 N_{13}^2$ P₁₃ h/D = 5.0 d_f/D = 6.38 D = 1.41 in.

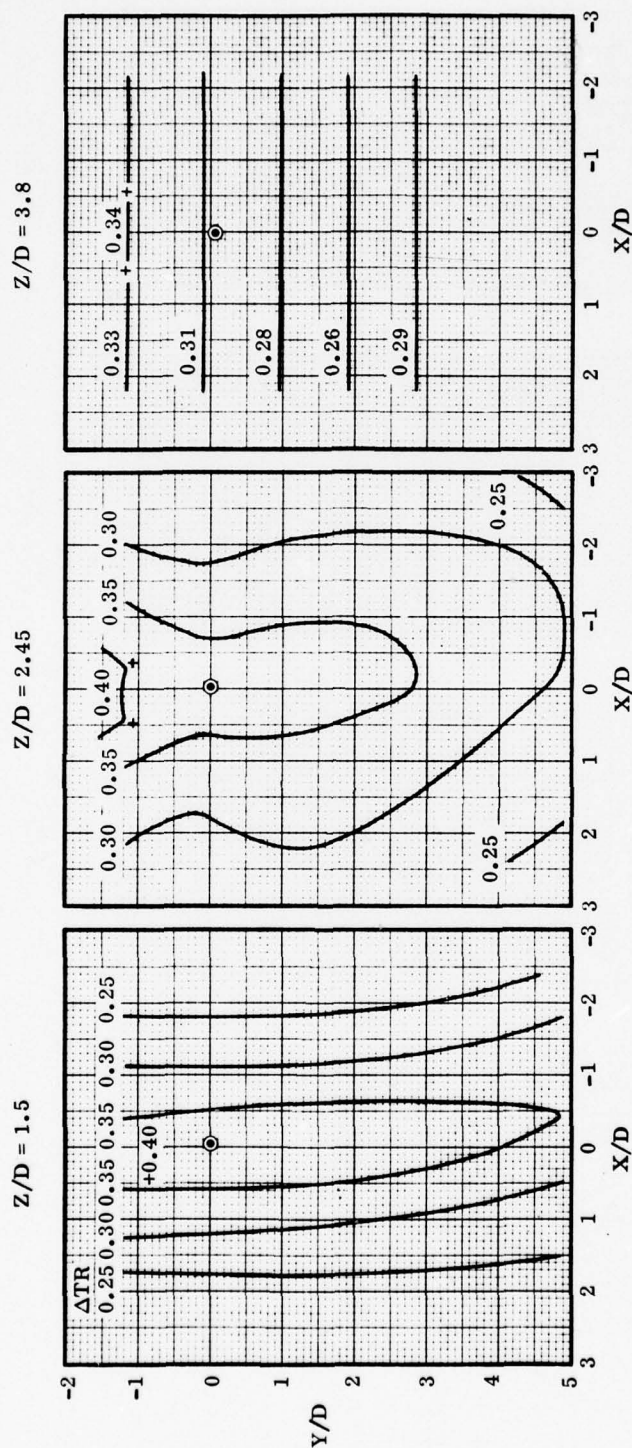
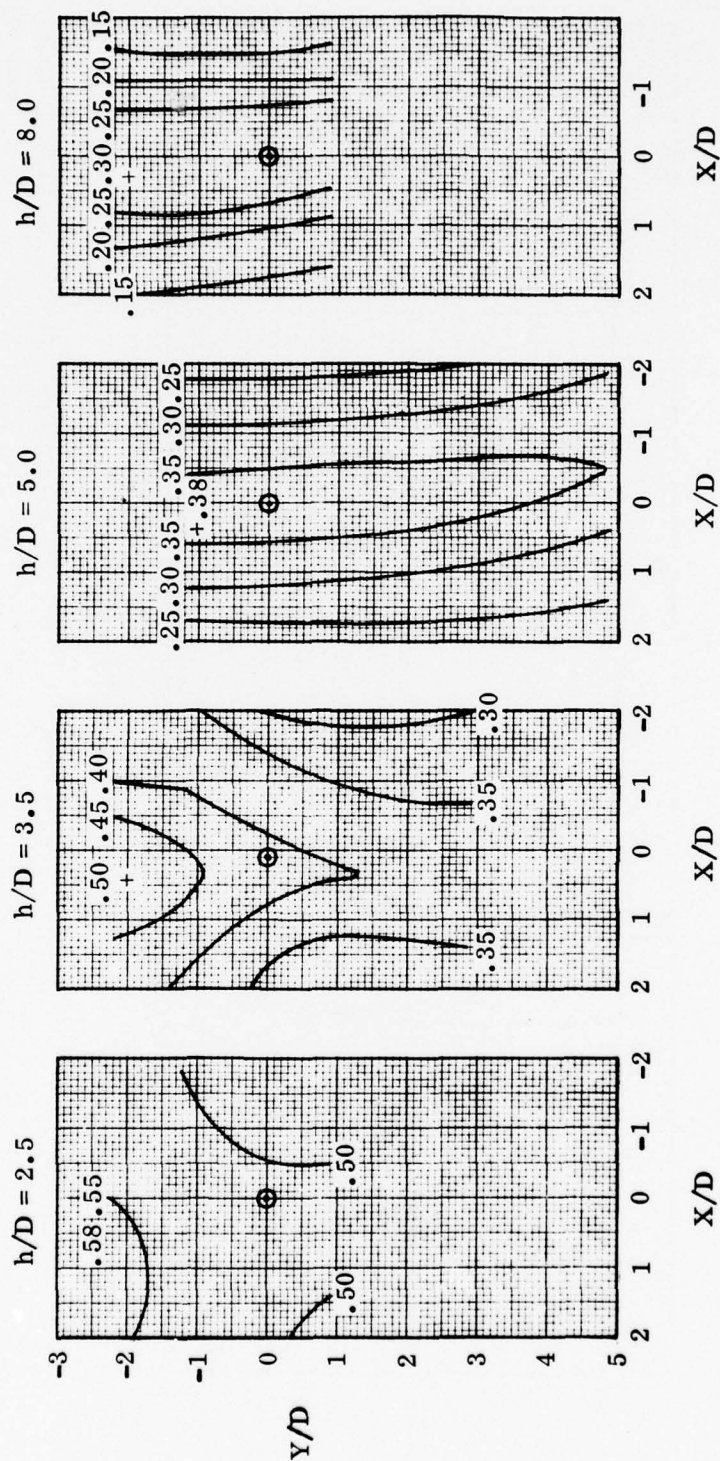


Figure 65. Flow Field Temperature Profiles for the Two Nozzles Configuration (d_f/D = 6.38) at h/D = 5.0

ΔT_R TEMPERATURE PROFILES

$N_3^2 N_{13}^2 P_{13}$ $Z/D = 1.5$ $D = 1.41$ in.



+ REPRESENTS MAX. VALUE RECORDED

65322-67

Figure 66. Flow Field Temperature Profiles for the Two Nozzles Configuration ($d_f/D = 6.38$) at $Z/D = 1.5$

relatively mild and are still reflecting a lateral bias in temperatures (maximum temperature occurs off geometric center).

The effect of model height on flow field temperatures at constant rake height ($Z/D = 1.5$) is displayed in Figure 66. At the lowest blocking surface height ($h/D = 2.5$), low temperature gradients at high fountain core temperatures reflect a relatively low rate of mixing between fountain gas and ambient air. As blocking surface height is increased, fountain core temperatures diminish due to increased ground jet entrainment. However, longitudinal temperature gradients increase as fountain maximum dynamic pressure increases for $d_f/D = 6.38$ (Figure 31). The previously noted asymmetry of the central core is evident at all model heights.

Test conditions for the three nozzle configuration ($D = 1.61$) are outlined in Figure 67. Corresponding temperature profiles at h/D of 5.0 are presented in Figure 68. Whereas the maximum fountain core temperature was aft of and in the negative Y direction of geometric center in the two nozzle case (Figure 66), the maximum is now noted in the opposite direction. This results from the higher ground jet strength of the aft closely spaced two nozzles as discussed in Section 3. Fountain angularity induces higher temperature gradients, i.e., higher entrainment on the side opposite to direction of fountain shift ($Z/D = 1.6$). Rapid dynamic pressure decay (Figure 32) is reflected in the thermal diffusion that occurs between the two rake heights shown in Figure 68.

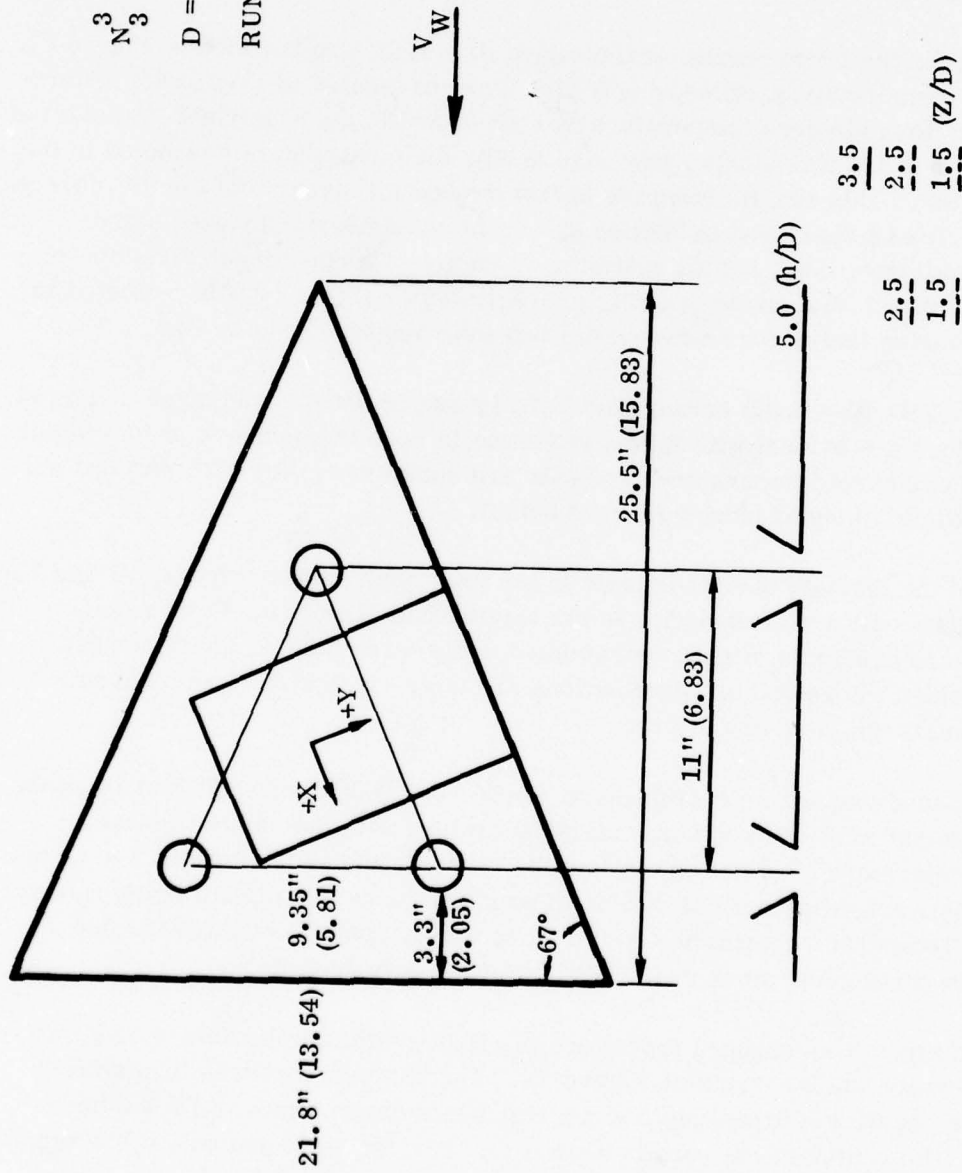
For the three nozzle ($D = 1.32$) arrangement of Figures 69 and 70, the same asymmetrical distributions are evident with minor reduction in core temperature at increasing rake height. Peripheral temperature gradients are somewhat lower with reduced nozzle diameter, diminishing at increased rake height.

Lateral shift of the fountain core is evident in the four nozzle case (Figures 71 and 72) at all rake heights with small deviation in the longitudinal direction. Once more, steep temperature gradients (higher entrainment rates) are noted on the side away from fountain shift. Fore and aft distributions are quite symmetrical with essentially no change in maximum core temperature.

The medium spaced two nozzle configuration ($d_f/D = 3.32$) of Figures 73 and 74 shows a small longitudinal shift of maximum core temperature with the same consistent increase in temperature gradient on the trailing side. In the widely spaced two nozzle case (Figure 66), a similar core shift did not produce the asymmetrical temperature distribution. Temperature gradients in the more widely spaced case were higher indicating more mixing and more redistribution of the entrained flow.

Model angle of attack was changed from zero to +10 deg with the medium spaced two nozzle configuration ($d_f/D = 3.32$) of Figure 75. The fountain core was thus shifted forward (in the negative X direction) and the trailing isotherms move with the core flow pattern. The center of the core is beyond the rake traverse and only a low temperature gradient area remains at the outer edge of the entrained flow.

N_3^3 N_{10}^3 N_{11}^3 P_{31}
 $D = 1.61$ in.
 RUNS 33 - 36 TEST 711-0



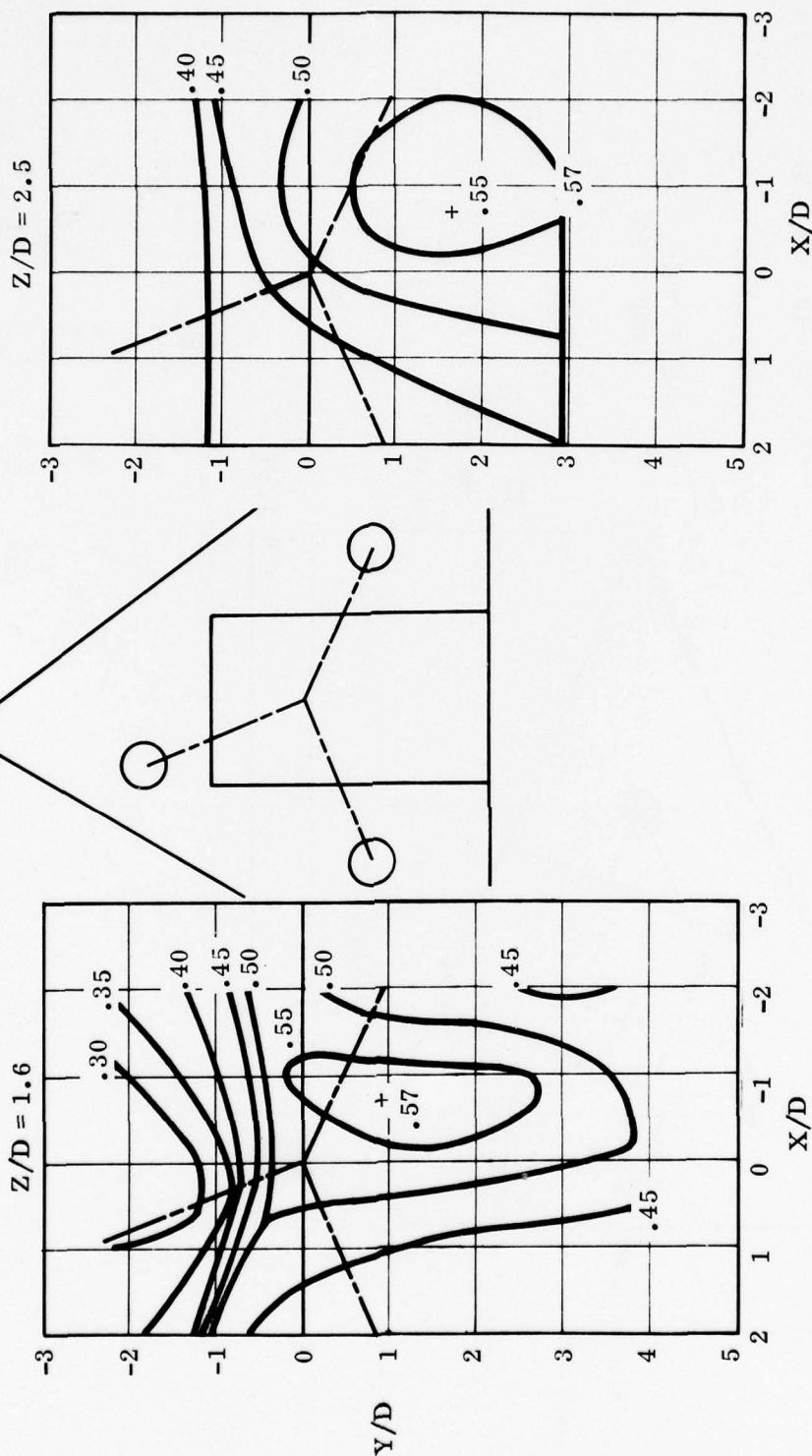
65322-68

Figure 67. Flow Field Temperatures Were Surveyed for the Three Nozzle Configuration ($D = 1.61$)

ΔT_R TEMPERATURE PROFILES

N_3^3 N_{10}^3 N_{11}^3 P_{31} $h/D = 5.0$

$D = 1.61$ in.



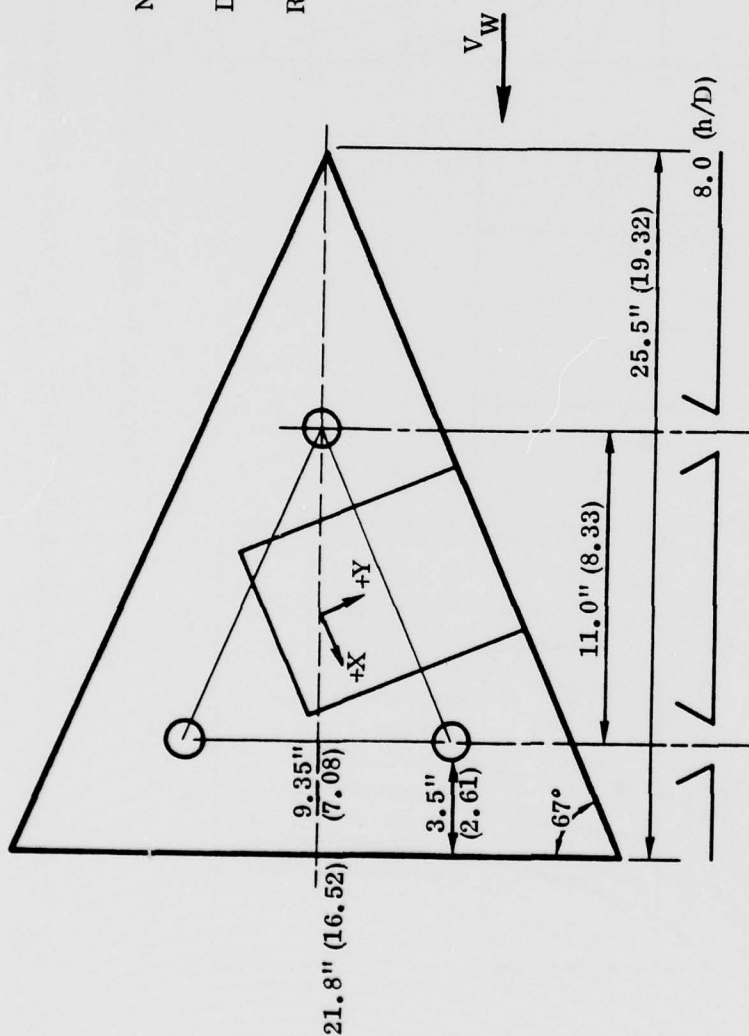
+ REPRESENTS MAX. VALUE RECORDED

65322-69

Figure 68. Flow Field Temperature Profiles for the Three Nozzle Configuration ($D = 1.61$) at $h/D = 5.0$

$$\begin{matrix} 1 & 1 & 1 \\ N^3 & N^{10} & N^{11} \\ & & P^{31} \end{matrix}$$
$$D = 1.32 \text{ in.}$$

RUNS 38-47
TEST 711-0

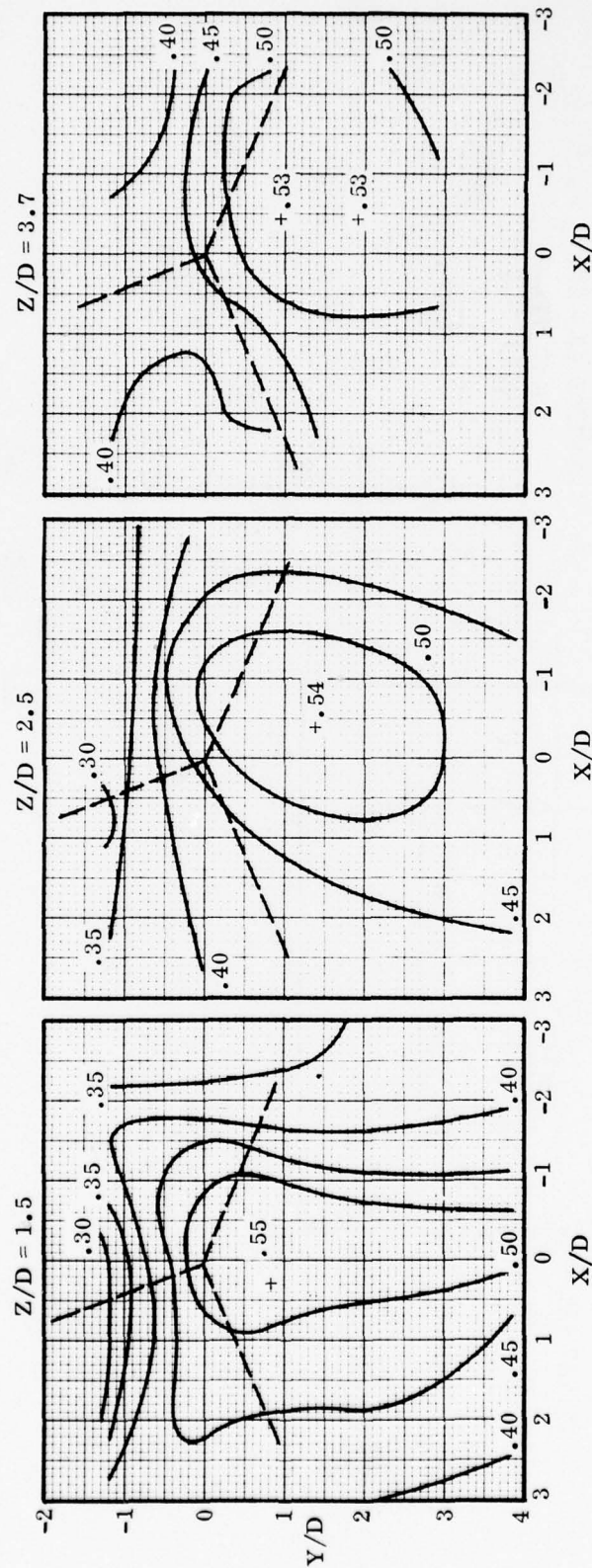

$$\begin{array}{r} 5.0 \\ \hline 3.5 \\ \hline 2.5 \\ \hline 1.5 \\ \hline 1.5 \\ \hline \end{array} \quad \begin{array}{r} 3.5 \\ \hline 2.5 \\ \hline 1.5 \\ \hline 1.5 \\ \hline \end{array} \quad \begin{array}{r} 2.5 \\ \hline 1.2 \\ \hline 0.9 \\ \hline 0.8 \\ \hline \end{array} \quad \begin{array}{r} (Z/D) \end{array}$$

65322-70

Figure 69. Flow Field Temperatures Were Surveyed for the Three Nozzle Configuration ($D = 1.32$)

ΔT_R TEMPERATURE PROFILES

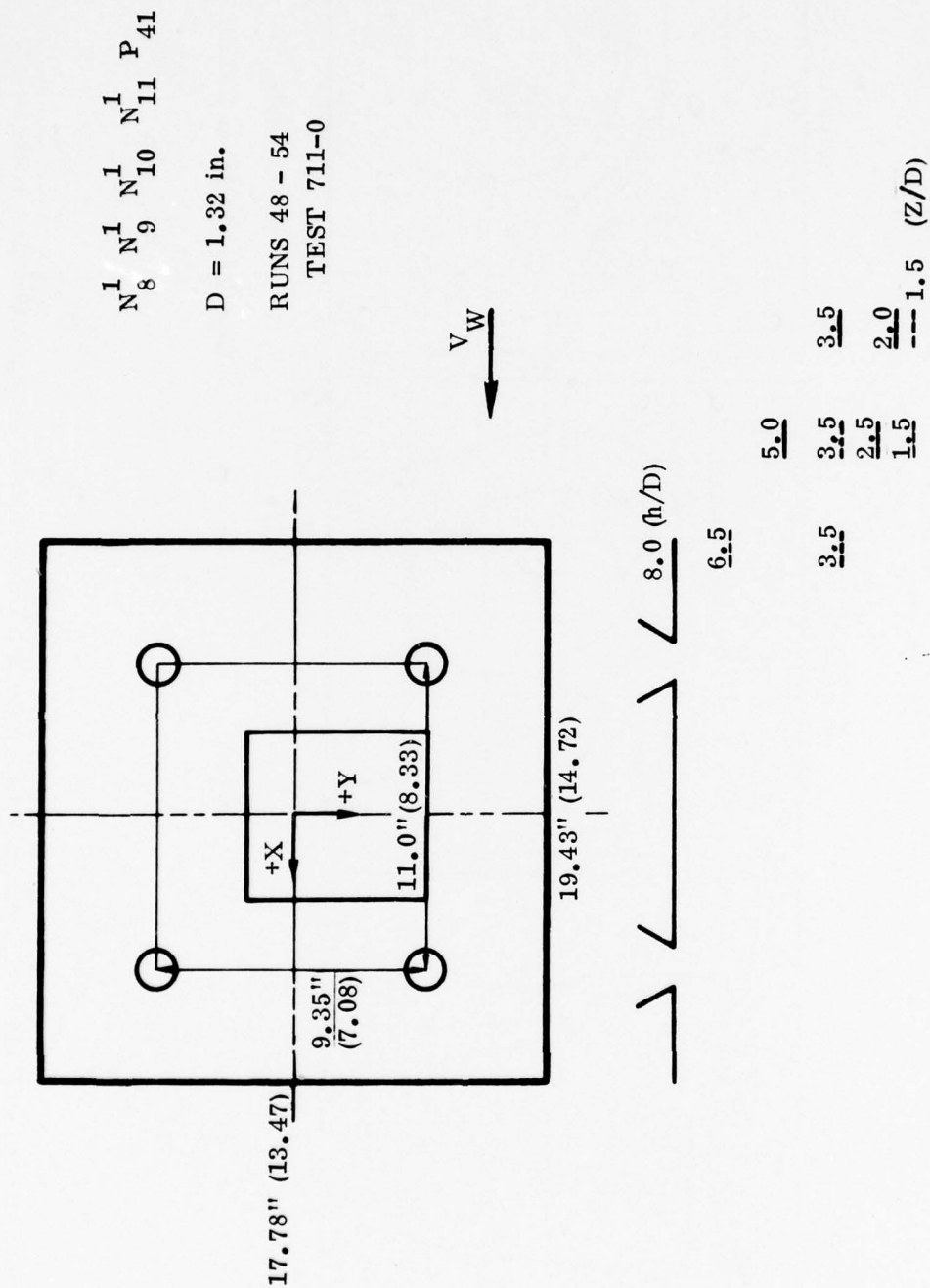
$N_3^1 N_{10}^1 N_{11}^1 P_{31}$ $h/D = 5.0$ $D = 1.32 \text{ in.}$



+ REPRESENTS MAX. VALUE RECORDED

65322-71

Figure 70. Flow Field Temperature Profiles for the Three Nozzle Configuration ($D = 1.32$) at $h/D = 5.0$



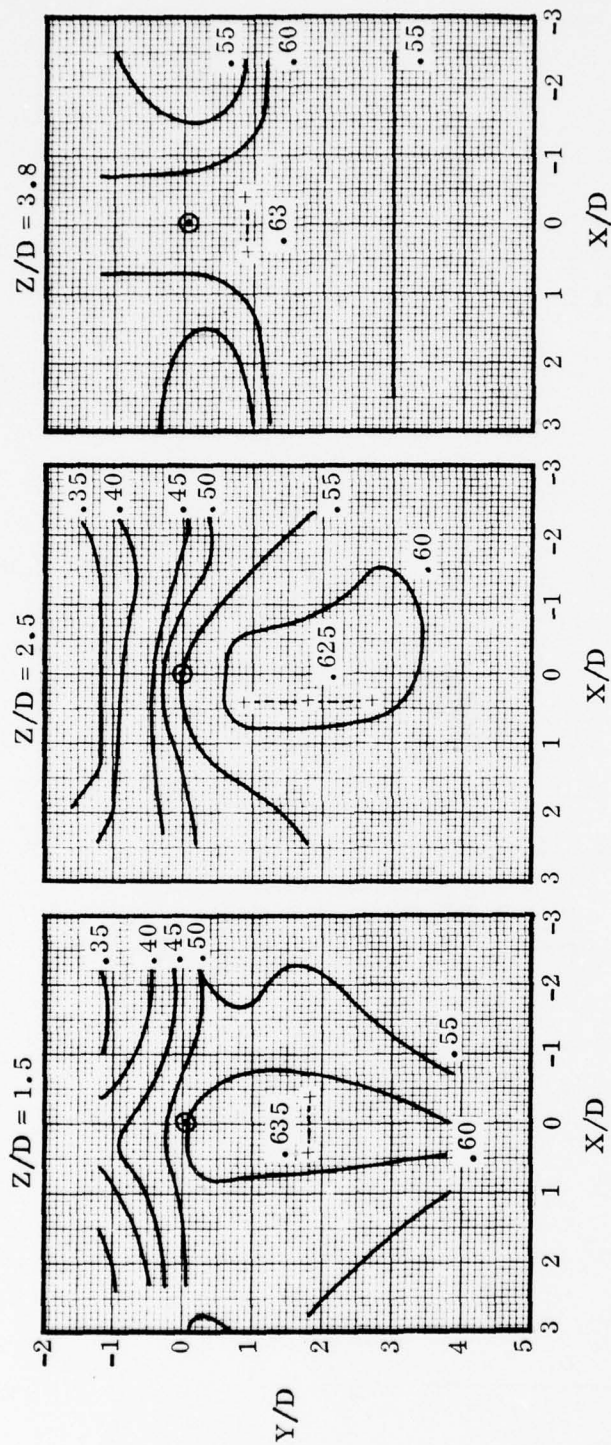
65322-72

Figure 71. Flow Field Temperatures Were Surveyed for the Four Nozzle Configuration

ΔT_R TEMPERATURE PROFILES

$N_8^1 N_9^1 N_{10}^1 N_{11}^1 P$
 $h/D = 5.0$

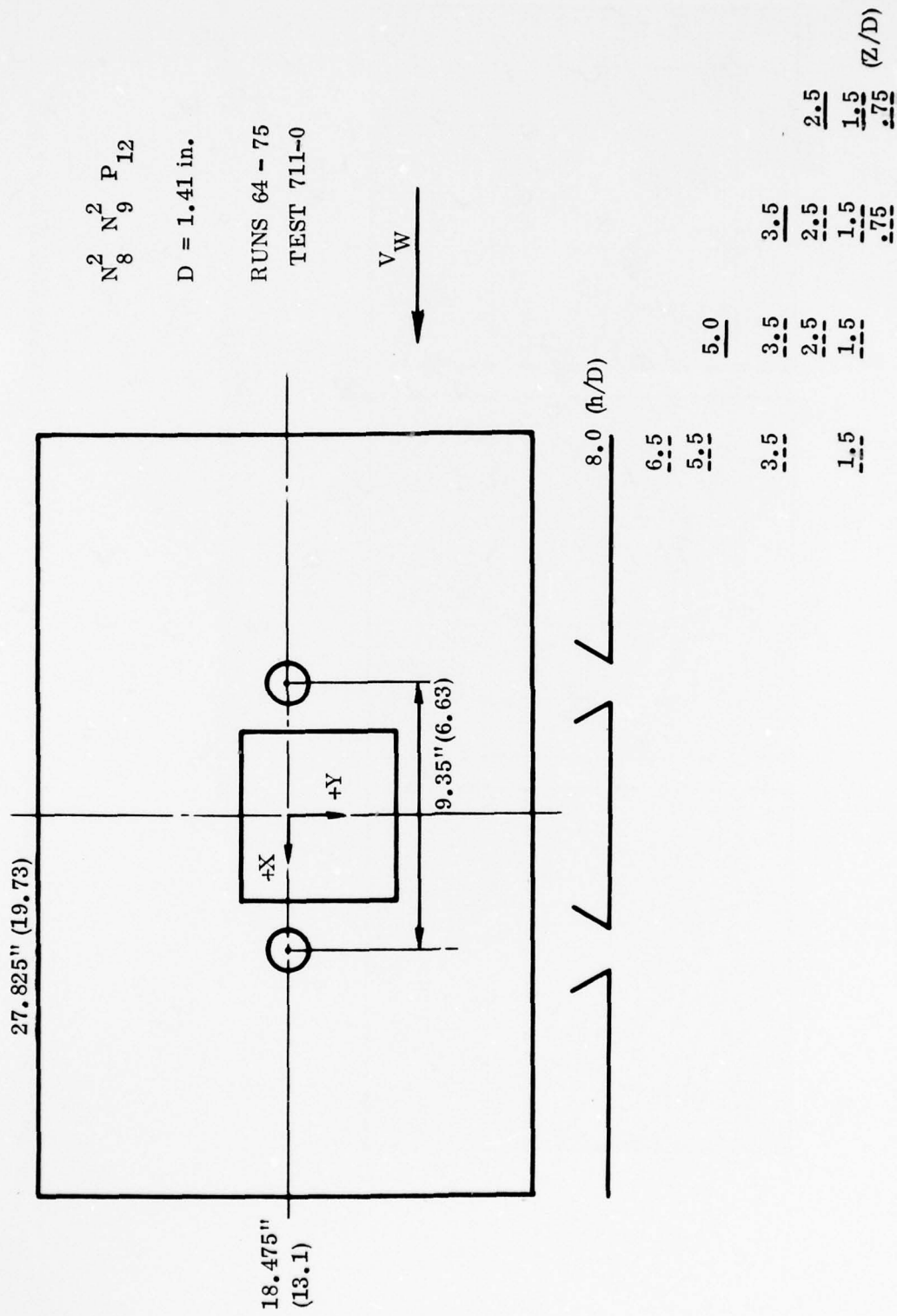
$D = 1.32 \text{ in.}$



+ REPRESENTS MAX. VALUE RECORDED

65322-73

Figure 72. Flow Field Temperature Profiles for the Four Nozzle Configuration at $h/D = 5.0$

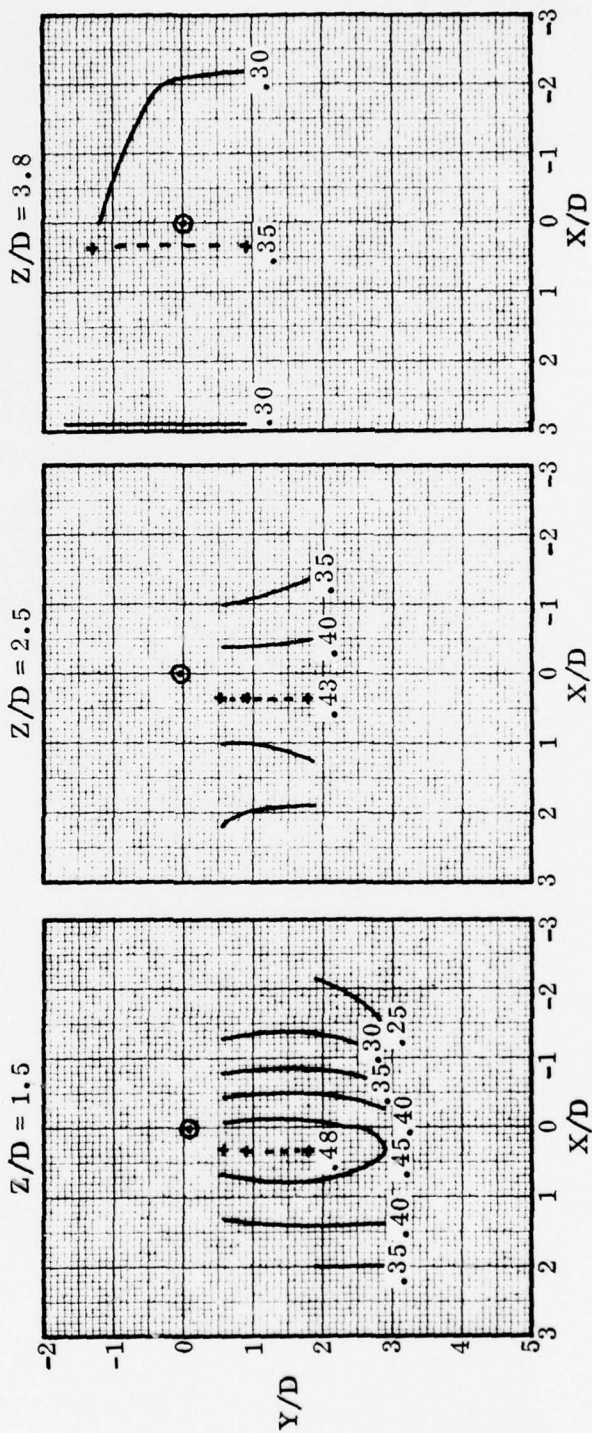


65322-74

Figure 73. Flow Field Temperatures Were Surveyed for the Two Nozzle Configuration ($d_f/D = 3.32$)

ΔT_R TEMPERATURE PROFILES

$N_8^2 N_9^2 P_{12}$ $h/D = 5.0$ $d_f/D = 3.32$ $D = 1.41$ in.



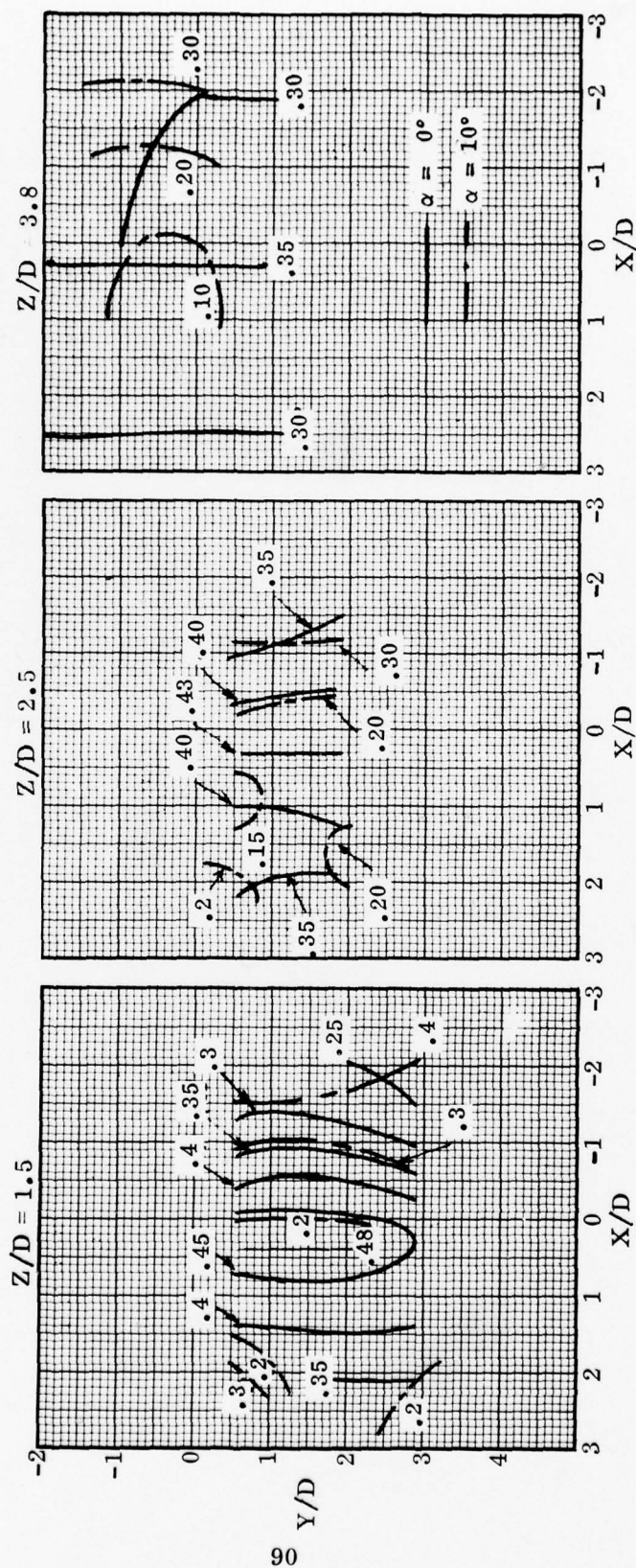
+ REPRESENTS MAX. VALUE RECORDED

65322-75

Figure 74. Flow Field Temperature Profiles for the Two Nozzle Configuration ($d_f/D = 3.32$) at $h/D = 5.0$

ΔT_R TEMPERATURE PROFILES

$N_8^2 N_9^2 P_{12}$ $h/D = 5.0$ $D = 1.41$ in. $d_f/D = 3.32$



65322-76

Figure 75. Model Pitch Shifts the Fountain Core Forward

Wind velocity was increased from 3 knots to 30 knots with the two nozzle ($d_f/D = 3.32$) configuration with insignificant effect on fountain temperature distribution (Figure 76). Maximum core temperatures were reduced, however, by approximately 10%.

Passing the rake along the edge of the blocking surface in a vertical plane produced the temperature distributions of Figure 77. At a model height of $h/D = 5.1$, all of the rake was below the blocking plane. Temperature levels are characteristic of entrained jet flow rather than ambient air. Presumably, then, the temperatures are representative of fountain flows emanating upwards and outwards from the impact regions (Figure 74). At a model height of $h/D = 2.6$, however, the rake spanned an area above the blocking plane revealing steep temperature gradients just under the plate that indicated locally high rates of ambient air entrainment. At several nozzle diameters above the plate, temperatures decay to ambient levels. Temperature distributions in both model height cases reflect the traverse surveys previously described in the horizontal plane (Figure 74) with some allowance for increased mixing with increased distance from the nozzle plane. The temperature levels above the blocking plate in this case are the only recordings that are compatible with the inlet reingestion readings presented in Section 5.

One test run was conducted with a nozzle jet temperature of 200°F instead of the 400°F used for all other testing. At each of three rake heights, three flow field temperatures were selected at corresponding points in the flow field for the 400°F and the 200°F nozzle jet temperature cases. The resulting correlation (Figure 78) indicates approximately 10% higher nondimensional temperatures in the colder jet temperature case. This nondimensional difference represents a delta of 5°F in temperature.

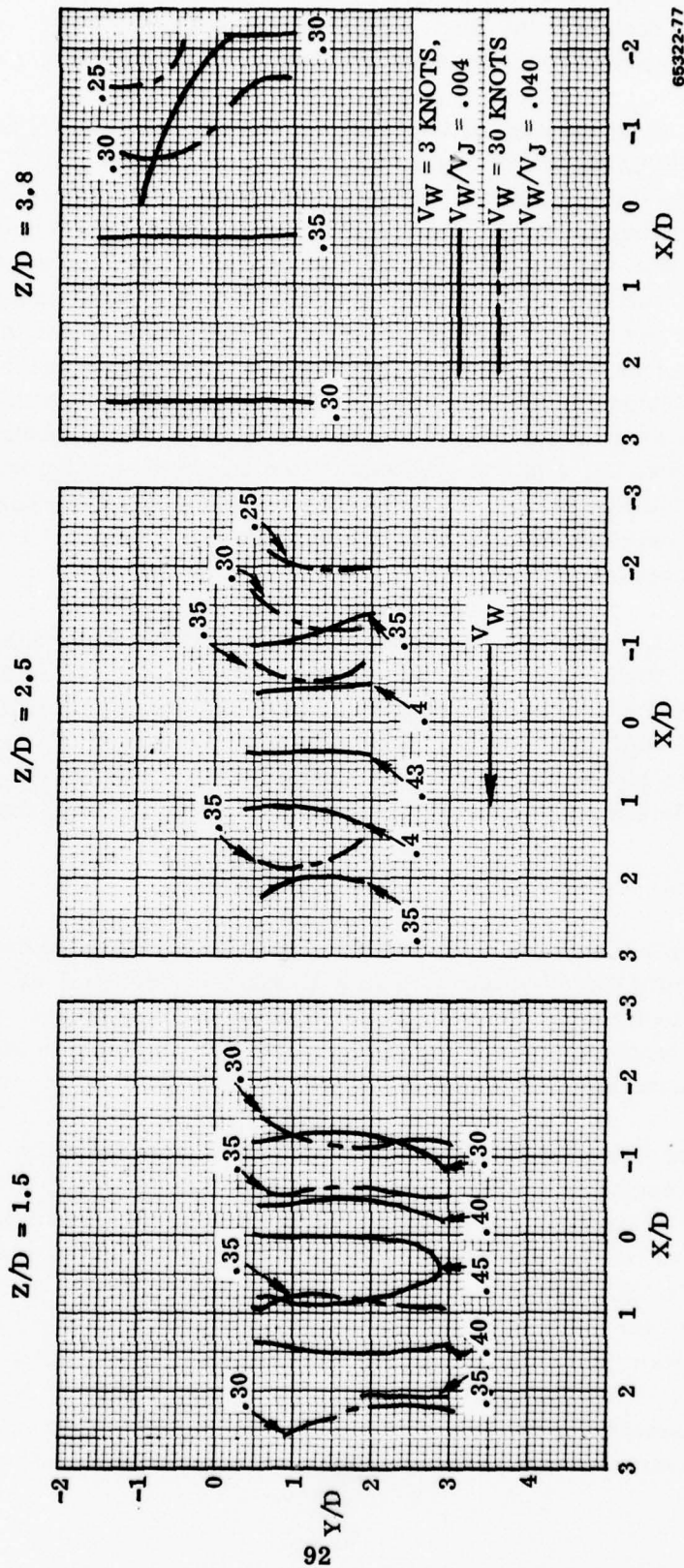
4.2 FOUNTAIN ENTRAINMENT CHARACTERISTICS

At this point, fountain mass flow distributions have been estimated (Section 3.4, and fountain temperature distributions have been described (Section 4.1). The interaction between fountain and ground jet entrainment is outlined in Sections 3.4 and 3.5. In this section, the temperature and mass flow data is consolidated in accordance with the flow field interactions visualized in these two sections.

The maximum fountain temperatures observed in the contour plots of Section 4.1 are summarized in Figures 79 (two nozzle) and 80 (three and four nozzles). The recorded values have been extrapolated to estimate temperatures at the ground plane and at the top of the fountain. At the same height (Z), fountain temperatures always diminish with increased blocking surface height (h). Two-nozzle fountain temperatures decay with height (Z) but three and four-nozzle temperatures are constant, i.e., independent of Z . The temperatures at the heel of the fountain predicted by single nozzle results with free ambient air entrainment (Reference 3) are superimposed on the above figures. The consistently higher values of temperature noted in this investigation substantiate the concept of restricted ambient air entrainment that was outlined in Sections 3.4 and 3.5.

ΔT_R TEMPERATURE PROFILES

N_8^2 N_9^2 P_{12} $h/D = 5.0$ $D = 1.41 \text{ in.}$ $d_f/D = 3.32$



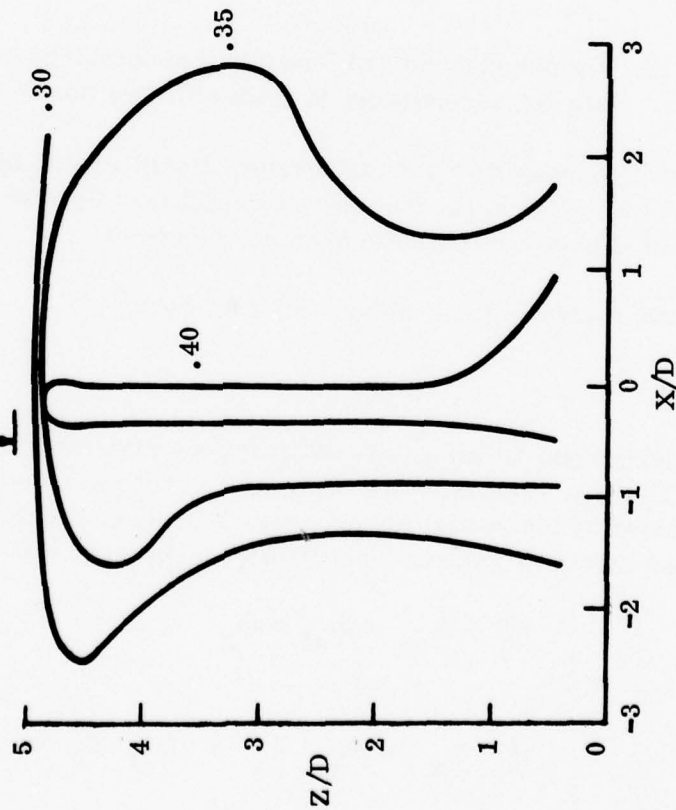
65322-77

Figure 76. Wind Reduces Fountain Temperatures, Two Nozzles

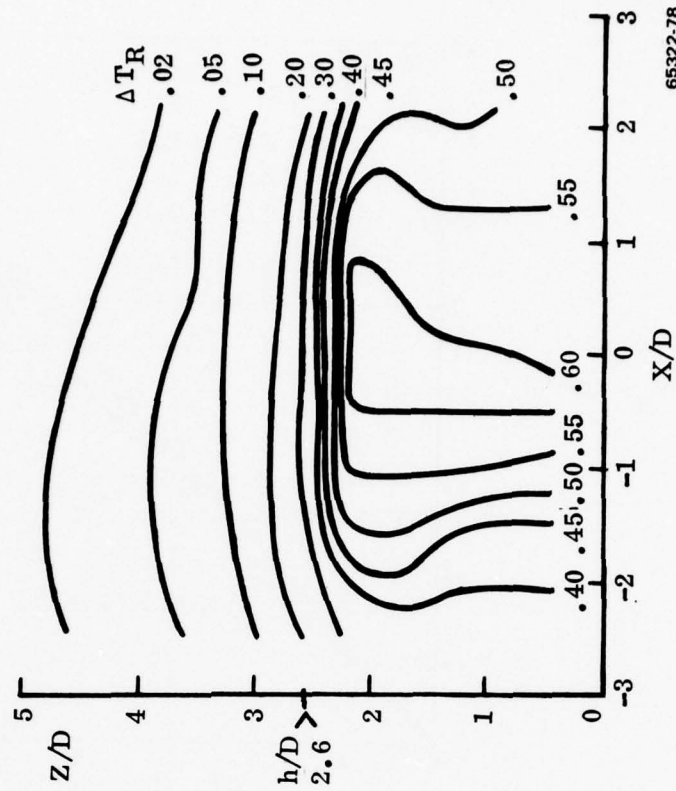
$N_8^2 \quad N_9^2 \quad P_{12}$

RAKE VERTICAL

$h/D = 5.1$



$d_f/D = 3.32$
 $D = 1.41 \text{ in.}$



65322-78

Figure 77. Flow Field Temperatures Decay Rapidly Near the Edge of the Blocking Surface

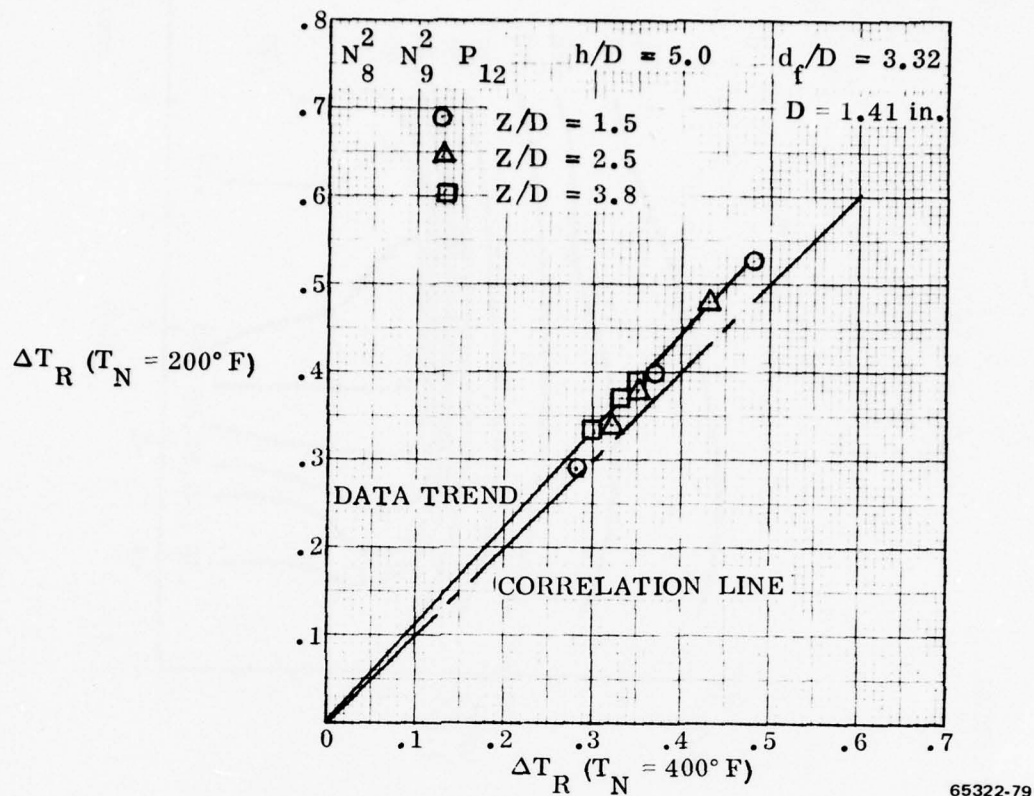


Figure 78. Nondimensionalized Fountain Temperatures Increase as Nozzle Jet Temperature is Reduced, Two Nozzles

With known fountain mass flow and temperature distributions, the Law of Conservation of Energy may be applied to the free jet-ground jet flow field and to the volume between any two horizontal planes through the fountain (Figure 81).

For an adiabatic control volume without external work:

$$\int d(\dot{m} c_p T) = 0$$

For the free jet-ground jet case, all configurations have the characteristic that $\dot{m}_2 > \dot{m}_j$ and $T_2 < T_N$. Following the concept of Section 3 that some fountain flow (\dot{m}_{af}) is entrained by the ground jet, an average fountain temperature (\bar{T}_f , calculated from the decay curves of Figures 79 and 80) is assigned to that mass flow (\dot{m}_{af}).

Thus:

$$\dot{m}_j + \dot{m}_{ea} + \dot{m}_{af} = \dot{m}_2$$

and

$$\dot{m}_j T_N + \dot{m}_{ea} T_a + \dot{m}_{af} \bar{T}_f = \dot{m}_2 T_2$$

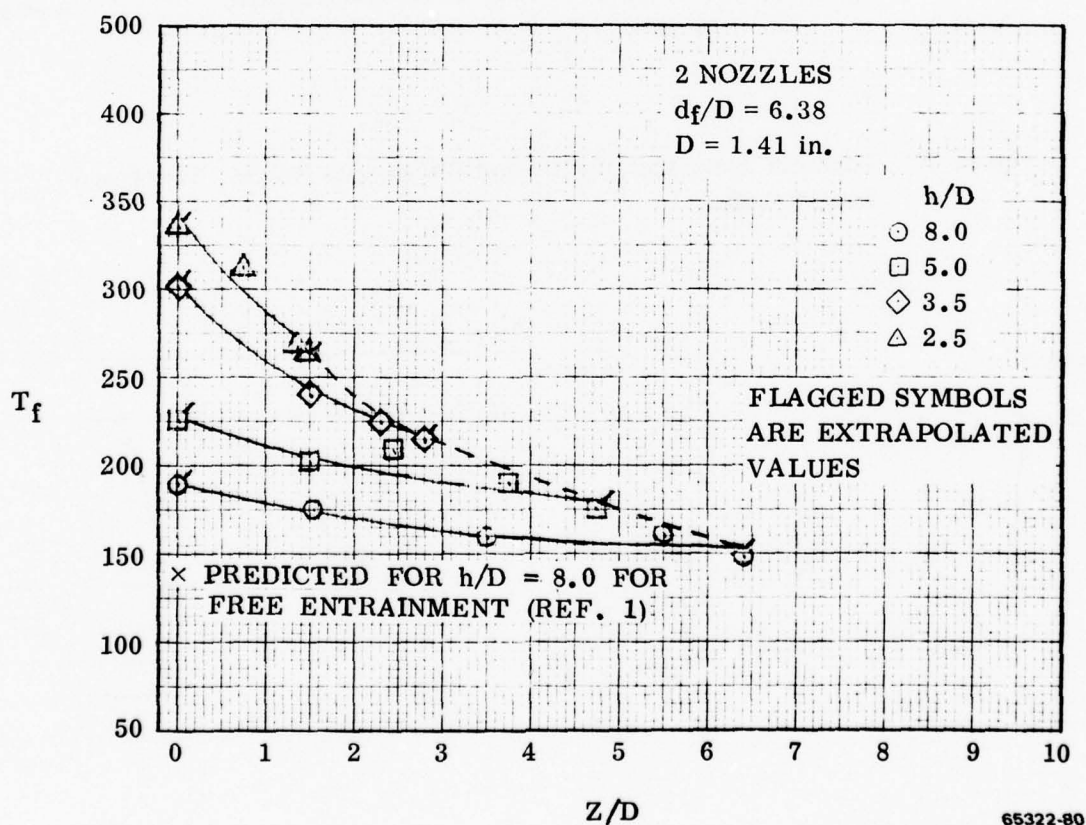
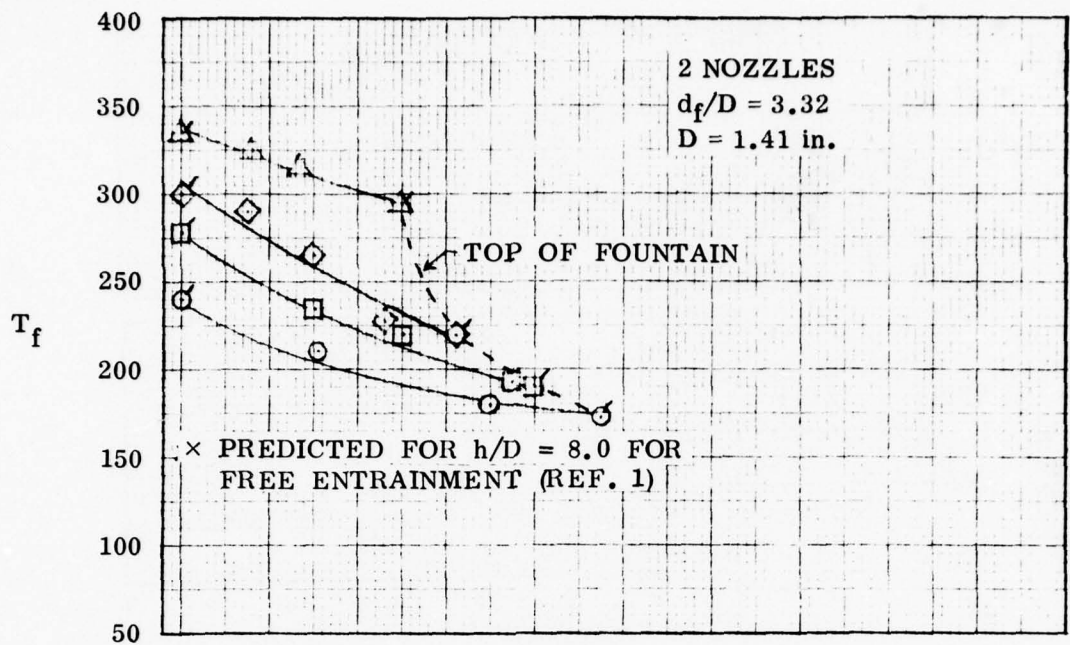
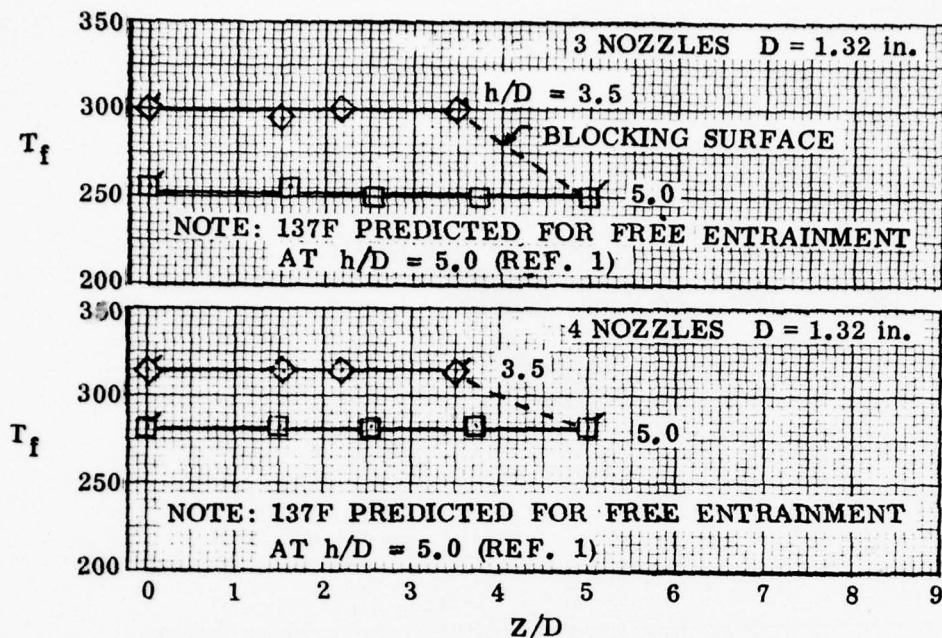


Figure 79. Fountain Temperatures Decay with Height, Two Nozzles



FLAGGED SYMBOLS ARE EXTRAPOLATED

65322-81

Figure 80. Fountain Temperatures Do Not Decay with Height, Three and Four Nozzles

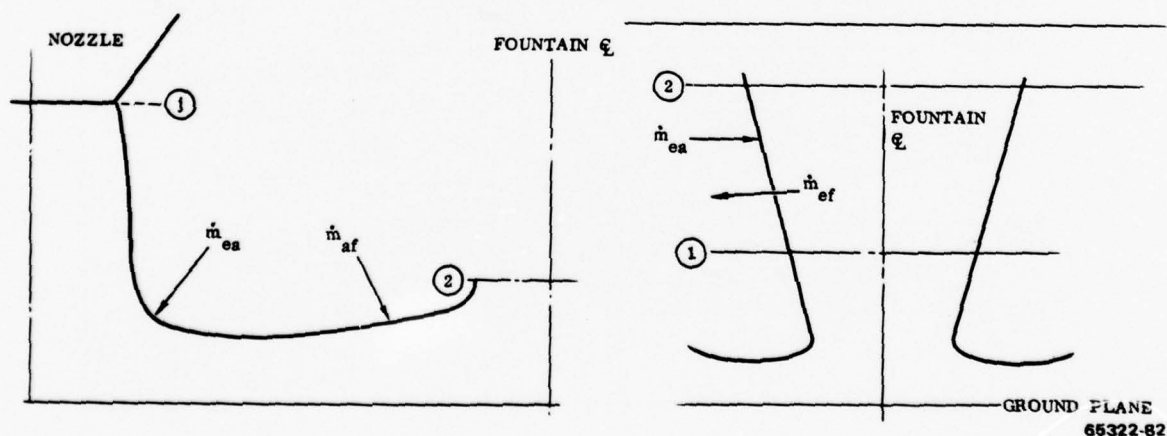


Figure 81. An Adiabatic Control Volume Defines Flow Field Thermal Balance

reducing to:

$$\frac{\dot{m}_{af}}{\dot{m}_j} = \frac{\frac{\dot{m}_2}{\dot{m}_j} (\Delta T_R)_2 - 1}{(\Delta T_R)_f}$$

it follows that:

$$\frac{\dot{m}_{ea}}{\dot{m}_j} = \frac{\dot{m}_2}{\dot{m}_j} - \frac{\dot{m}_{af}}{\dot{m}_j} - 1$$

where

$$\frac{\dot{m}_2}{\dot{m}_j} = \left(\frac{\dot{m}_f}{\dot{m}_j} \right) \quad \text{as determined in Section 3.}$$

$Z/D \approx 0$

For fountain flow, (Figure 81) the energy equation is applied to the three basic nozzle configurations:

In the two-nozzle cases, $\dot{m}_2 < \dot{m}_1$, and $T_2 < T_1$. Therefore, some fountain flow is lost (\dot{m}_{ef}) and some is entrained (\dot{m}_{ea}). It is assumed that \dot{m}_{ea} is at ambient temperature and that \dot{m}_{ef} is at T_1 .

Thus:

$$\dot{m}_2 - \dot{m}_1 = \dot{m}_{ea} - \dot{m}_{ef}$$

$$\dot{m}_2 T_2 - \dot{m}_1 T_1 = \dot{m}_{ea} T_a - \dot{m}_{ef} T_1$$

or:

$$\frac{\dot{m}_{ef}}{\dot{m}_j} = \frac{\dot{m}_1}{\dot{m}_j} - \frac{\dot{m}_2}{\dot{m}_j} \frac{(\Delta T_R)_2}{(\Delta T_R)_1}$$

$$\frac{\dot{m}_{ea}}{\dot{m}_j} = \frac{\dot{m}_2}{\dot{m}_j} - \frac{\dot{m}_1}{\dot{m}_j} + \dot{m}_{ef}$$

In the three-nozzle case, data indicates that $\dot{m}_2 < \dot{m}_1$ and $T_2 = T_1$:

$$\frac{\dot{m}_{ef}}{\dot{m}_j} = \frac{\dot{m}_1}{\dot{m}_j} - \frac{\dot{m}_2}{\dot{m}_j}, \quad \dot{m}_{ea} = 0$$

In the four nozzle case, $\dot{m}_2 > \dot{m}_1$ and $T_2 = T_1$

$$\frac{\dot{m}_{ef}}{\dot{m}_j} = \left(\frac{\dot{m}_1}{\dot{m}_j} - \frac{\dot{m}_2}{\dot{m}_j} \right), \quad \frac{\dot{m}_{ea}}{\dot{m}_j} = 0$$

$\frac{\dot{m}_{ef}}{\dot{m}_j}$ is negative, implying entrained flow at fountain

temperature $T_1 = T_2$.

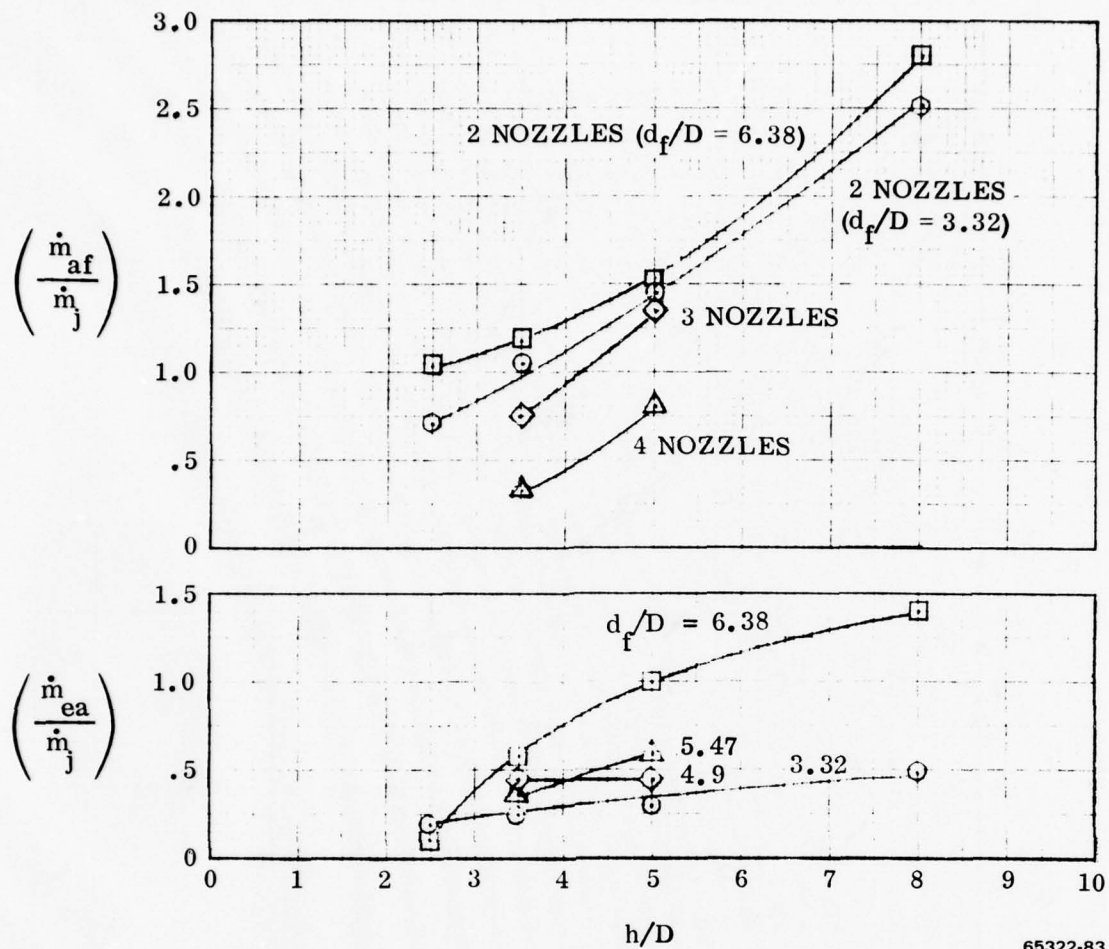
Free Jet-Ground Entrainment

The mass flow entrained by the ground and free jet from ambient and from the fountain are influenced by blocking surface height and configuration (Figure 82). Mass flow entrained from the fountain is highest for the two-nozzle configurations, followed by the three and four-nozzle configurations. The ground and free jets of the wider spaced ($d_f/D = 6.68$) two-nozzle configuration entrains more flow from the fountain than the intermediate ($d_f/D = 3.32$) spacing arrangement. In all cases, entrainment of the fountain by the ground jet increases with blocking surface height (h/D). The entrainment of ambient air increases with h/D excepting the three nozzle case where mass flow entrainment is constant. The level of entrainment generally follows the nozzle-fountain spacing (d_f/D) with higher entrainment at higher spacing.

The fountain mass flow at the ground plane [\dot{m}_f for $Z/D = 0$] was determined by extrapolation of integrated flow survey data in Section 3. The fraction of that total flow that is entrained by the ground jet is a function of maximum fountain height (h_f/D) and blocking surface height (h/D) with small deviation due to configuration (Figure 83). Fountain entrainment by the ground jet diminishes with increased fountain height along a constant h/D curve until the fountain just touches the blocking plate. This intersection point is characterized by an entrainment ratio of 40 to 50% increasing with increased h/D .

Fountain Entrainment

The fountain entrainment characteristics were determined from the equations developed in the beginning of this section using the integrated flow survey data of Section 3. For two-nozzle cases (Figure 84), accumulated ambient air entrainment ($\Sigma \dot{m}_{ea}/\dot{m}_j$) increases with height in the fountain, tapering off at the higher levels. Ambient air entrainment by the fountain increases with blocking surface height (h/D). Flow leaving the vertical component of the fountain is designated by negative values of (\dot{m}_{ef}/\dot{m}_j) with the accumulated value designed by Σ . The leaving flow increases with h/D ,



65322-83

Figure 82. Free Plus Ground Jet Entraines Ambient Air and Fountain Mass

accelerating at the higher Z/D due to blocking surface turning. This effect is particularly strong at $h/D = 2.5$. The curve shapes and absolute values of these parameters are similar for both two nozzle configurations suggesting that nozzle spacing (d_f/D) does not have a strong influence on fountain flow mass transfer.

Since the three and four nozzle fountains are isothermal, the only characteristic parameter is mass leaving or entering the fountain at constant temperature (Figure 85). The three nozzle fountain loses mass as a function of Z/D in a manner similar to the two nozzle cases but at a lower rate. The four nozzle fountain gains mass in the same manner and at the same rate as the two nozzle configuration gains ambient air (Figure 84).

The slopes of the mass transfer curves of Figures 84 and 85 represent the local entrainment/leaving rate. These values are related to the local vertical component of fountain dynamic pressure reported in Section 3 (Figure 86). The results correlate

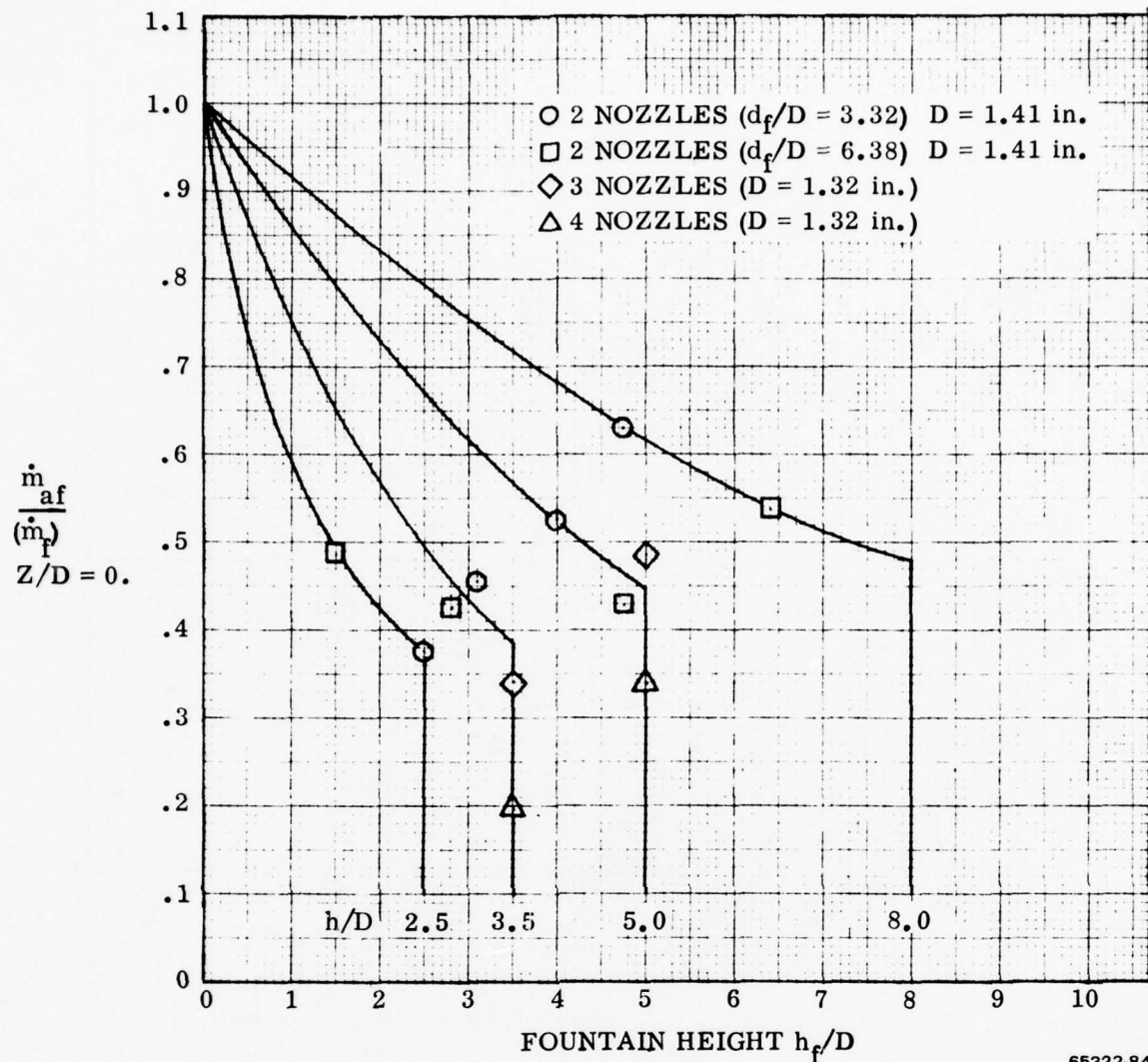


Figure 83. Fountain Flow Entrained by the Ground Jet Diminishes with Fountain Height

with the intuitive assumption that strong fountain segments (high dynamic pressure) entrain more and lose less mass flow. A striking correlation is obtained with the parameter of maximum fountain height as a fraction of blocking surface height (h_f/h). Local entrainment and leaving rates are reduced as h_f approaches h . Leaving rates suddenly depart from the overall trends when the fountain intersects the blocking surface.

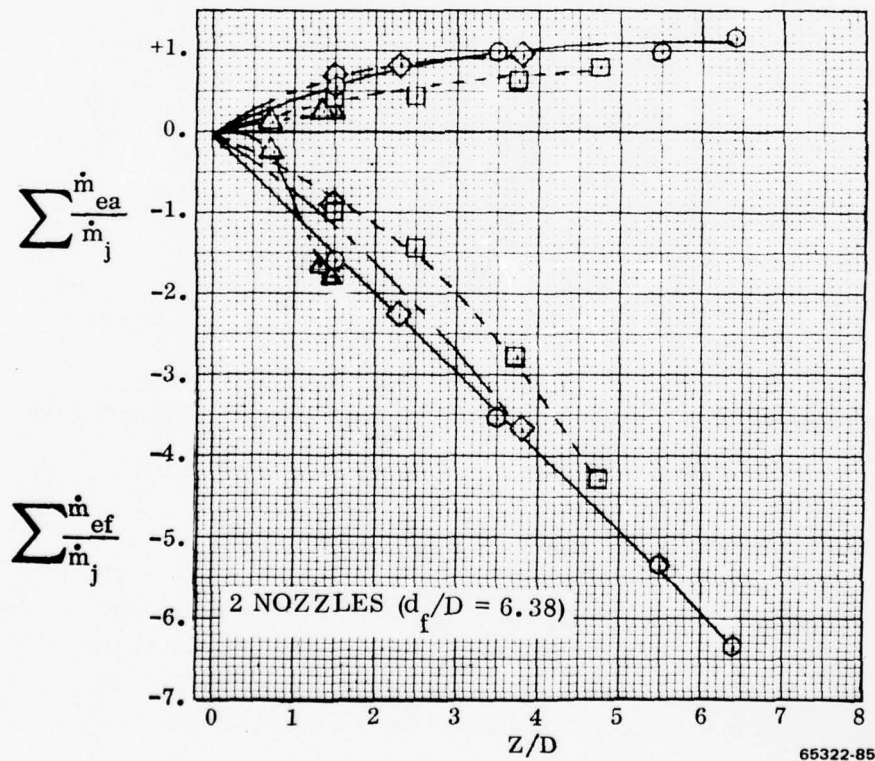
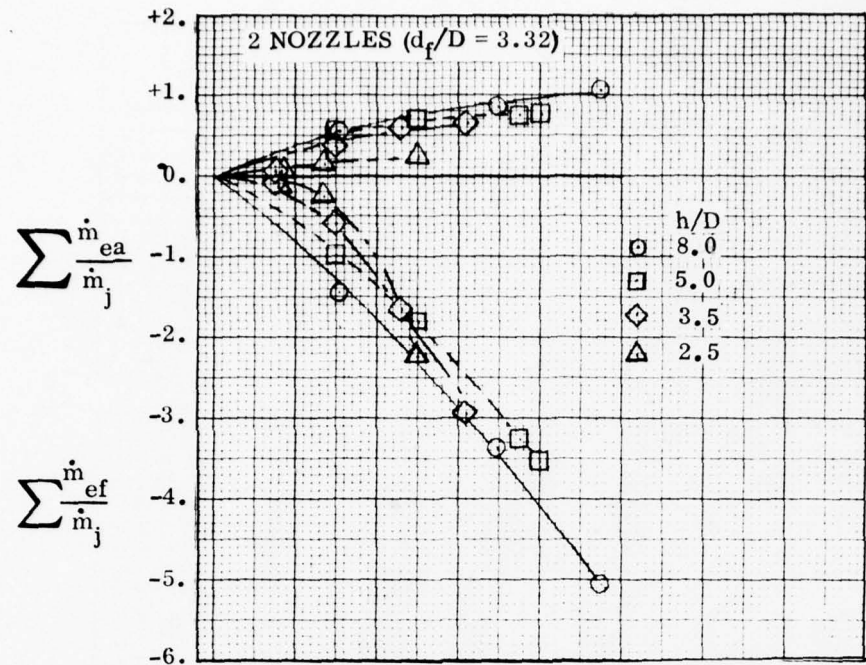
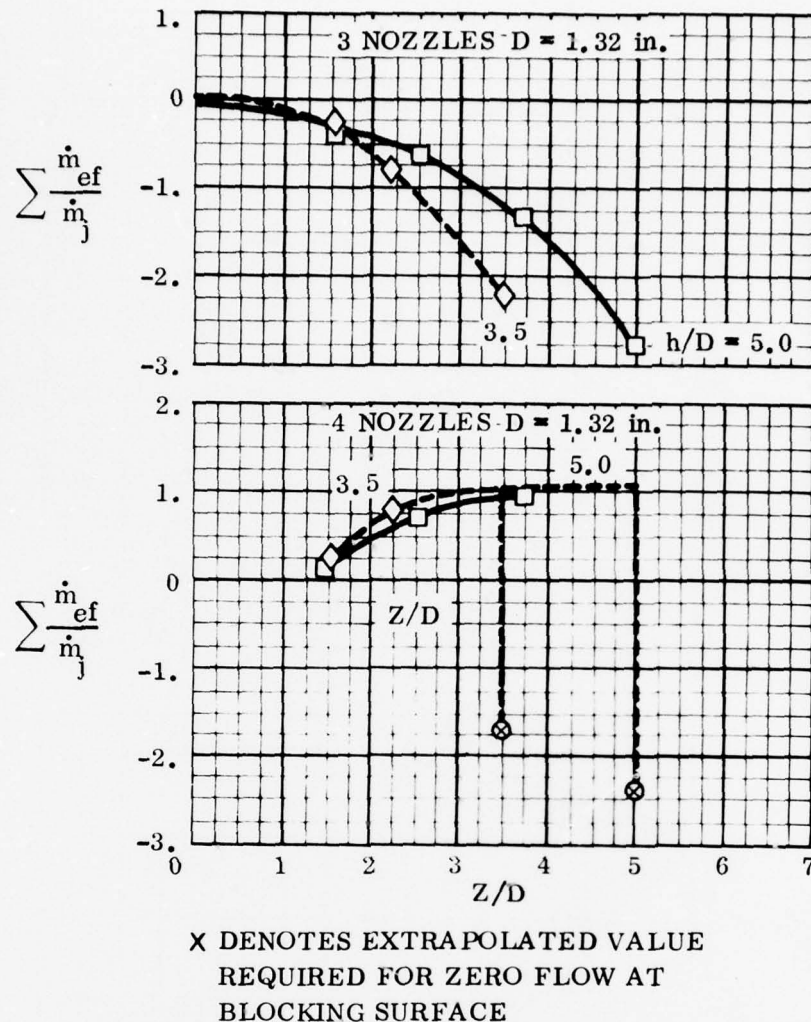


Figure 84. The Fountain Loses Mass and Entraines Ambient Air, Two Nozzle Configurations



65322-86

Figure 85. The Three Nozzle Fountain Loses Mass, The Four Nozzle Fountain Gains Mass

4.3 METHOD OF ESTIMATING FOUNTAIN TEMPERATURES

The previous Sections 4.1 and 4.2 have described the measured fountain temperatures in flow fields confined by nozzles and blocking surface with associated radial ground jets. The resulting nondimensional temperatures (ΔT_R) are considerably higher than the temperature values that would be calculated for a corresponding radial ground jet.

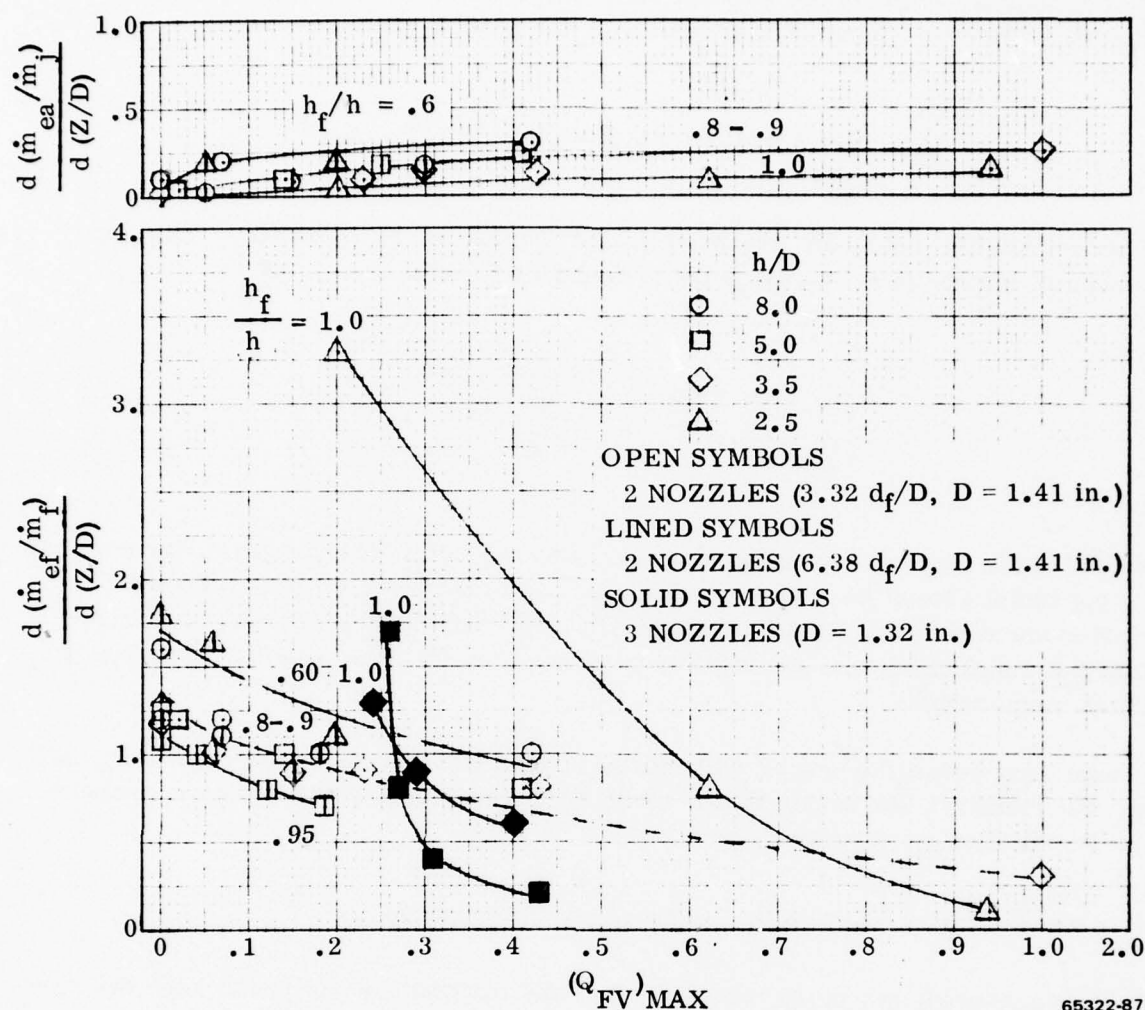


Figure 86. Fountain Entrainment and Mass Loss is Influenced by Local Dynamic Pressure and Fountain/Model Height Ratio

Using the methodology of Reference 3, the entrainment of a free nozzle jet $\left(\frac{\dot{m}_e}{\dot{m}_j}\right)$ may be calculated from the equation:

$$\frac{\dot{m}_e}{\dot{m}_j} = 0.194 + 0.121 (h/D)$$

For a radial ground jet without fountains:

$$\frac{\dot{m}_e}{\dot{m}_j} = 0.107 + 1.121 (d_f/D - 0.5)$$

Assuming that the height of the fountain (Z/D) may be used as an extension of ground jet distance (Figures 22 and 23) and combining the above equations:

$$\frac{\dot{m}_e}{\dot{m}_j} = 0.121 (h/D) + 1.121 (d_f/D + Z/D) - 0.367$$

The above relation holds for any point in the ground jet and fountain. The non-dimensional temperature at that point is found by the relation:

$$\Delta T_R = \frac{1}{\frac{\dot{m}_e}{\dot{m}_j} + 1}$$

For each of the fountain core temperatures measured in this test program, the corresponding radial ground jet ΔT_R was calculated and the differential (ΔT_R) plotted against calculated radial jet ΔT_R (Figure 87). The slopes are extremely steep indicating that small changes in the radial jet temperature will lead to large increases in fountain temperatures.

The user may enter this curve with his own estimate of radial ground jet ΔT_R and apply the indicated correction factor to obtain an estimate of the fountain temperatures for similar geometries.

4.4 RECOMMENDATIONS FOR ADDITIONAL RESEARCH

It is recommended that more extensive thermal mapping be conducted with the current or similar model. By measuring simultaneously the thermal and dynamic pressure profiles at various stations in the nozzle efflux, ground jet, and fountain, the entrainment characteristics can be determined as a function of flow distance. Thus, the critical geometric factors, such as nozzle spacing and arrangement, that are known to influence the fountain entrainment by the ground jet, would be determined.

ΔT_R
 FOR
 FOUNTAIN
 (TEST DATA)
 $-\Delta T_R$
 RADIAL
 GROUND
 JET
 (WITHOUT
 FOUNTAIN)

○ 2 NOZZLES $d_f/D = 3.32$
 △ 2 NOZZLES $d_f/D = 6.38$
 □ 3 NOZZLES $d_f/D = 4.90$
 ▽ 4 NOZZLES $d_f/D = 5.47$

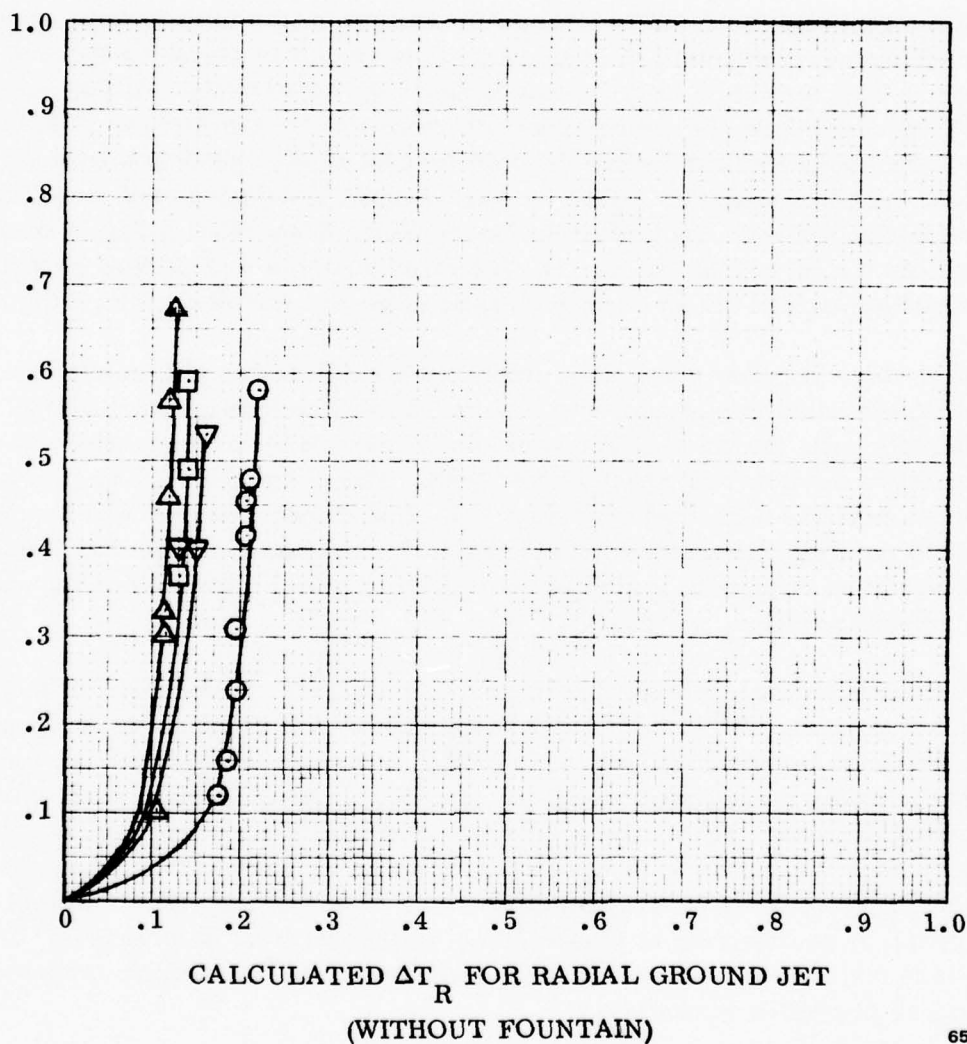


Figure 87. Fountain Temperatures are Considerably Higher than Comparable Temperatures in Radial Ground Jet

SECTION 5

FAR-FIELD TEMPERATURE DISTRIBUTIONS

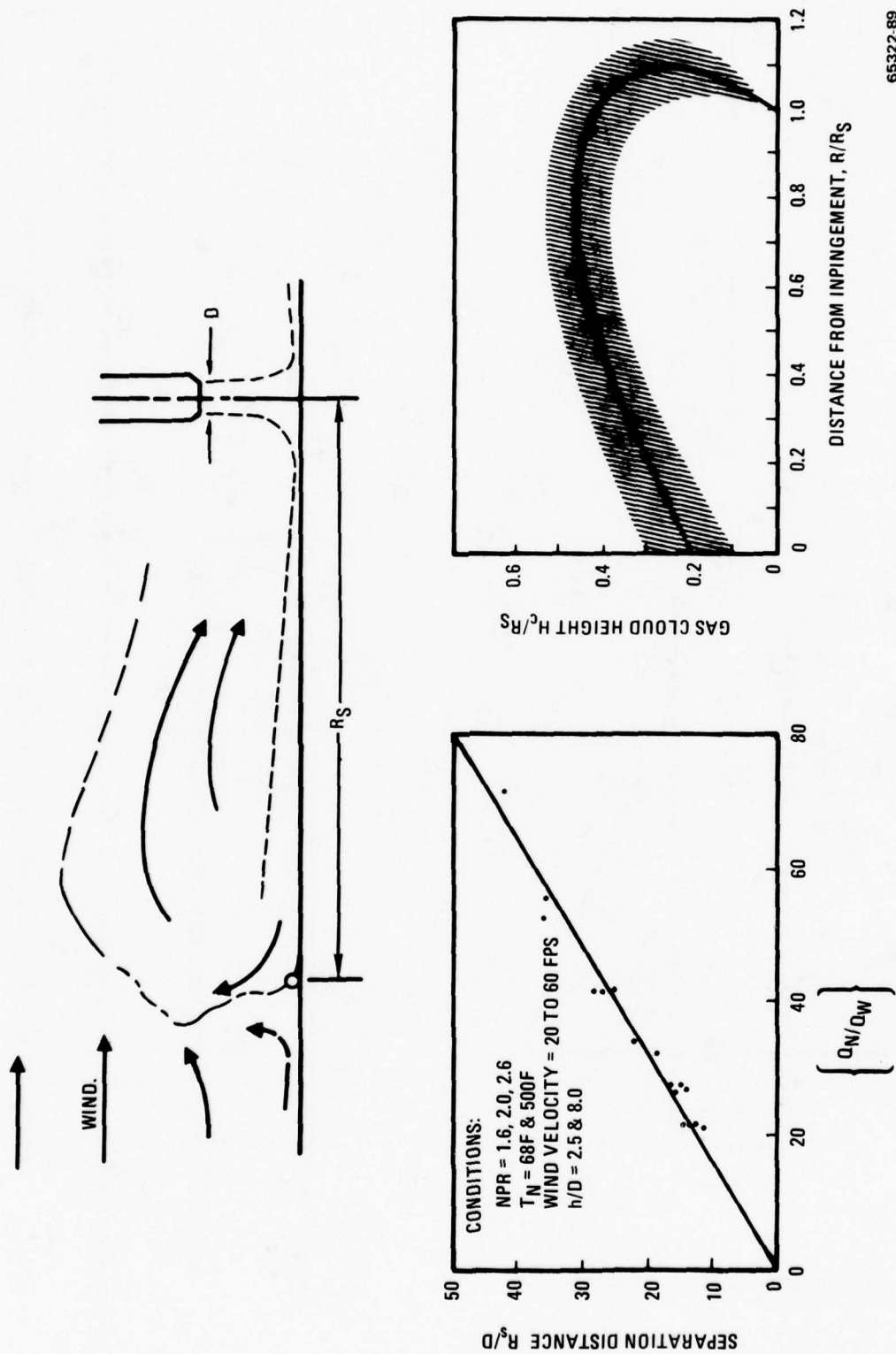
VTOL aircraft operating in the ground effects region are subject to hot gas reingestion that can cause thrust loss and/or compressor surge. Hot gases are drawn into the inlets from both the near and far flow fields. The near-field reingestion is usually the result of the hot fountain gases impinging on the aircraft's lower surfaces and then flowing around those surfaces into the inlets. Near-field reingestion must be eliminated or controlled by general design considerations of the inlet-nozzle-airframe geometry, or the aircraft configuration will not be viable from an operational standpoint.

Far-field reingestion is depicted in Figure 88. The ground jet flows radially outward from the impingement area until its momentum is too small to overcome the buoyancy forces (for no wind condition) or the counteracting wind components. At this point the ground jet separates from the ground plane and rises into the freestream. Without crosswind, the hot gases drift toward the inlet because of the sink action induced by the inlet and the entraining jets. When wind is present the hot gases are swept back toward the inlets; however, separation occurs earlier and the cloud height is usually much less than for the no-wind case. The temperature of the recirculated gases is usually significantly less for far-field reingestion than for near-field reingestion.

The purpose of the far-field reingestion tests was to evaluate the rise in inlet temperatures and to correlate this phenomenon with far-field temperature distributions. To accomplish this goal, the selected approach was to acquire the data necessary to define the properties in the flow field ahead of the inlets. The instrumentation employed to acquire these data was described in Section 2.3. Specifically, the plan was to survey the flow field acquiring temperature, total pressure, and flow direction data from which a description of the reingestion cloud could be obtained in terms of temperature profiles, velocity profiles, and flow direction.

Figure 89 illustrates the locations of instrumentation relative to the model of a typical flow-field survey test. Traverses were taken at positions (station planes) in front of the model and each traverse typically had six sampling stops (in buttock line planes). At all test conditions one traverse was made as close as possible to the nose of the model. At some model heights, traverses were made at two or three rake heights (waterline of the rake handle) to provide a longer profile. The locations of the traverses were selected based on our pretest knowledge of the reingestion flow field. This knowledge is summarized in Figure 88 and is derived from Reference 6.⁶ This description of the recirculation cloud's shape and extent was determined by high speed photography of impinging smoke jets.

⁶Gay, A., Jet Induced Effects With Fundamental Geometries, General Dynamics Convair Aerospace Division Report, CASD-ERR-74-044, December 1974.



65322-89

Figure 88. The Hot-gas Recirculation-cloud Geometry Had Been Appraised

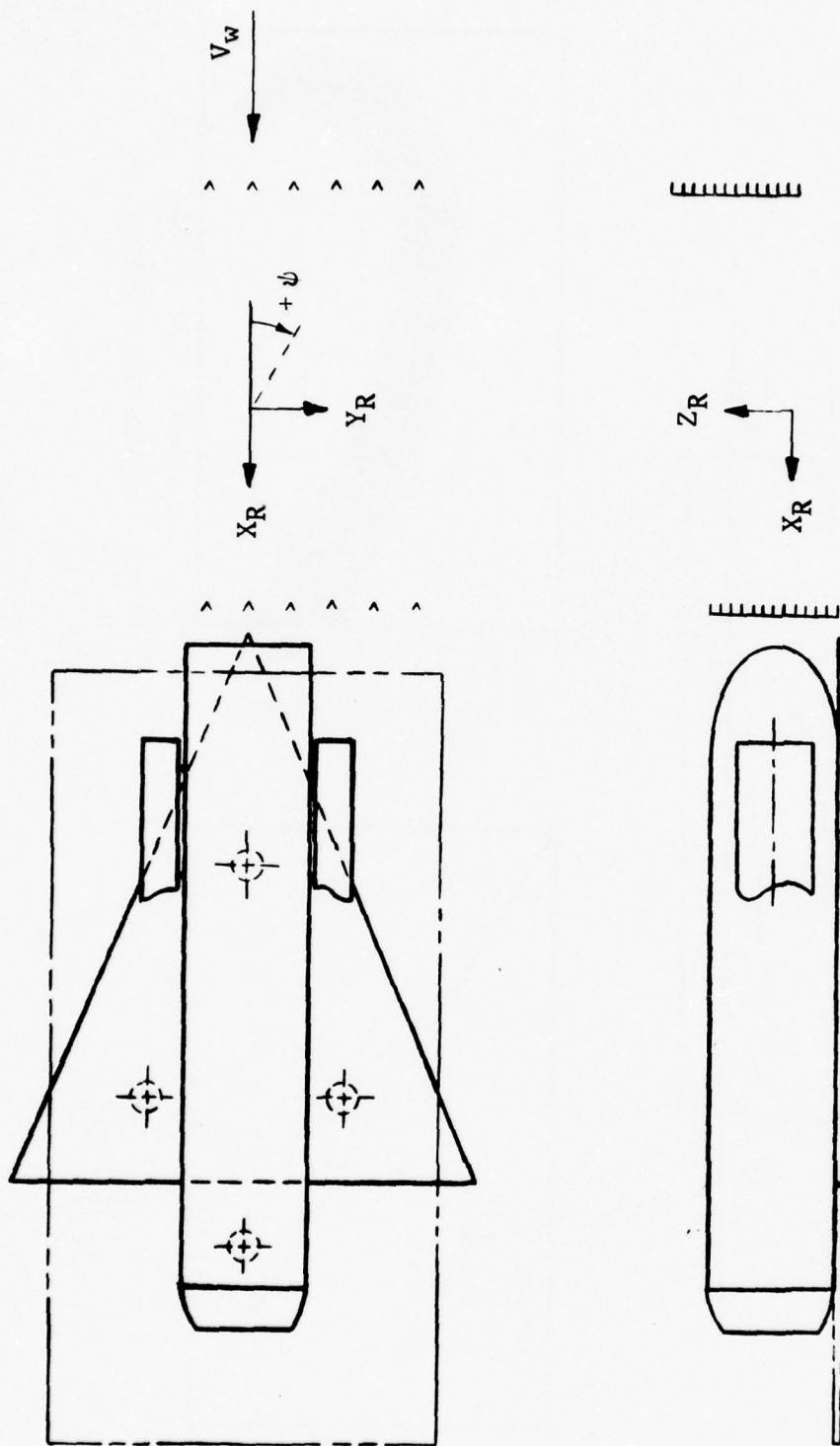


Figure 89. The Flow Field Was Surveyed at Various Locations in Front of the Model

65322-90

An outline of the reingestion test program is given in Figure 90. Three model configurations were tested at heights above the ground plane from 2.5 to 8.0 jet diameters. Reingestion flow-field data were taken at various locations ahead of the model for wind velocities of 3 and 20 knots. Inlet temperatures were recorded at all times. As shown in Figure 12 each inlet had four-manifolded thermocouples internally and three external thermocouples. Typically the upper external thermocouple and the one on the inlet centerline read the same value; hence, they are plotted as the upper external temperature in the curves that follow. The lower external thermocouple usually read a higher value than the other two, indicating that the lower TC reading was influenced by the exhaust flow field.

TEST PROGRAM

MODEL:	$N_3^1 N_{10}^1 N_{11}^1 P_{31} (\psi = 0^\circ, -67)$ $N_3^1 N_{10}^1 N_{11}^1 P_{31-2} (\psi = 0^\circ)$ $N_3^2 N_{13}^2 P_{13} (\psi = 0^\circ)$
MODEL HEIGHT:	$h/D = 2.5, 3.5, 5.0, 8.0$
RAKE HEIGHT:	$Z_R/D = 5 \text{ to } 24$
RAKE TRAVERSE:	$Y_R/D = -2 \text{ to } +6$
RAKE AXIAL POSITION:	$X_R/D = 1.5 \text{ to } 16.6$
WIND VELOCITY:	$V_w = 3, 20 \text{ KNOTS}$
INSTRUMENTATION:	INLET, INLET PROXIMITY THERMOCOUPLES, RAKE THERMOCOUPLES, AND CONE PROBES

65322-91

Figure 90. The Reingestion Test Utilized 3 Model Configurations and Various Model and Rake Positions

5.1 FAR-FIELD TEMPERATURE DISTRIBUTION AND EFFECT ON INLET TEMPERATURE

Figure 91 presents the flow-field temperature as measured by the rake for a typical traverse. Note that there is very little difference in the profile for the various steps across the flow field. Hence, for clarity, a single profile was drawn through the data, and these "average" profiles are used in the analysis that follows.

Figure 92 presents the flow-field temperatures, at two stations ahead of the model, at both 3 and 20 knots wind velocity for the two-jet rectangular plate configuration. Figure 93 presents the inlet temperatures for the same test conditions. At 3 knots, the

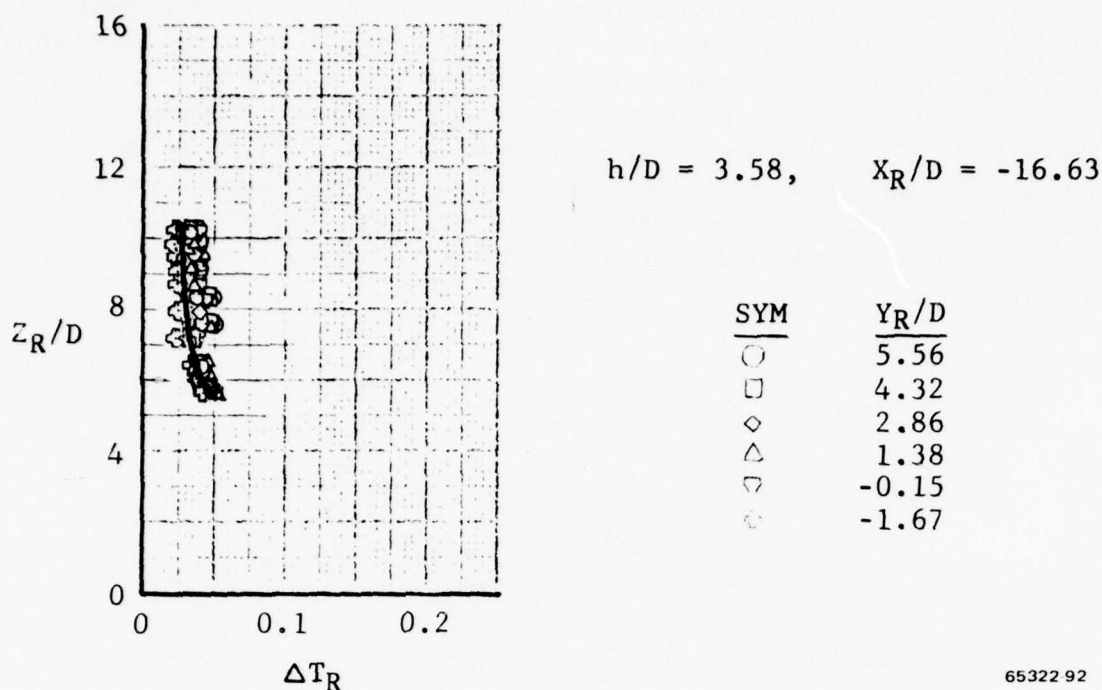


Figure 91. The Temperature Profiles in Front of the Model Were Typically Independent of Transverse Location

temperature profiles at both 1.4 and 16.5 jet diameters ahead of the model are identical (within the accuracy of the instrumentation) at all model heights. Also the temperatures are not significantly higher at Z/D 's of 2.5 to 5 than at 12 and above. Thus, at these test conditions, far-field reingestion could not contribute more than $0.025 \Delta T_R$ to the inlet temperature rise. Figure 93 shows the inlet temperature rise to be about $0.04 \Delta T_R$. Thus at very low wind velocities it appears that the exhaust gases flow along the ground plane and separate from the ground plane at relatively large distances (greater than 50 jet diameters) from the model; hence the hot gases are mixed with a large volume of ambient air and the temperature of the resulting mixture is only slightly above ambient. For a wind velocity of 20 knots, the temperature profiles at 1.4 and 10.5 jet diameters ahead of the model are shown in Figure 92. Below Z_R/D of about 10 there is a significant increase in the flow-field temperature compared to the 3 knot case. Figure 93 shows a significant increase in inlet temperature at a model height of 2.5 D , but as the model is raised the inlet temperature decreases until it merges with the 3 knot case at an h/D of 5. Thus it appears that the wind is sweeping the hot exhaust gases into the inlets at h/D below 5, and above h/D of 5 the hot gases are swept beneath the inlet.

Figure 94 presents the flow-field temperatures at two stations ahead of the model for the three jet, triangular plate configuration; profiles are shown for both 3 and 20 knots

$T = 400^\circ\text{F}$

$D = 1.41\text{ in.}$

$V_W = 20\text{ KTS, } V_W/V_J = .027$

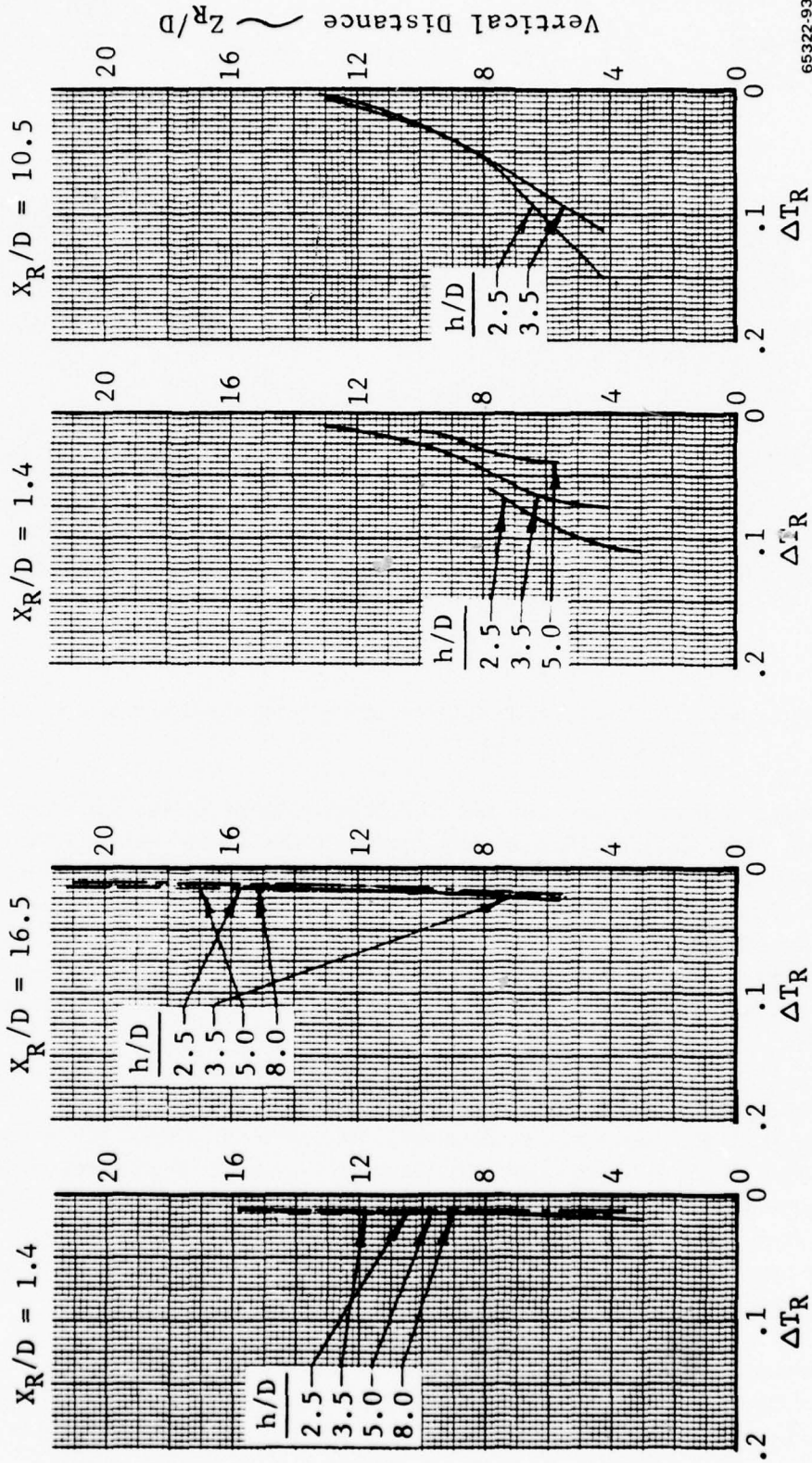


Figure 92. The Flow-field Temperature Profiles in Front of the 2-jet Configuration are influenced by Wind Velocity

$T = 400^\circ \text{F}$
 $D = 1.41 \text{ in.}$

○ - INTERNAL	$V_w, \text{ KTS}$	V_w/V_J
□ - LOWER EXTERNAL	— 3	.004
△ - UPPER EXTERNAL	- - - 20	.027

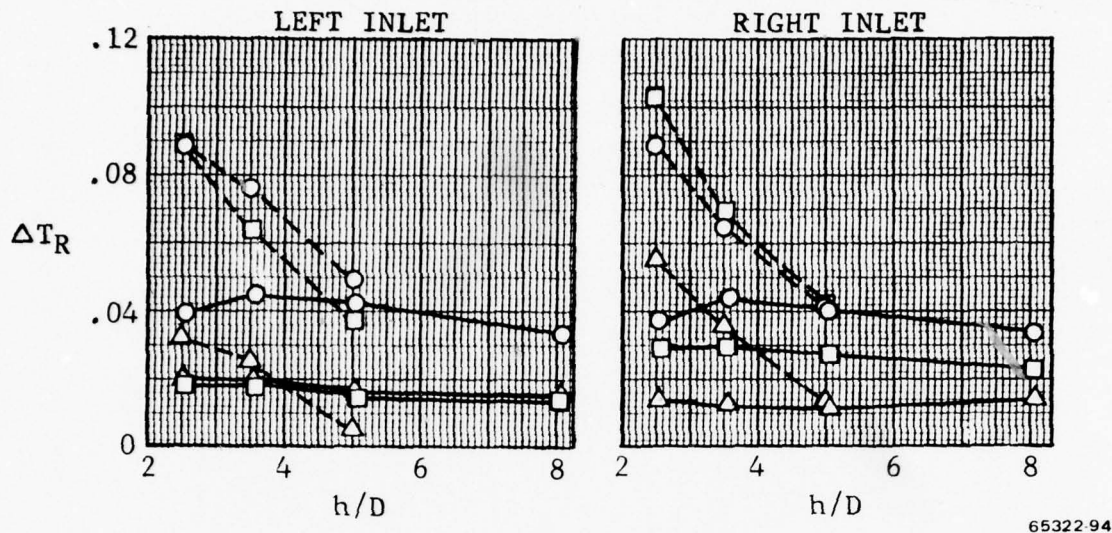


Figure 93. The Inlet Temperatures of the 2-jet Configuration are Influenced by Velocity

wind velocity. Figure 95 presents the inlet temperatures for the same test conditions. For $V_w = 3$, at an X_R/D of 16.6 the temperature increase in the flow field is affected very little by model height and the temperature rise is ΔT_R of 0.02 to 0.05. At X_R/D of 1.48 the flow-field temperature rise is about the same, but the temperature profiles appear to be influenced more by the model height. From Figure 95 it is seen that the inlet temperature varies slightly with model height from a ΔT_R of 0.045 to 0.062. Again, it is apparent that the rise in inlet temperature is not entirely due to far-field reingestion.

For a 20 knot wind velocity, the flow field temperature gets as high as 0.075 to 0.1 ΔT_R at $X_R/D = 10.6$, but close to the model, at $X_R/D = 1.48$, the temperature rise is 0.07 to 0.085 ΔT_R . It is not clear why the temperature is less nearer the model. From Figure 95 it is seen that the inlet temperatures are not symmetrical for this series of runs. One run was made during the test at $V_w = 0$; the internal inlet temperatures for this run are given in Figure 95 also. The inlet temperature is significantly less at $V_w = 3$ and 20 knots.

During the test a "scab-on" plate was added to the triangular plate in an effort to isolate the inlets from any influence of the exhaust jets (P_{31-2} , Figure 8). The "scab-on" plus the triangular plate have the same planform as the P_{13} rectangular plate in the region

$T = 400^\circ\text{F}$, $D = 1.32$ in.

$V_M = 3$ KTS, $V_W/V_J = .004$

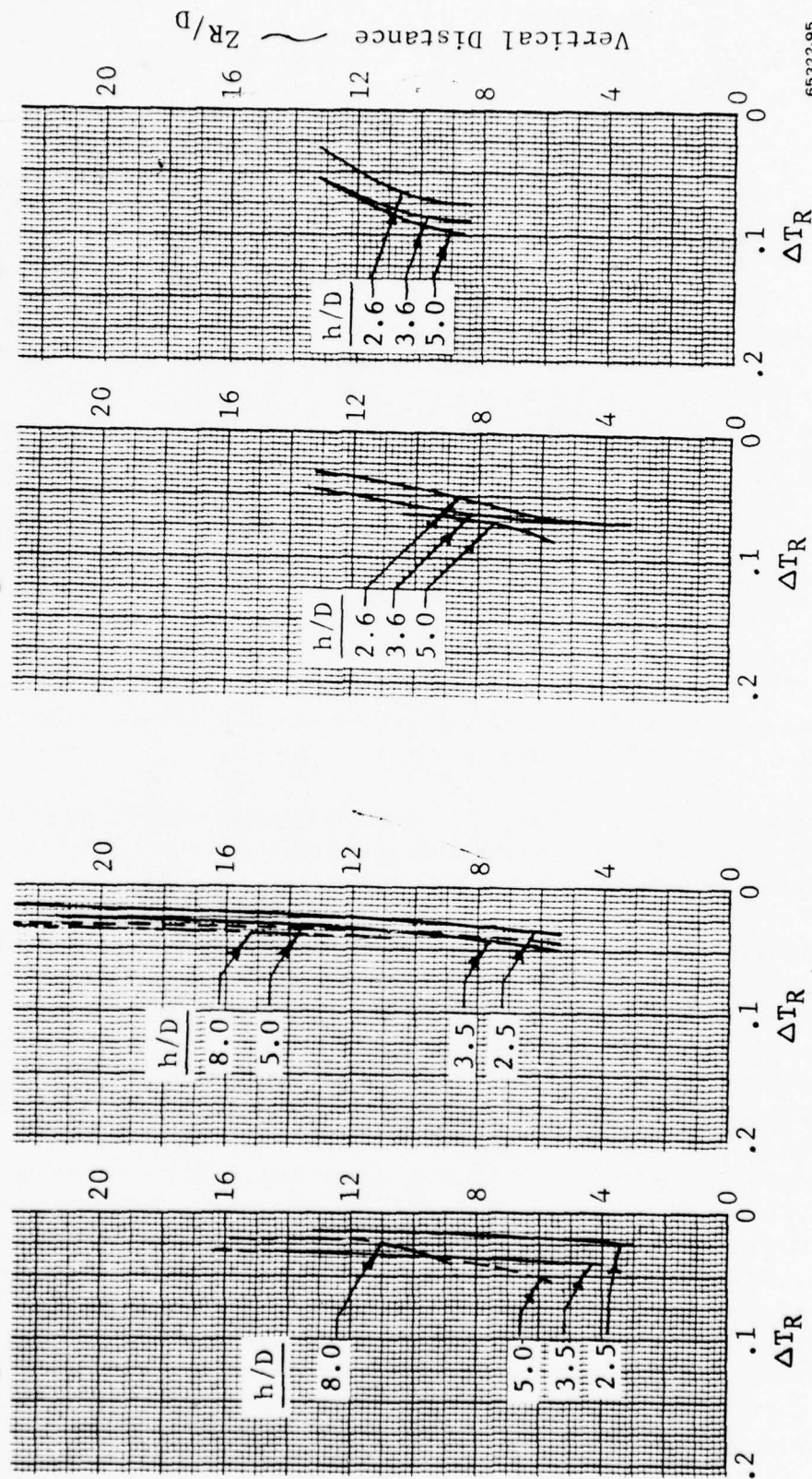
$V_W = 20$ KTS, $V_W/V_J = .027$

$X_{R/D} = 1.48$

$X_{R/D} = 16.6$

$X_{R/D} = 1.48$

$X_{R/D} = 10.6$



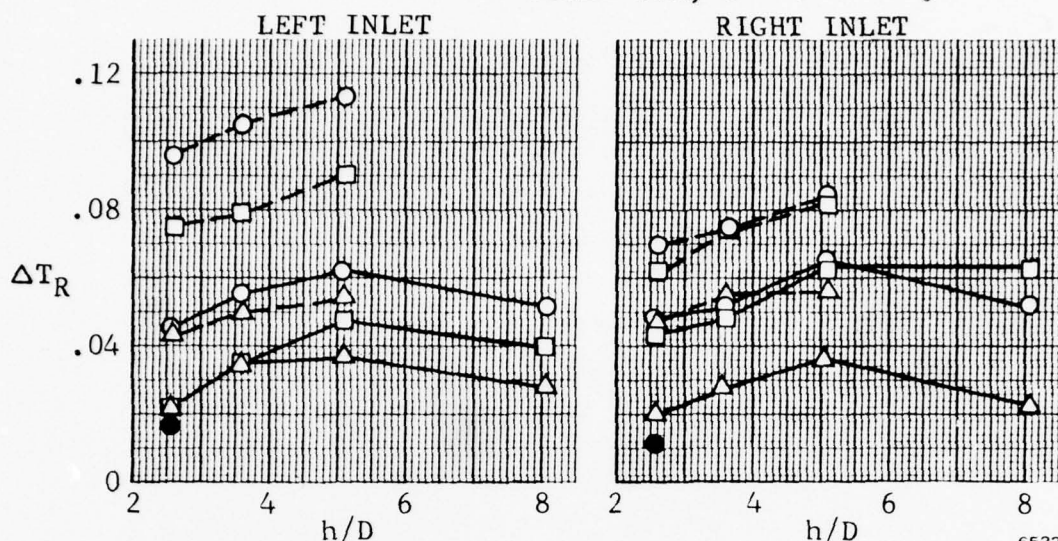
65322-95

Figure 94. The Flow-field Temperature Profiles in Front of the 3-jet Configuration are Influenced by Wind Velocity

$T = 400^\circ \text{F}$ \bigcirc - INTERNAL
 $D = 1.32 \text{ in.}$ \square - LOWER EXTERNAL
 \triangle - UPPER EXTERNAL

V_w , KTS	V_w/V_j
3	.004
20	.027
0	0

SOLID SYM, \bullet



65372-96

Figure 95. The Inlet Temperatures of the 3-jet Configuration are Influenced by Wind Velocity

forward of the exhaust jets. Data presented in Figure 96 show the effect of the "scab-on" plate. Apparently the only effect was to decrease the rise in inlet temperature as the model was raised through $h/D = 5.0$.

Some runs were made with the three jet triangular plate model at -67° angle of sideslip, ψ , and a wind velocity of 20 knots. Figure 97 presents a comparison of the $\psi = 0$ and $\psi = -67^\circ$ flow field temperatures. With the model at -67° ψ , the closest a traverse could be made was at 5.3 jet diameters forward of the inlet nose. Figure 97 shows that the flow field ahead of the model is cooler at $\psi = -67^\circ$ than at $\psi = 0$. Figure 98 presents a comparison of the inlet temperatures at $\psi = 0$ and -67° deg. The internal temperature of both inlets decreased at $\psi = -67^\circ$ deg. Also, the inlet temperatures decrease with increasing model height for $\psi = -67^\circ$ deg; this is opposite to the trend at $\psi = 0$ for the three model heights tested. This is a result of the coalescence of the fountain legs into a strong central core, as discussed in Section 3. At $\psi = 0$, the flow field in front of the model is subjected to the conventional ground jet flow emanating from the forward jet, see Figure 88. However, at $\psi = -67^\circ$ deg, the forward flow field is more dependent on the formation of a fountain leg between the nozzles. This leg is present only at low Z/D since the flow feeds inward to the central core as Z/D is increased. Furthermore, the formation of the central core becomes more pronounced with increasing h/D . Thus, less hot gas flows in front of the model,

$D = 1.32 \text{ in.} \quad T = 400^\circ \text{F}$

$V_W = 20 \text{ KTS}, \quad \frac{V_W}{V_J} = .027$

ψ
 0°
 $----- -67^\circ$

\bigcirc - INTERNAL
 \square - LOWER EXTERNAL
 \triangle - UPPER EXTERNAL

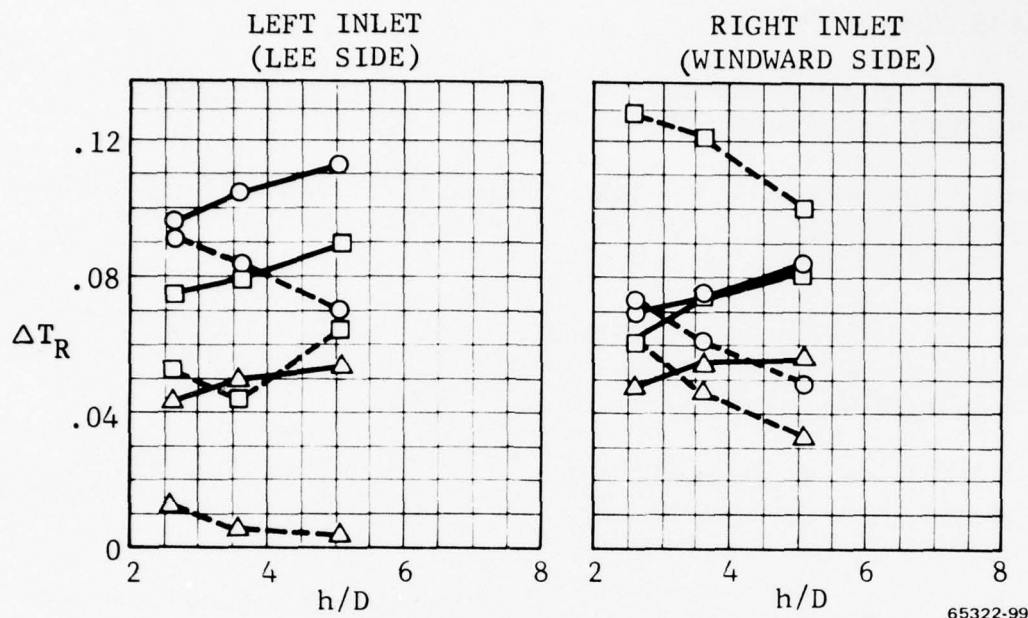


Figure 98. The Inlet Temperatures of the 3-jet Model are Influenced by Sideslip

did not indicate a sharp gradient through the shaded area shown in Figure 88. Figure 88 was derived by visual studies of a smoke jet. Apparently, the diffusion rate of the smoke in the freestream air was considerably different from the thermal diffusion from the hot exhaust gas. The flow field temperature distributions presented herein indicate that

- At $V_W = 0$, inlet ΔT_R was less than 2%.
- At $V_W = 3$ knots, inlet ΔT_R was about 6% or less with the inlets facing the wind.
- At $V_W = 20$ knots, inlet ΔT_R reached almost 12% with the inlets facing the wind.

It is recommended that further surveys of external flows be conducted in the far field, concentrating on areas closer to the ground plane. The use of a laser velocimeter to measure these very low local flow velocities may provide a higher degree of velocity discrimination than was achieved by the cone probes used in this investigation.

REFERENCES

1. Eilert, et al, Report GDLST 711 & 712, Low Speed Wind Tunnel Tests to Evaluate the Aerodynamic and Thermodynamic Characteristics of VSTOL Fountains and Inlet Reingestion, 29 August 1977.
2. Tyler, S. P., Calibration of the V/STOL Propulsion Induced Interference Research Model Jet Nozzles, Convair Report TM-73-VSTOL-02, 1973.
3. Karemaa, A. and Ramsey, J.C., Aerodynamic Methodology For the Prediction of Jet-Induced Lift in Hover, General Dynamics Convair Aerospace Division Report CASD-ERR-73-012, December 1973.
4. Karemaa, A., Abbreviated Methodology for the Prediction of Jet-Induced Lift in Hover, General Dynamics Convair Aerospace Division Report CASD-ERR-74-024, December 1974.
5. Kotansky, D. R., et al, Multi-Jet Induced Forces and Moments on VTOL Aircraft Hovering in and out of Ground Effect, Naval Air Development Center Report Number, NADC-77-229-30, June 1977.
6. Gay, A., Jet Induced Effects With Fundamental Geometries, General Dynamics Convair Aerospace Division Report, CASD-ERR-74-0044, December 1974.

APPENDIX A

FOUNTAIN INDUCED FORCES

The induced forces and moments on the flat plate blocking surfaces were recorded for correlation with the fountain flow characteristics determined from the rake surveys. In addition, force data were obtained for several other conditions and configurations for which no rake data were obtained. The lift force data for each of the configurations tested are presented in this appendix.

Figures A-1 through A-7 present the data that were used to obtain the fountain incremental effects shown in Figures 15 and 16. The data for the single nozzle run of the triangular plate, Figures A-5 and A-6, required a minor adjustment since the single nozzle portion of the plate was not exactly equal to one third of the total plate area. The adjusted level is shown by the dashed line and was used to obtain the incremental fountain effects.

As discussed in Section 3.1, there is very little effect of reducing the jet exhaust temperature from 400 to 200°F. This is shown for one and two nozzle configurations in Figures A-8 and A-9. Additional single nozzle temperature effects are presented in Figures A-10 through A-13. In all cases the cold jet (70°F) data exhibits lower induced lift losses at the lower values of h/D than the hot jet (400°F) data. However, for the two nozzle configuration with the fountain present, the hot jet produces a more positive net effect than the cold jet. This leads to the positive increase in the net fountain effect for the hot jet over the cold jet shown in Figure 16.

Increased jet temperature increases the induced lift losses for a single jet configuration because the higher temperature causes higher velocities (at constant NPR). This in turn leads to more turbulent jets that entrain surrounding gases at a higher rate, thus leading to higher lift losses. However, with two jets the flow pattern becomes much more complex than the symmetrical ground jet produced by the single nozzle. The two jet flow produces a weak fountain and a reinforced ground jet between the free jets. Additional rake surveys with cold jets are required to explain the reversal in the temperature effect from the single nozzle case.

A comparison of the force data obtained in this test with that obtained for the same configuration in the outdoor Hover Facility, Reference 4, is included in Figure A-13. Very good agreement is evident.

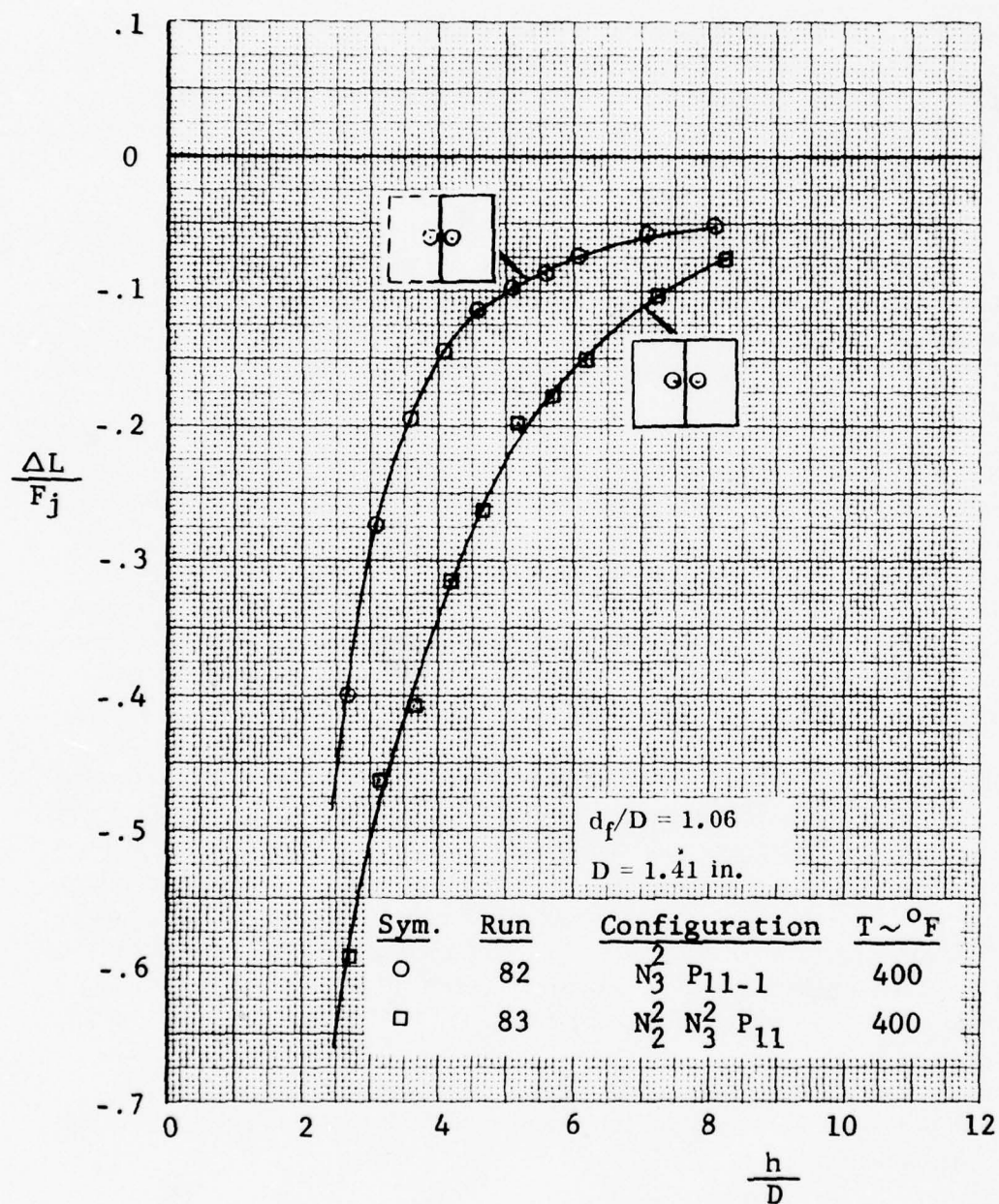


Figure A-1 Fountain Effect on Lift with Two Closely-Spaced Nozzles

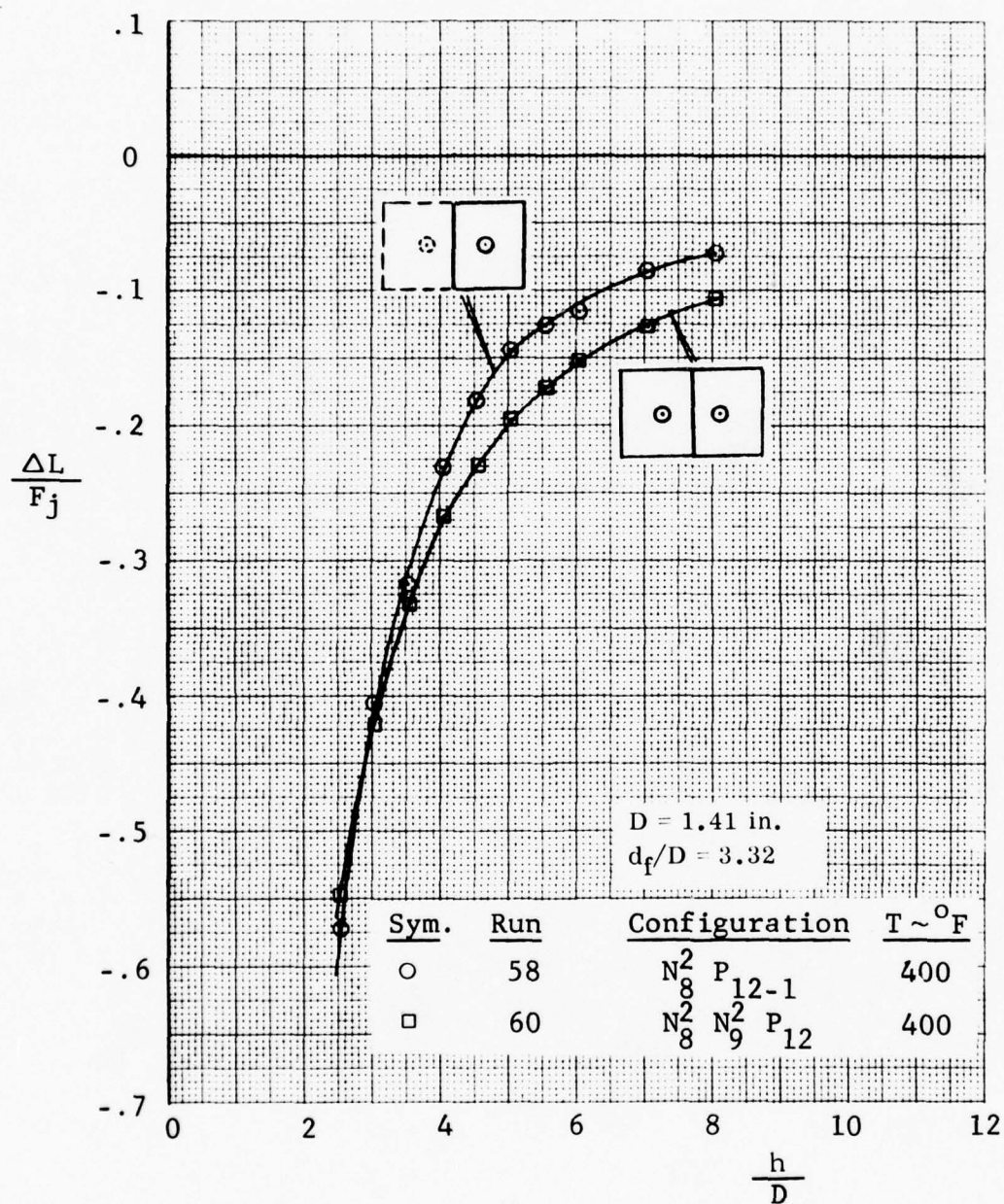


Figure A-2 Fountain Effect on Lift with Two Medium-Spaced Nozzles at 400°F

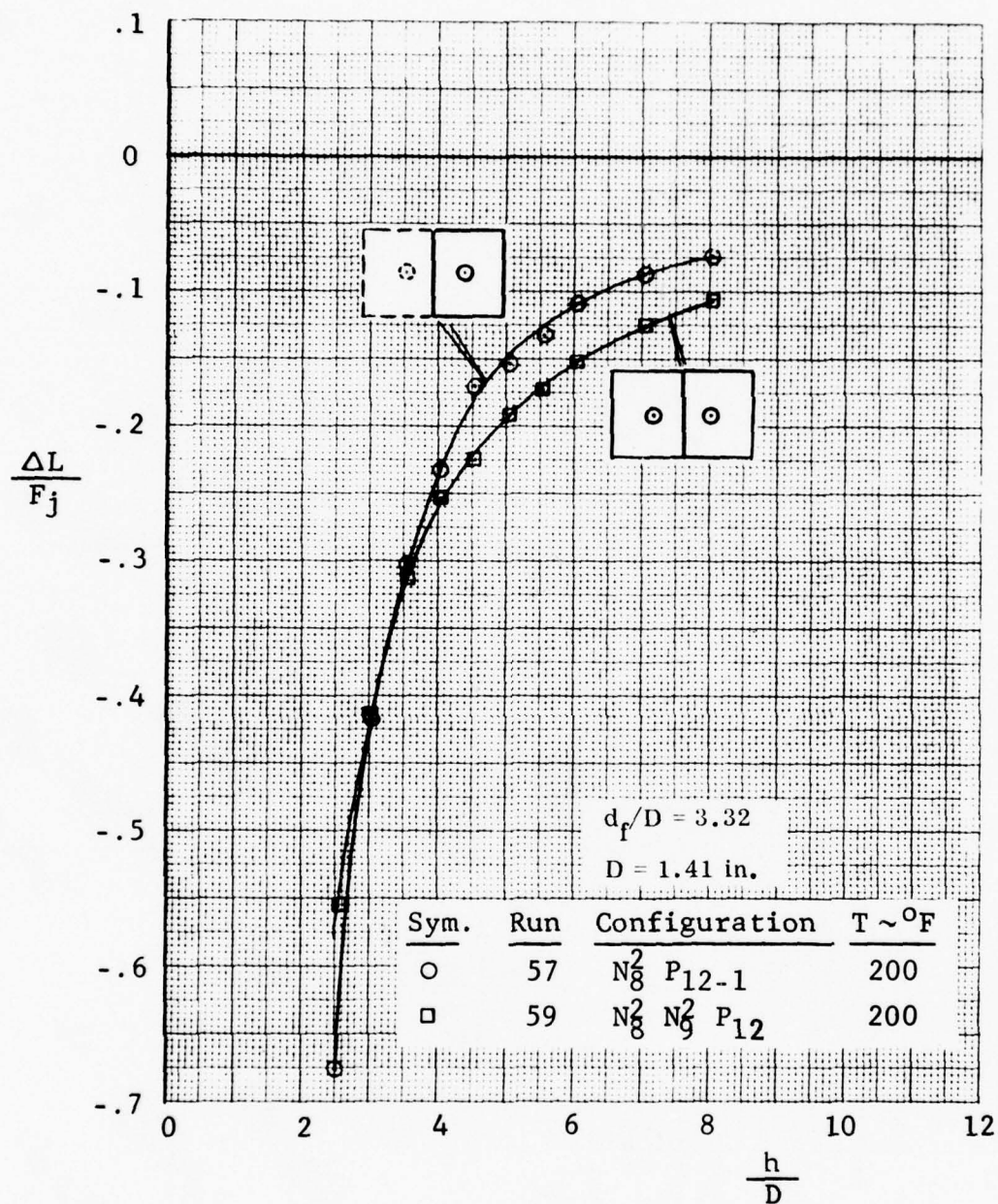


Figure A-3 Fountain Effect on Lift with Two Medium-Spaced Nozzles at 200°F

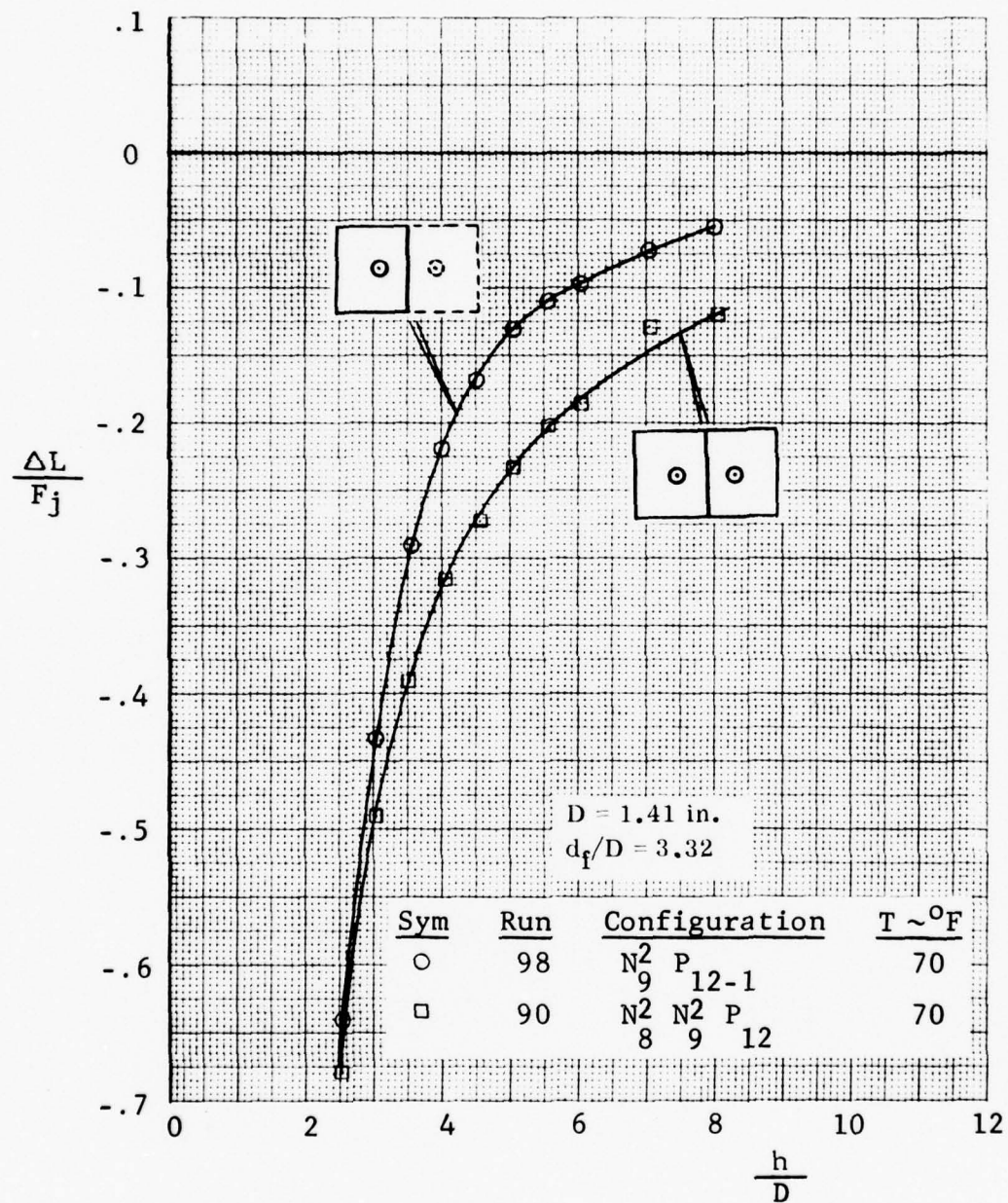


Figure A-4 Fountain Effect on Lift with Two Medium-Spaced Nozzles at 70°F

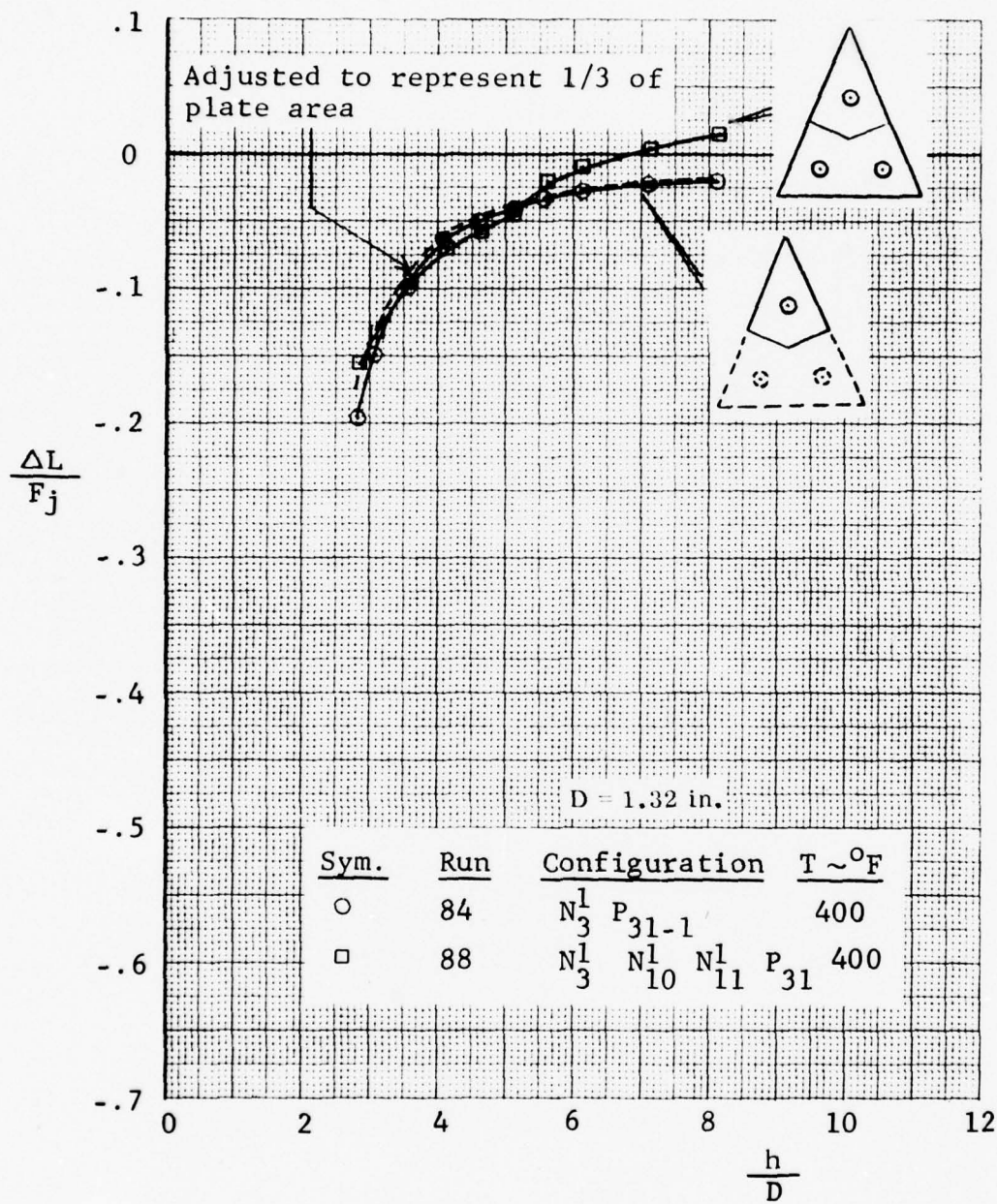


Figure A-5 Fountain Effect on Lift with Three Small Nozzles

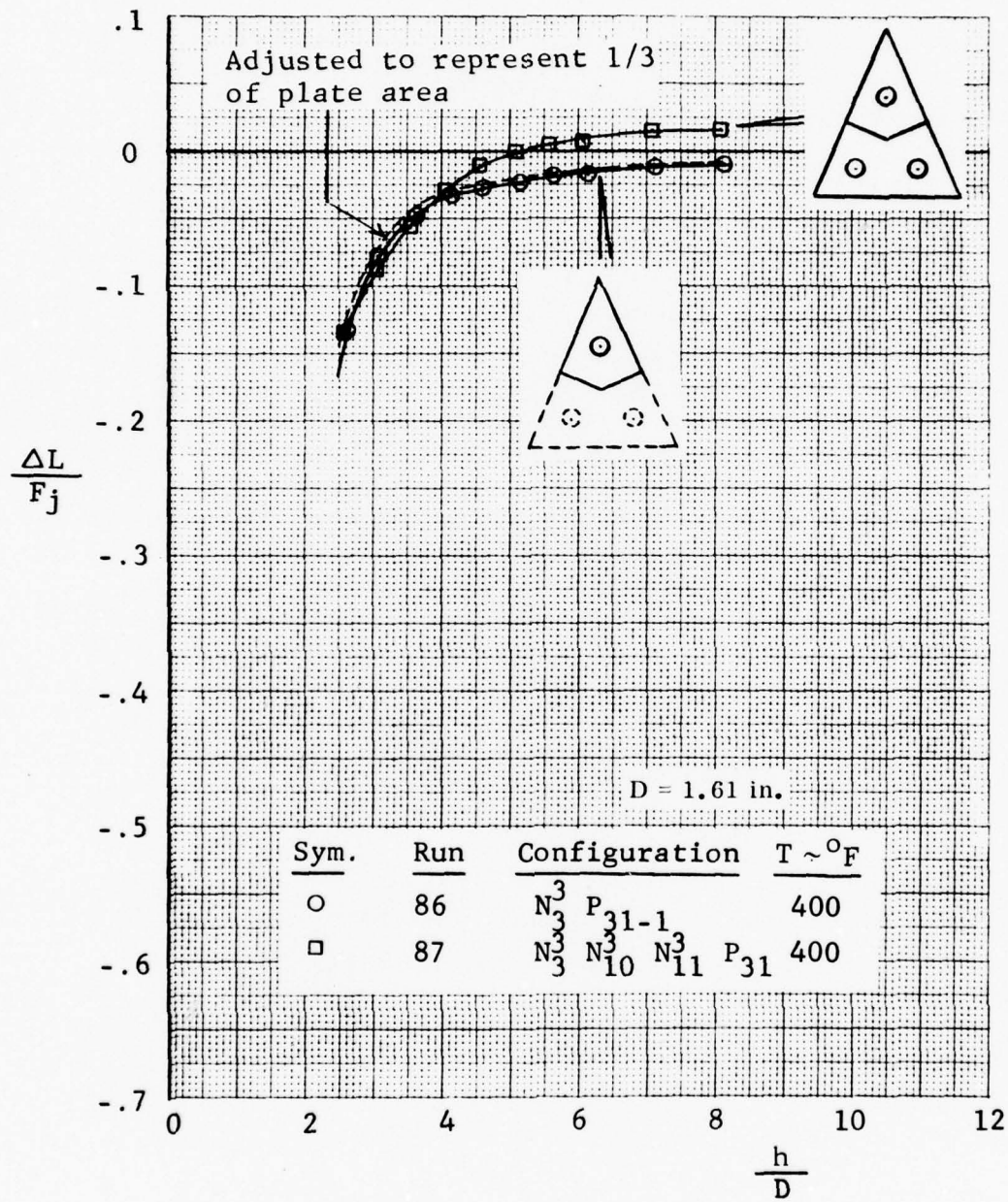


Figure A-6 Fountain Effect on Lift with Three Large Nozzles

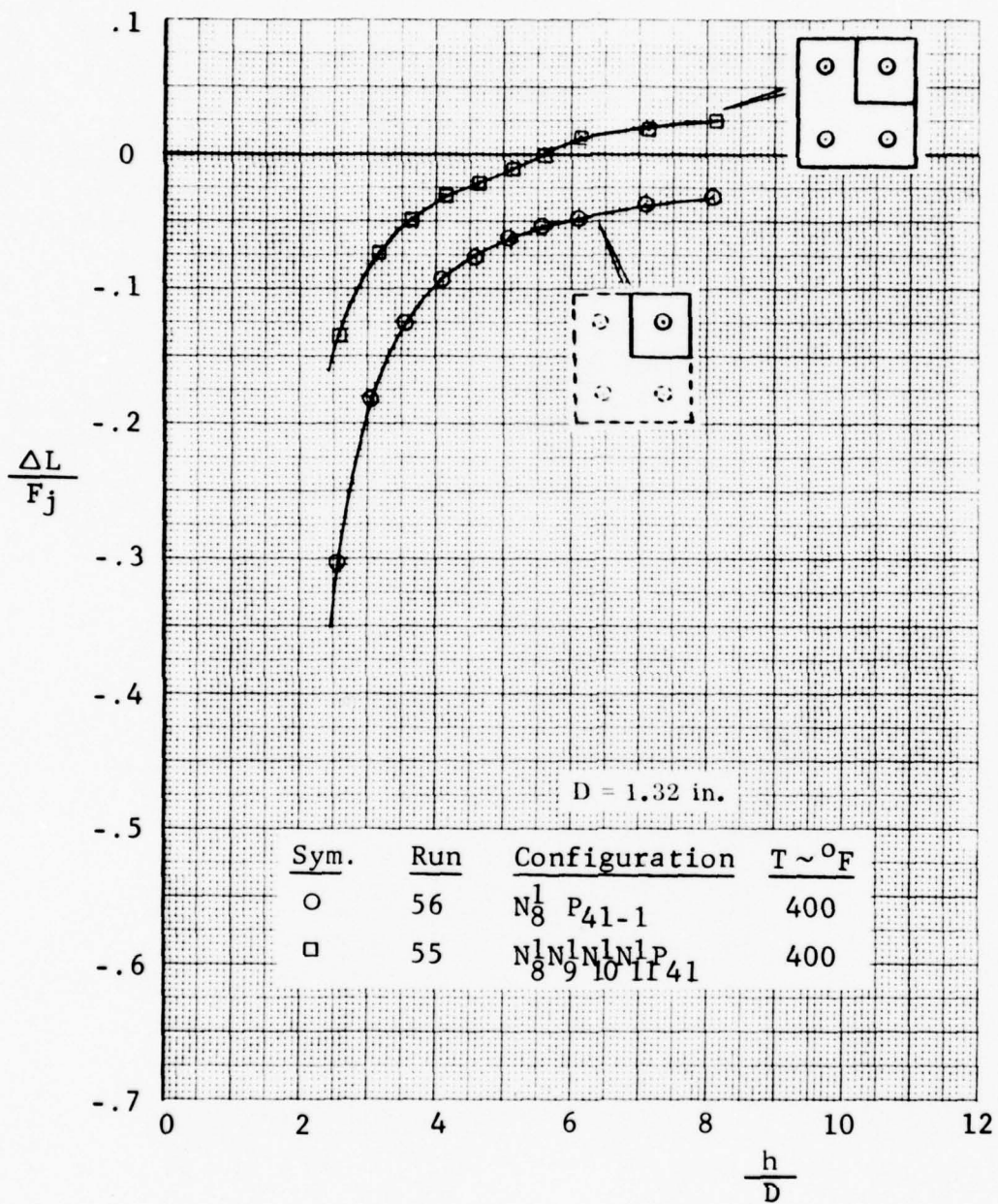


Figure A-7 Fountain Effect on Lift with **Four** Small Nozzles

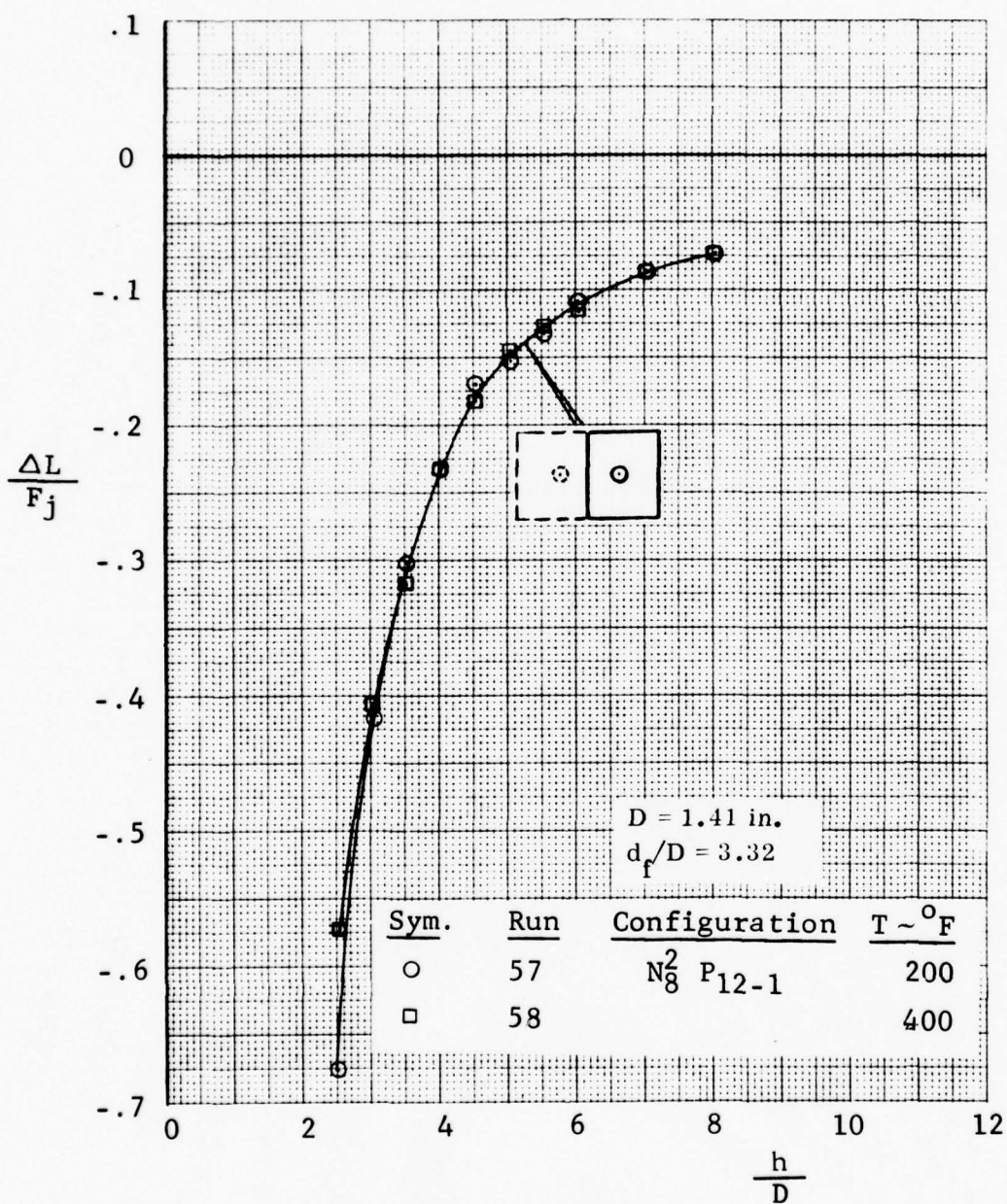


Figure A-8 Temperature Effect on Lift with a Single Nozzle and a Rectangular Plate

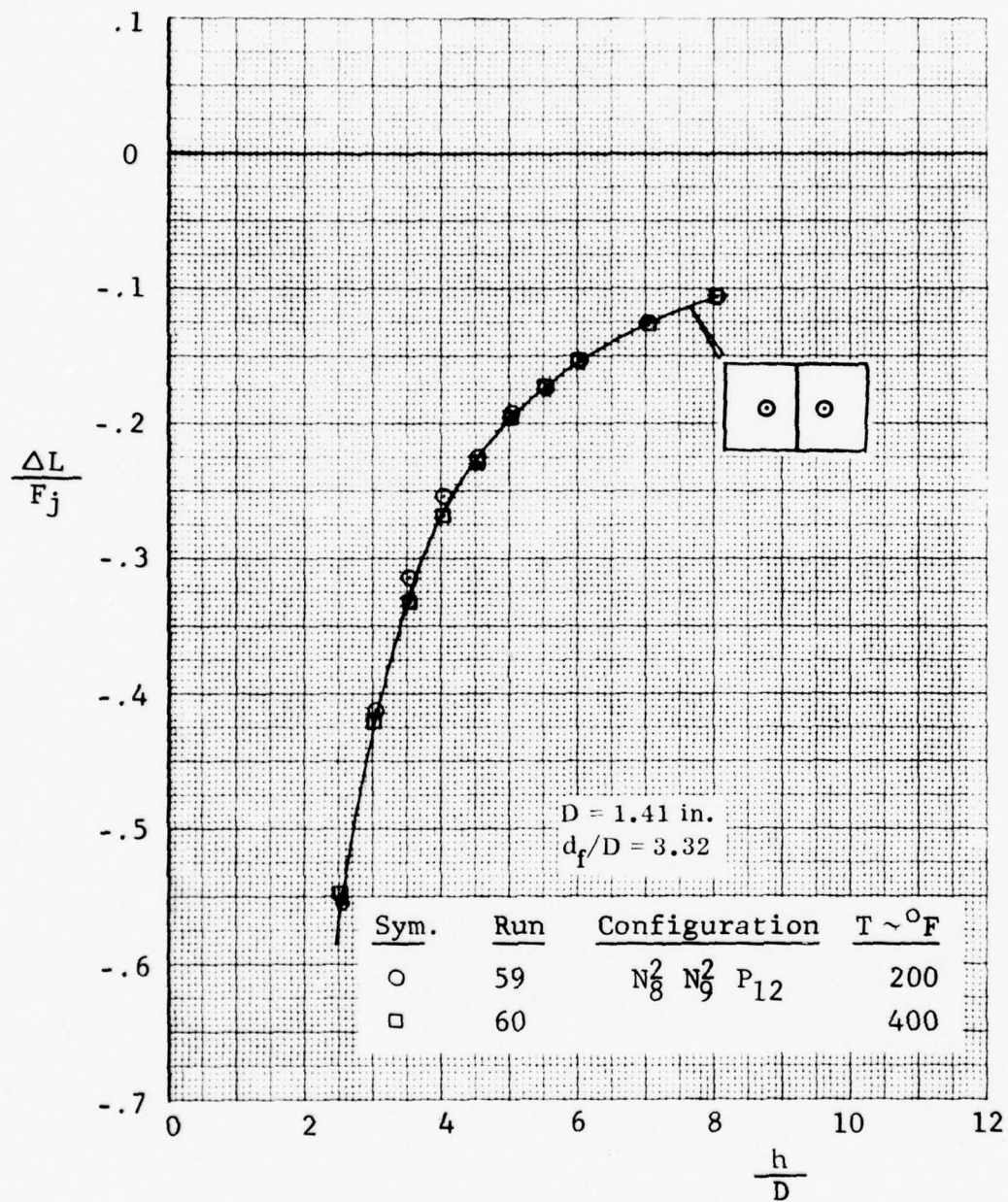


Figure A-9 Temperature Effect on Lift with Two Nozzles and a Rectangular Plate

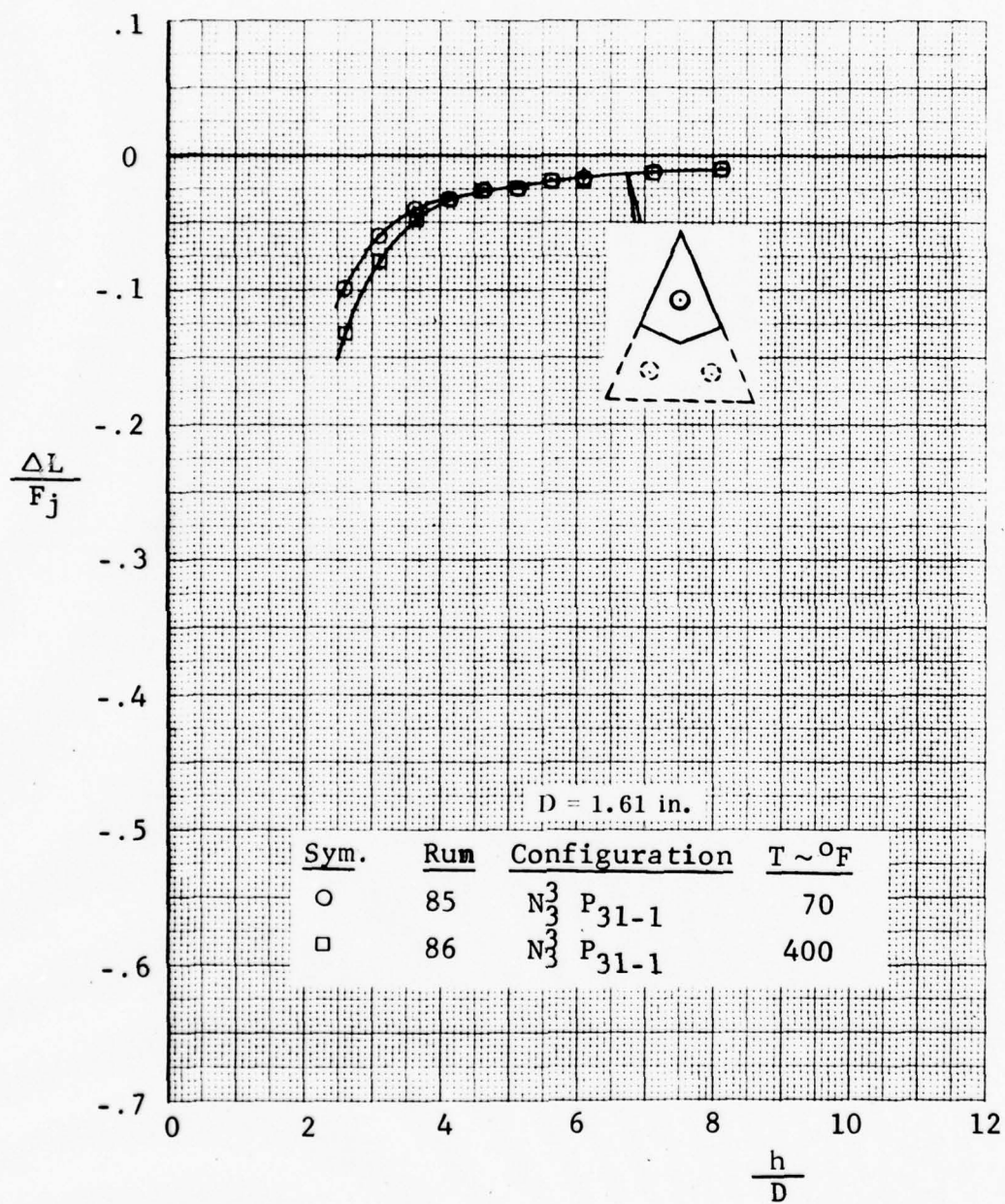


Figure A-10 Temperature Effect on Lift with a Single Nozzle and a Triangular Plate

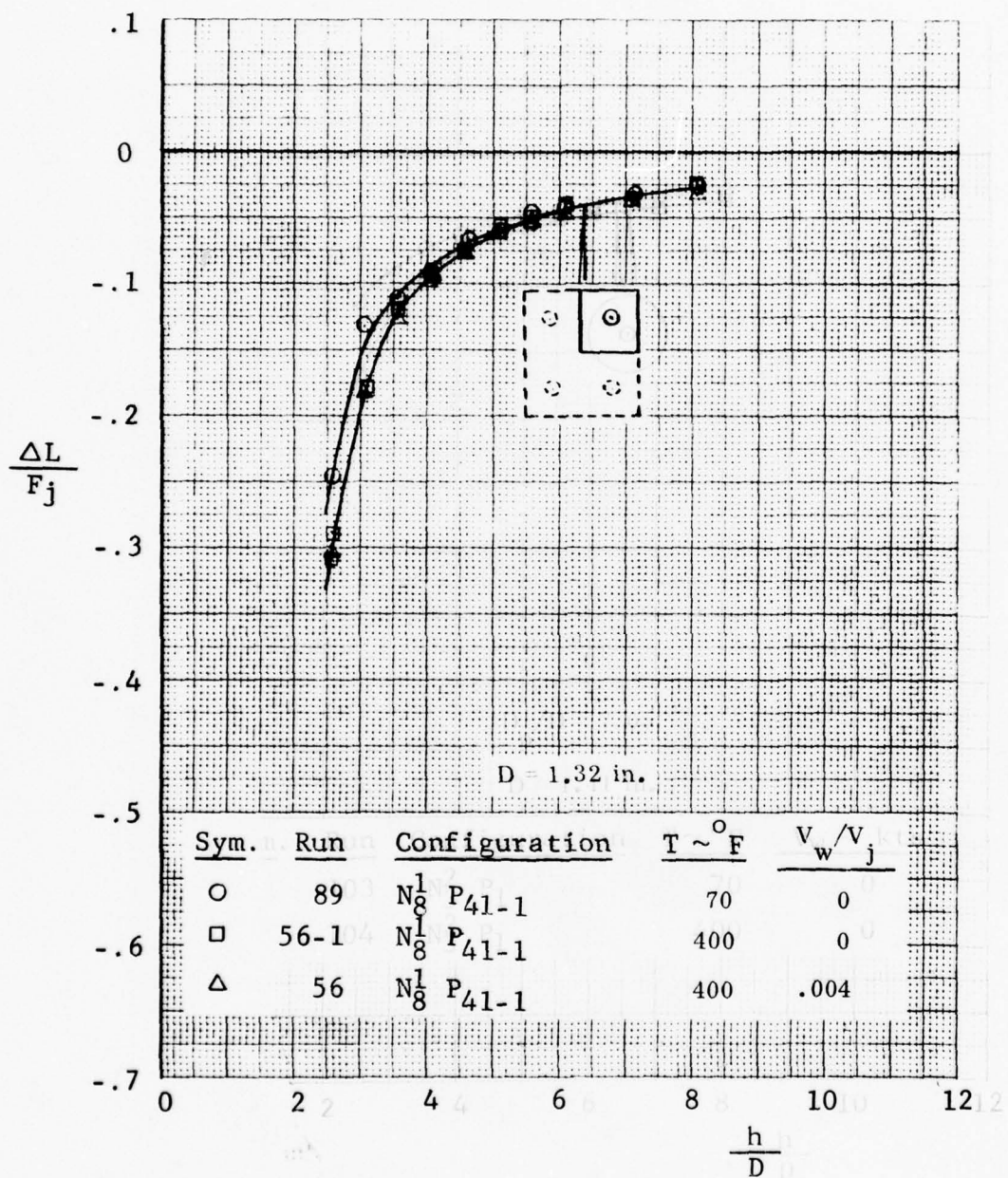


Figure A-11 Temperature Effect on Lift with a Single Nozzle and a Rectangular Plate

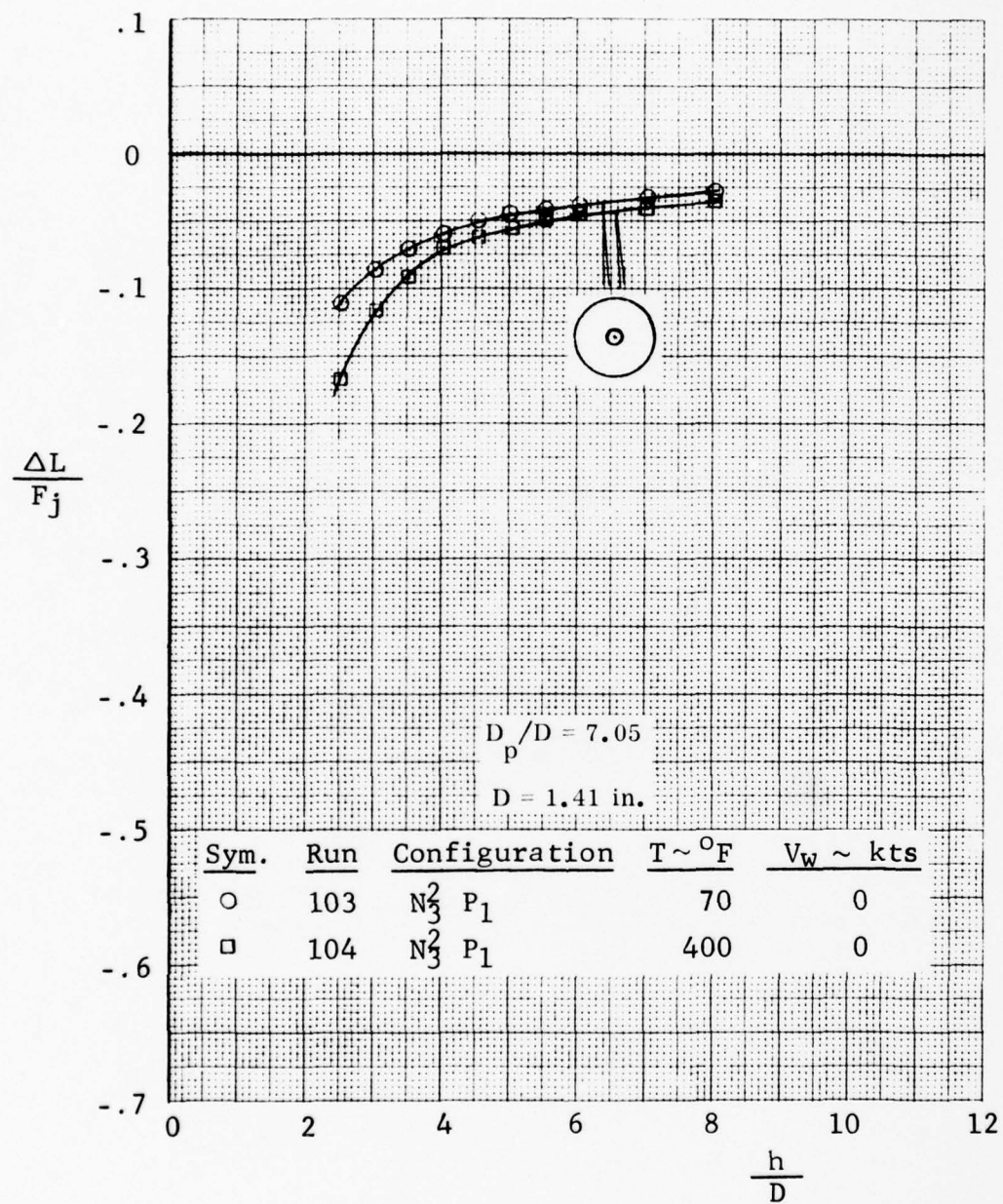


Figure A-12 Temperature Effect on Lift with a Single Nozzle and a Small Circular Plate

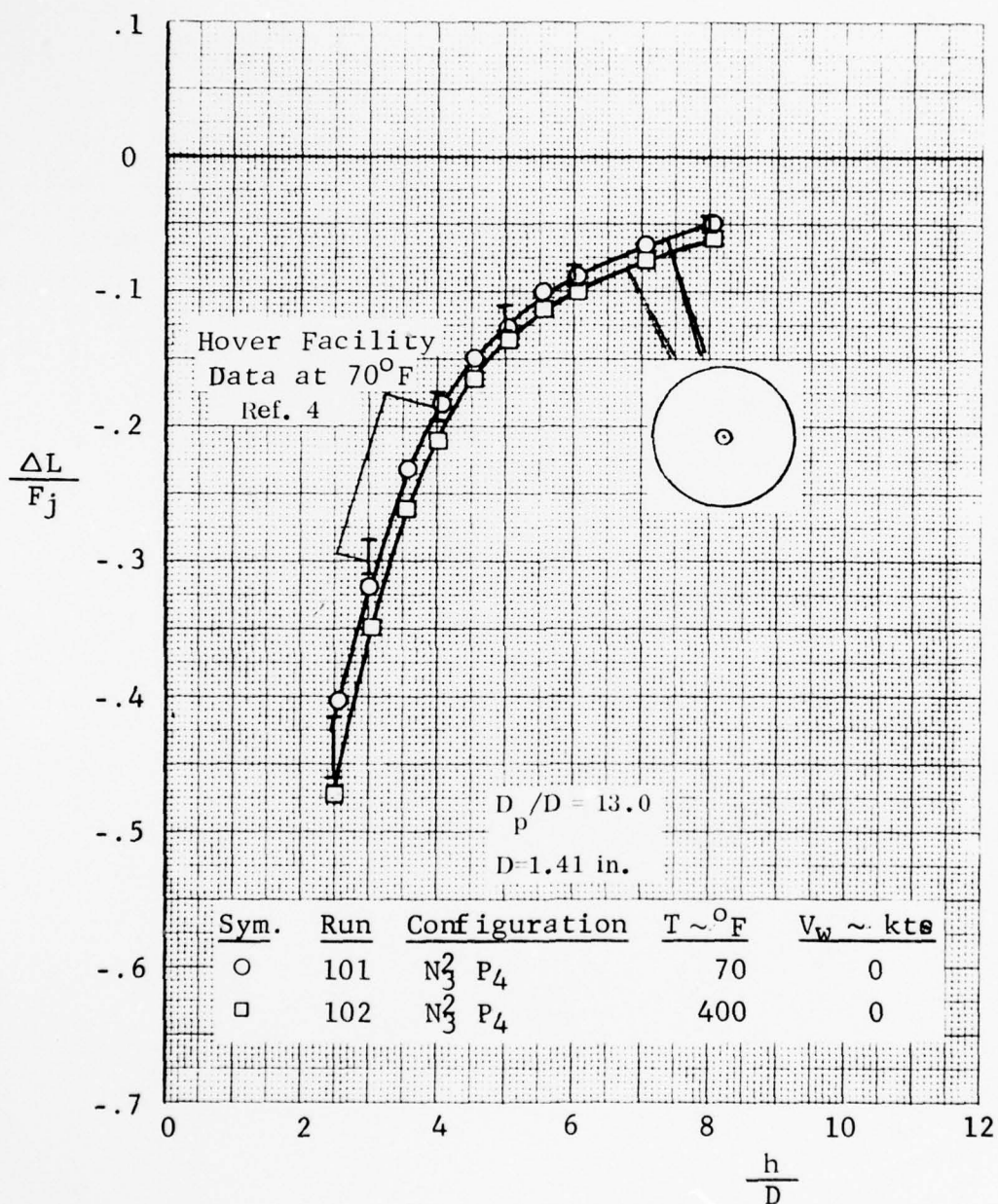


Figure A-13 Temperature Effect on Lift with a Single Nozzle and a Large Circular Plate

APPENDIX B

FOUNTAIN VELOCITY AND MASS FLOW CHARACTERISTICS

The methods employed to integrate the fountain dynamic pressure and mass flow data to obtain the fountain core force and mass entrainment characteristics are discussed in Section 3. The data were edited and faired prior to integration by using an interactive graphics procedure at the Fort Worth Division. The faired data are included in this appendix for each configuration for which rake surveys indicated the presence of a fountain. These data are presented in the form of dynamic pressure and mass flow profiles across the fountain (X-direction) at various locations along the fountain (Y-direction) for each model height, h/D , and rake height, Z/D . (See Figure 22 for axes system definition.)

Figures B-1 through B-40 contain the basic data for the two, three and four nozzle configurations with 400°F jets. Data for 200°F jets with the intermediate two nozzle spacing are presented in Figures B-41 through B-43. Data for the same configuration with 10 degrees pitch angle, and with zero pitch and a 30 knot wind, are shown in Figures B-44 through B-47.

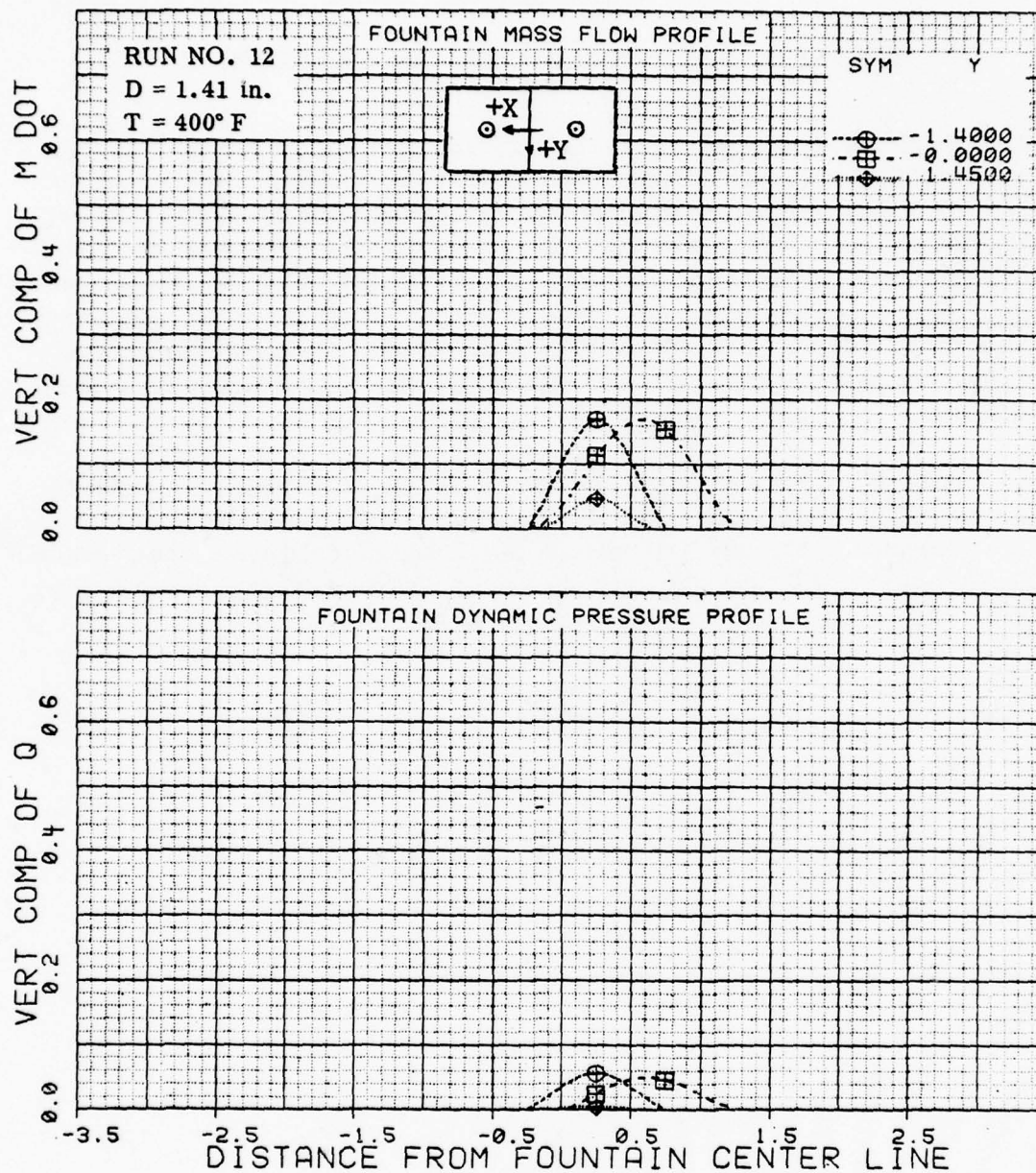


Figure B-1 Mass Flow and Dynamic Pressure Profiles with Two Nozzles; $d_f/D=6.38$, $h/D=2.52$, $Z/D=1.36$

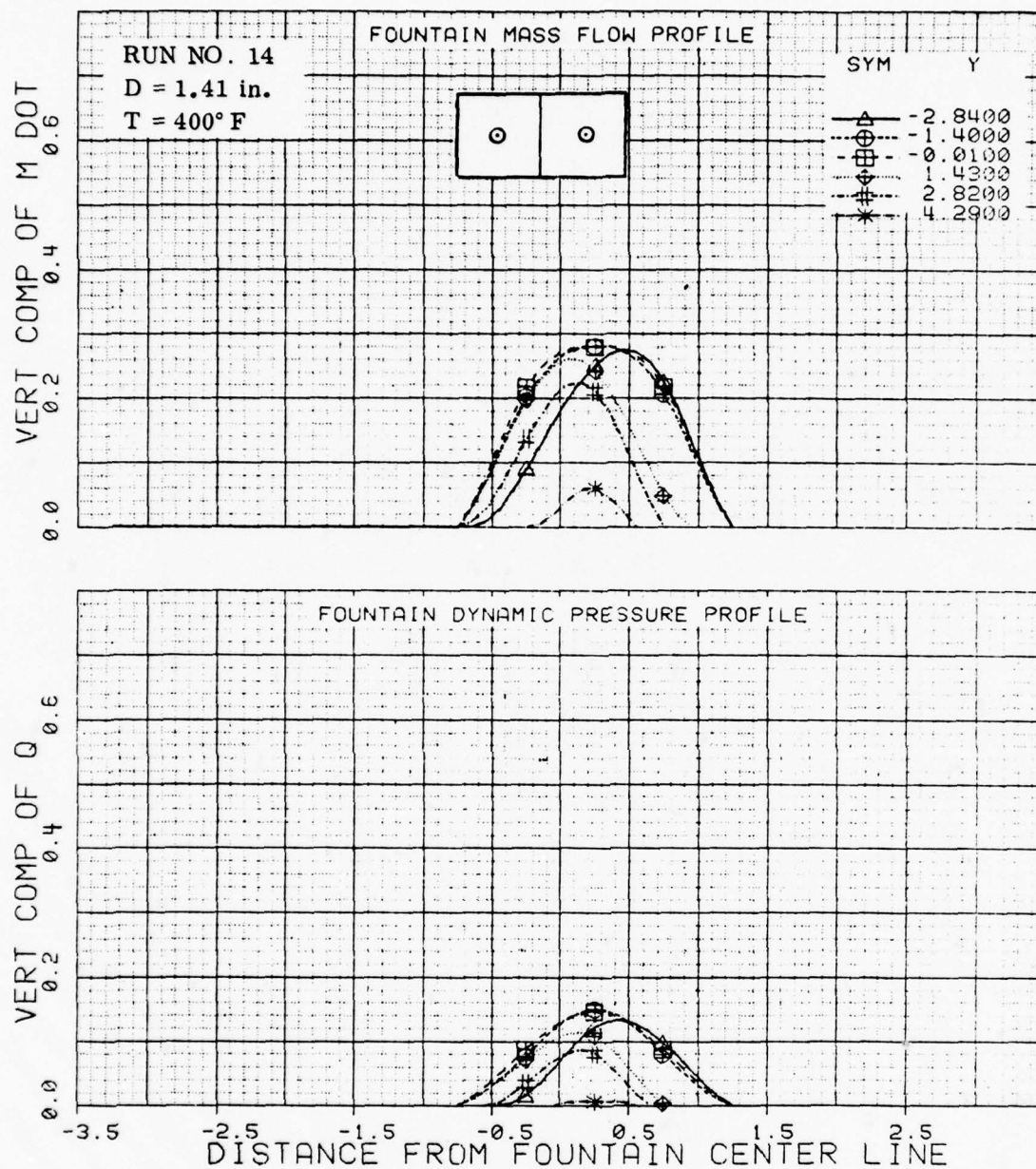


Figure B-2 Mass Flow and Dynamic Pressure Profiles with Two Nozzles; $d_f/D=6.38$, $h/D=3.53$, $Z/D=1.55$

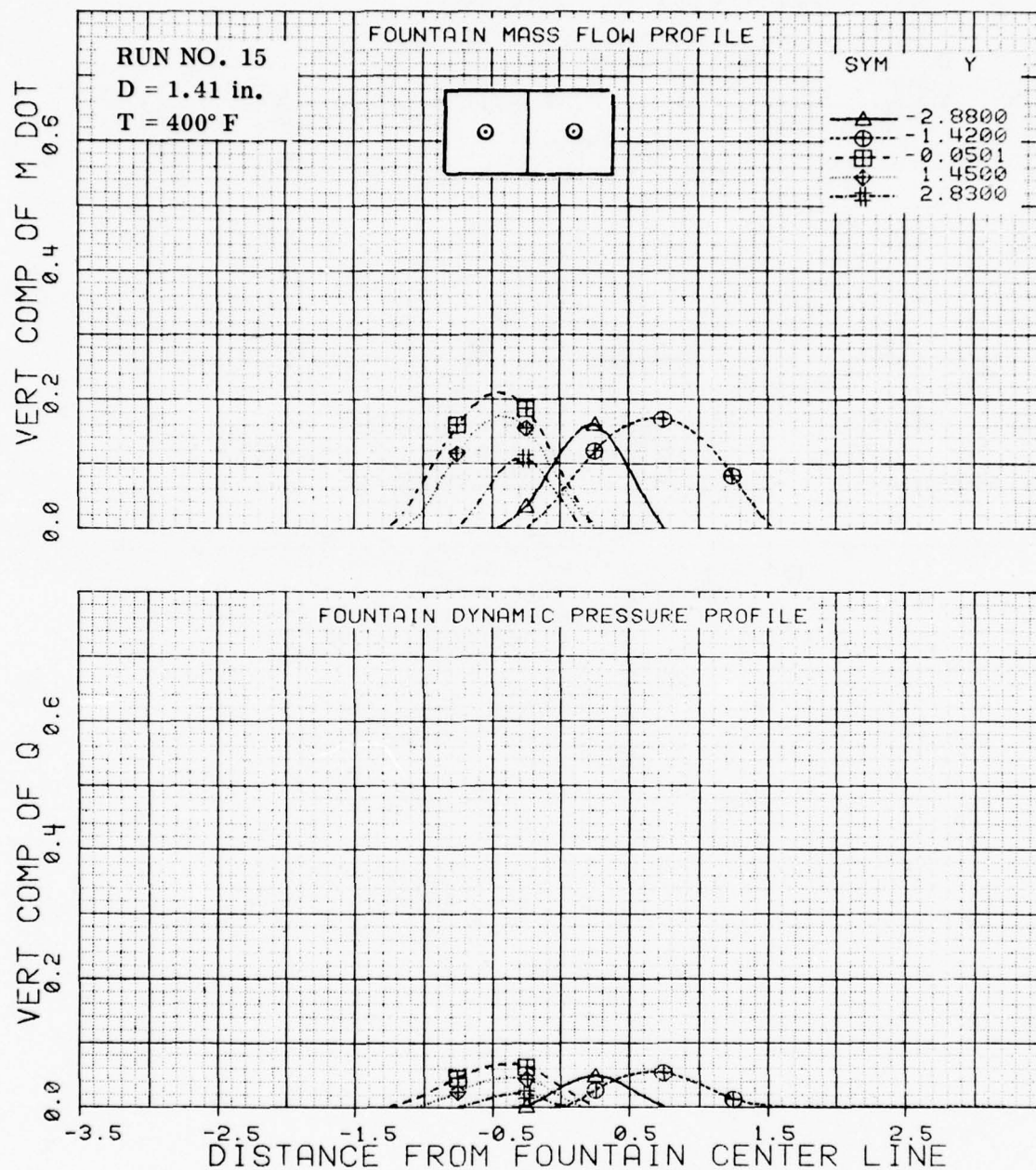


Figure B-3 Mass Flow and Dynamic Pressure Profiles with Two Nozzles; $d_f/D=6.38$, $h/D=3.53$, $Z/D=2.35$

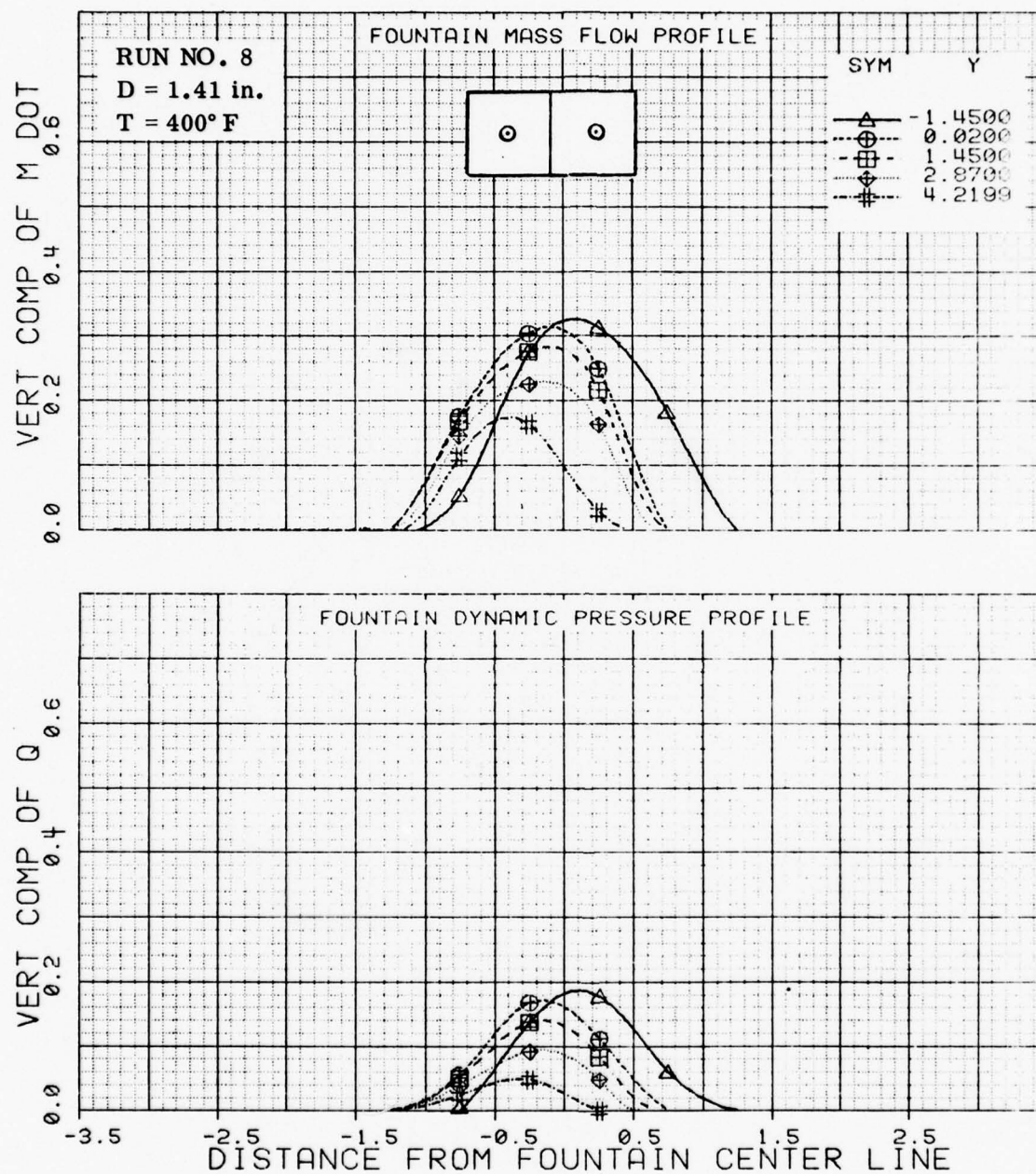


Figure B-4 Mass Flow and Dynamic Pressure Profiles with Two Nozzles; $d_f/D=6.38$, $h/D=5.03$, $Z/D=1.48$

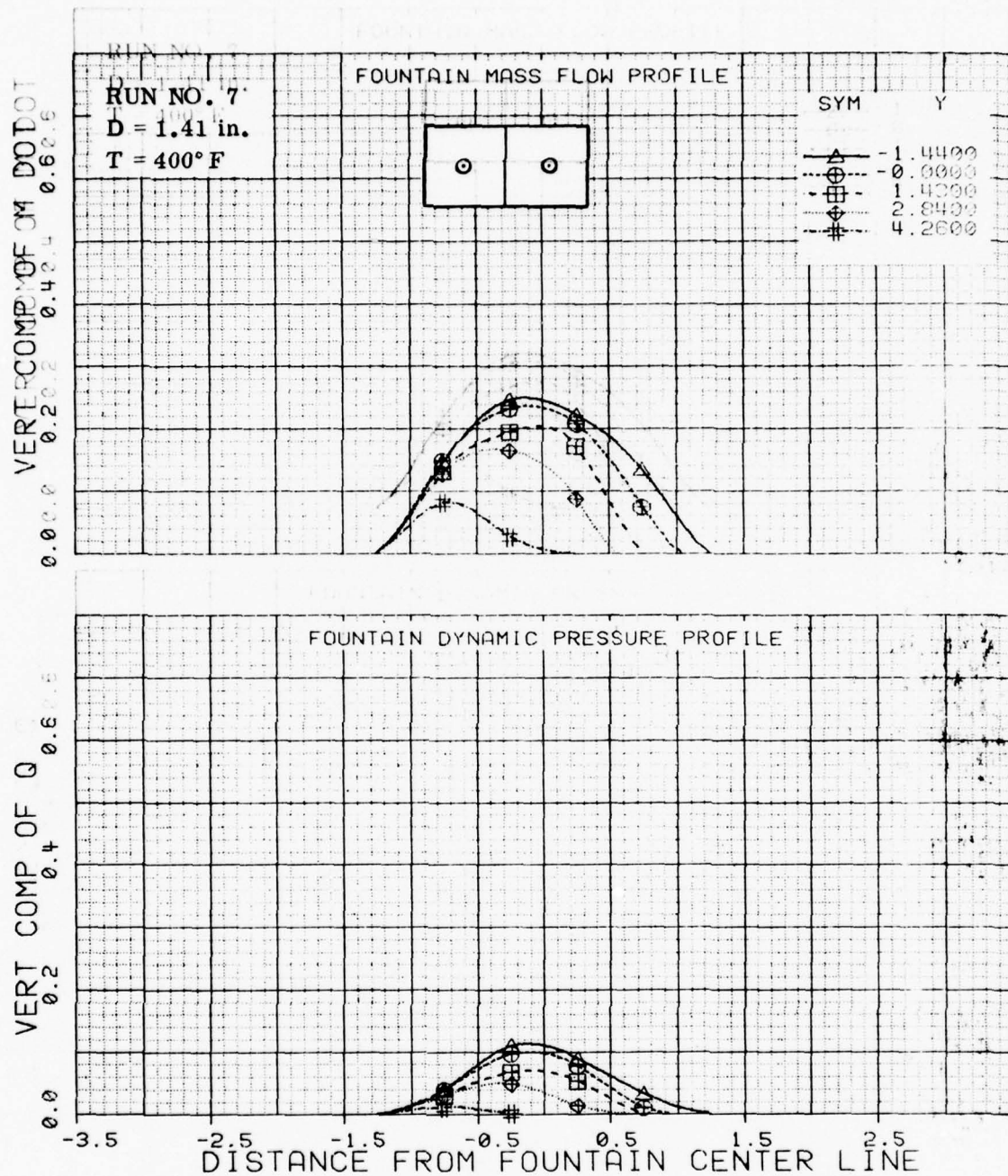


Figure B-5 Mass Flow and Dynamic Pressure Profiles with Two Nozzles; $d_f/D=6.38$, $h/D=5.04$, $Z/D=2.48$

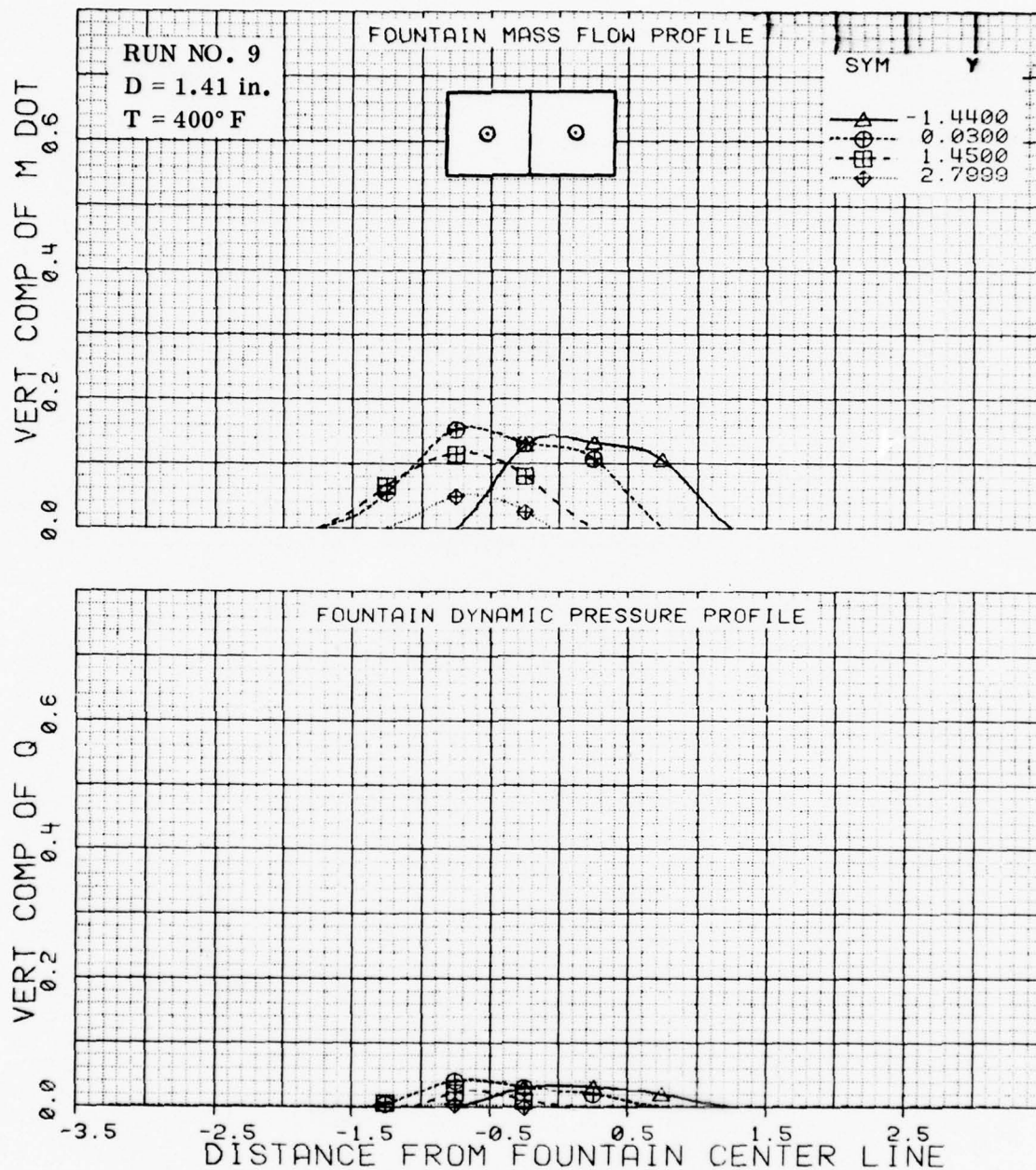


Figure B-6 Mass Flow and Dynamic Pressure Profiles with
Two Nozzles; $d_f/D=6.38$, $h/D=5.04$, $Z/D=3.80$

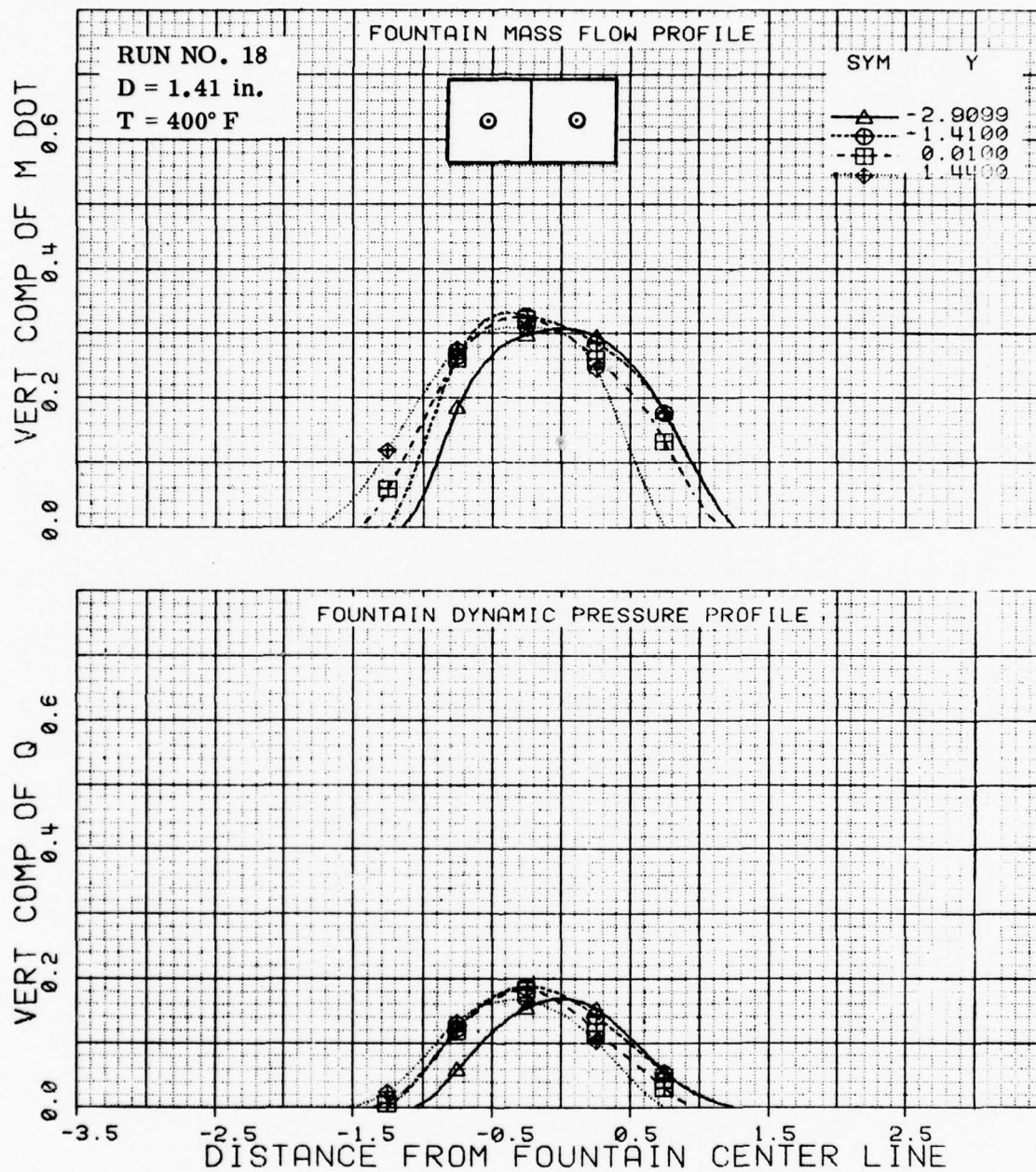


Figure B-7 Mass Flow and Dynamic Pressure Profiles with
 Two Nozzles; $d_f/D=6.38$, $h/D=8.03$, $Z/D=1.55$

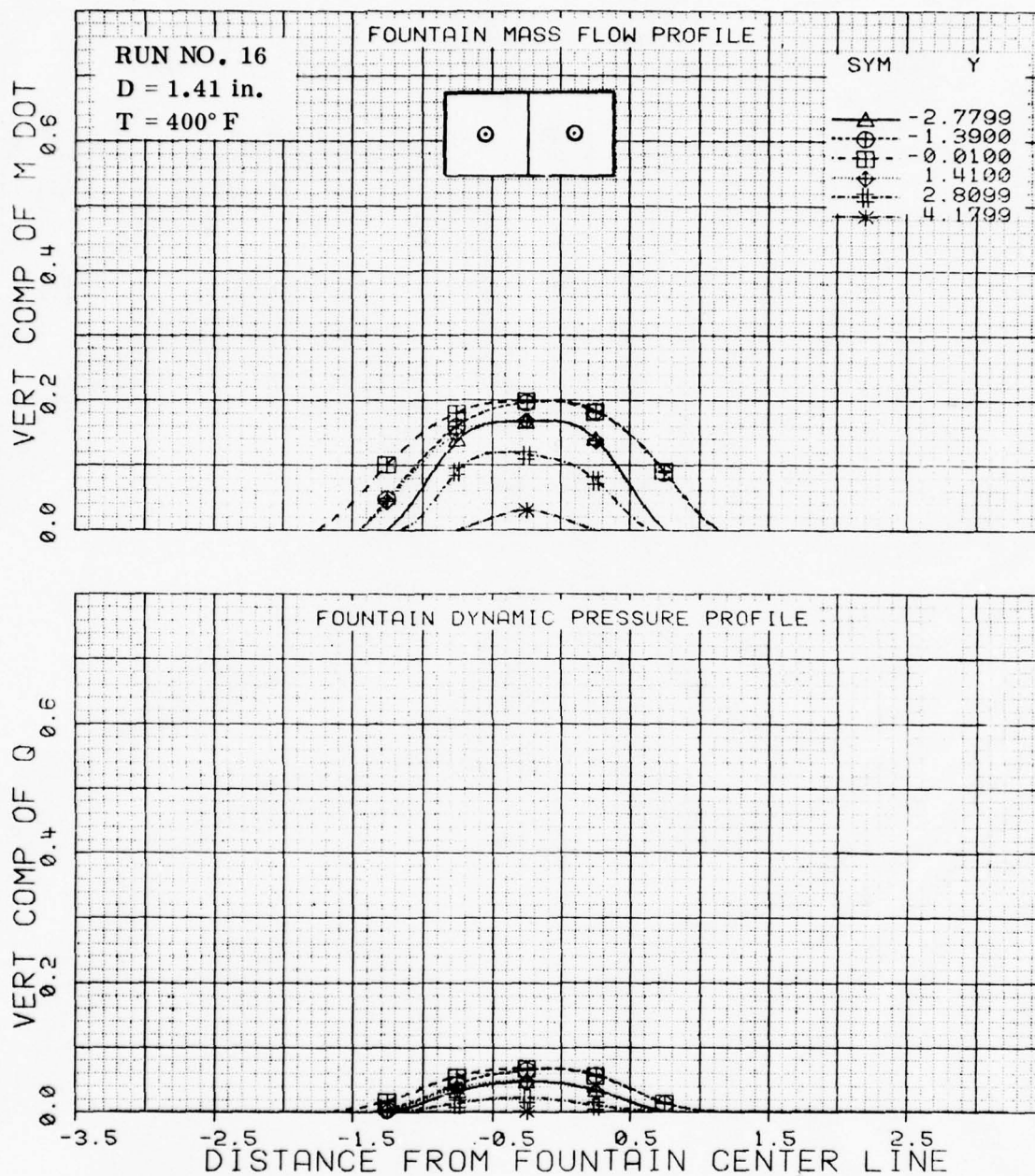


Figure B-8 Mass Flow and Dynamic Pressure Profiles with Two Nozzles; $d_f/D=6.38$, $h/D=8.03$, $Z/D=3.52$

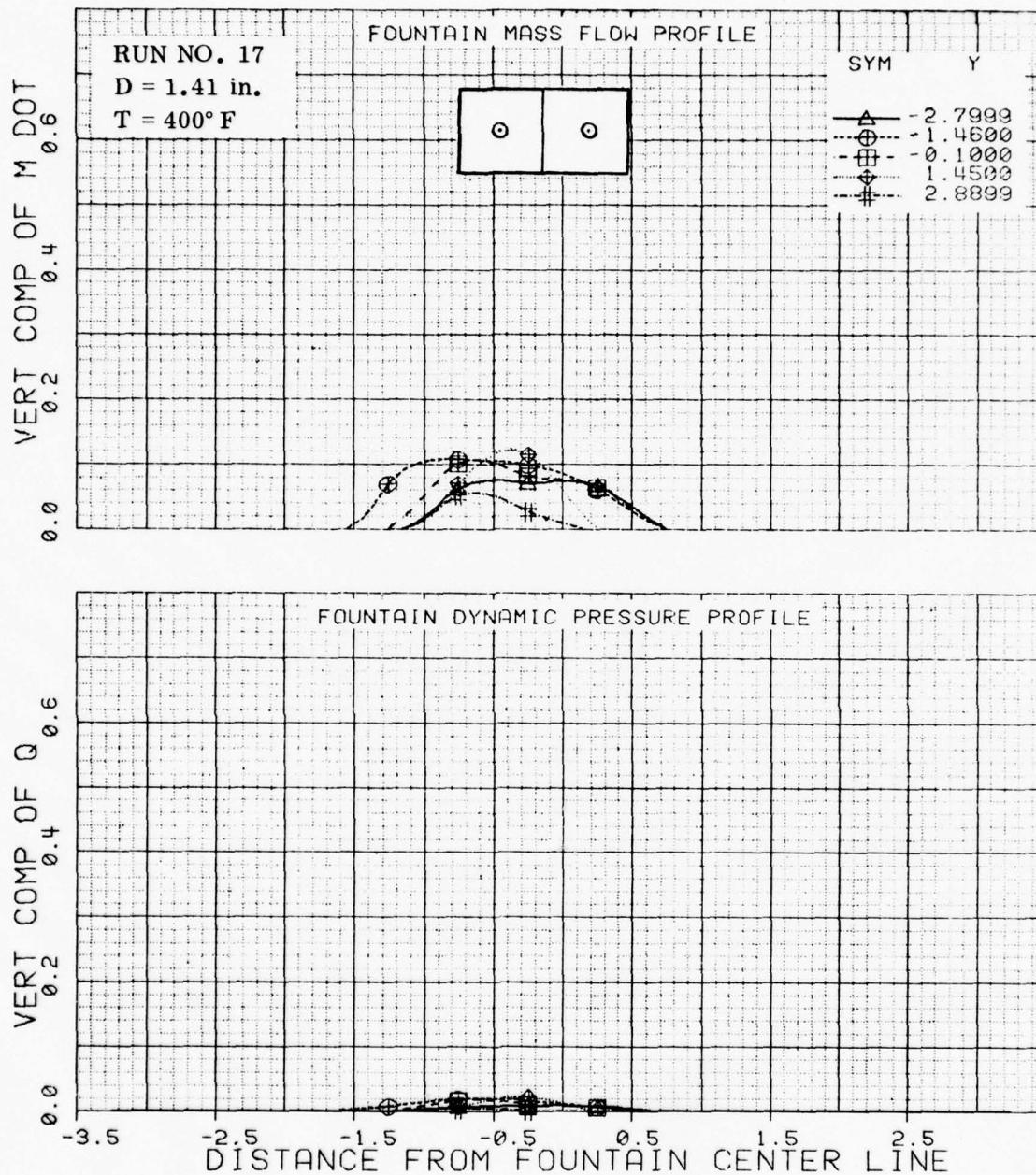


Figure B-9 Mass Flow and Dynamic Pressure Profiles with
Two Nozzles; $d_f/D=6.38$, $h/D=8.03$, $Z/D=5.55$

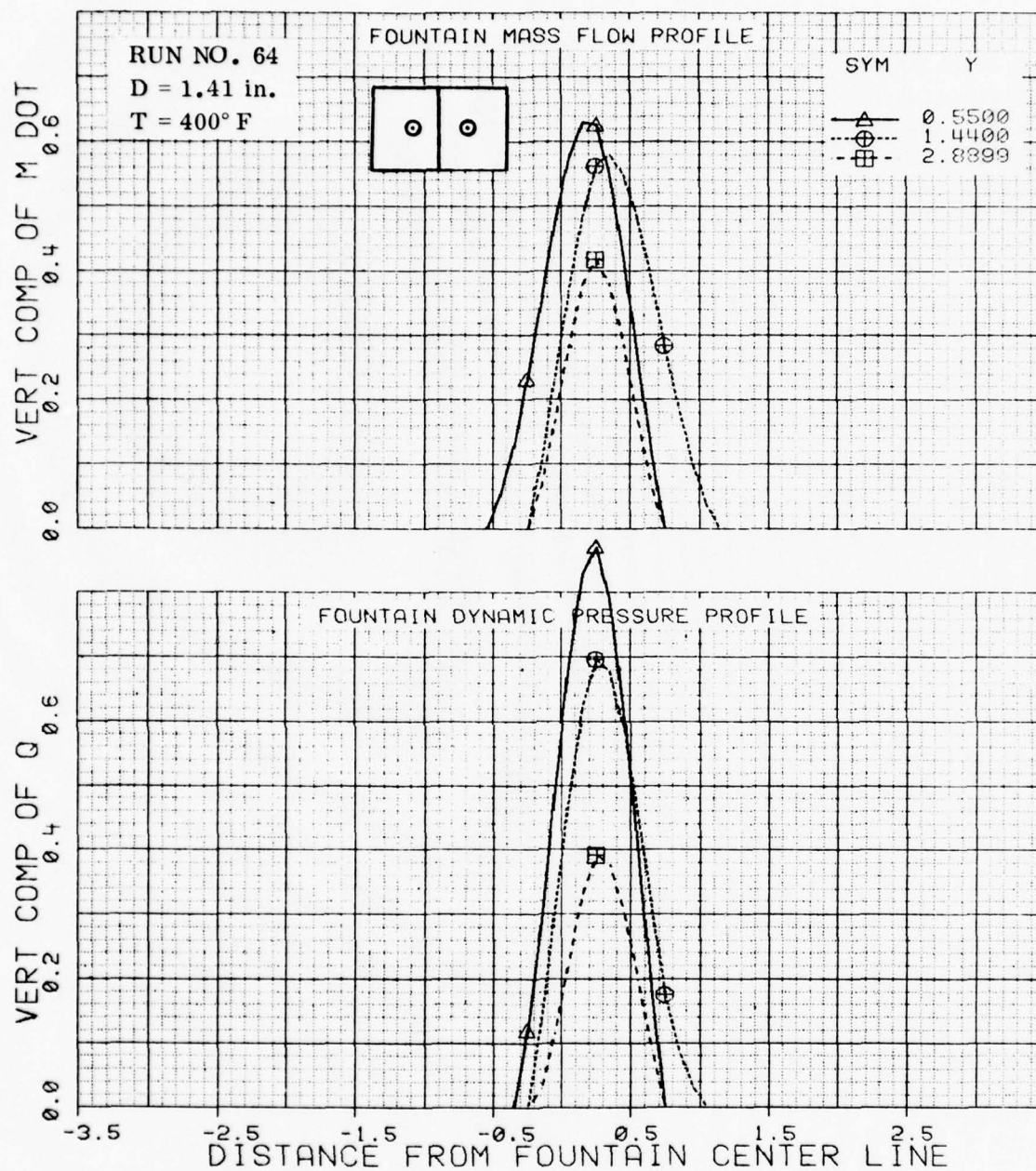


Figure B-10 Mass Flow and Dynamic Pressure Profiles with Two Nozzles; $d_f/D=3.32$, $h/D=2.52$, $Z/D=0.79$

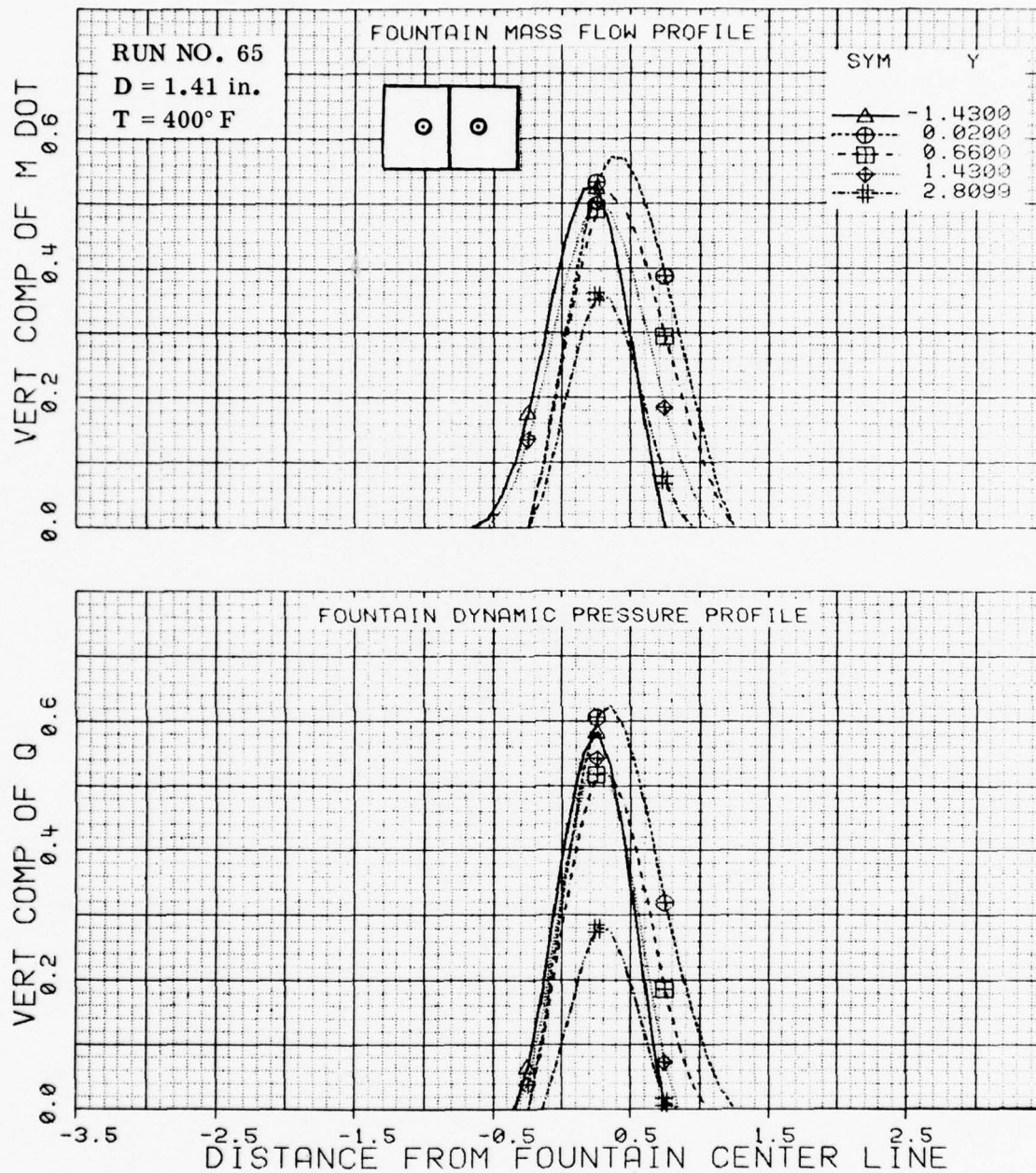


Figure B-11 Mass Flow and Dynamic Pressure Profiles with Two Nozzles; $d_f/D=3.32$, $h/D=2.52$, $Z/D=1.35$

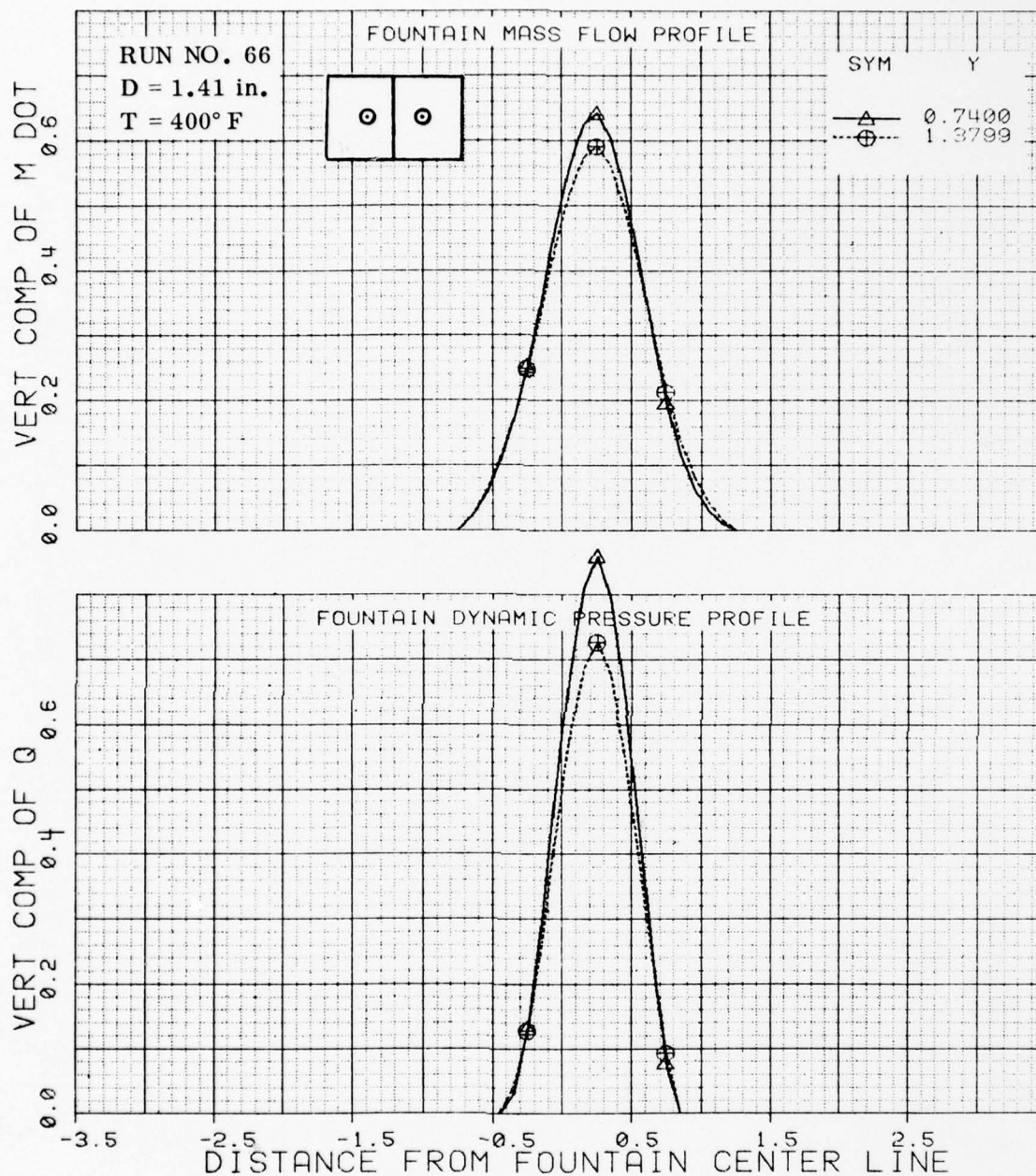


Figure B-12 Mass Flow and Dynamic Pressure Profiles with Two Nozzles; $d_f/D=3.32$, $h/D=3.56$, $z/D=0.77$

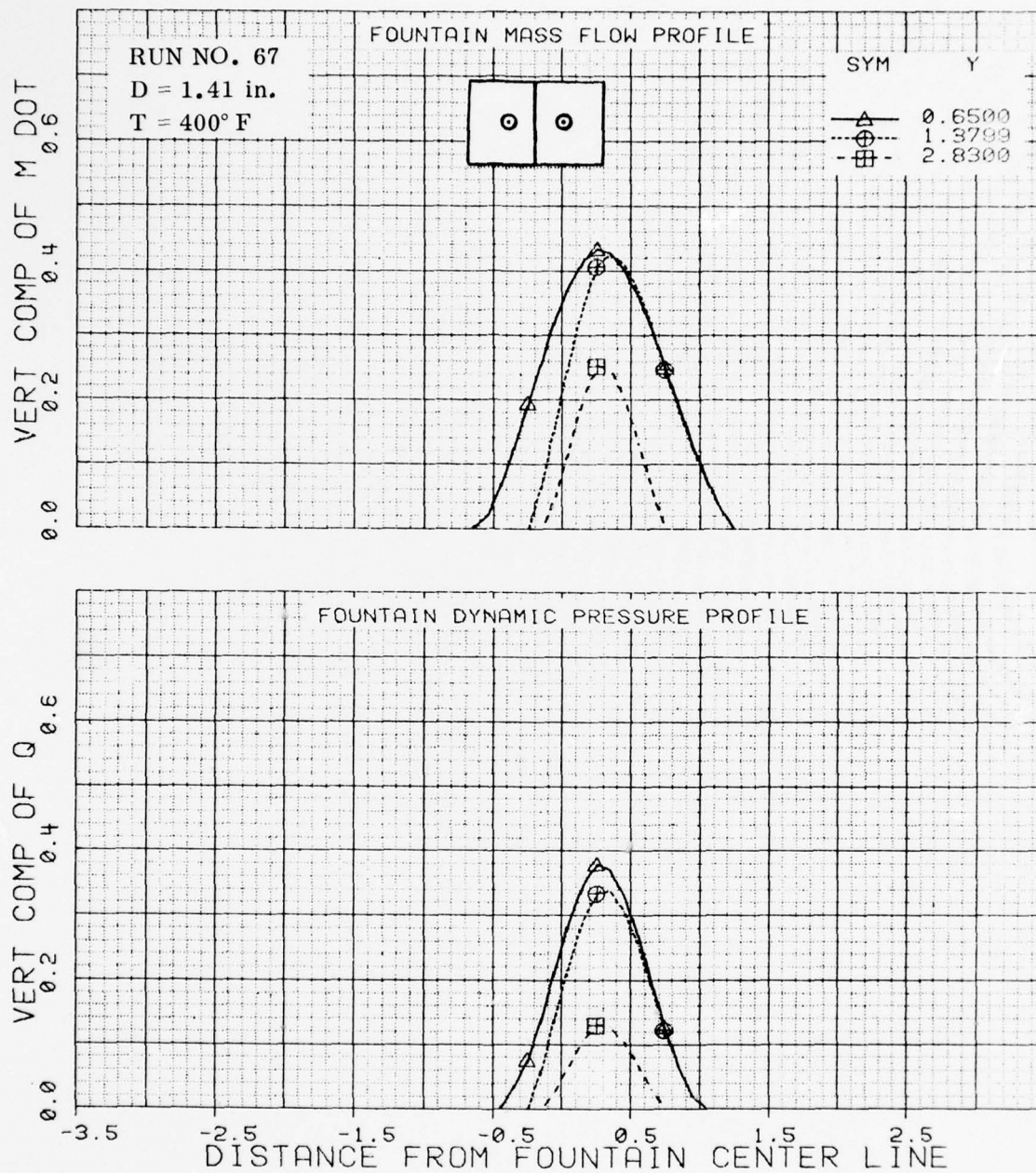


Figure B-13 Mass Flow and Dynamic Pressure Profiles with Two Nozzles; $d_f/D=3.32$, $h/D=3.56$, $Z/D=1.50$

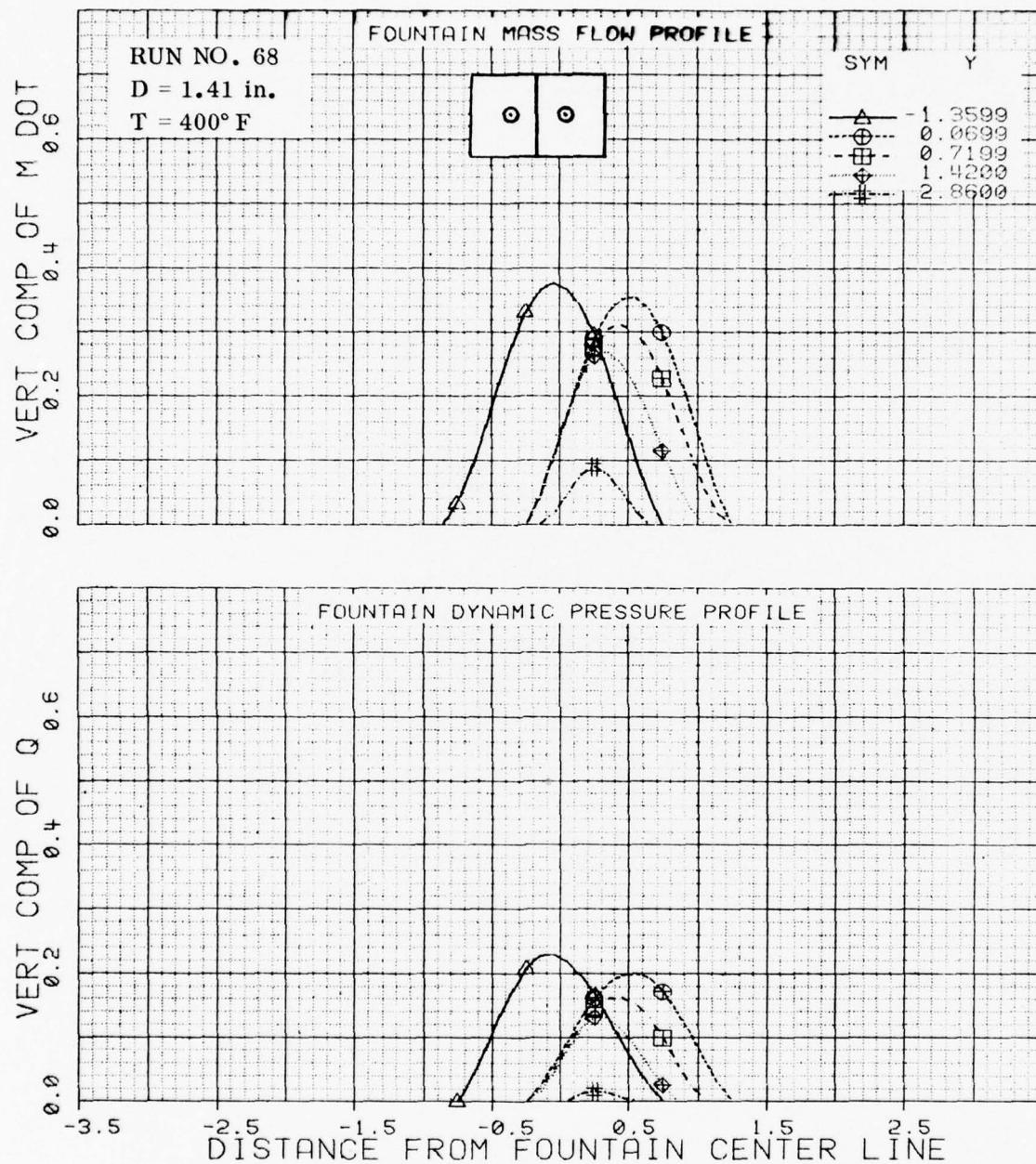


Figure B-14 Mass Flow and Dynamic Pressure Profiles with Two Nozzles; $d_f/D=3.32$ $h/D=3.55$, $Z/D=2.29$

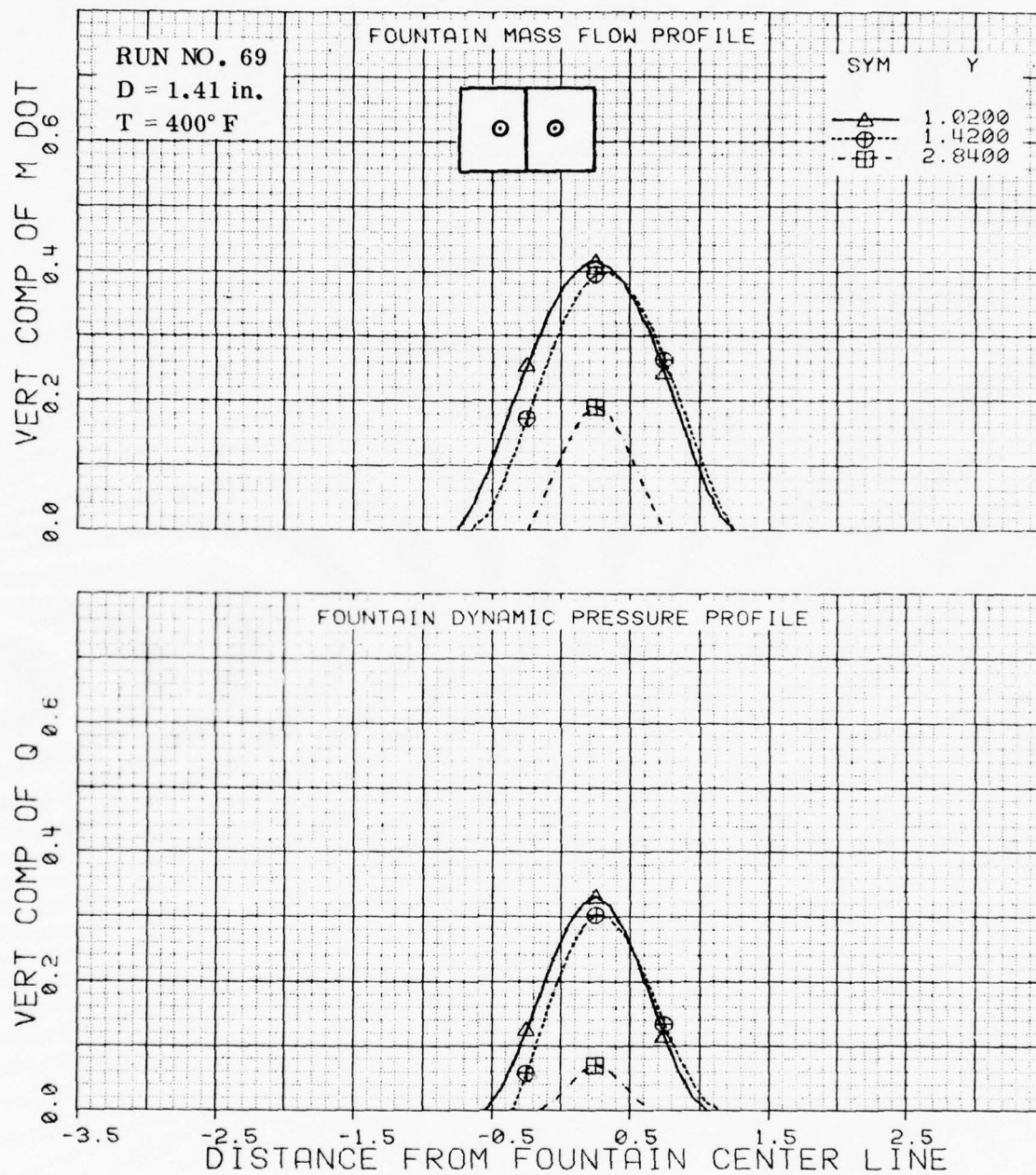


Figure B-15 Mass Flow and Dynamic Pressure Profiles with
Two Nozzles; $d_f/D=3.32$ $h/D=3.05$, $Z/D=1.51$

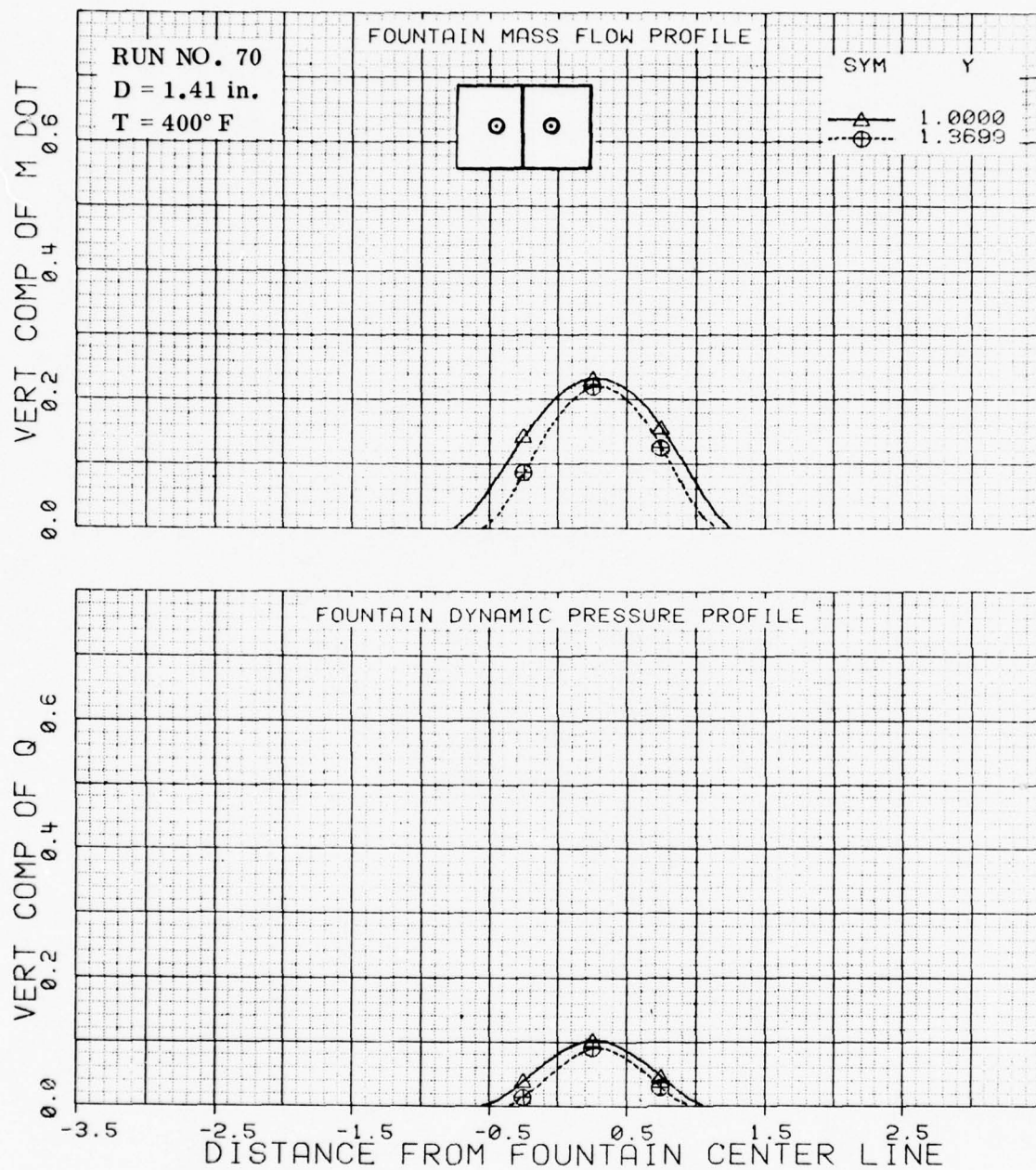


Figure B-16 Mass Flow and Dynamic Pressure Profiles with Two Nozzles; $d_f/D=3.32$, $h/D=5.05$, $Z/D=2.48$

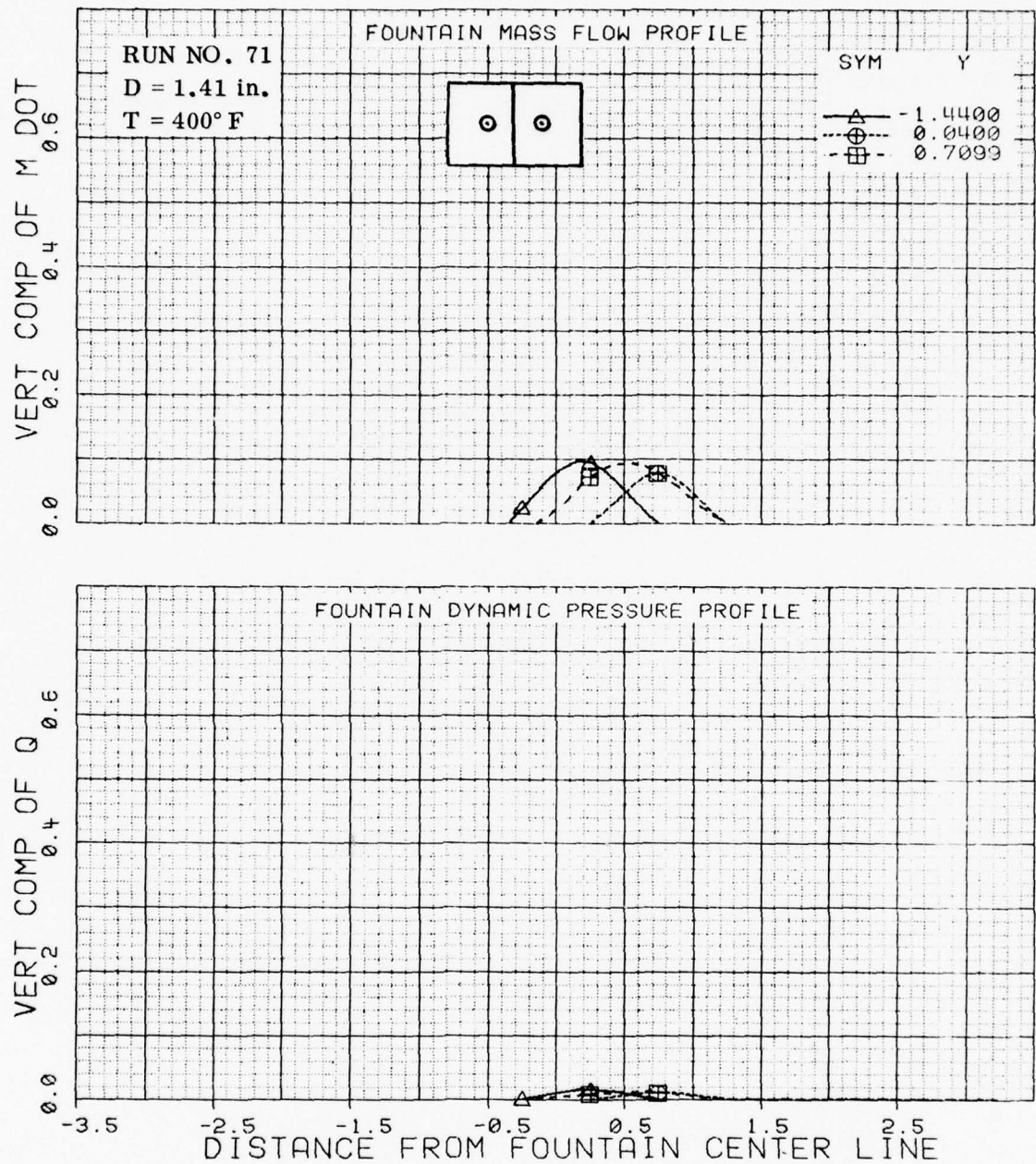


Figure B-17 Mass Flow and Dynamic Pressure Profiles with Two Nozzles; $d_f/D=3.32$ $h/D=5.05$, $Z/D=3.75$

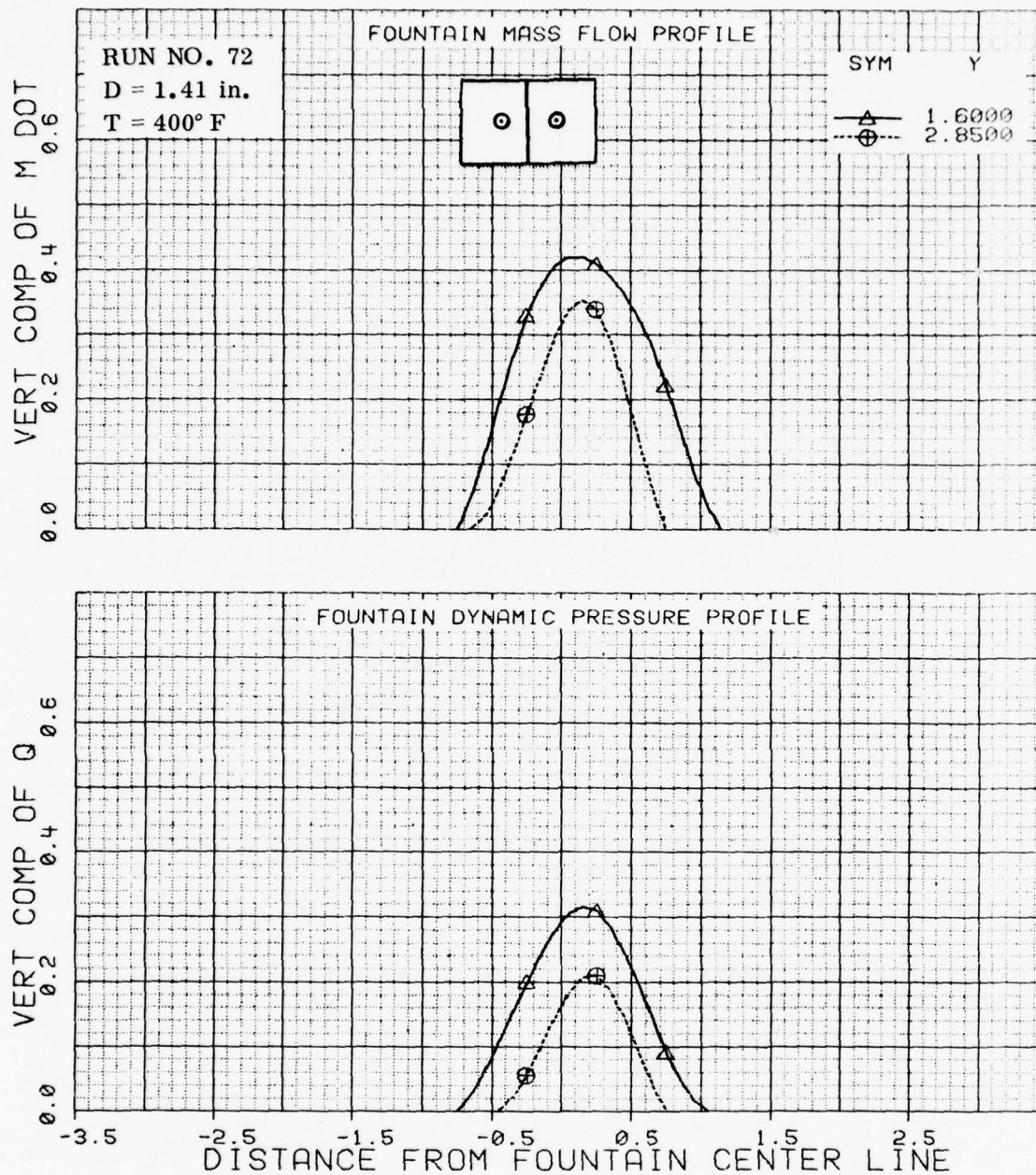


Figure B-18 Mass Flow and Dynamic Pressure Profiles with Two Nozzles; $d_f/D=3.32$ $h/D=8.04$, $Z/D=1.55$

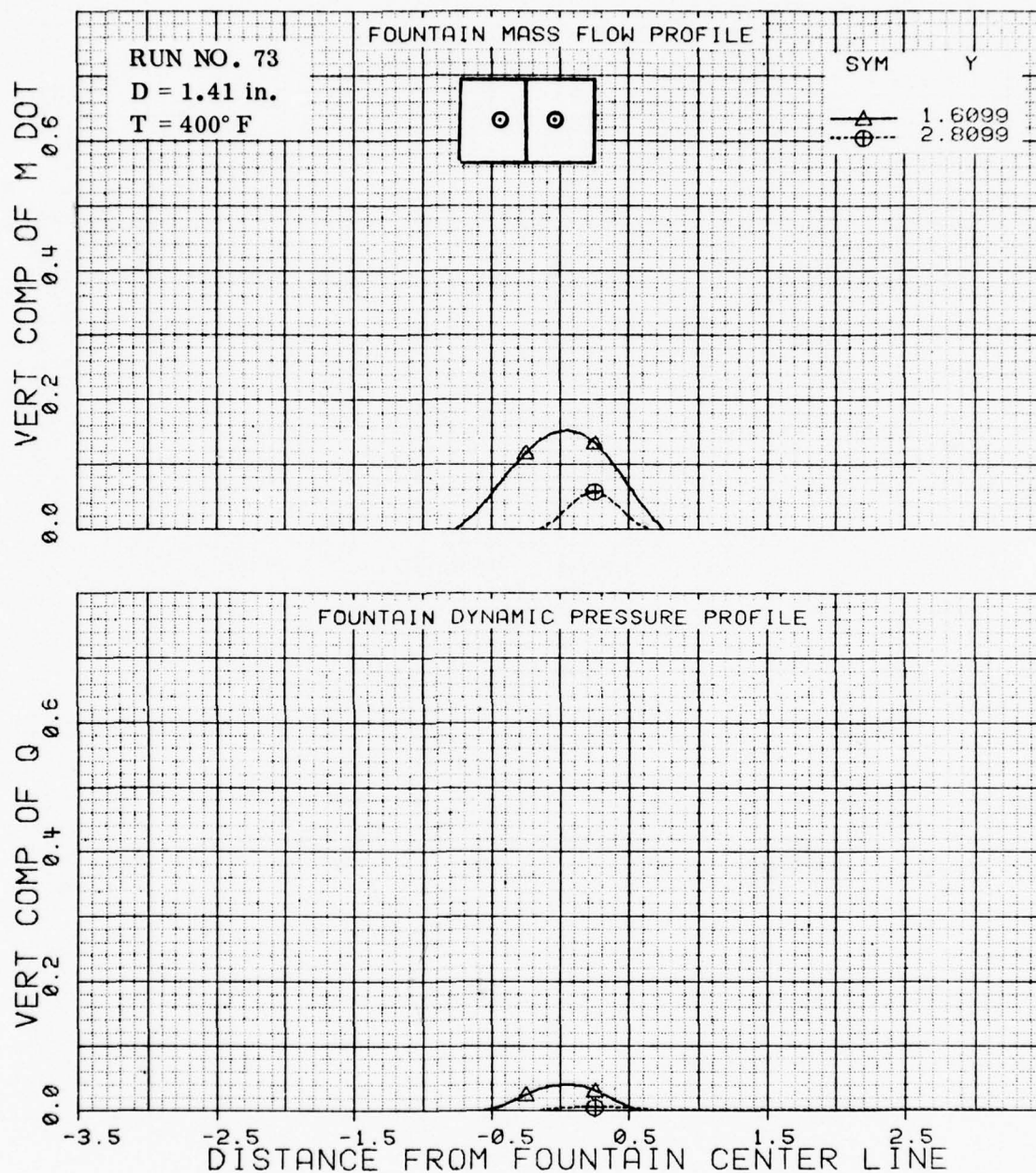


Figure B-19 Mass Flow and Dynamic Pressure Profiles with
Two Nozzles; $d_f/D=3.32$ $h/D=8.05$, $Z/D=3.47$

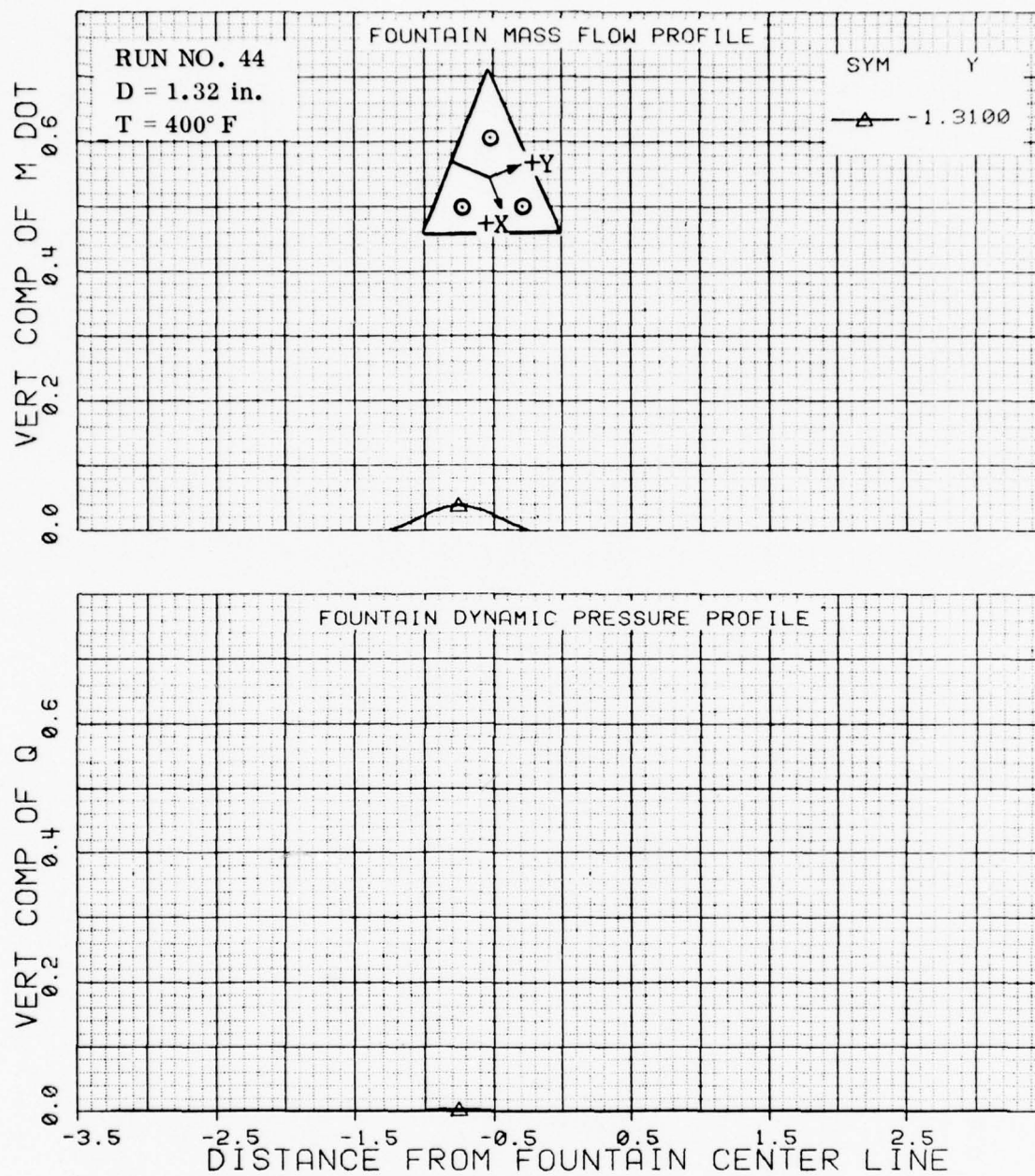


Figure B-20 Mass Flow and Dynamic Pressure Profiles with Three Nozzles; $D=1.32$, $h/D=2.58$, $Z/D=0.83$

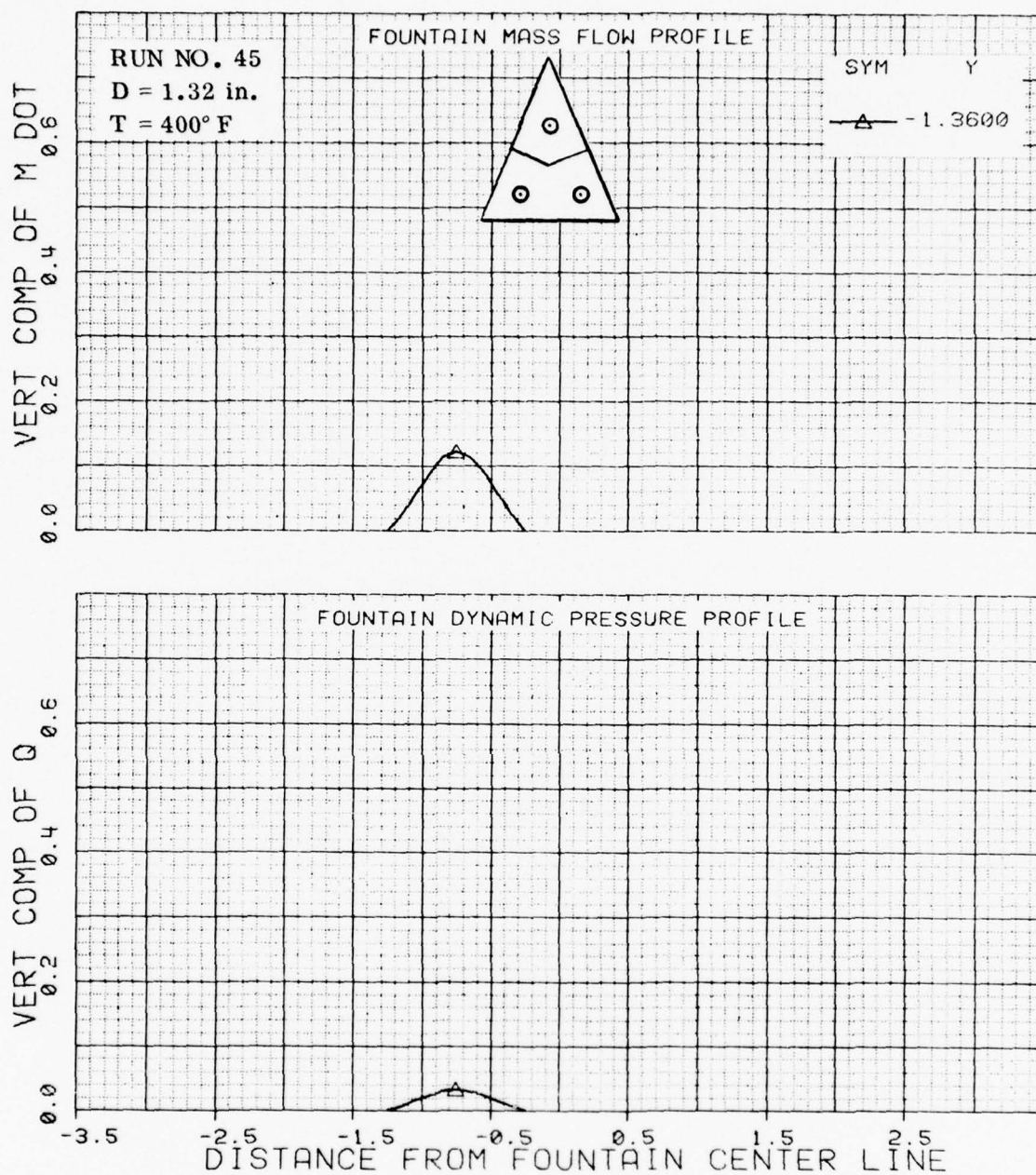


Figure B-21 Mass Flow and Dynamic Pressure Profiles with Three Nozzles; $D=1.32$, $h/D=2.58$, $Z/D=0.90$

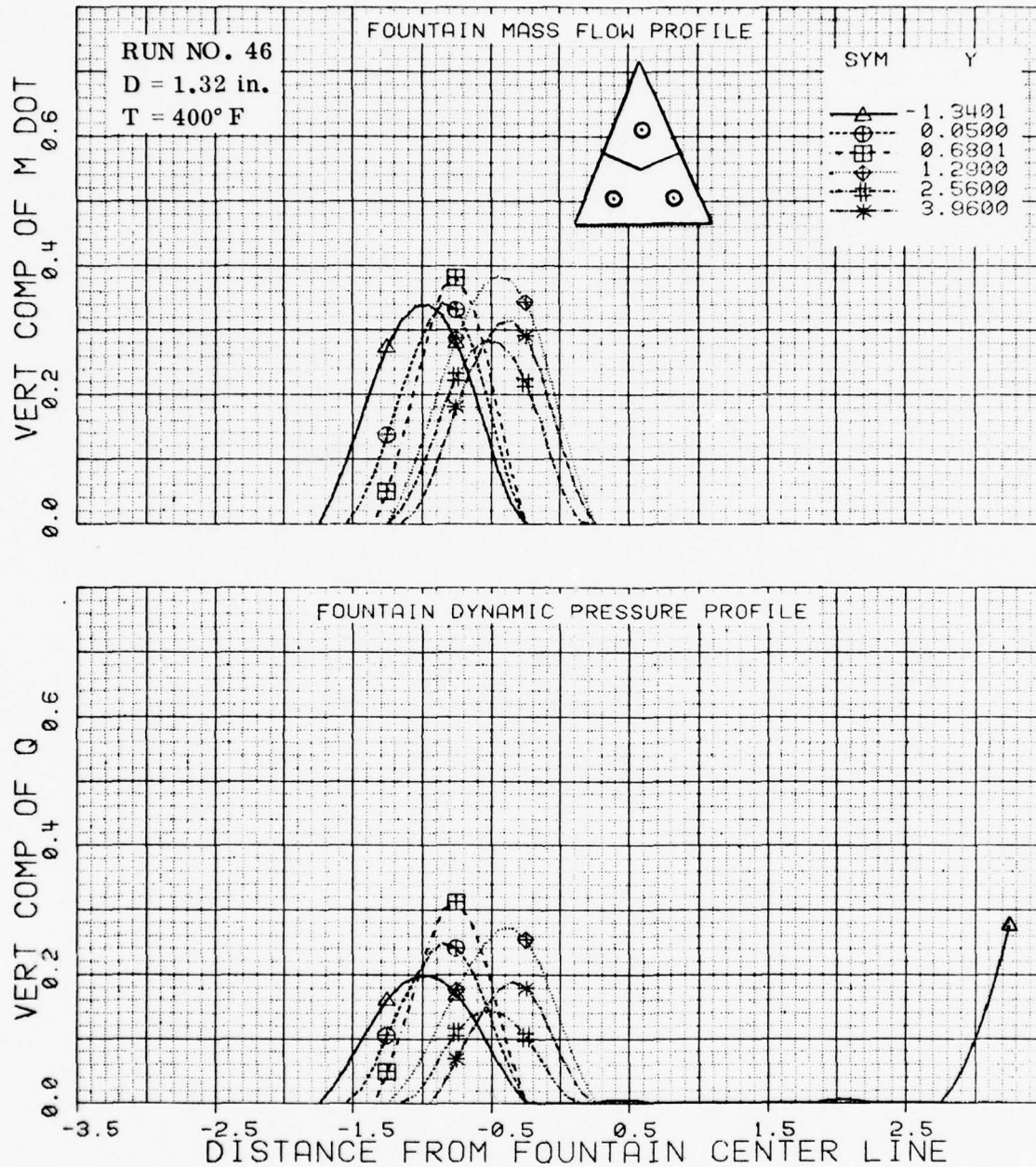


Figure B-22 Mass Flow and Dynamic Pressure Profiles with Three Nozzles; $D=1.32$, $h/D=2.58$, $Z/D=1.22$

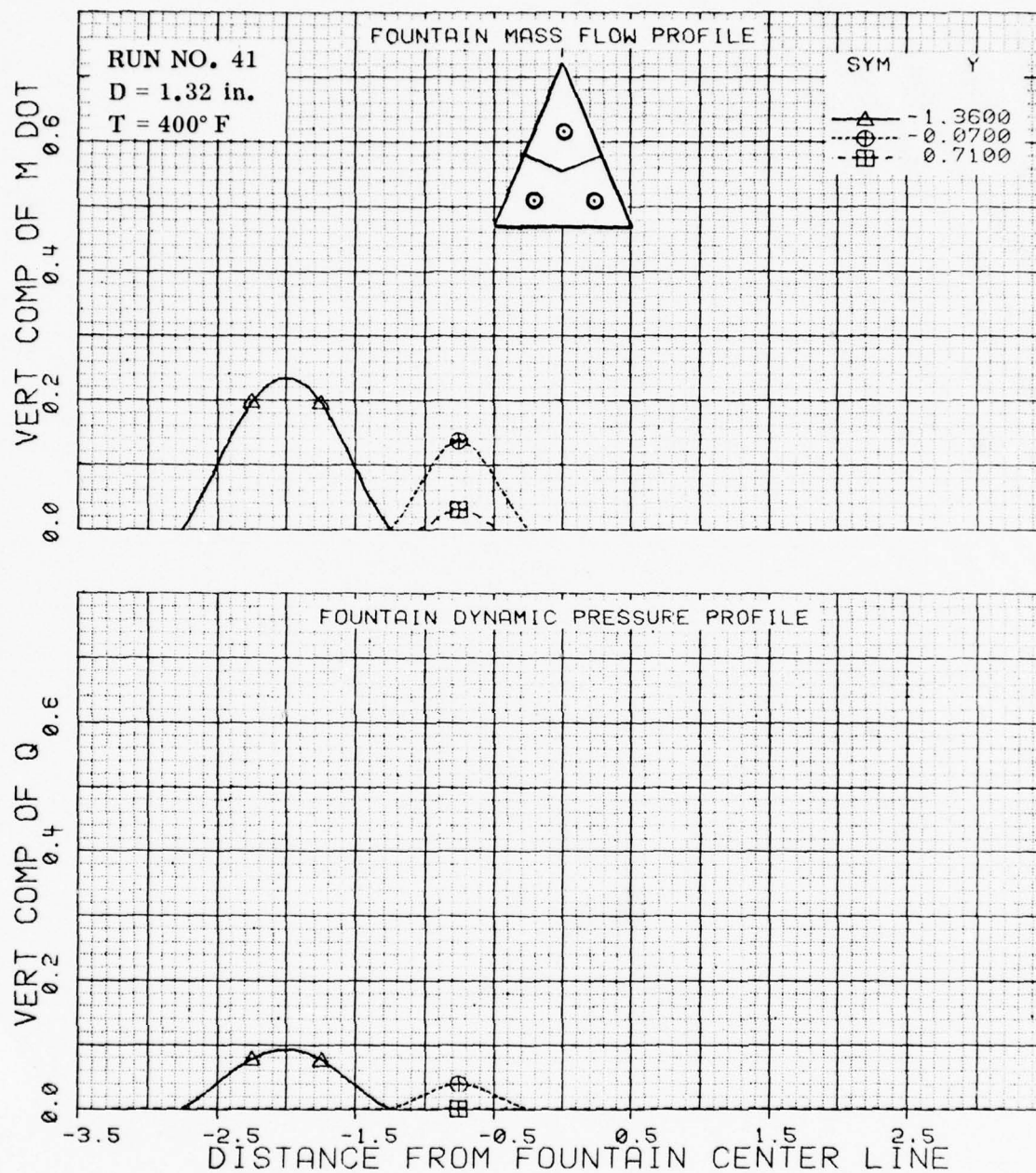


Figure B-23 Mass Flow and Dynamic Pressure Profiles with Three Nozzles; $D=1.32$, $h/D=3.56$, $Z/D=0.72$

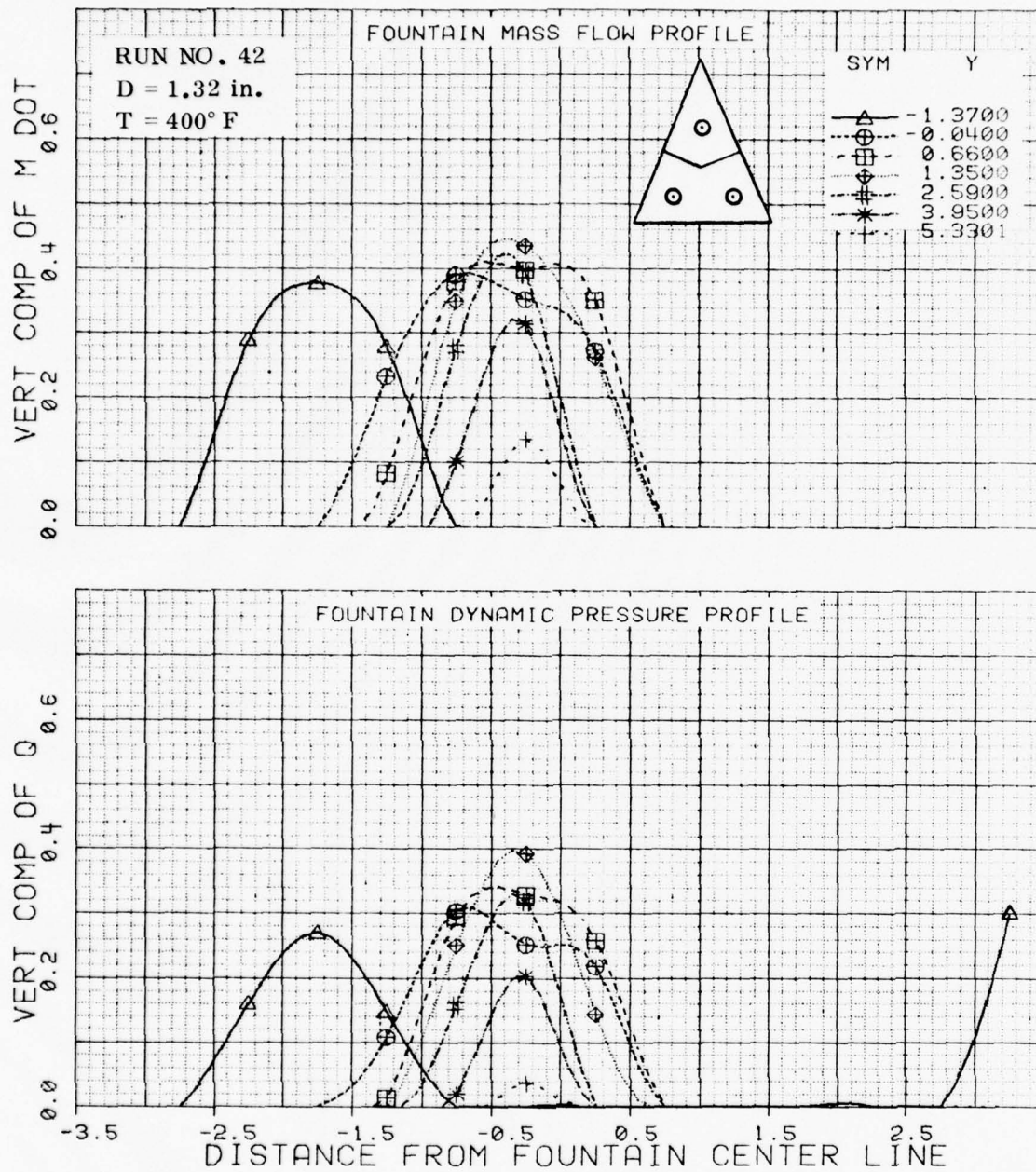


Figure B-24 Mass Flow and Dynamic Pressure Profiles with Three Nozzles; $D=1.32$, $h/D=3.56$, $Z/D=1.52$

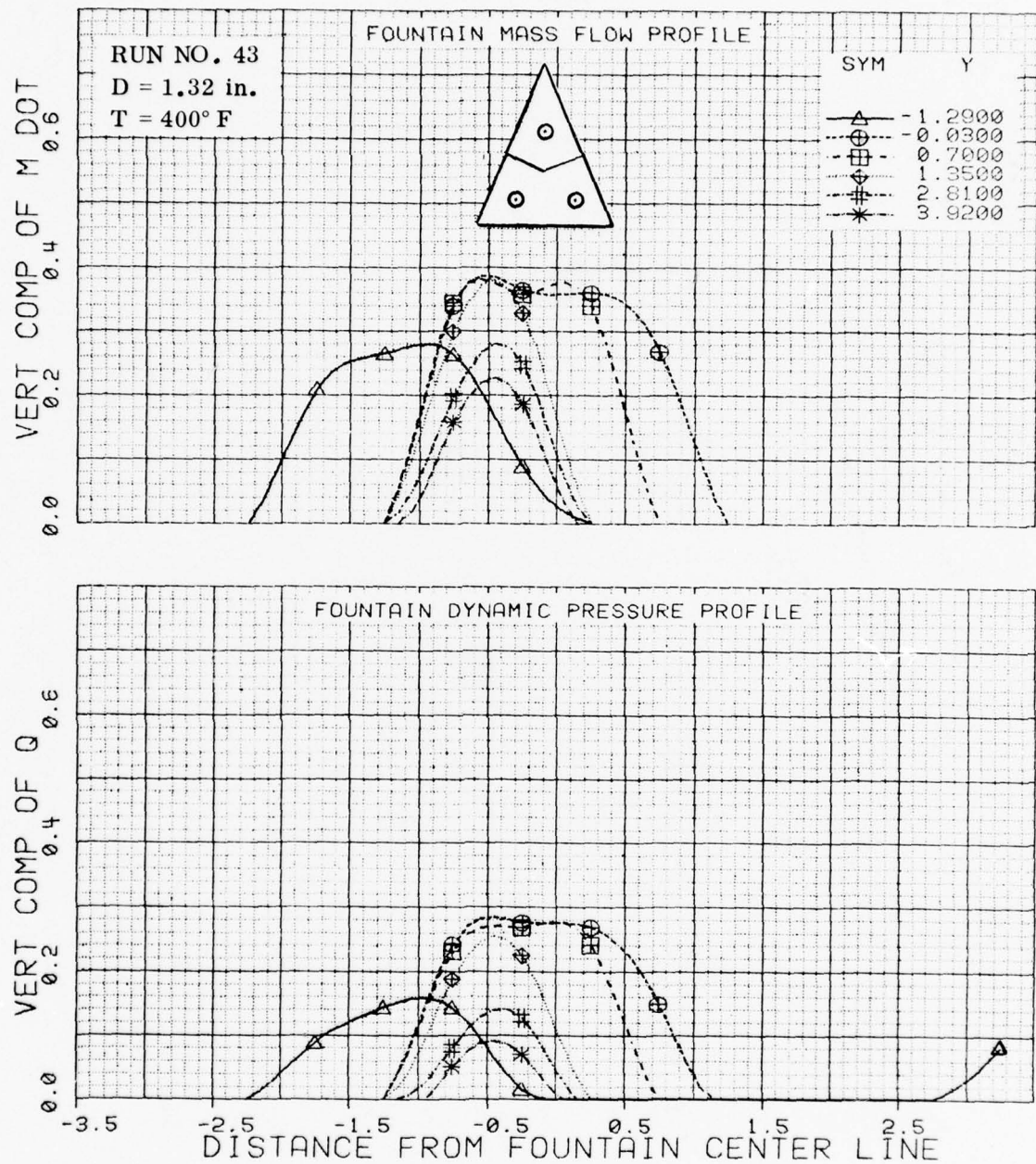


Figure B-25 Mass Flow and Dynamic Pressure Profiles with Three Nozzles; $D=1.32$, $h/D=3.56$, $Z/D=2.24$

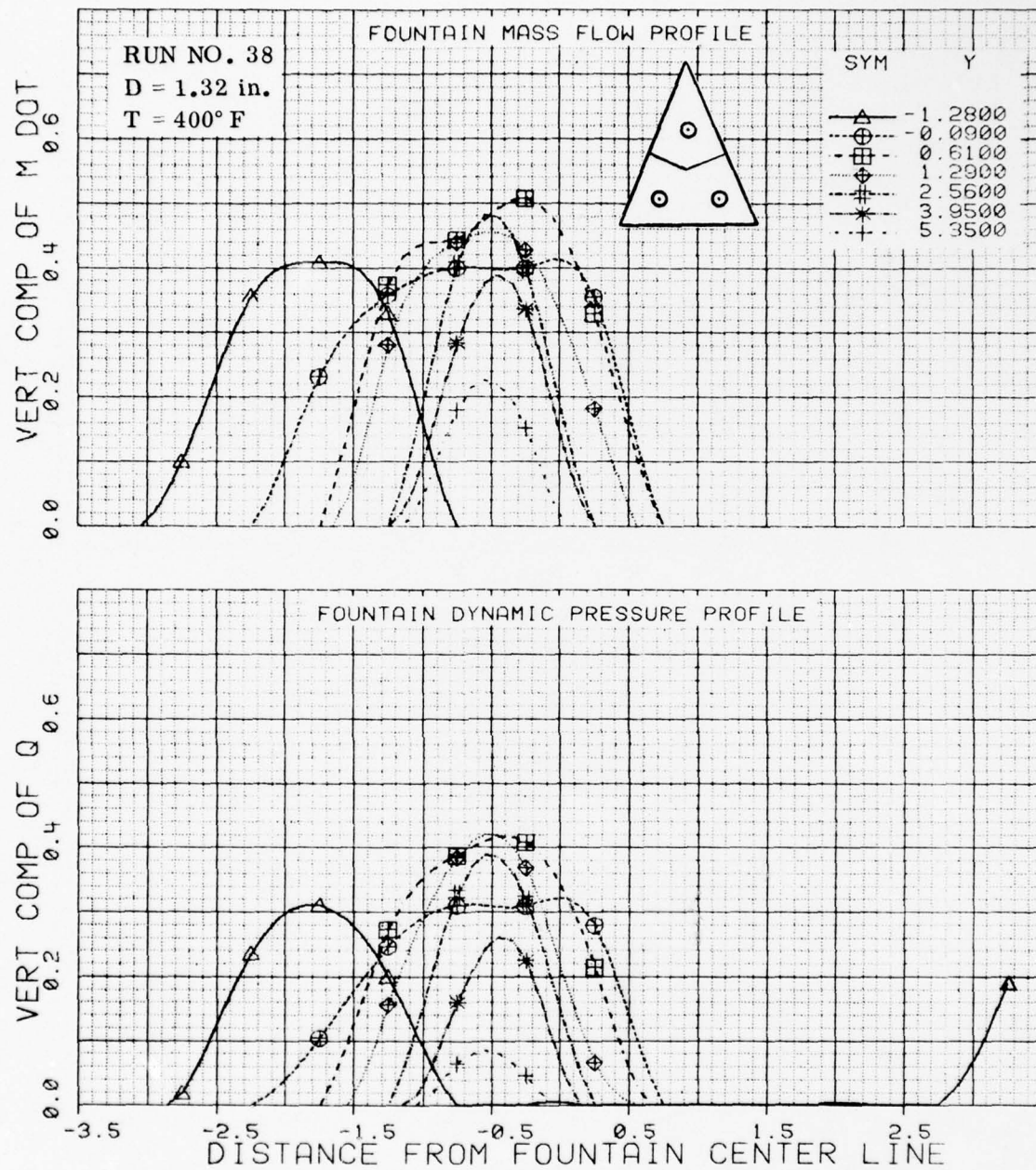


Figure B-26 Mass Flow and Dynamic Pressure Profiles with Three Nozzles; $D=1.32$, $h/D=5.05$, $Z/D=1.57$

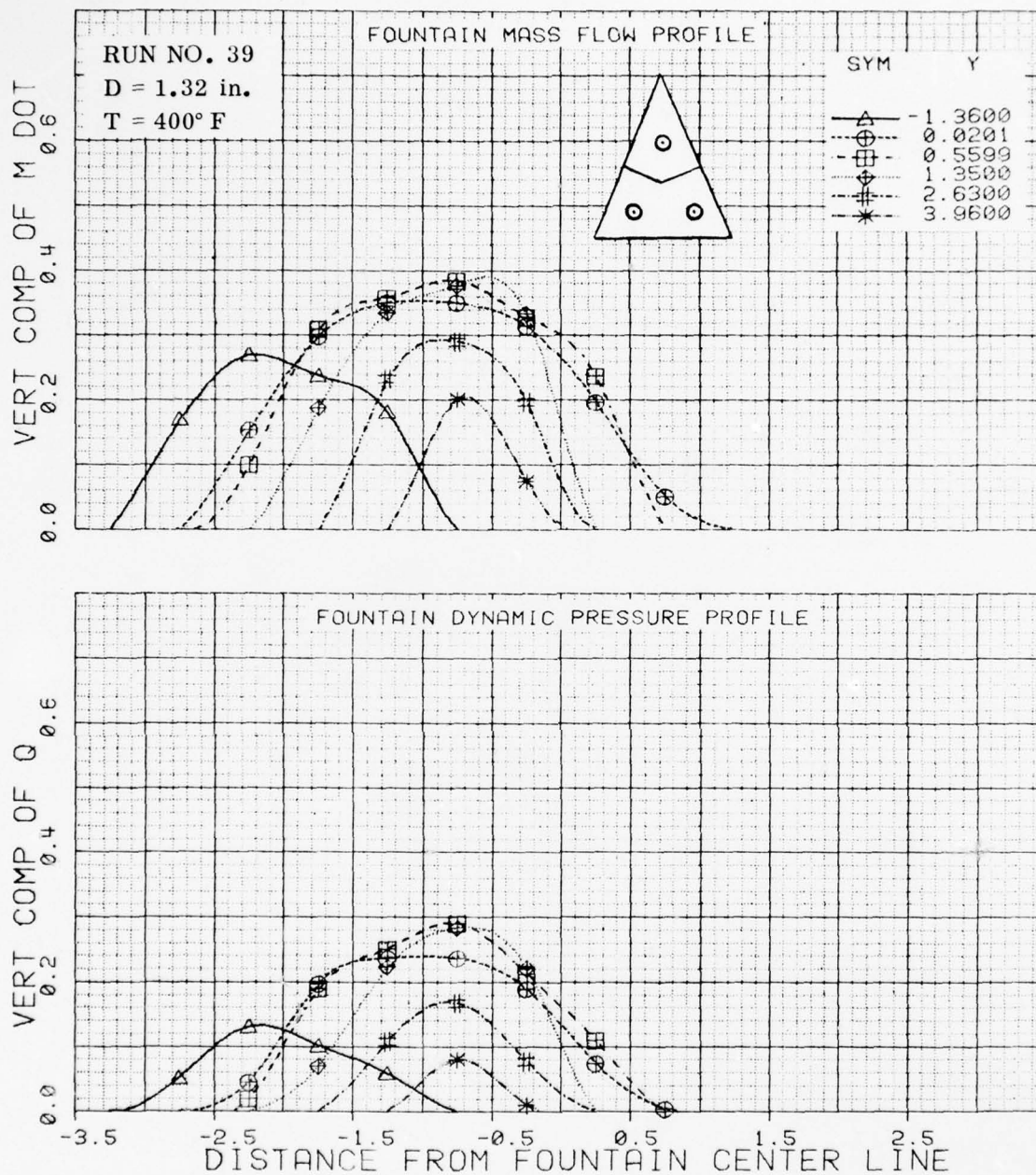


Figure B-27 Mass Flow and Dynamic Pressure Profiles with Three Nozzles; $D=1.32$, $h/D=5.05$, $Z/D=2.56$

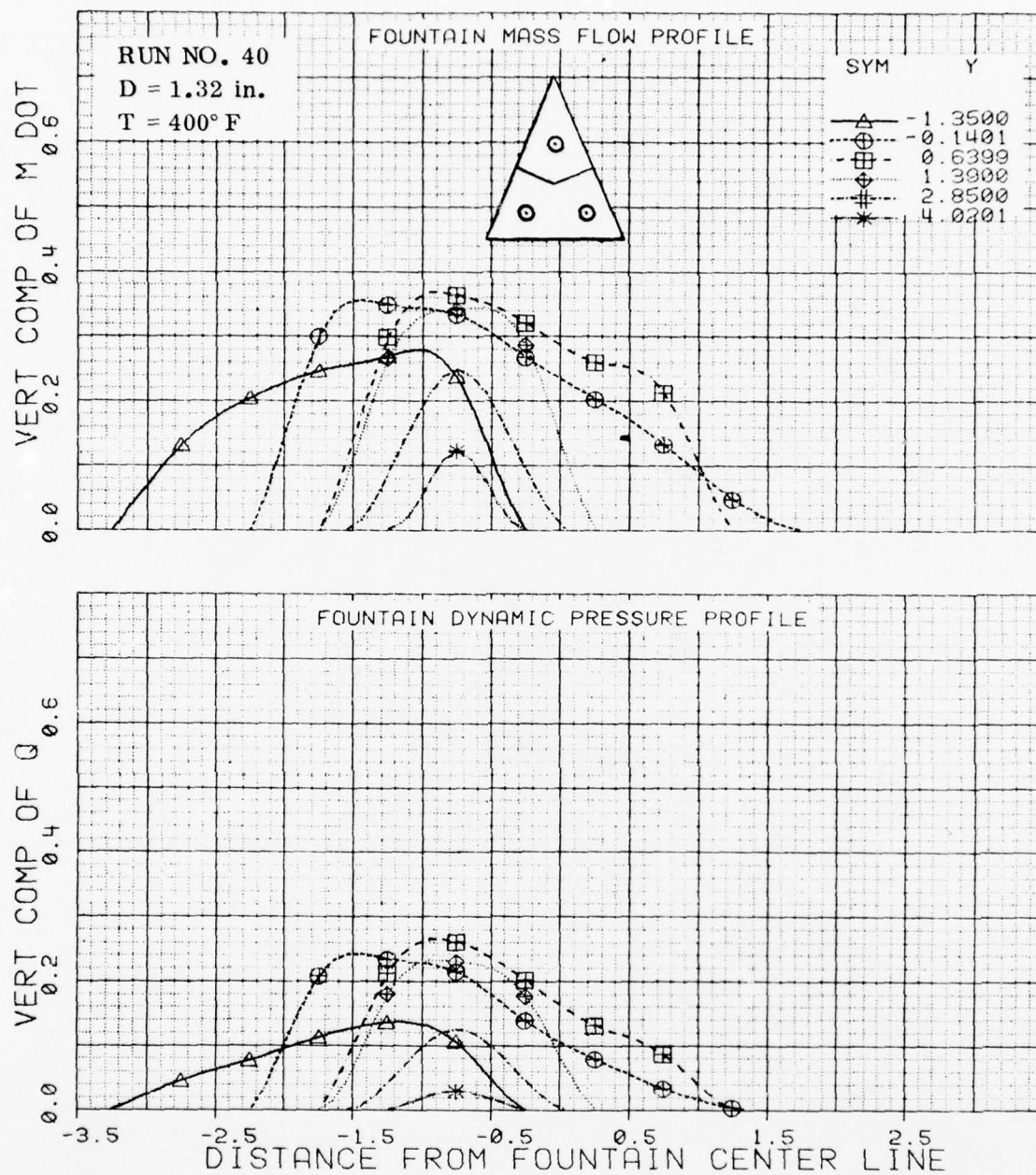


Figure B-28 Mass Flow and Dynamic Pressure Profiles with Three Nozzles; $D=1.32$, $h/D=5.05$, $Z/D=3.74$

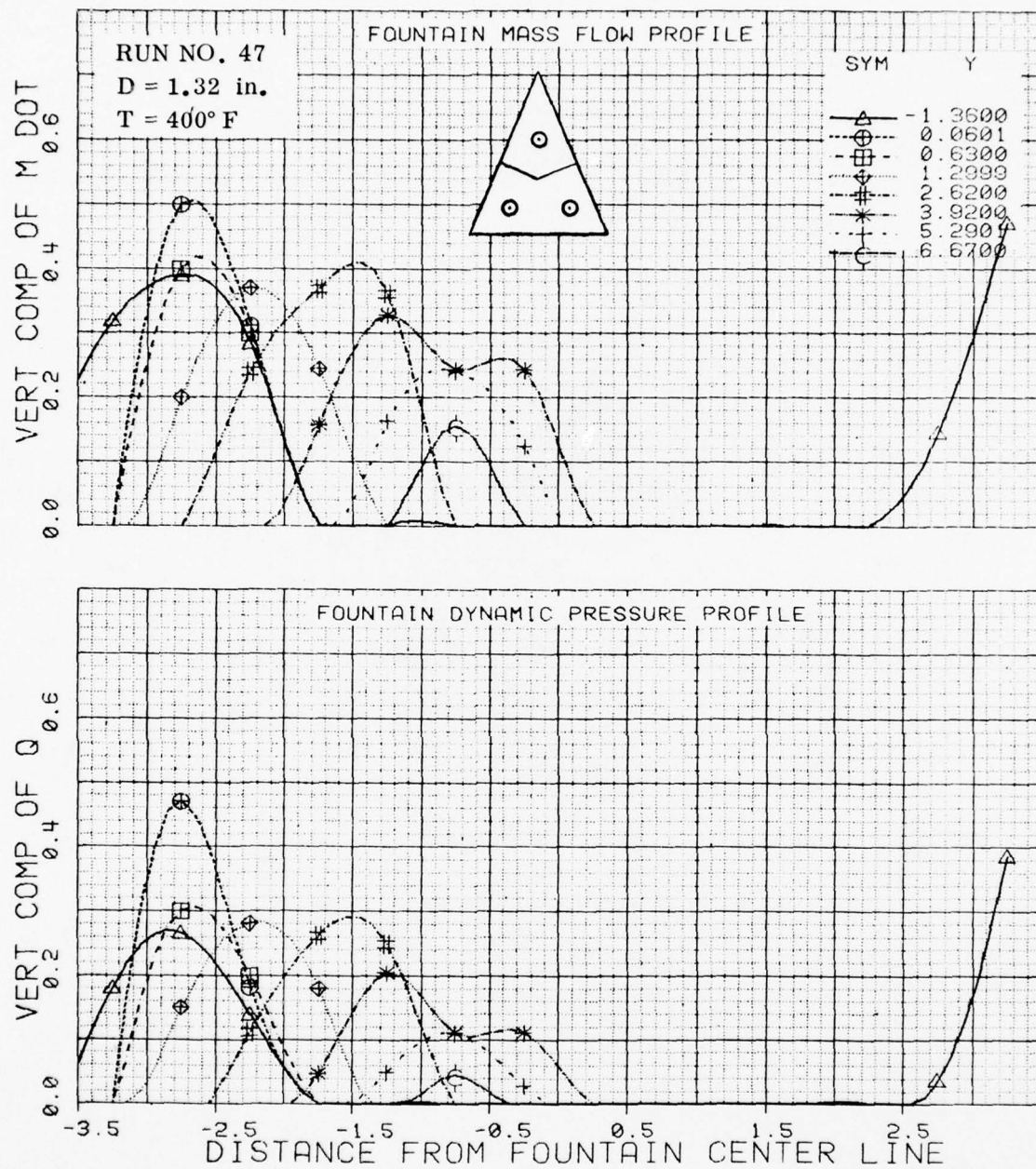


Figure B-29 Mass Flow and Dynamic Pressure Profiles with Three Nozzles; $D=1.32$, $h/D=8.07$, $Z/D=1.57$

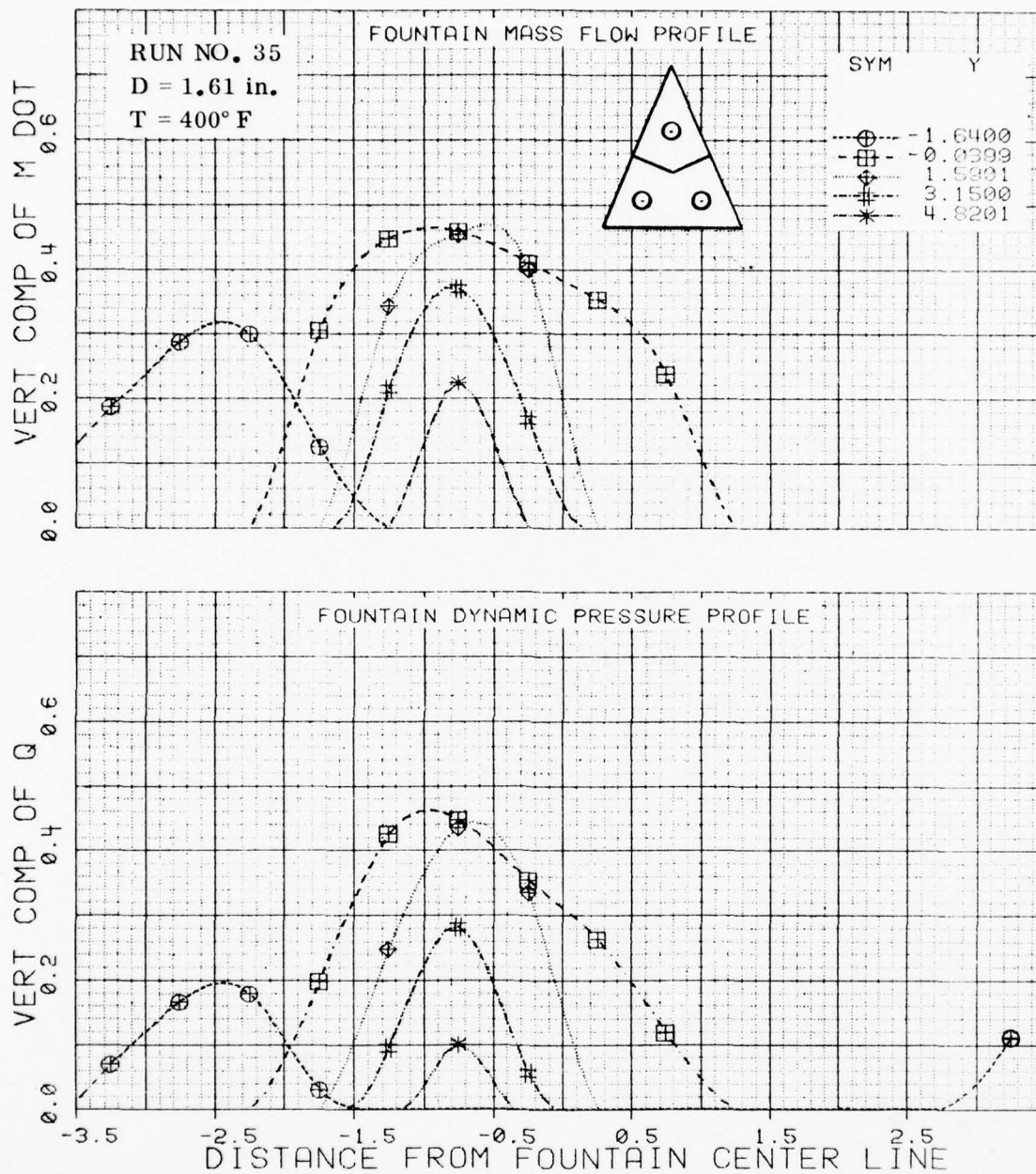


Figure B-30 Mass Flow and Dynamic Pressure Profiles with Three Nozzles; $D=1.61$, $h/D=3.58$, $Z/D=1.52$

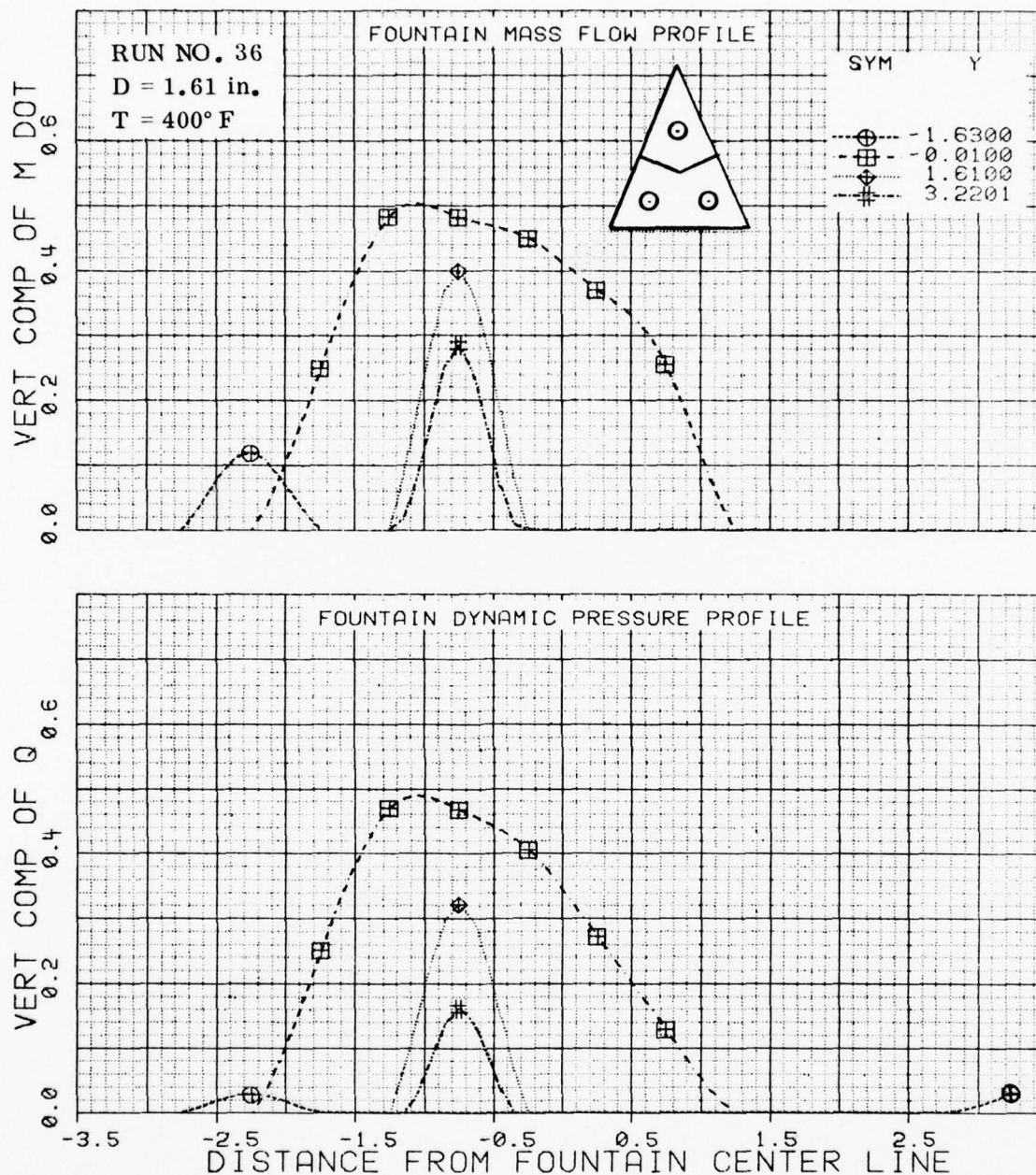


Figure B-31 Mass Flow and Dynamic Pressure Profiles with
Three Nozzles; $D=1.61$, $h/D=3.58$, $Z/D=2.44$

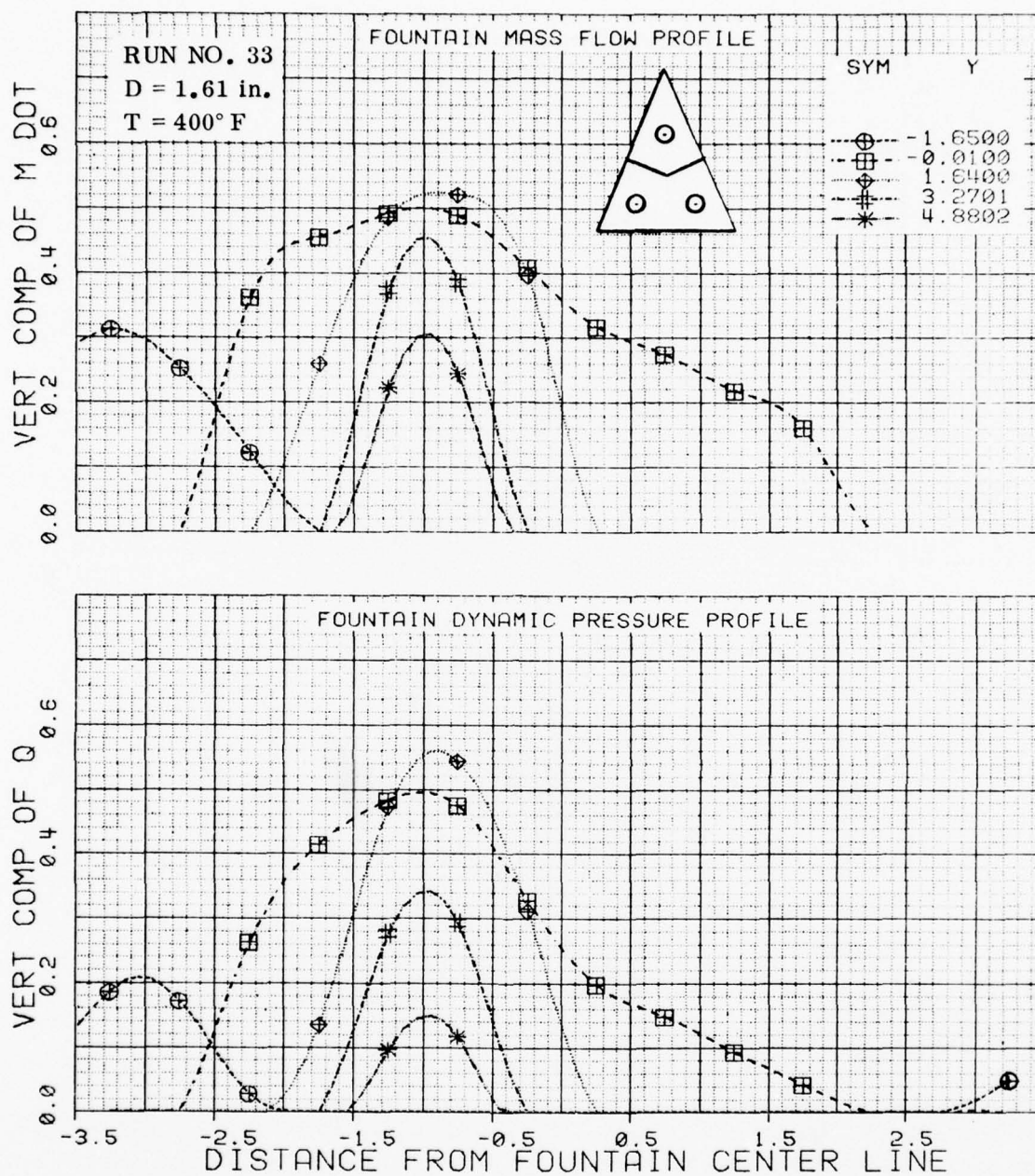


Figure B-32 Mass Flow and Dynamic Pressure Profiles with Three Nozzles; $D=1.61$, $h/D=5.07$, $Z/D=1.63$

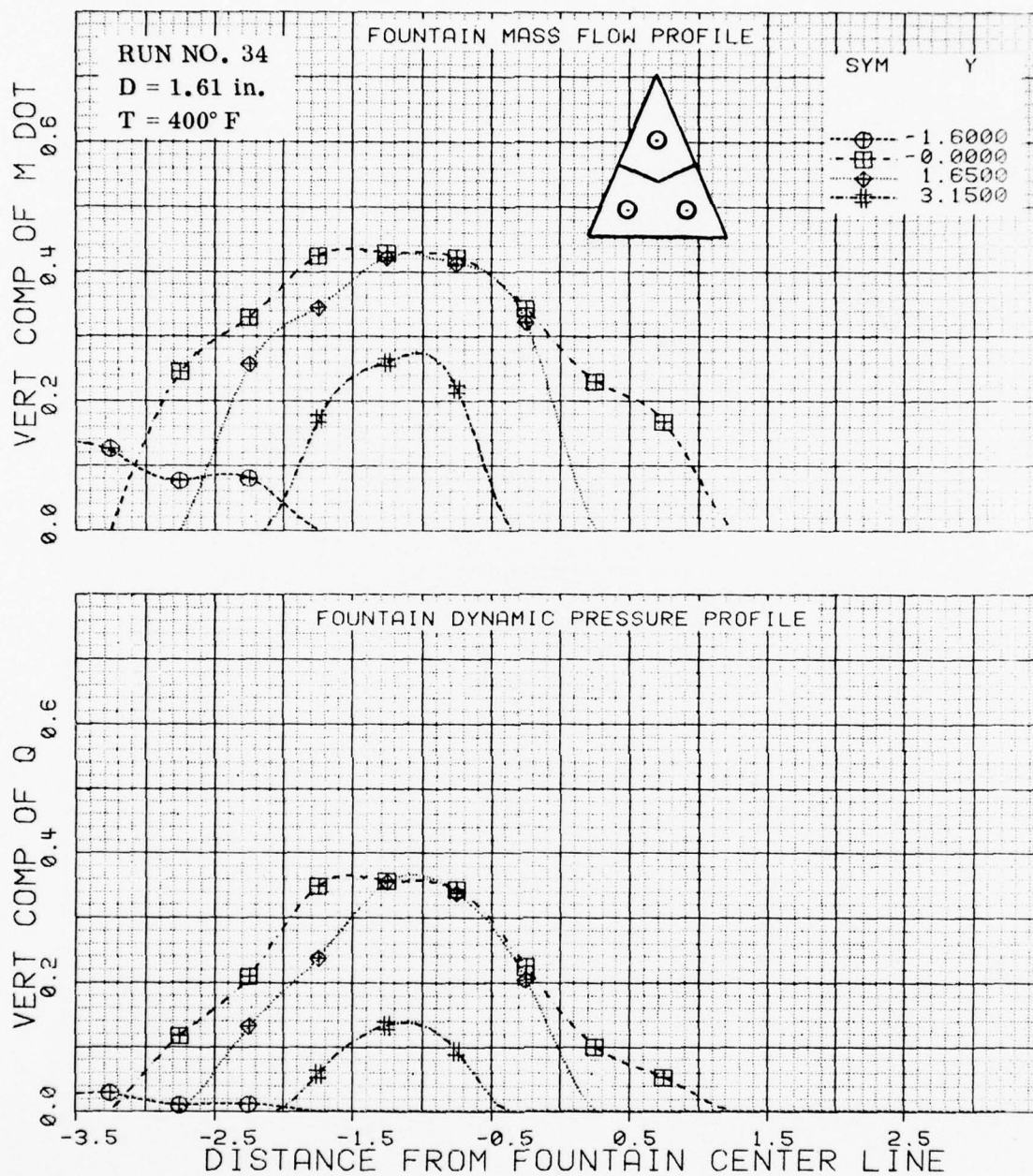


Figure B=33 Mass Flow and Dynamic Pressure Profiles with
Three Nozzles; $D=1.61$, $h/D=5.08$, $Z/D=2.56$

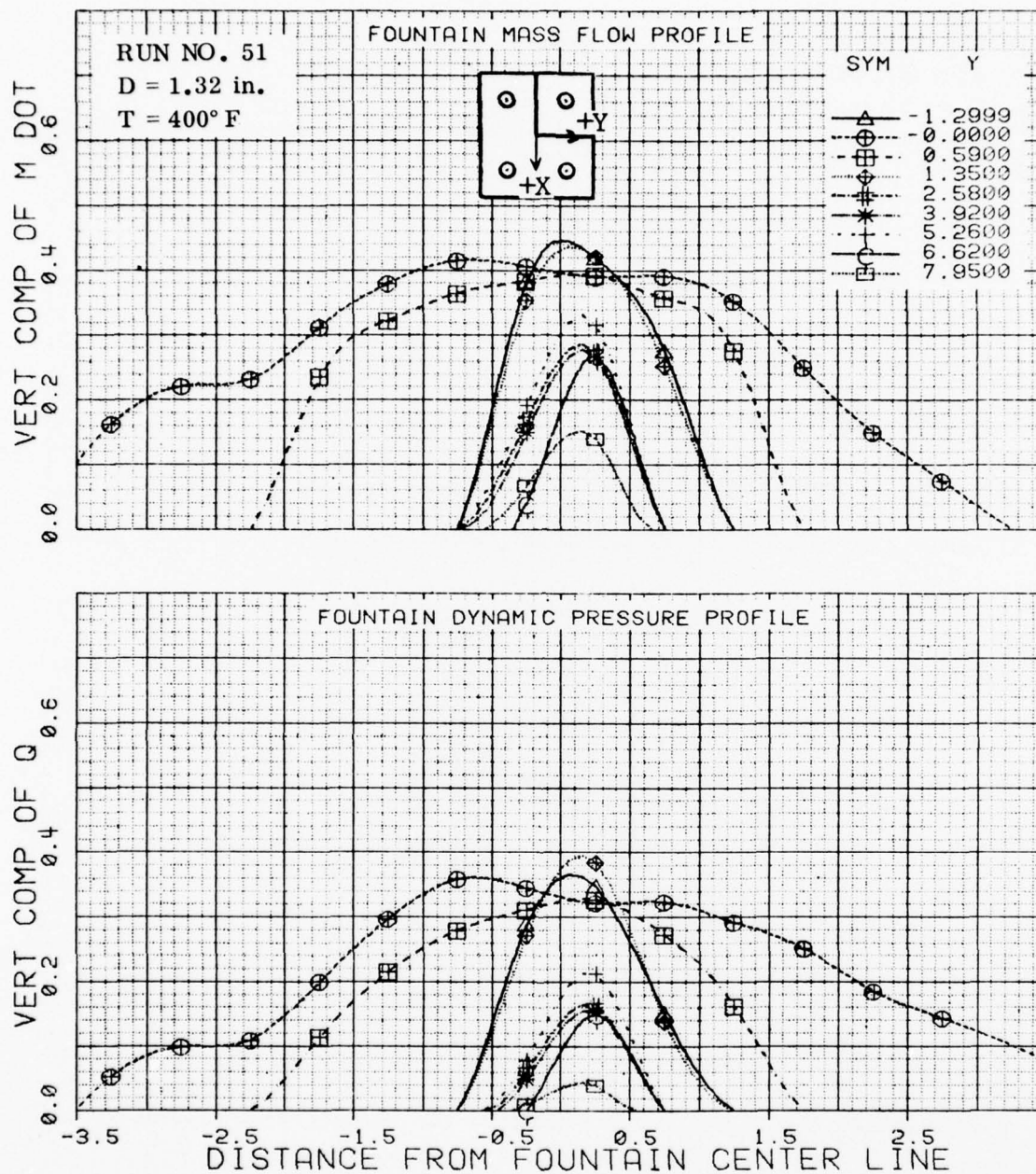


Figure B-34 Mass Flow and Dynamic Pressure Profiles with Four Nozzles; $D=1.32$, $h/D=3.60$, $Z/D=1.56$

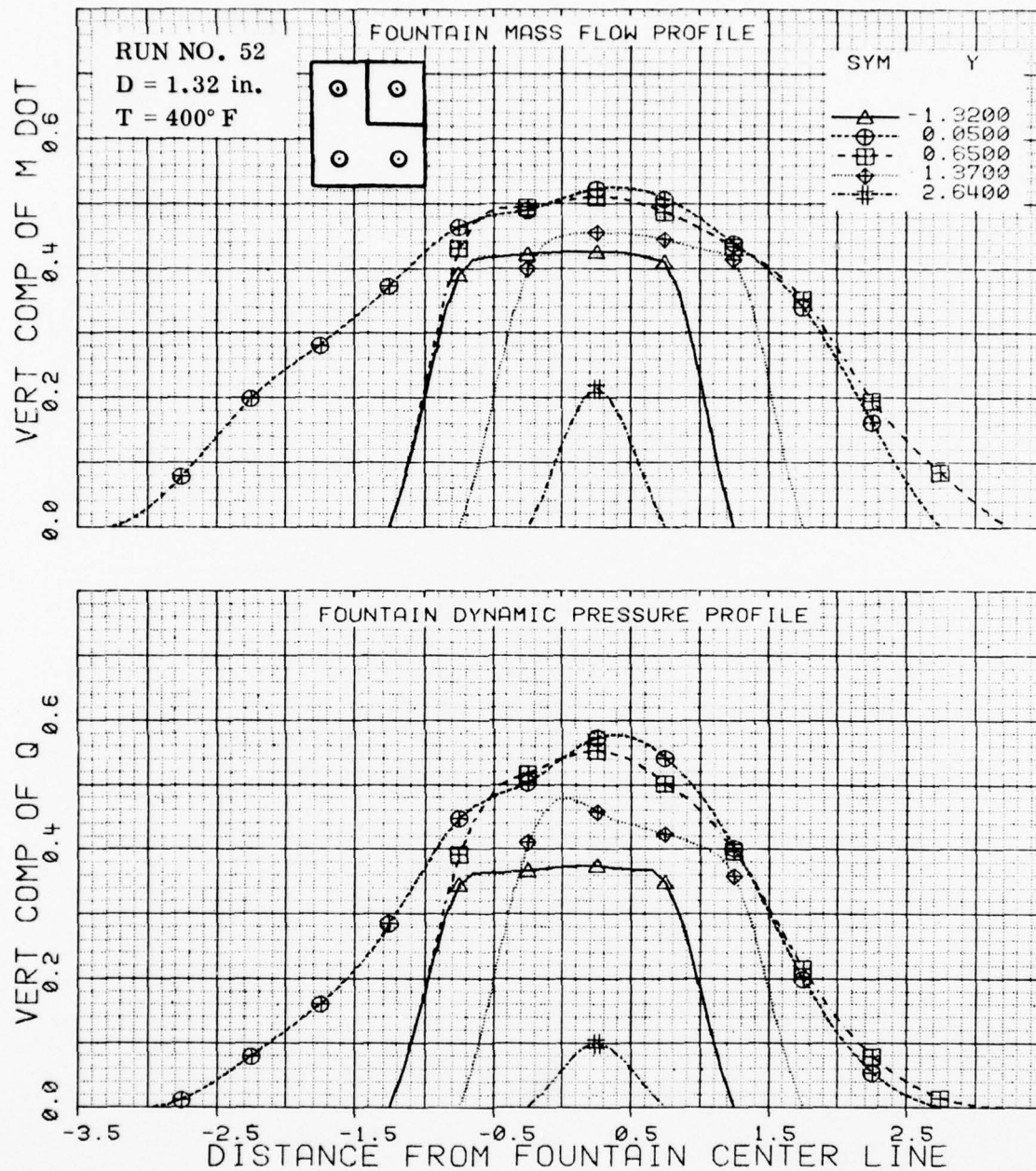


Figure B-35 Mass Flow and Dynamic Pressure Profiles with Four Nozzles; $D=1.32$, $h/D=3.62$, $Z/D=2.20$

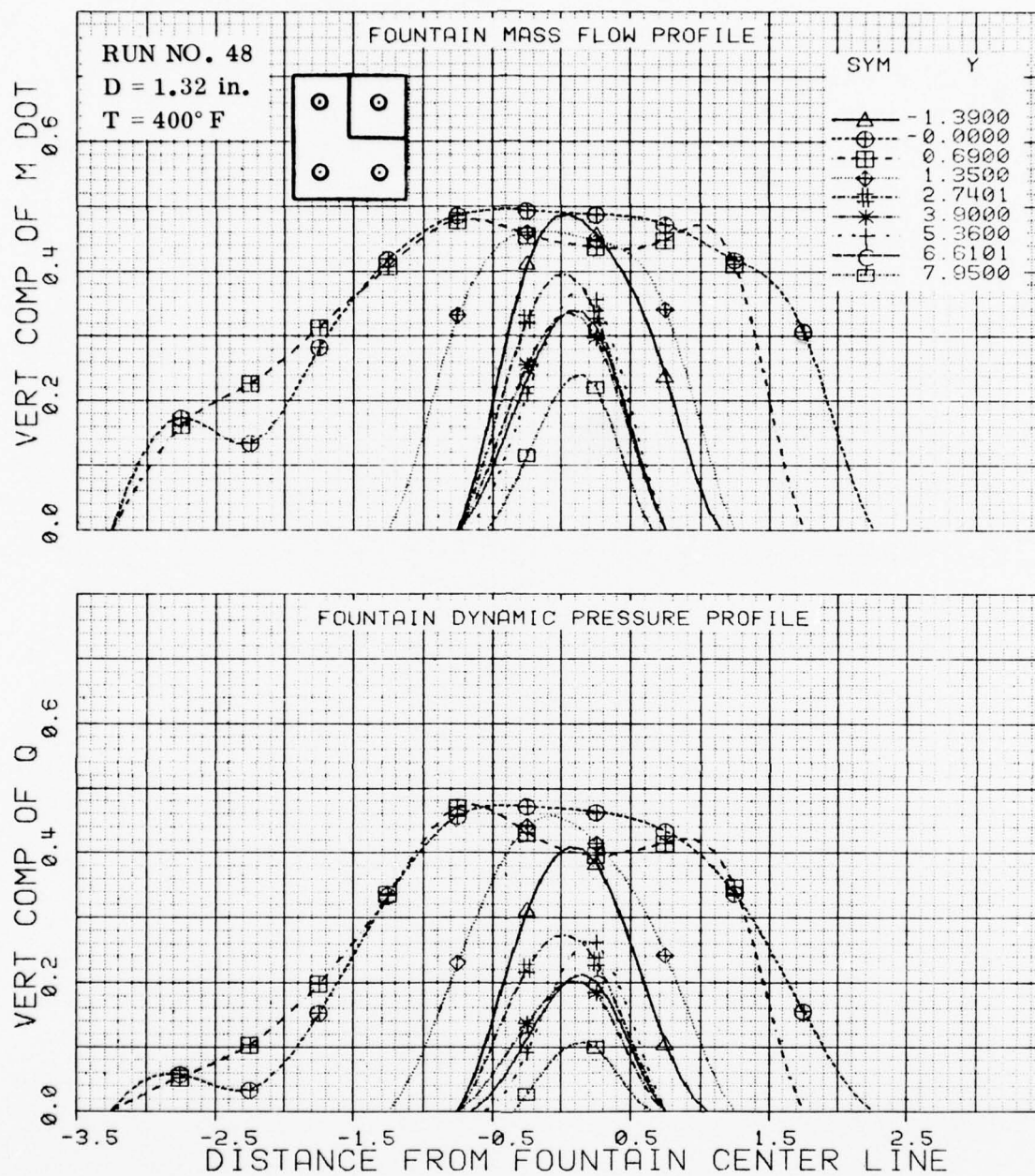


Figure B-36 Mass Flow and Dynamic Pressure Profiles with Four Nozzles; $D=1.32$, $h/D=5.15$, $Z/D=1.55$

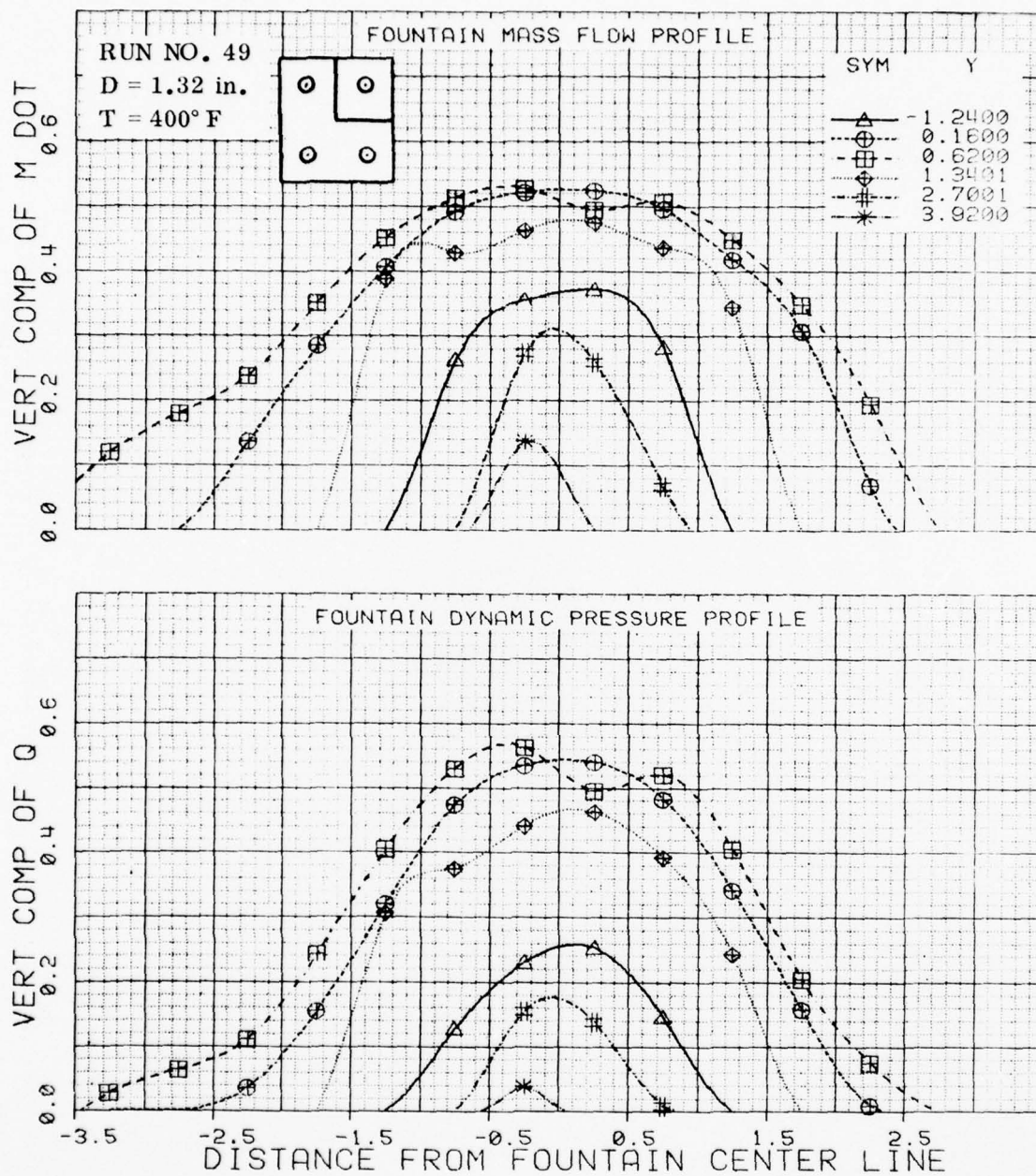


Figure B-37 Mass Flow and Dynamic Pressure Profiles with Four Nozzles; $D=1.32$, $h/D=5.11$, $Z/D=2.55$

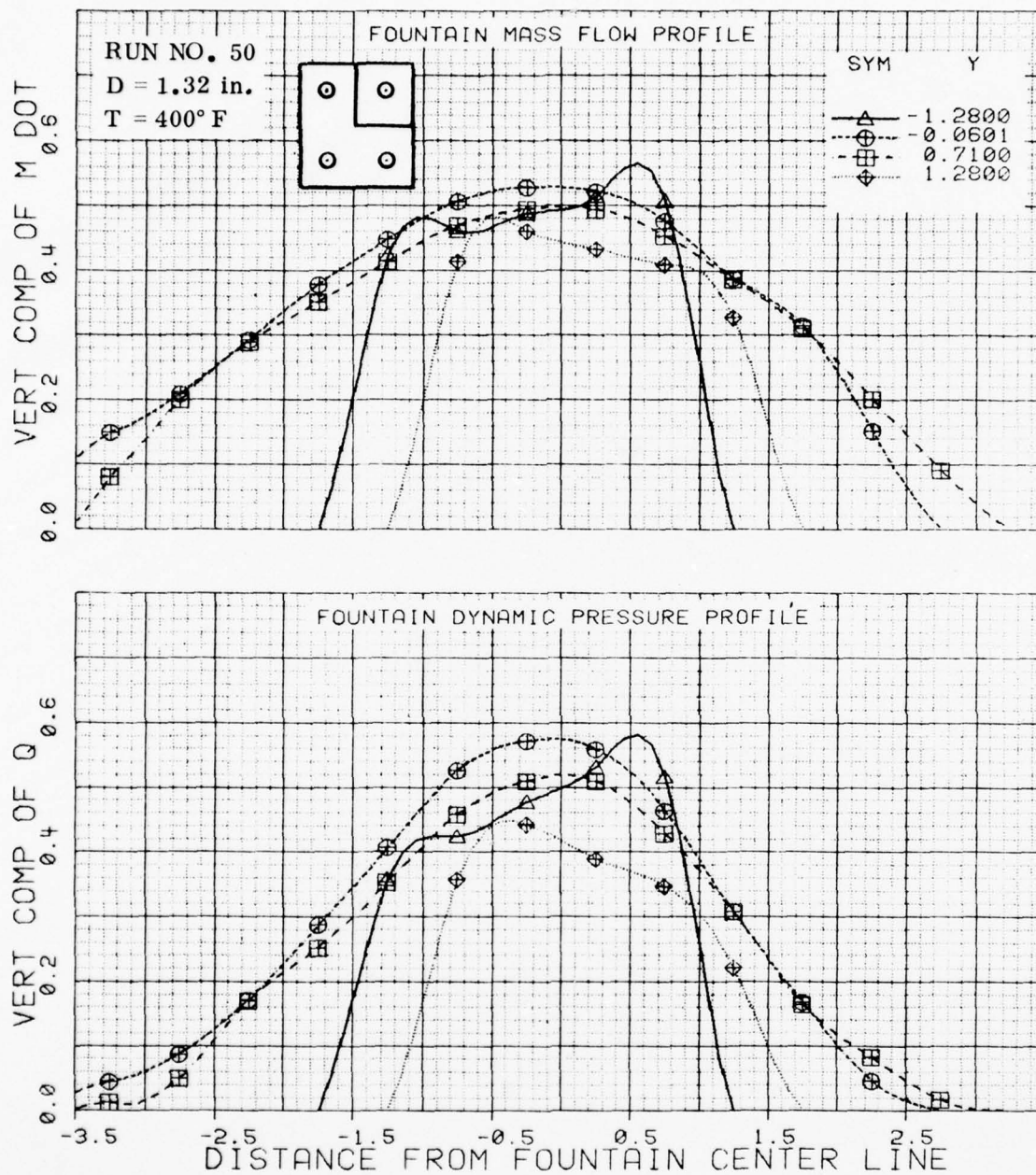


Figure B-38 Mass Flow and Dynamic Pressure Profiles with Four Nozzles; $D=1.32$, $h/D=5.11$, $Z/D=3.75$

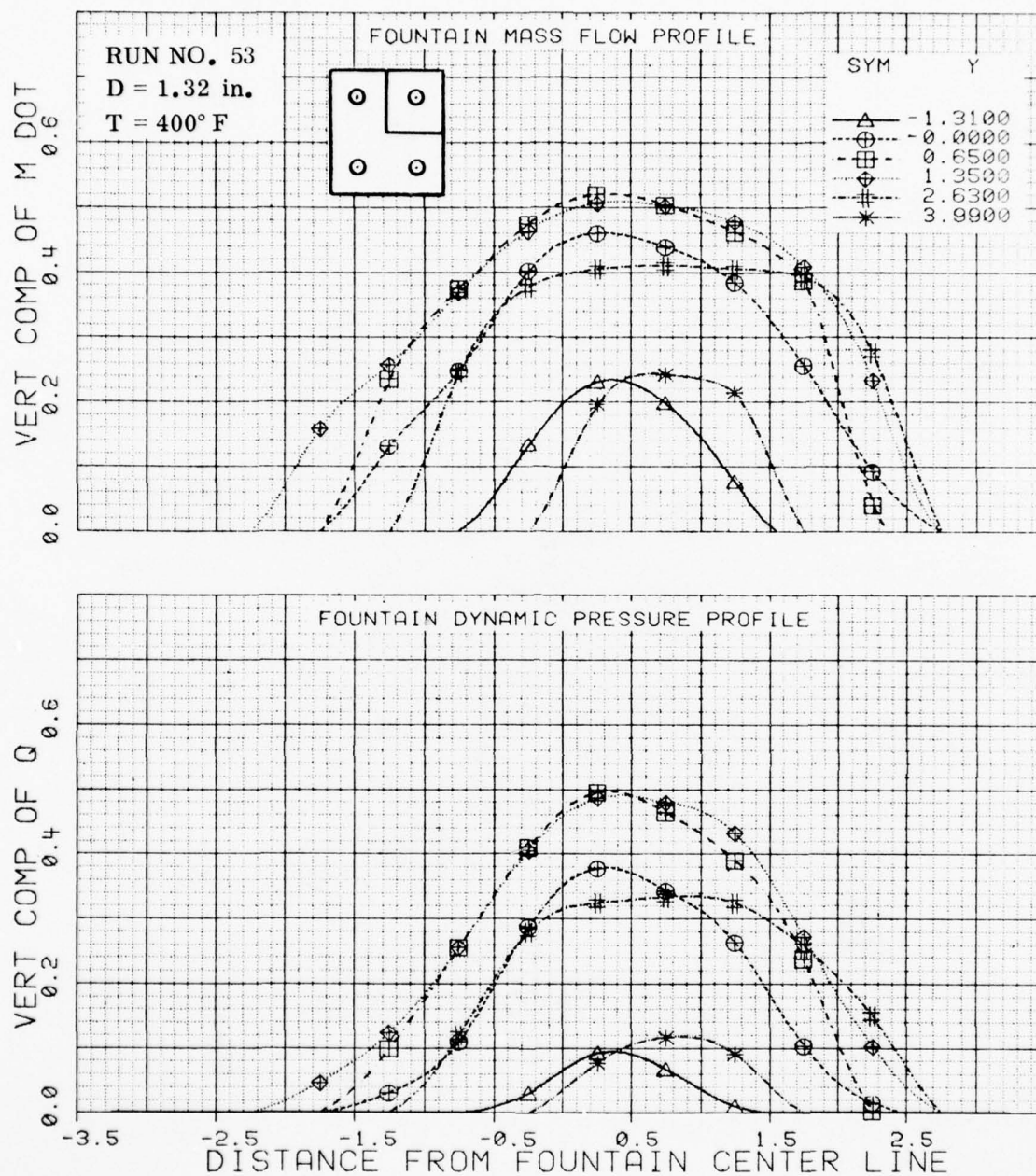


Figure B-39 Mass Flow and Dynamic Pressure Profiles with Four Nozzles; $D=1.32$, $h/D=8.11$, $Z/D=3.56$

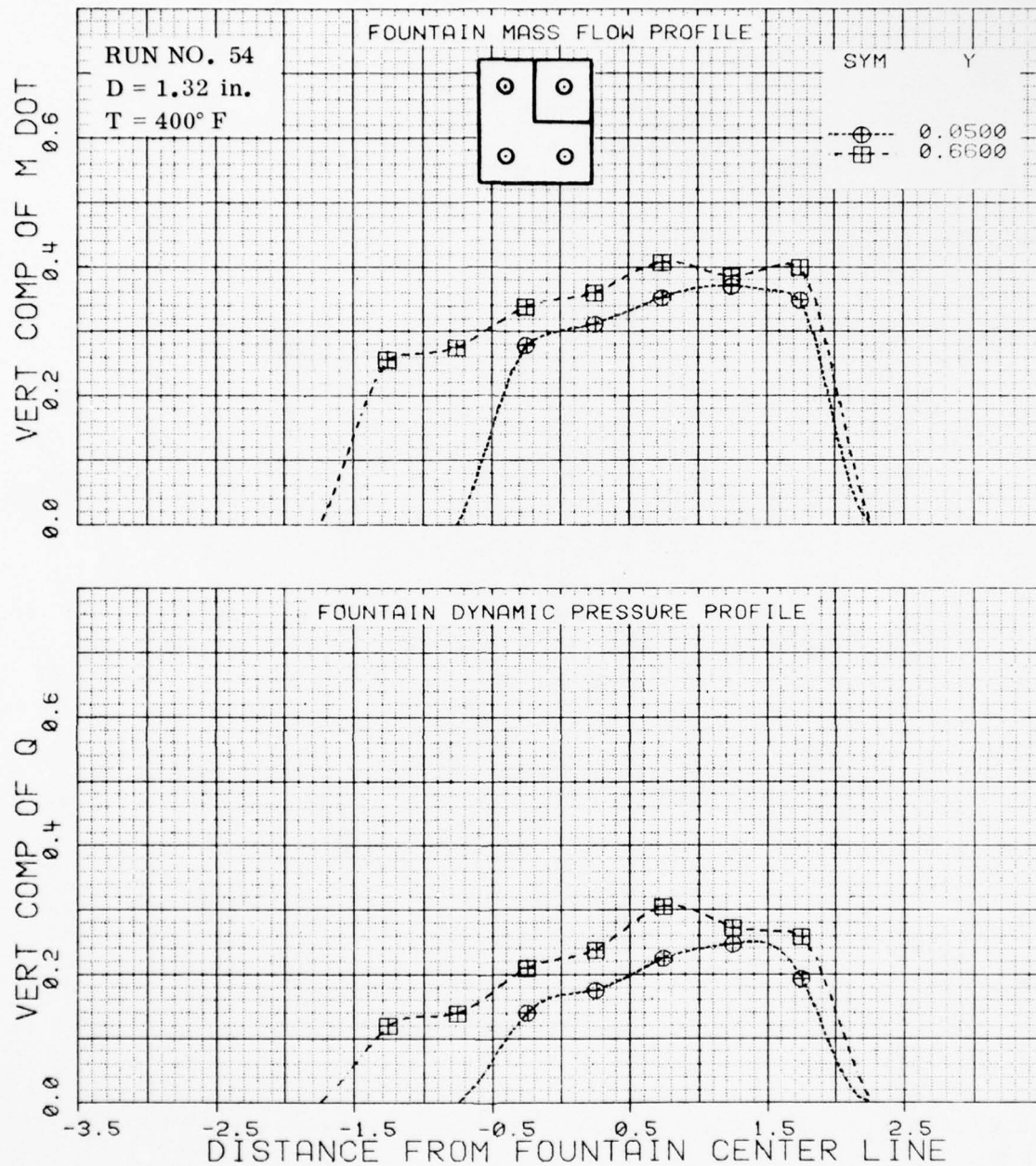


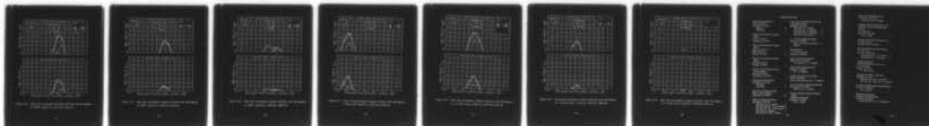
Figure B-40 Mass Flow and Dynamic Pressure Profiles with Four Nozzles; $D=1.32$, $h/D=8.10$, $Z/D=6.70$

AD-A061 335

GENERAL DYNAMICS SAN DIEGO CA CONVAIR DIV
THE AERODYNAMIC AND THERMODYNAMIC CHARACTERISTICS OF FOUNTAINS --ETC(U)
AUG 78 A KAREMAA, C W SMITH, H A WEBER N00014-76-C-0698
CASD-NSC-78-001 ONR-CR212-237-1F NL

UNCLASSIFIED

3 OF 3
AD
A061335



END
DATE
FILMED

2 - 79
DDC

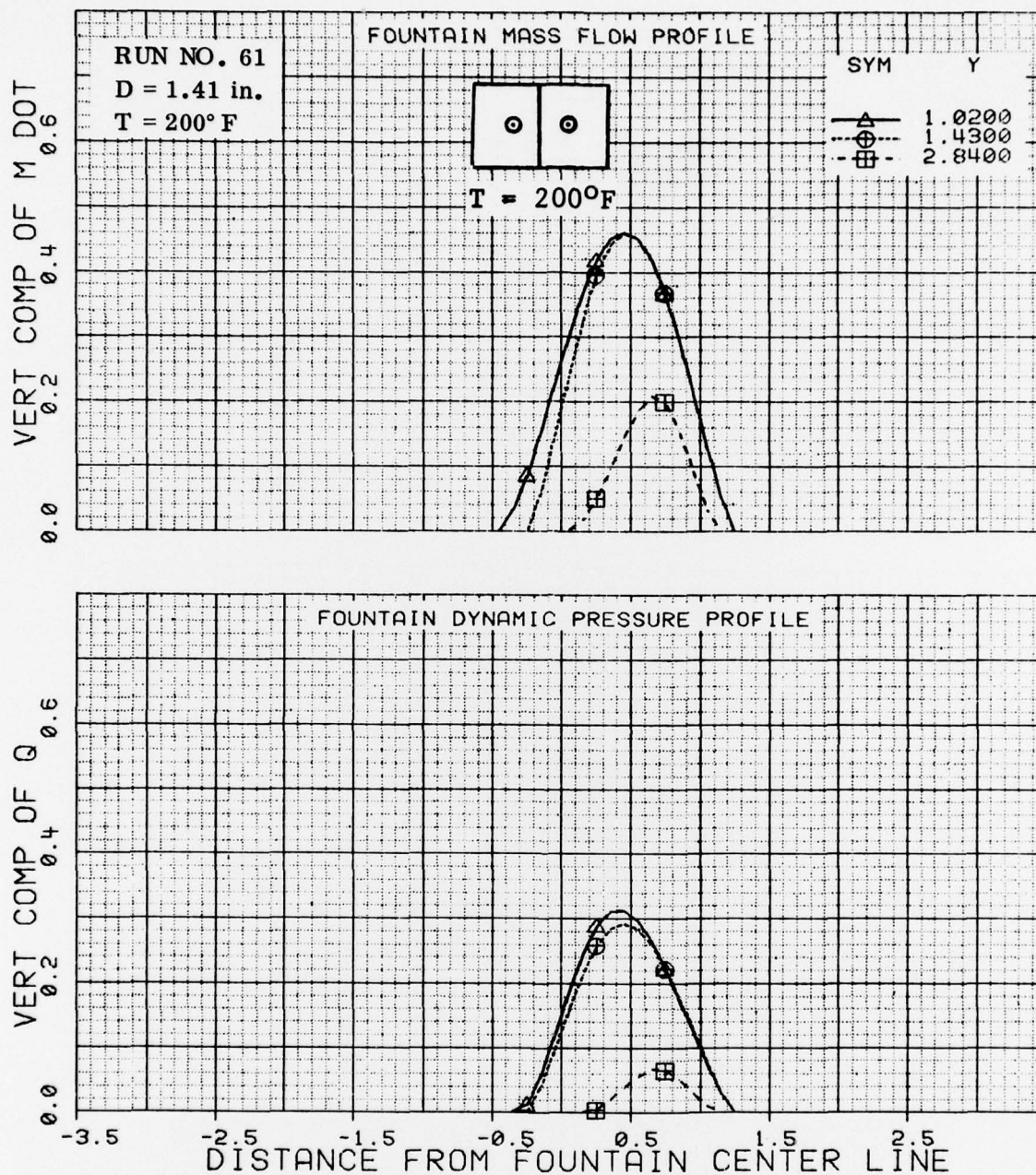


Figure B-41 Mass Flow and Dynamic Pressure Profiles with Two Nozzles at 200°F ; $d_f/D=3.32$, $h/D=5.05$, $Z/D=1.52$

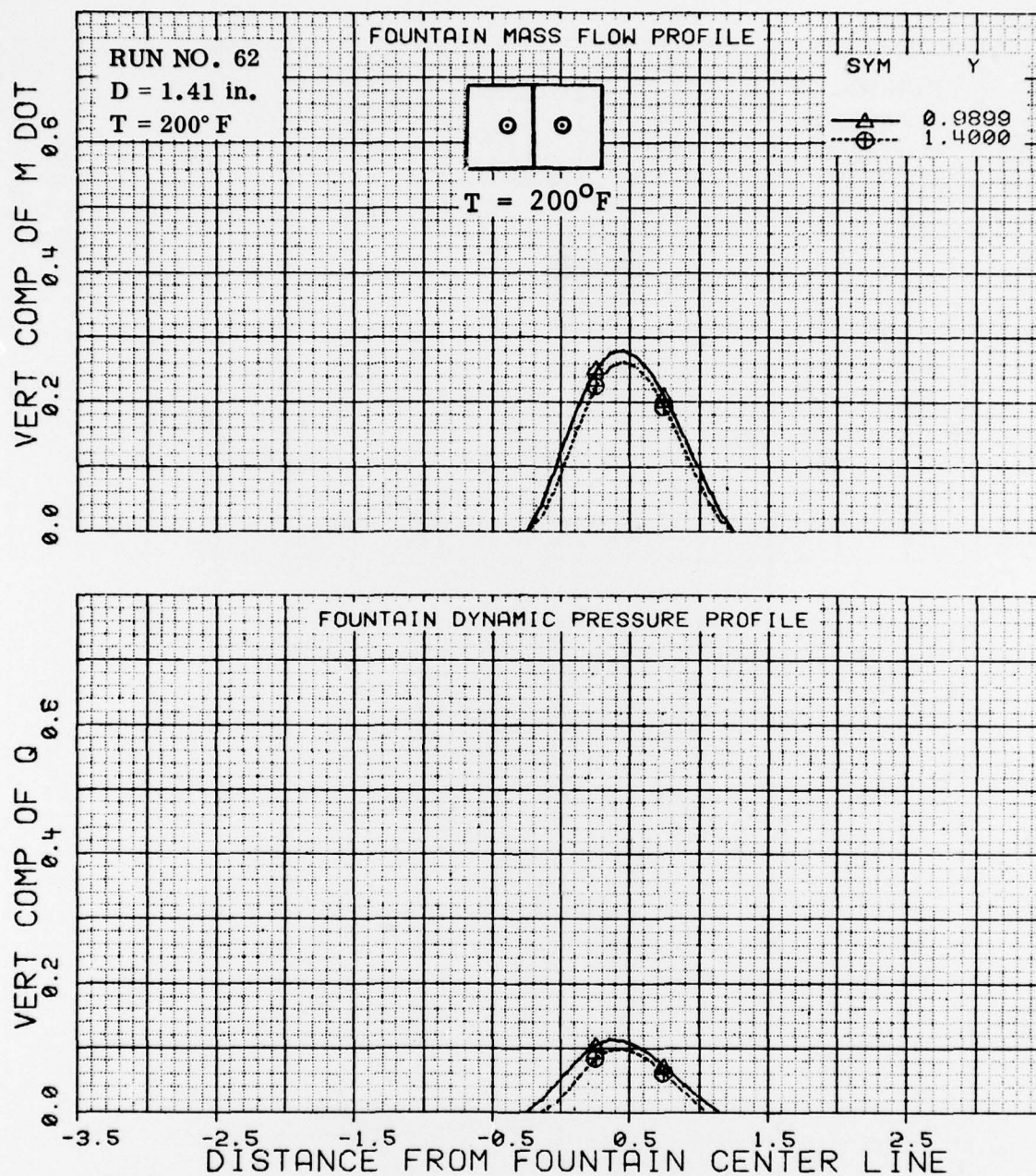


Figure B-42 Mass Flow and Dynamic Pressure Profiles with Two Nozzles
at 200°F; $d_f/D=3.32$, $h/D=5.05$, $Z/D=2.52$

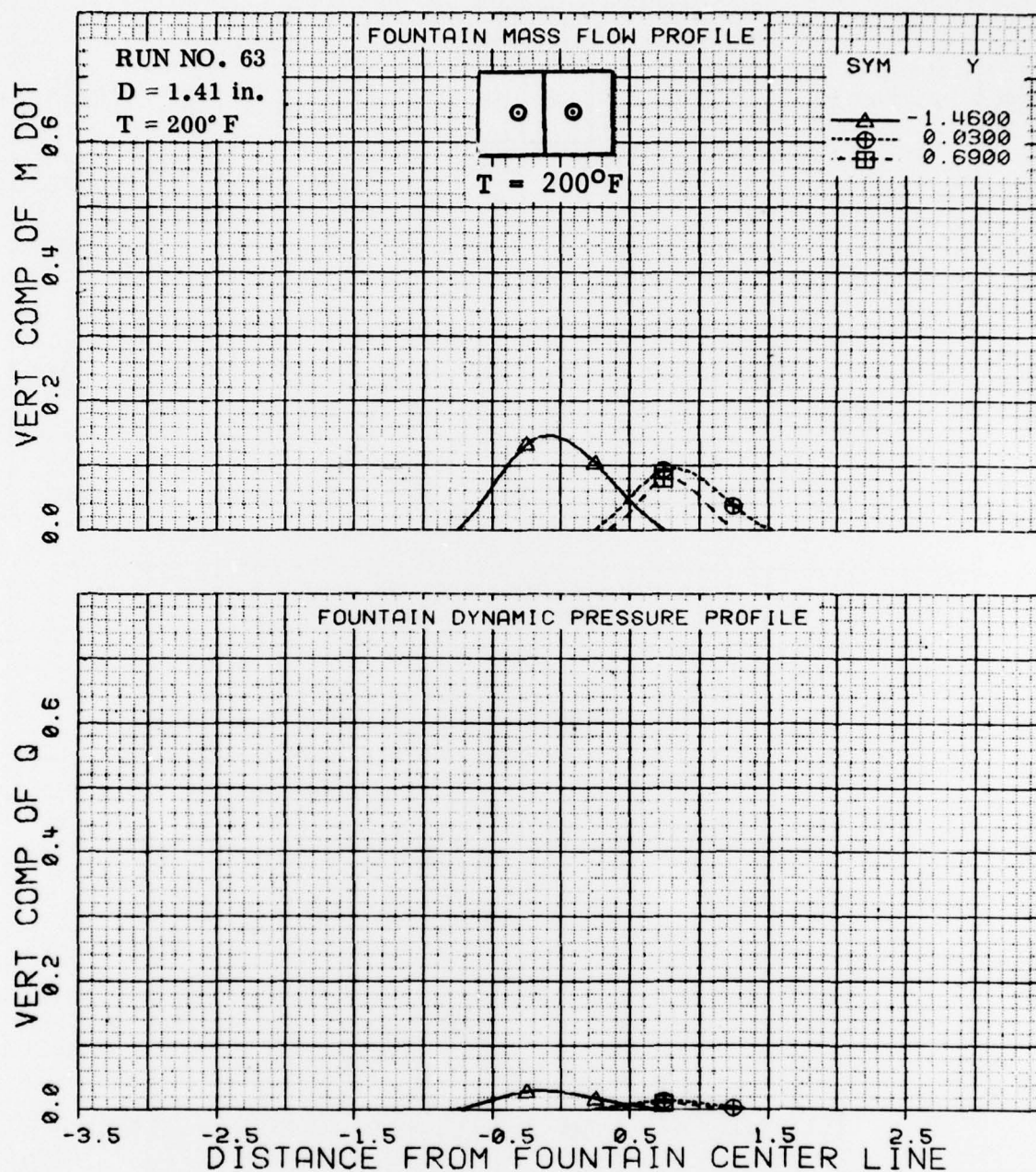


Figure B-43 Mass Flow and Dynamic Pressure Profiles with Two Nozzles
 at 200°F ; $d_f/D=3.32$, $h/D=5.05$, $z/D=3.82$

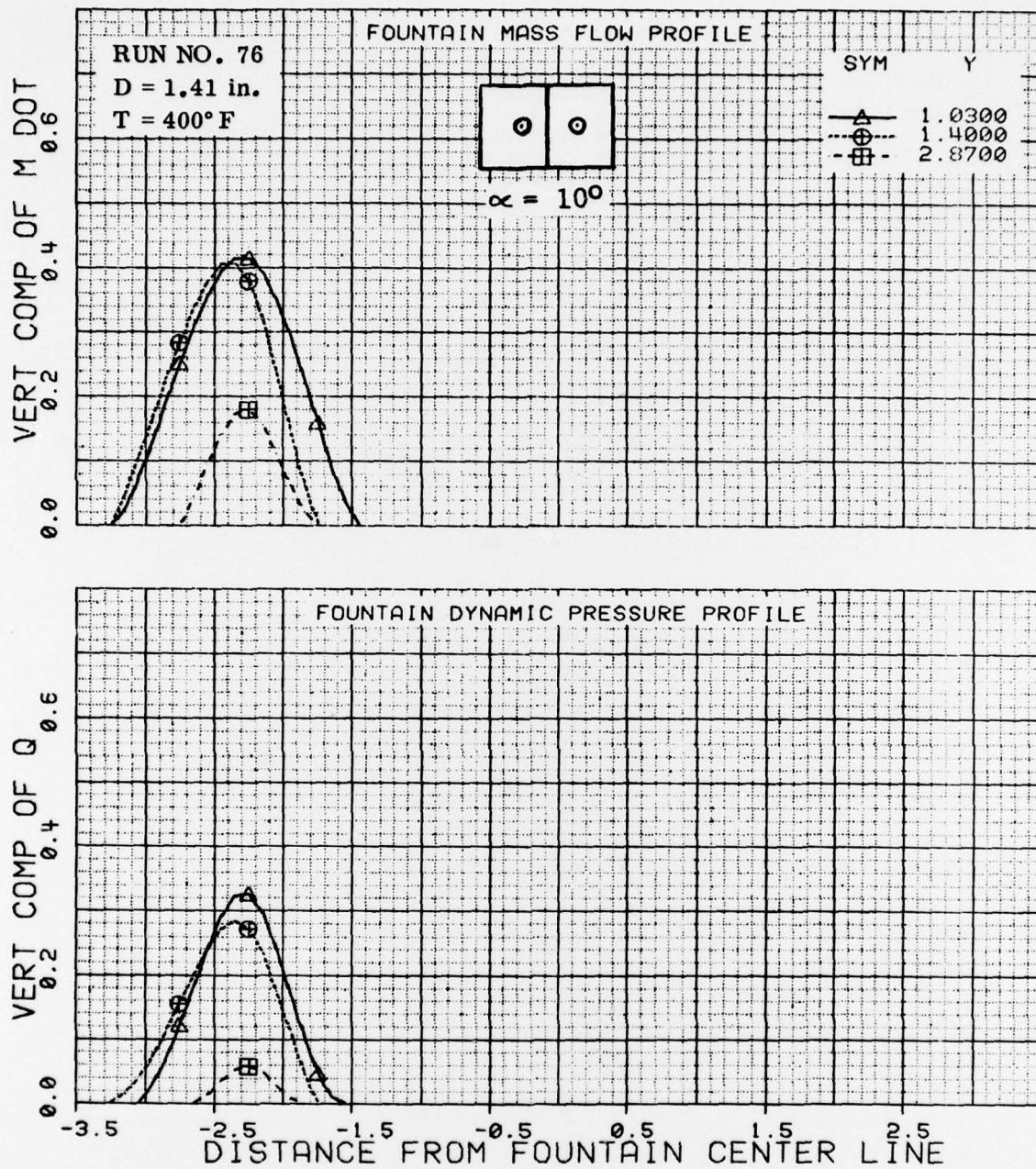


Figure B-44 Mass Flow and Dynamic Pressure Profiles with Two Nozzles
 Pitched 10° ; $d_f/D=3.32$, $h/D=5.04$, $Z/D=1.50$

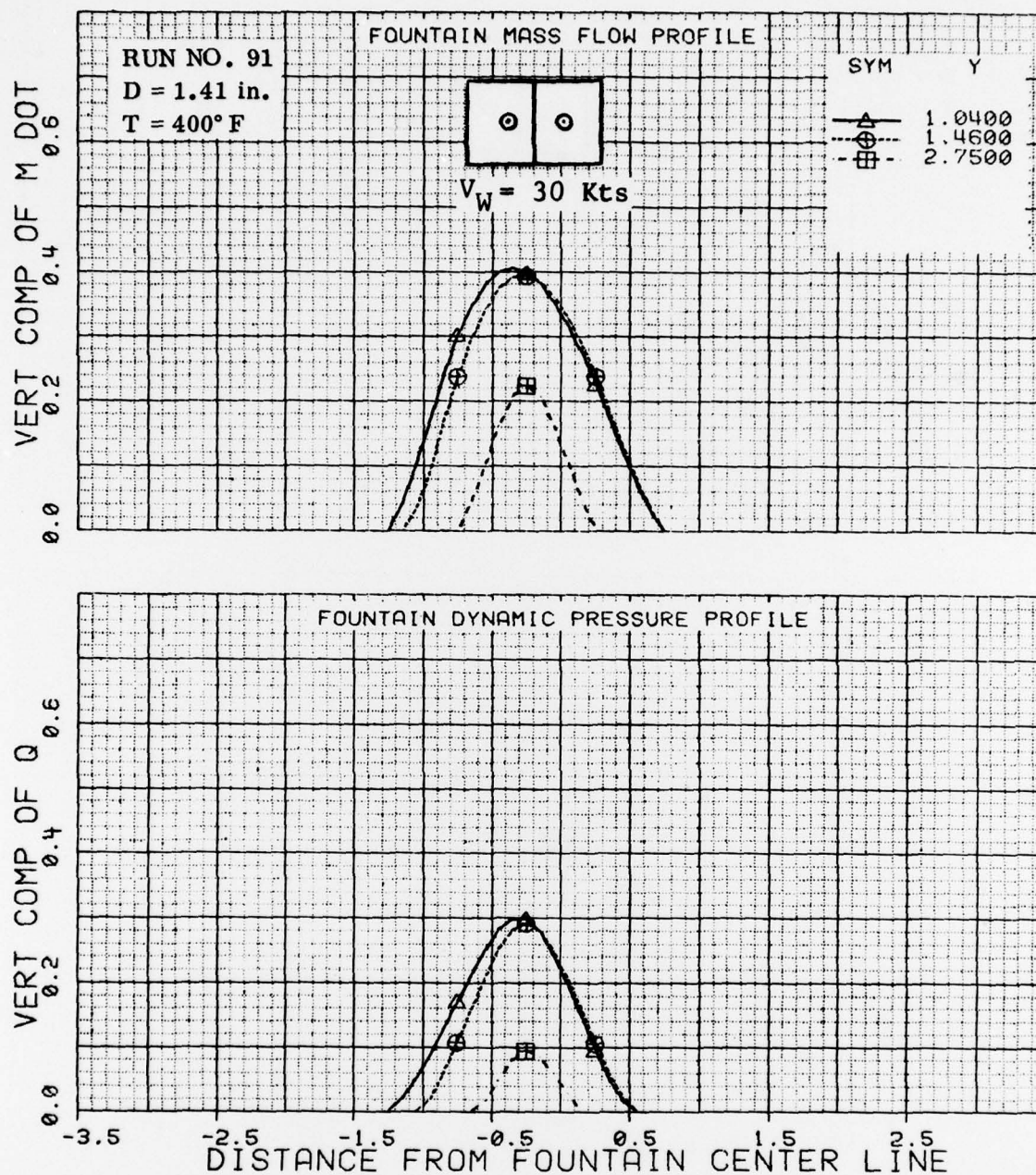


Figure B-45 Mass Flow and Dynamic Pressure Profiles with Two Nozzles in a 30 Knot Wind; $d_f/D=3.32$, $h/D=5.03$, $Z/D=1.50$

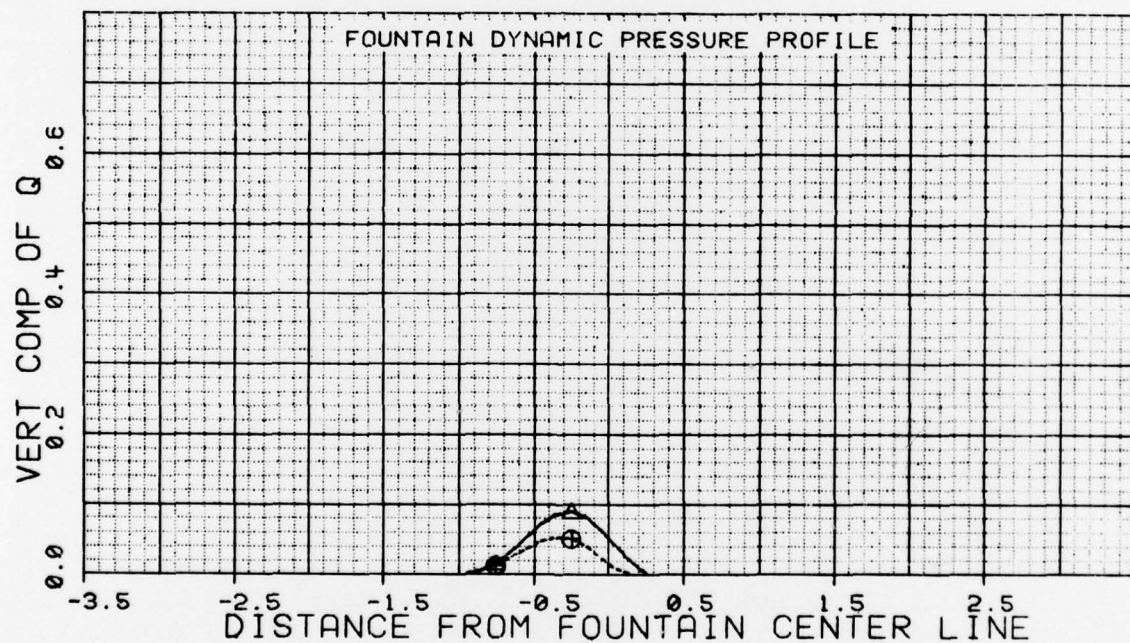
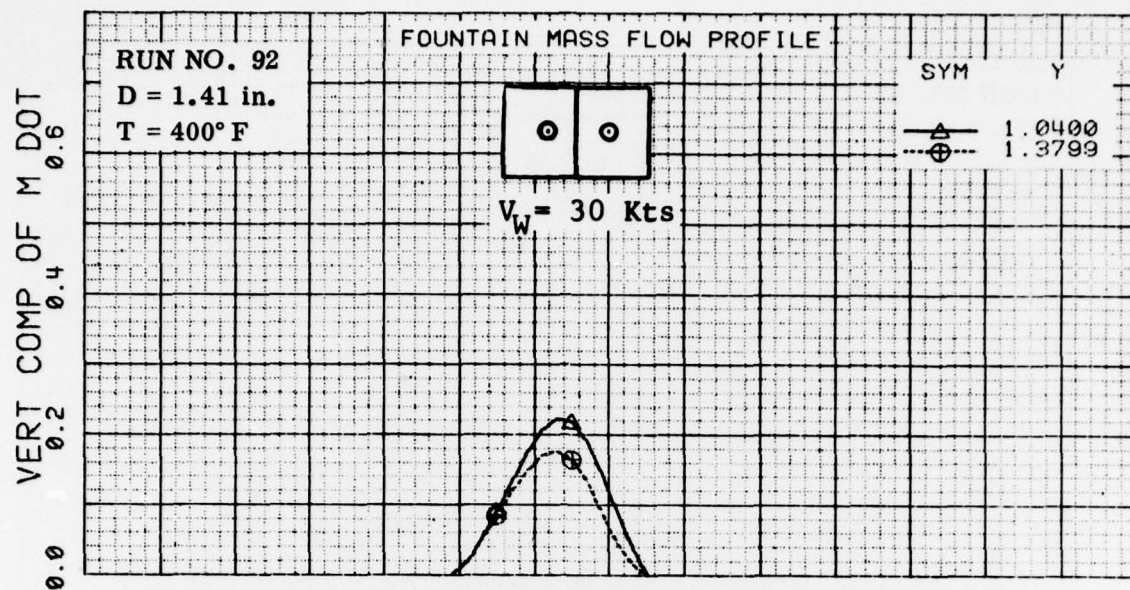


Figure B-46 Mass Flow and Dynamic Pressure Profiles with Two Nozzles
 in a 30 Knot Wind; $d/D=3.32$, $h/D=5.03$, $Z/D=2.48$

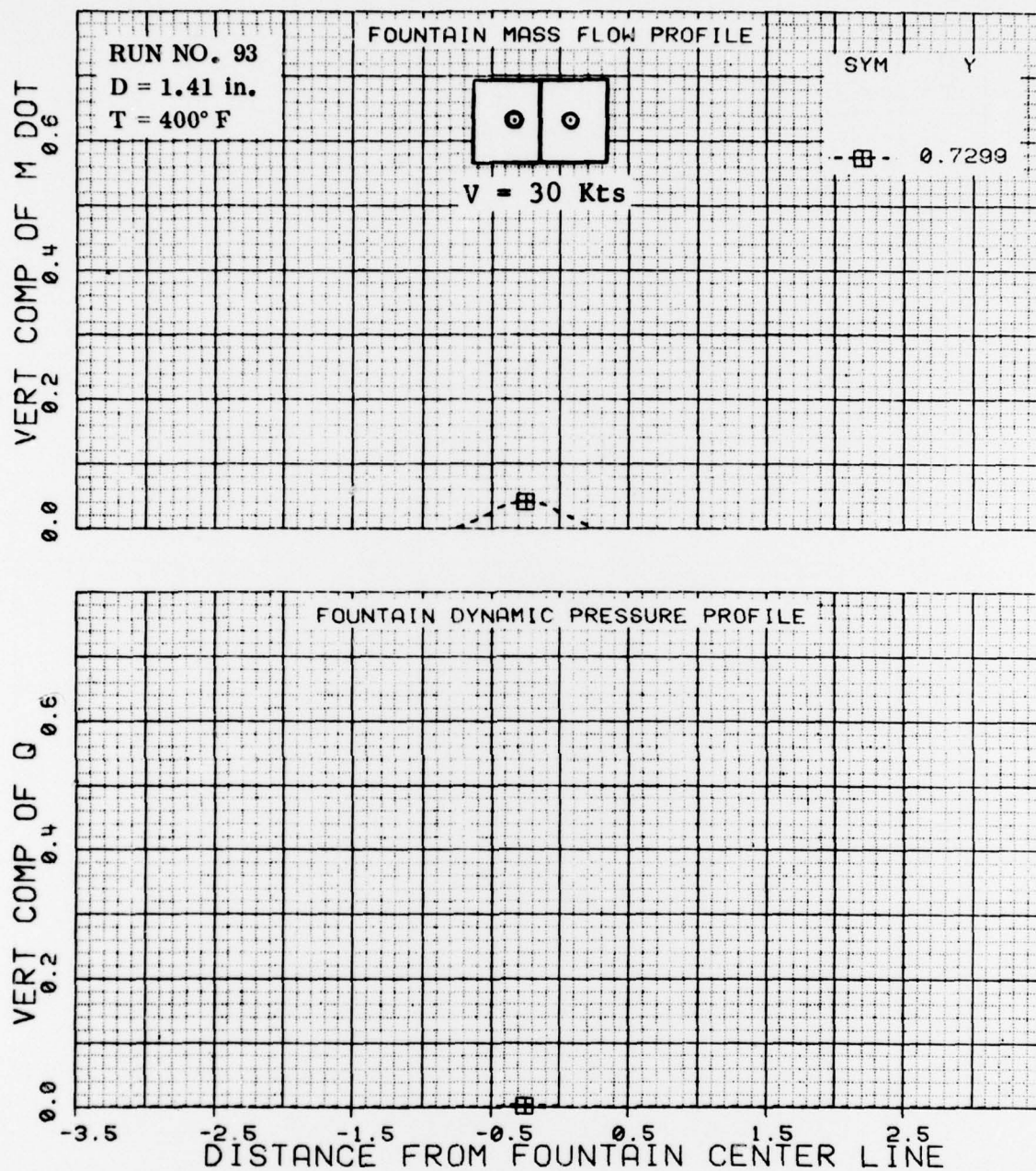


Figure B-47 Mass Flow and Dynamic Pressure Profiles with Two Nozzles in a 30 Knot Wind; $d_f/D=3.32$, $h/D=5.03$, $z/D=3.77$

DISTRIBUTION LIST

Office of Naval Research		David Taylor Naval Ship Research and	
800 N. Quincy St.		Development Center	
Arlington, VA 22217		Bethesda, MD 20084	
ONR 211	4	Code 16 (Dr. H. Chaplin)	1
ONR 430B	1	Code 1660 (Mr. J. Nichols)	1
		Code 1613 (Mr. R. Schaeffer)	1
		Code 522.3 Aero Library	1
Office of Naval Research Branch			
Office		U. S. Naval Postgraduate School	
1030 E. Green St.		Monterey, CA 93940	
Pasadena, CA 91106	1	Dept. of Aeronautics (Code 57)	1
		Library	
Office of Naval Research Branch			
Office		Superintendent	
Bldg. 114 Section D		U. S. Naval Academy	
666 Summer St.		Annapolis, MD 21402	1
Boston, MA 02210	1		
Office of Naval Research Branch		NASA Ames Research Center	
Office		Moffett Field, CA 94035	
536 South Clark St.		FAE Branch (Dr. T. Gregory)	1
Chicago, IL 60605	1		
Defense Contract Administration		NASA Langley Research Center	
Services Region		Hampton, VA 23665	
866 Malcolm Road		Mr. R. Margason	1
Burlingame, CA 94010	1		
Naval Research Laboratory		Wright Patterson Air Force Base	
Washington, DC 20375		Dayton, OH 45433	
Code 2627	1	Aero & Airfram Branch (Dr. T. Weeks)	1
Code 2629	1		
		Air Force Office of Scientific Research	
		Bolling AFB, DC 20332	
		Code NA (Dr. J. Wilson)	1
Defense Documentation Center			
Bldg. 5 Cameron Station		Defense Advanced Research Projects	
Alexandria, VA 22314	12	Agency	
		1400 Wilson Boulevard	
Naval Air Systems Command		Arlington, VA 22209	
Washington, DC 20361		Mr. R. Moore	1
AIR 320D (Mr. R. Siewert)	1		
AIR 5301-33B (Mr. Lynn Trobaugh)	1		
AIR 5301-33A (Mr. R. Weinraub)	1		
AIR 03PA (H. Andrews)	1		
AIR ADPO-16 (CDR E. Lewis)	1		

Naval Air Development Center Warminster, PA 18974 Code 6053 (Mr. C. Mazza)	2
Lockheed Missiles & Space Co., Inc. Huntsville Research & Engineering Center P.O. Box 1103 Huntsville, AL 35807 Mr. A. Zalay	1
Nielsen Engineering & Research, Inc. 510 Clyde Avenue Mountain View, CA 94043	1
McDonnell Douglas Aircraft Company P.O. Box 516 St. Louis, MO 63166 Aerodynamics (Dr. D. Kotansky) Propulsion (Mr. J. Kamman)	1 1
Vought Corporation Advanced Technology Center, Inc. P.O. Box 6144 Dallas, TX 75222 Dr. John Porter	1
Grumman Aerospace Corporation Bethpage, NY 11714 Research Dept. (Dr. R. Melnik) Advanced Dev. Dept. (Mr. F. Berger)	1 1
McDonnell Douglas Research Laboratories St. Louis, MO 63166 Dr. W. Bower	1
Rockwell International Columbus Aircraft Division Columbus, OH 43216 Research Dept. (Dr. P. Bevilaqua)	1